Raman Microscopic Studies of PVD Deposited Hard Ceramic Coatings

Christopher Paul Constable

A thesis in part fulfilment of the requirements of Sheffield Hallam University for the degree of Doctor of Philosophy

January 2000

Collaborating Organisation: Renishaw plc

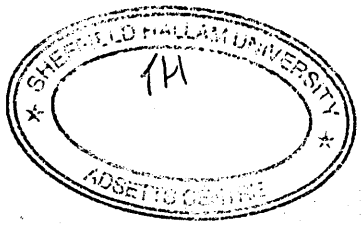
SHEFFIELD HALLAM UNIVERSITY
ADSETTS CENTRE

Declaration

The work described in this thesis was carried out by the author in the Materials Research Institute, Sheffield Hallam University, Sheffield, between October 1997 and December 2000. The author declares that this work has not been submitted for any other degree. The work is original except where acknowledged by reference.

Author :

(Christopher Paul Constable)

Supervisors:

(Professors Jack Yarwood and Wolf-Dieter Münz)

Acknowledgements

I would first like to acknowledge my supervisory team Prof. Jack Yarwood, Prof. Wolf-Dieter Münz (Sheffield Hallam University) and Prof. David Pitt (Renishaw plc), for their support and advice throughout this project. I would also like to thank Dr Brian Lewis (Big B) for help, guidance and being essentially my unofficial supervisor. Thanks also go out to past and present members of the Surface Engineering Group, especially Jörg, Uwe and Ralph.

Secondly, I'd like to thank my colleagues and friends at Sheffield for making the three years fun and for help and advice. Thanks go out to the Irish contingent Jeff (What are you on about?) and Paul (The Internet Lover), the French lot Christophe (AKA The Mad One), Delphine and Jean-Phillippe (The Short One), not forgetting the Brits Nigel, Paul H, Pierre, Jane, Chris S (The Lyricist), Franny and past members who have long gone Peda and Carine.

Huge thanks go to my family, especially my mum and dad for love and support throughout my academic career. My biggest thanks go to my fiancée Heather for her support and patience throughout my PhD, especially during the time of writing this thesis. I could not have done it without you.

This work is dedicated to my fiancée Heather Smillie and my parents Barbara and Aubrey Constable

Contents

Abstract

PVD hard ceramic coatings grown via the combined cathodic arc/unbalance magnetron deposition process were studied using Raman microscopy. Characteristic spectra from binary, multicomponent, multilayered and superlattice coatings were acquired to gain knowledge of the solid-state physics associated with Raman scattering from polycrystalline PVD coatings and to compile a comprehensive spectral database. Defect-induced first order scattering mechanisms were observed which gave rise to two pronounced groups of bands related to the acoustical (150-300cm^{-1}) and optical (400-750cm^{-1}) parts of the phonon spectrum. Evidence was gathered to support the theory that the optic modes were mainly due to the vibrations of the lighter elements and the acoustic modes due to the vibrations of the heavier elements within the lattice.

A study into the deformation and disordering on the Raman spectral bands of PVD coatings was performed. TiAlN and TiZrN coatings were intentionally damaged via scratching methods. These scratches were then analysed by Raman mapping, both across and along, and a detailed spectral interpretation performed. Band broadening occurred which was related to "phonon relaxation mechanisms" as a direct result of the breaking up of coating grains resulting in a larger proportion of grain boundaries per-unit-volume. A direct correlation of the amount of damage with band width was observed. Band shifts were also found to occur which were due to the stresses caused by the scratching process. These shifts were found to be the largest at the edges of scratches. The Raman mapping of "droplets", a defect inherent to PVD deposition processes, found that higher compressive stresses and large amounts of disorder occurred for coating growth onto droplets.

Strategies designed to evaluate the ability of Raman microscopy to monitor the extent of real wear on cutting tools were evaluated. The removal of a coating layer and subsequent detection of a base layer proved successful. This was then expanded to real wear situations in which tools were monitored after 3,6,12,64,120 and 130 minutes-in-cut. A PCA chemometrics model able to distinguish between component layers and oxides was developed.

Raman microscopy was found to provide structural and compositional information on oxide scales formed on the surfaces of heat-treated coatings. Wear debris, generated as a consequence of sliding wear tests on various coatings, was also found to be primarily oxide products. The comparison of the oxide types within the debris to those formed on the surface of the same coating statically oxidised, facilitated a contact temperature during sliding to be estimated.

Raman microscopy, owing to the piezo-spectroscopic effect, is sensitive to stress levels. The application of Raman microscopy for the determination of residual compressive stresses within PVD coatings was evaluated. TiAlN/VN superlattice coatings with engineered stresses ranging -3 to -11.3 GPa were deposited onto SS and HSS substrates. Subsequent Raman measurements found a correlation coefficient of 0.996 between Raman band position and stress (determined via XRD methods). In addition, there was also a similar correlation coefficient observed between hardness and Raman shift (cm^{-1}). The application of mechanical stresses on a TiAlCrN coating via a stress rig was investigated and tensile and compressive shifts were observed.

Chapter 1

Introduction

Chapter 1 Introduction

1.1 Objectives and Aims

The principal aim of this research was to investigate how the application of Raman microscopy to the analysis of PVD deposited hard coatings could be beneficial and complement an already established range of surface specific analytical tools. These include SEM and TEM, and other techniques such as X-ray diffraction, GDOES (Glow Discharge Optical Emission Spectroscopy), along with a range of physical testing equipment such as scratch testing, Pin-on-Disk, ball cratering and various indentation techniques. A gap was evident which Raman microscopy could potentially fill. The technique gives molecular information, a feature which none of the above-mentioned techniques could yield. In addition, Raman microscopy has additional desirable attributes, for example; it is non-destructive, rapid and requires very little sample preparation.

An understanding of the phenomenon of Raman scattering from ceramic hard coatings was sought. Only a handful of authors[1-4] had previously performed Raman spectroscopy on similar systems, the majority of work being concentrated on the analysis of TiN and other first-generation binary coatings e.g. ZrN and AlN. Second-generation multi-component coatings or the more advanced structured coatings i.e. multi-layered or superlattice coatings had not been explored.

It is well known that Raman spectroscopy can discern the effects of disorder/crystallinity in materials[5-9] via bandwidths and also changes in the stress state via spectral shifts. This has been performed routinely for polymer[10,11] and

various fibre types[12-14], ceramic materials[15] but not for ceramic hard coatings. There was therefore a definite niche for this type of research. Accordingly the study of spectral changes due to deformation and disorder on ceramic hard coating was investigated. Following on from this, changes in the Raman spectra caused by wear seemed a logical progression, and the development of a Raman based method for the quantification of the amount of wear on commercial cutting tools e.g. end mills, was performed. Included in this section was the development of a qualitative chemometrics model to enable distinction between similar coating spectra and oxides that occurred on tools in real wear situations.

Another important question that arose from the above work was whether Raman could measure/quantify coating residual stresses. This is an extremely important parameter and can affect many coating parameters such as adhesion and hardness. Therefore a study into the ability of Raman to discern stresses in ceramic hard coatings was performed. This was then expanded to the design and construction of a stress rig to study externally applied stresses and eventually to develop a piezo-spectroscopic calibration for various coating compositions.

1.2 The PVD (Physical Vapour Deposition) Coating Technique

PVD is a coating deposition process where one or more of the usually metallic constituents is physically vaporised from a solid (usually from a target) within a vacuum chamber to form a solid condensate on the substrate surface[16]. There are four basic types of PVD equipment in use today which all fall into the broad category of ion plating. The difference between the four is the way in which the source/target

material is vaporised (either evaporation or sputtering), the way the plasma is created, and the makeup of the plasma[17]. The four PVD hard coating techniques are low-voltage electron beam evaporation, cathodic arc deposition, triode high-voltage electron beam evaporation, and (most recently) unbalanced magnetron sputtering[18].

All of the above coating techniques are reactive processes. The metal species is vaporised from a target and a gas is fed into the coating chamber that then reacts with the metal species to form the desired compound, e.g., the use of titanium targets and a reactive gas of N_2 would result in the formation of TiN on the substrates.

The two processes that will be detailed further are cathodic arc and magnetron sputtering as these are the processes utilised by the Bodycote-SHU coating centre which was the source of all the coatings studied in this thesis. The collaboration of SHU, through the Materials Research Institute (Surface Engineering Group), with Bodycote PLC has resulted in a new commercial venture. Accommodation, personnel and technology are shared between the partners and successful cutting edge coating technology is transferred directly from R & D to production and is monitored as it moves directly into industrial applications.

1.2.1 Cathodic Arc Etching/Deposition

Cathodic arc processes use an electric arc which flash evaporates material from the surface of the target. As the evaporating material passes through the arc it becomes highly ionised. Estimates put the degree of ionisation as high as 90%. A high proportion of the reactive gas species is also ionised[17]. A potential problem with conventional cathodic arc processes is that they produce "macroparticles" or "droplets", which are particles of pure metal ejected from the surface of the target that become embedded in the coating structure. Cathodic arc discharges are also commonly used as metal ion sources to carry out, in vacuo, the pre-cleaning procedure in cathodic arc evaporation and combined cathodic arc(CA)/unbalanced magnetron processes(UBM)[18] which combined is given by the acronym ABS™ (Arc Bond Sputtering). By polarising the substrates with a negative bias voltage, typically –1200 V, metal ions generated during the vigorous evaporation of target material by CA initiate high "in vacuo" etching rates. In addition to this a proportion of the ions become implanted into the substrate material resulting in the formation of a graded substrate interface zone enriched with the elemental target species. Both the above effects have been shown to enhance practical adhesion, as measured by a scratch adhesion test[18]. During this etching step, "droplets" are generated. On top of which, "growth defects" are generated during the UBM sputtering phase, which extend through the growing film[18] (Figure 1.1: Petrov and Lobischler [19-21]).

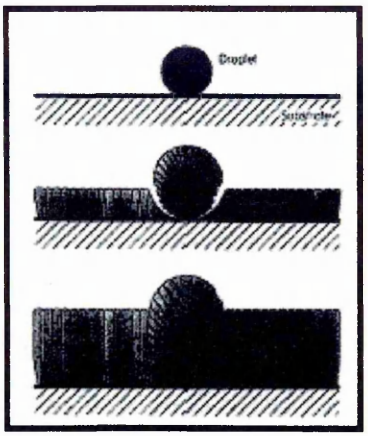

Figure 1.1 Droplet formation and subsequent defective growth

The growth defects contribute significantly to an increase in the coating micro roughness due to the presence of cone shaped defects (Figure 1.2 (below) shows a ESEM image of the surface of a PVD coating TiAlN/VN highlighting the problem of macroparticles).

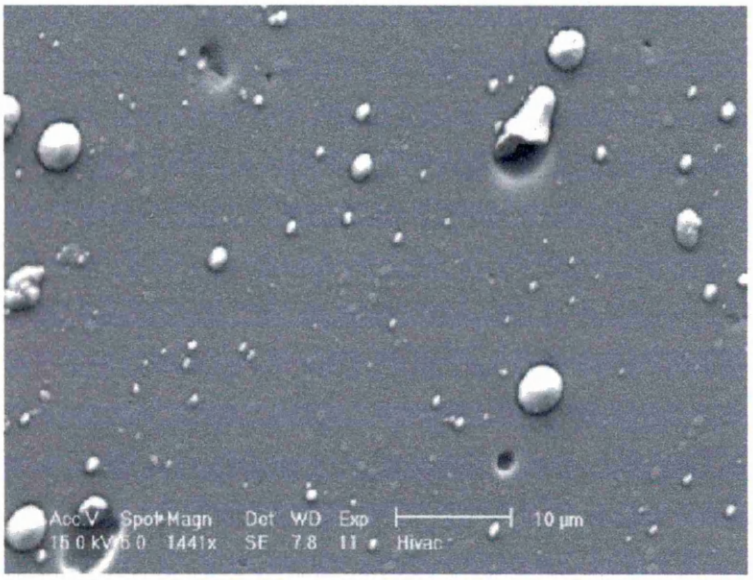

Figure 1.2 ESEM image showing growth defects

The existence of droplets and the subsequent occurrence of growth defects influences the performance of coated tools. Under severe conditions of dry drilling operations, the life of coated High-Speed-Steel (HSS) drills was markedly reduced. This was obviously due to a strong frictional effect brought about by the roughened

surface[16]. During cathodic arc metal-ion-etching a pronounced influence of the melting point of the target material on droplet formation was found[20,21]. Low melting point materials showed quite enhanced tendency to generate droplets with respect to number and size. The use of etching materials with high melting points e.g. Cr (1870°C) or Nb (2450°C) reduced the number and size of droplets on the etched samples, as well as the number of subsequent growth defects in the UBM deposited films.

Filtering or steering the arc evaporation process greatly reduces or eliminates the macroparticle problem, but there can be a reduction in the deposition rate when these techniques are applied.

1.2.2 Magnetron Sputtering

Conventional magnetron sputtering does not supply a dense plasma in the substrate region and is tightly confined to the face of the cathode[17]. Very little plasma expands into the region where the substrates are placed. For many applications where ion-bombardment can lead to damage in the film, such as in micro-electronic applications, this tight confinement is beneficial, but where high substrate ion bombardment is necessary, as with ceramic hard coatings, conventional magnetron sputtering does not supply the desired flux of ions. It was not until the magnetron cathode was unbalanced[22] that high substrate ion current densities of the order of 5 $mAcm^{-2}$ were found, (which matched those found in other successful PVD coating processes), that magnetron sputtering technology was realised. The effect of the unbalanced magnetic field is to trap the fast secondary electrons that escape from the

target surface. It is these electrons that undergo ionising collisions with gas atoms away from the target surface and produce a secondary plasma that can form in the region of the substrate. Ions from this secondary plasma are attracted to the negatively biased substrates, and this ion bombardment controls many of the properties of the growing film. The most efficient way of trapping fast secondary electrons is to arrange the magnets in the cathodes such that the magnets that face each other have opposite polarities, the magnetic fields close or link up with one another, forming an efficient three-dimensional trap. UBM systems with more than two cathodes like the Hauzer Techno Coating Europe B.V HTC 1000-4 ABS PVD coating unit used by the Bodycote-SHU coating centre, (Figure 1.3 below), also require that the magnetic field lines from each cathode link up with the next nearest cathode to achieve good trapping of electrons. The magnetic trap is closed effectively in a multicathode system only when there is an even number of cathodes. Odd numbers of cathodes lead to a hole from which electrons can escape[23].

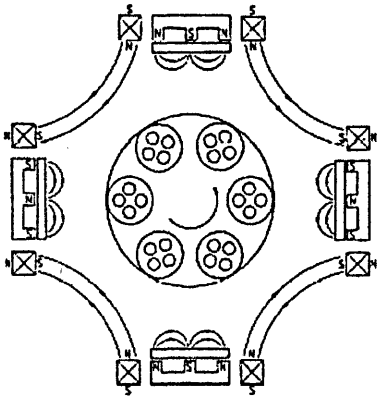

Steps Involved	
i)	Pump down to ~ 6.5 x 10^{-5} mbar and heating to ~400°C
ii)	Metal ion etch e.g. Ti or Cr ions
iii)	Reactive deposition e.g. TiN
iv)	Cool down and venting

N.B. N and S: north and south poles of the permanent and the electromagnets (For a brief description of their use, see below).

Figure 1.3 Schematic cross-section of the combined arc-magnetron (Hauzer B.V HTC 1000-4 ABS multi-cathode) PVD coating unit[37]

The magnets positioned directly behind the targets are for sputter mode or alternatively they maybe withdrawn for steered arc mode. The unbalancing effect is achieved using the electromagnets displaced around each cathode.

Magnetron sputtering has developed rapidly over the last decade to the point where it has become established as the process of choice for the deposition of a wide variety of industrially important coatings[24]. In many cases, magnetron sputtered films now out perform films deposited by other PVD processes, and can offer the same functionality as much thicker films produced by other surface coating procedures.

1.2.3 Substrate Ion Bombardment

The ion bombardment during the growth of the film provides energy to the atoms arriving at the surface of the growing film, allowing them to move around on the surface and find energetically favourable sites. This ion bombardment also results in re-sputtering and forward sputtering of the surface atoms. The sputtering then fills voids that would naturally occur along the columnar grains from shadowing effects. Forward sputtering places atoms in interstitial sites, which results in compressive residual stresses in the PVD coatings. Ion bombardment of the growing film results in energy being transferred to the film and substrate, and energy or heat is beneficial to the properties of the hard coatings. For tool steel substrates, the coating process typically operates at a substrate temperature of 450°C, but for other engineering alloys such a high coating temperature results in a softening of the substrate during coating. Too much ion bombardment can result in overheating the substrate that becomes more

critical as the application for hard coatings moves away from the more traditional tool coatings.

All these factors have to be taken into account before achieving hard, dense and well-adhered coatings.

1.2.4 Influence of Deposition Parameters on the Properties and the Microstructure of Magnetron Deposited Coatings

During the PVD process, the film material is usually deposited atom by atom on a substrate by condensation from the vapour phase to the solid. The condensation step cannot be considered as a random impingement of atoms, which stick on the growing surface at the point of impact, due to the development of interatomic attractive/repulsive forces, thermal mobility and surface defects. A four stage dynamic process generally occurs. First, the nucleation of single atoms on the surface occurs. These atoms then join together to form islands and the islands then coalesce. Finally, the continuous growth of the film takes place. If the atoms are deposited at a low substrate temperature the condensed atoms do not have sufficient kinetic energy and surface mobility to reach positions that are favourable i.e. of lower potential energy. Similarly for high deposition rates, the adatoms have insufficient time to find low energy sites before additional layers bury them.

The relationship between the substrate temperature and the microstructure can be represented by a STRUCTURE ZONE MODEL (Movchan and Demchishin Figure 1.4, [25]).

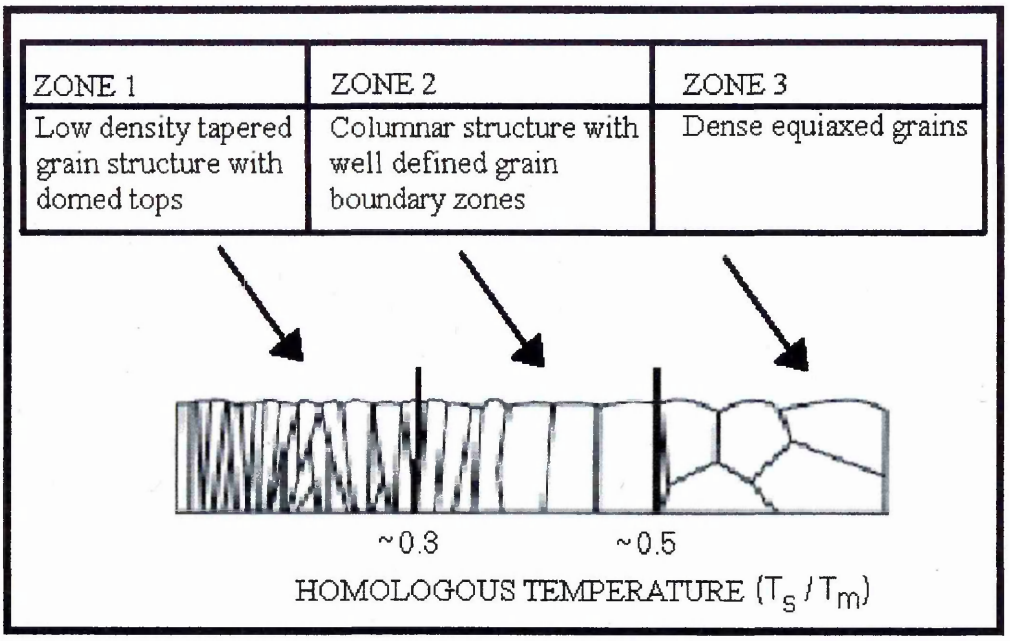

Figure 1.4 Structure Zone Model

T_s = substrate temperature during deposition; T_m = melting point of the coating material (in Kelvin). As Ts/Tm approaches 1.0, the coating density approaches bulk material density.

Ceramics have relatively high T_m values; therefore very high substrate temperatures would be needed to give fully dense ceramic coatings. Such high temperature would limit the choice of substrate material. It should be noted that the T_s/T_m values quoted in the model are lowered for ion assisted deposition techniques.

1.3 PVD Coating Architecture

1.3.1 Binary Coatings

The most widely used of all PVD coatings is TiN and this is a good example of a binary coating. Such coatings usually involve one metallic component, such as Ti, Cr, Nb, Al, Ta, Zr, V and W, etc. reactively sputtered with nitrogen as the reactive

gas, producing the desired compound. These coating types were developed first due to their relative ease of deposition. Much of the development in PVD coatings has been aimed at tooling applications, but most can be used in many different applications. A good example of this is TiN itself. It was first used on tools, but today it is used for tribological coatings, anticorrosion, microelectronic, and decorative applications.

Work on improving TiN has in the past concentrated on adding additional elements to the compound, e.g. Al, Cr and Y, to make a multicomponent compound with three or more constituent elements. These are not always metallic elements as carbon within the lattice can give desirable properties especially for tribological applications as the carbon can act as a solid lubricant[26].

1.3.2 Multicomponent Coatings

Adding the new element(s) changes the properties of the coatings such that the new coatings can operate at higher temperatures or are more wear resistant. TiAlN and TiCN are good examples of this. Many workers have been involved in the development of TiAlN coatings [27-29]. They have shown that the cubic NaCl structure is maintained as aluminium and is substituted for titanium in TiN to form TiAlN until the ratio exceeds approximately 1:1. This substitution is known to be at random from XRD measurements. Additional reflections would be observed if this substitution lead to an ordered system. Figure 1.5 (below) shows the TiAlN unit cell.

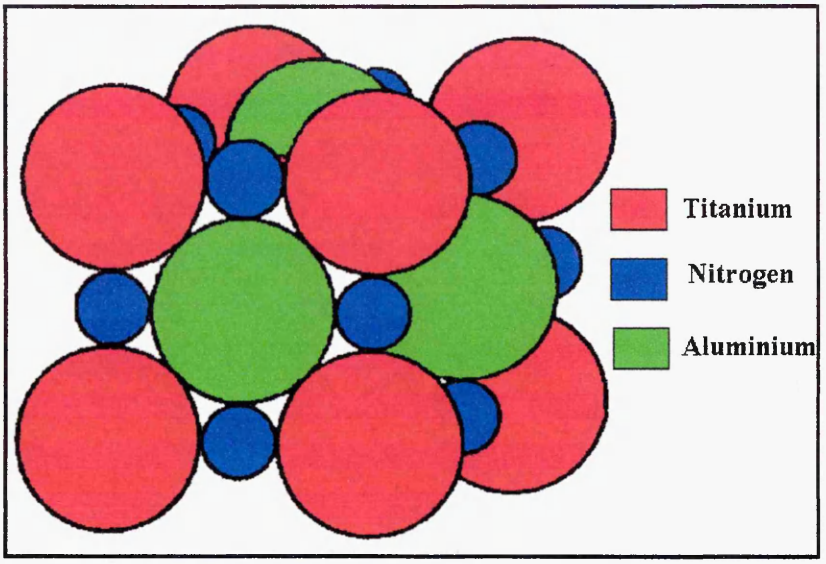

Figure 1.5 TiAlN unit cell

The cubic TiAlN structure is metastable, and will separate into TiN and AlN if heated to high temperatures. The main advantage of TiAlN is that it has higher oxidation resistance than TiN. TiN starts to oxidise at about 500°C whereas TiAlN does not start oxidising until about 700°C (see Figure 1.6). This has made TiAlN very attractive as a wear resistant barrier for high-speed cutting. The majority of Bodycote-SHU commercial coatings are based on TiAlN. The addition of small amounts of other elements such a Cr, Y and C have been shown to further enhance the properties of TiAlN, especially the wear resistance through increased hardness (due to increased residual stresses and solid solution hardening) and oxidation resistance[30]. $TiAlCr_{(3at\%)}N$ does not start to rapidly oxidise until 920°C and $TiAlCr_{(3at\%)}Y_{(2at\%)}N$ until 950°C[30,31]. (Figure 1.6 shows a TGA (Thermo Gravimetric Analysis) plot comparing the Mass Gain vs. Temperature for the aforementioned coatings[30]).

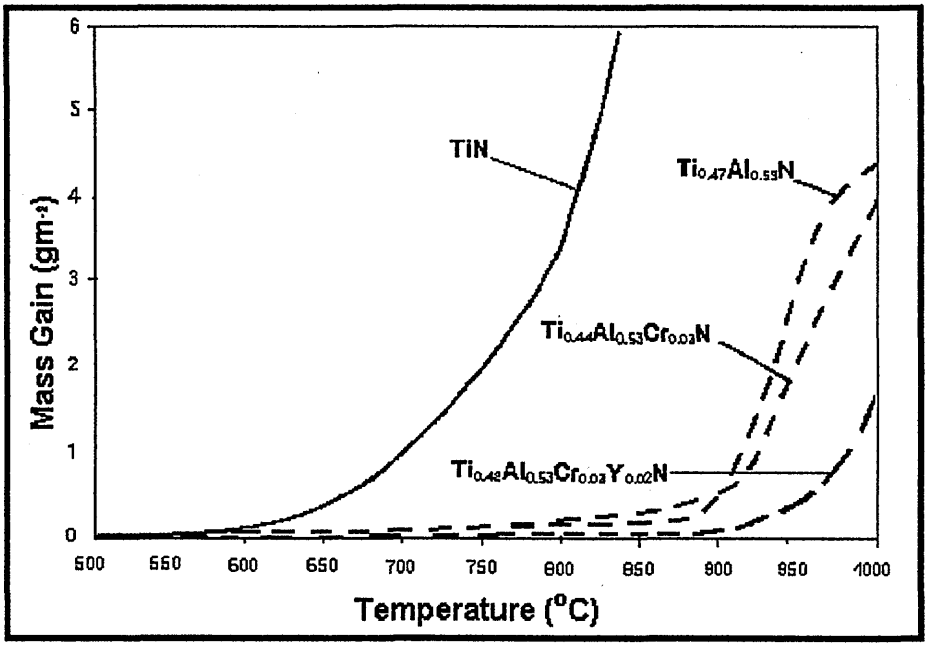

Figure 1.6 TGA trace demonstrating Al, Cr and Y all increase oxidation resistance when incorporated in the TiN lattice

1.3.3 Multilayered and Superlattice Coatings

Holleck, in his work designed to improve hard coatings[32-34], recommended that PVD coatings be deposited as a series of alternating layers of two coatings. He also suggested that such a multilayer would have added toughness and hardness (compared to single-component coatings) because favourable low-energy interfaces would be effective in dissipating energy within the layers, as long as there was coherency at the interfaces. A relatively recent idea for multilayer PVD coatings that has proved successful was that of "superlattice" coatings. Holleck and Schier[34] classified them as "Isostructural single layer materials, similar in chemical bonding, similar atomic radii and lattice distances and a single layer thickness in the size of lattice dimensions". "If these conditions are met, entirely new materials, with properties and characteristics not directly related to the individual layer materials result". There is usually a large increase in hardness and strength when the multilayer superlattice

period, (which is the smallest bi-layer repeated period), is of the order of 5 to 10nm. (Figure 1.7 shows an XTEM micrograph of a TiAlN/CrN superlattice coating[35]).

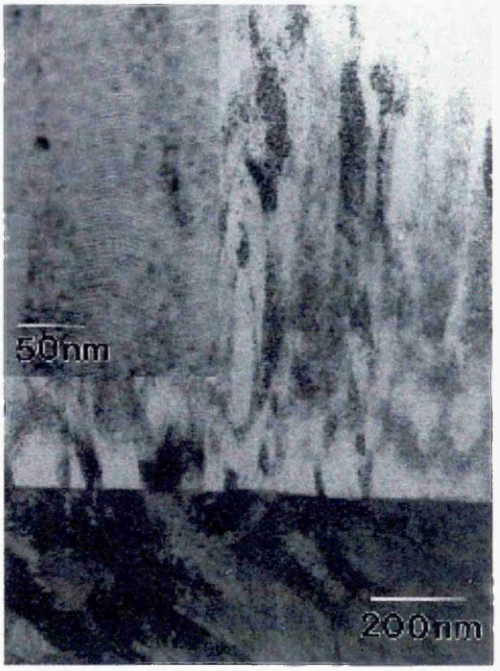

Figure 1.7 XTEM micrograph of a TiAlN/CrN superlattice coating; showing columnar polycrystalline structure in the TiAlN base layer and TiAlN/CrN top layer, (insert shows higher magnification, indicating multilayered structure).

The higher hardness in these superlattice coatings is due to several factors, all of which relate to restricted dislocation movement. For these superlattice coatings to achieve high hardness, there should be coherency at the interfaces between layers but there is always some mismatch between the lattices that leads to strain at the interfaces[34]. It is thought that the strain at the coherent interface restricts the movement of dislocations and increases the hardness of the material. Another factor that influences dislocation movement is the thickness of the individual layers. When the layer thickness is small, dislocation sources cannot operate, and again dislocation movement is restricted[34]. The third factor is the energy required to move a dislocation from one material to the other (i.e. shear modulus), the higher this

difference the better. Another favourable property is higher crack propagation resistance. The mechanism for this is thought to be due to a crack deflection process in which cracks are deflected along the multilayer interfaces similar to delamination where a number of layers are lost, as opposed to cracks in monolithic coatings which propagate to the substrate and result in coating failure.

PVD processes are well suited to deposit multilayer coatings in the range 100 to 1500 individual layers, resulting in high fractions of interface volume, allowing strength and toughness of the coating to be adjusted. Proper materials selection and the adjustment of number and thickness of the single layers[36,37] as well as the stress and strain of the coating contribute to an exceptionally high wear reduction for many applications[34].

1.4 The Applications of PVD Coatings

PVD coatings possess many favourable physical parameters such as hardness, aesthetically pleasing appearance, wear resistance, oxidation resistance, chemical inertness, wide-band-gap etc. These all lend PVD coatings to a variety of uses.

The obvious application for PVD hard coatings is for wear resistance and protection of cutting tools for the automotive and aerospace industries. Today there are three primary PVD tool coatings TiN, TiCN and $Ti_{(0.5)}Al_{(0.5)}N$. In addition there are slight modifications of the TiAlN by addition of small amounts of other elements to further enhance the properties. There are also other coatings such as ZrN, TiZrN, diamond-like-carbon (DLC) that can be used also but are not as popular as the aforementioned.

TiN, the first really successful PVD tool coating, is the most universal tool coating and traditionally has been tried before all other coatings because it is easiest to apply (and cheapest). It can be applied by all four PVD tool coating processes, and PVD TiN is a fully dense, very hard (2200HK) coating with a very pleasing gold-like colour. PVD TiN was first used on HSS tooling because it could be applied below 500°C (the temperature at which most HSS starts to soften). The advantages of PVD TiN soon became apparent to the cemented carbide industry, and in 1985 the first PVD TiN coated cemented carbide cutting tool inserts were introduced for milling applications[23]. For carbide tooling, the lower PVD deposition temperature prevented the formation of brittle phases. Also the PVD coatings can be applied to sharp edges, unlike CVD coatings[38]. TiCN is produced commercially today using all four PVD processes. Titanium is vaporised either by evaporation or sputtering and two reactive gases, nitrogen and methane, are used to combine with Ti to form TiCN. TiCN offers better wear resistance and toughness than TiN in high speed milling applications and in cutting some abrasive materials such as cast iron or aluminium-silicon[23]. $Ti_{(0.5)}Al_{(0.5)}N$ was first developed and used in Europe[27,28], but quickly spread across the world. This performed better than both TiN and TiCN because of its higher oxidation resistance at >700°C. Also an amorphous layer of Al_2O_3 forms on the surface of the coating that prevents degradation of the coating. It is usually made by sputtering targets of 50-50 at % titanium and aluminium (made from a mechanical alloying process from powders or by casting a TiAl intermetallic material). Another example of tooling applications is TiN-coated HSS circular saw blades for machining tool steel[39]. There are still, however, problems in making low friction coatings that are oxidation resistant, which is important for high-speed-cutting in order to decrease the torque on the spindle. The addition of carbon-enriched layers in TiAlN has shown

much promise in high temperature and high-speed-cutting applications because of a reduction in the friction coefficient due to carbon diffusion to the surface, the fine grain size and high hardness[40].

Other applications include (1) coatings for die-casting dies to protect the steel surface from erosion and soldering of aluminium and improve the resistance against thermal cracking[41], (2) Cr_xN coatings for piston rings to replace electroplated chromium layers[42] and for machine parts and moulds for plastic transformation processes to protect against corrosive agents evaporating from plastics at elevated temperatures and hard fibres (i.e. for reinforced plastics)[43], (3) TiN as a protective coating for vacuum deposition chambers to enable ease of removal of soft metals by either chemical cleaning or glass bead blasting[44] and (4) biocompatible coatings such as DLC, CN and TiN for human prosthetic devices on both metallic and polymeric substrates (e.g. artificial hip joints)[45,46]. Other fields of application include electronics[47], reflective coatings and passive diffusion barriers. Another novel application is for glass moulding applications where the sticking of the molten glass to the mould can be prevented[48]. The high oxidation resistance and low surface roughness of TiAlCrYN lends itself to this application[48].

References

1 C.C. Chen, N.T. Liang, W.S. Tse, I.Y. Chen, J.G. Duh, Chin. J. Phys. 32(2) (1994) 205.

2 W. Spengler, R. Kaiser, Solid State Commun. 18 (1976) 881.

3 W. Spengler, R. Kaiser, A.N. Christensen, G. Muller-Vogt, Phy. Rev. B 17(3) (1978) 1095.

4 W. Spengler, R. Kaiser, H. Bilz, Solid State Commun. 17 (1975) 19.

5 R.K. Islamgaliev, R. Kuzel, E.D. Orbraztsova, J. Burianek, F. Chmelik and R.Z. Valiev, Mater. Sci. Eng. A2 49 (1998) 152.

6 H. Hobert, H. Dunken, R. Menzel, T. Bachmann and W. Wesch, J. Non-cryst. Solids, 220 (1997) 187.

7 C. Uzan-Saguy, C Cytermann, R. Brener, V. Richter, M shaanan, R. Kalish, Appl. Phys. Lett. 67 (1995) 1194.

8 R. Kalish, A. Reznik, K.W. Nugent and S. Prawer, Nuc. Instr. Meth. Phys. Res. B 148 (1999) 626.

9 G. Pezzotti, Comp. Sci. Techno. 59 (1999) 821.

10 T. Kitagawa, K. Yabuki and R.J. Young, Polymer 42 (2001) 2101.

11 Y.-N. Wang, C. Galiotis and D.L. Bader, J. of Biomechanics, 33 (2000) 483.

12 X. Yang and R.J. Young, British Ceramic Transactions 93(1) (1994) 1.

13 X. Yang and R.J. Young, Composites 25(7) (1994) 488.

14 S. Narayanan and L.S. Schadler, Comp. Sci. Technol. 59 (1999) 1589.

15 I. De Wolf, G. Pozzat, K. Pinardi, D.J. Howard, M. Ignat , S.C. Jain and H.E. Maes, Microelectron. Reliab., 36(11/12) (1996) 1751.

16 K.S. Fancey, A.Matthews Surf. Coat. Technol. 33(1-4) (1987) 17.

17 W-.D. Sproul, J. Vac. Sci. Technol. A12 4(1) (1994) 1595.

18 W-.D. Münz, Surf. Coat. Technol. 48 (1991) 81.

19 I. Petriv, P. Losbichler, D. Bergstrom, J.E. Greene, W-.D. Münz, T. Hurkmans and T. Trinh, Thin Solid Films 302 (1997) 179

20 W-.D. Münz, I.J. Smith, D.B. Lewis and S. Creasey, Vacuum 48(5) (1997) 473.

21 S. Creasey, D.B. Lewis, I.J. Smith and W-.D. Münz, Surf. Coat. Technol. 97(1-3) (1997) 163.

22 B. Window and N. Savrides, J. Vac. Sci. Technol. A 4 (1986) 196.

23 W.D. Sproul, Surf. Coat. Technol. 81 (1996) 1.

24 P.J. Kelly and R.D. Arnell, Vacuum 56 (2000) 159-172.

25 B.A. Movchan and A.V. Demchishin, Phys. Met. 28 (1969) 83.

26 C.P.Constable, J. Yarwood, P. Hovsepian, L.A. Donohue, D.B. Lewis and W.D. Münz, J. Vac. Sci. Technol. A 18(4) (2000) 1681.

27 O. Knotek, M. Böhmer and T. Leyendecker, J. Vac. Sci. Technol. A 4 (1986) 2695.

28 W-.D. Münz, J. Vac. Sci. Technol. A 4 (1986) 2717.

29 D. McIntyre, J.E. Greene, G. Häkansson, J-.E. Sundgreen and W-.D. Münz, J. Appl. Phys. 67 (1990) 1542.

30 I.J. Smith, D. Gillibrand, J.S. Brooks, W-.D. Münz, S. Harvey, R. Goodwin, Surf. Coat. Technol. 90 (1997) 164.

31 D.B. Lewis, L.A. Donohue, M. Lemke, W-.D. Münz, R. Kuzel Jr., V. Valvodo and C.J. Blomfield, Surf. Coat. Technol. 114 (1999) 187.

32 H. Holleck, J. Vac. Sci. Technol. A 4 (1986) 2661.

33 H. Holleck, J. Vac. Sci. Technol. 36 (1988) 151.

34 H. Holleck and V. Schier, Surf. Coat. Technol. 76-77 (1995) 328.

35 Q. Luo, W.M. Rainforth, L.A. Donohue, I. Wadsworth and W.D. Münz, Vacuum 53 (1999) 123.

36 L.A Donohue, J. Cawley, D.B. Lewis, J.S. Brooks and W-.D. Münz, Surf. Coat. Technol. 76-77 (1995) 149.

37 W.-D. Münz, L.A. Donohue. P.Eh. Hovsepian, Surf. Coat. Technol. 125 (2000) 269.

38 W. Sproul, Cutting Tool Eng., 46(1) (1994) 52.

39 D.B. Lewis, S.R. Bradbury and M.Sarwar, Surf. Coat. Technol. 82 (1996) 187.

40 Jorg Neidhardt, Diploma Thesis "Comparison of Structure and Properties of Various Carbon-Enriched TiN, TiAlN Based Coating Systems", Sheffield Hallam University, Materials Research Institute 1999.

41 C. Mitterer, F. Holler, F. Üstel and D. Heim, Surf. Coat. Technol. 125 (2000) 233.

42 C. Friedrich, G. Berg, E. Broszeit, F. Rick and J. Holland, Surf. Coat. Technol. 97 (1997) 661.

43 L. Cunha, M. Andritschky, K. Pischow and Z. Wang, Thin Solid Films 355-356 (1999) 465.

44 S. Komiya, N. Umezu and C. Hayashi, Thin Solid Fils 63 (1979) 341.

45 J. Narayan, W.D. Fan, R.J. Narayan, P. Tiwari and H.H. Stadelmaier Mater. Sci. Eng. B25 (1994) 5.

46 R.J. Narayan, Q. Wei, A.K. Sharma, J.J. Cuomo and J. Narayan, Mat. Res. Symp. Proc. 526 (1998) 355.

47 L.E. McNeil, J. Am. Ceram. Soc. 76(5) (1993) 1132.

48 G. Kleer, W. Doell, Surf. Coat. Technol., 94-95 (1997) 647.

Chapter 2

Raman Spectroscopy

Chapter 2: Raman Spectroscopy

2.1: Introduction and History

The Raman effect was first predicted theoretically by Brillouin[1] in 1922 and then by Smekal in 1923[2]. Raman and Krishnan however made the first experimental observation in 1928[3]. They discovered that the (visible) wavelength of a small fraction of the radiation scattered by certain molecules differs from that of the incident beam and furthermore that the shifts in wavelength depend on chemical structure of the molecule responsible for the scattering. C.V. Raman was awarded the 1931 Nobel Prize for Physics for the discovery and exploration of the phenomenon [4]. Initially there was a great deal of excitement at this new discovery. This soon diminished, as technologies at the time were not advanced enough to gain a reasonable throughput. It was not until the late 50's and early 60's with the invention of Lasers that progress was made. Since then there have been a steady stream of technological advancements that have benefited Raman spectroscopy. These include holographic notch filters and very sensitive charge coupled device detectors (CCDs). The coupling of a Raman spectrometer with an optical microscope was then implemented[5] resulting in a Raman microscope which enables the user to obtain high quality spectra from micrometer-sized particles[5,6]. These advances have resulted in many more research groups and commercial companies realising the potential of Raman microscopy (see section 2.3).

Raman microscopy today is still primarily considered as a research tool. However, as technology continues to improve the technique will find a greater part to play in industry (for an example see chapter 5 (section 5.2)).

2.2 The Raman Effect

When a substance is irradiated with a monochromatic beam of laser light, most of the photons are scattered elastically with no change in frequency. This is termed Rayleigh scattering and is >99% of all the scattered light. A very small proportion of the incident photons (<0.1%) are scattered inelastically and either gains energy (anti-Stokes; the resultant scattered photons are higher in frequency than the incident radiation) or loses energy (Stokes; the resultant scattered photons are lower in frequency (see figure 2.2)). Therefore a spectrum, featuring a set of bands at particular frequencies characteristic of the substance under investigation, results. Figure 2.1 (below) shows the above processes schematically. In addition to the above processes much of the light can be reflected without interaction. This is especially the case for materials with metallic properties.

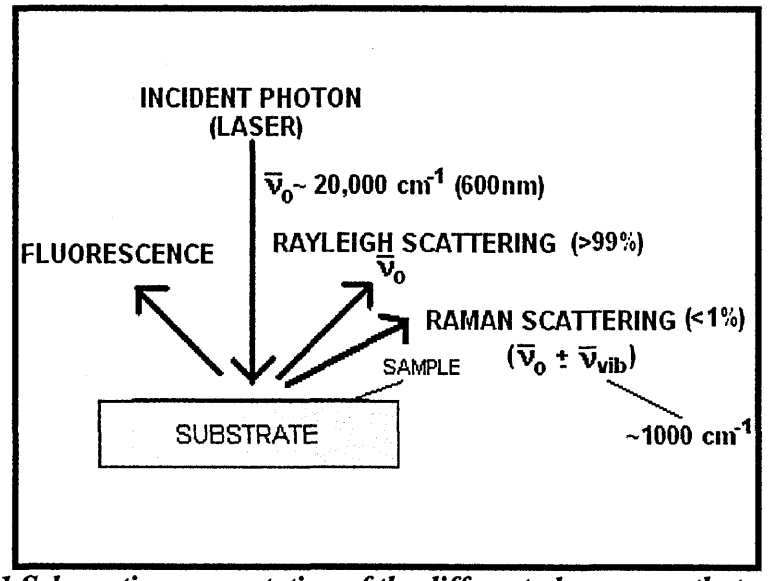

Figure 2.1 Schematic representation of the different phenomena that occur when laser light is incident on a sample. (N.B. fluorescence is discussed in section 2.2.4.2 of this chapter)

2.2.1 Classical Theory of Raman Scattering

When a molecule is placed in an electric field, there is a change in the distribution of electrons within the electron cloud surrounding the molecule i.e. the shape is changed. This is due to the electrons being displaced in the direction of the positive pole of the field and the predominantly positive nucleus being attracted to the negative pole. This separation of charge results in an induced dipole moment. This dipole moment, μ, is proportional to the electric field strength, ε, and the polarisability of the molecule in question, α.

$$\mu = \alpha\ \varepsilon \qquad \textbf{Equation 1}$$

The magnitude of μ is dependent on the ease to which the electron cloud is displaced relative to its nucleus and can be represented as an ellipsoid.

A fluctuating applied electric field will produce a fluctuating dipole moment at the same frequency. The oscillating electric field may be expressed as:

$$\varepsilon = \varepsilon^t \cos 2\pi t \nu_0 \qquad \textbf{Equation 2}$$

Where ε^t = electric field at time t

ν_0 = angular frequency of the radiation

This induced dipole will scatter radiation of frequency υ_o i.e. Rayleigh scattering.

If we consider a diatomic molecule that vibrates with a frequency of, υ_{vib}, performing simple harmonic vibrations, then a coordinate q_{vib} along the axis of vibration at time, t, is given by:

$$q_{vib} = q_0 \cos 2\pi \upsilon_{vib} t \qquad \textbf{Equation 3}$$

If the polarisability changes during the vibration, its value for a small amplitude is given by:

$$\alpha = \alpha^0 + \left(\frac{\partial \alpha}{\partial q_{vib}}\right)_0 q_{vib} \qquad \textbf{Equation 4}$$

Substitution of Equation 3 in Equation 4 yields:

$$\alpha = \alpha^0 + \left(\frac{\partial \alpha}{\partial q_{vib}}\right)_0 q_0 \cos 2\pi \upsilon_{vib} t \qquad \textbf{Equation 5}$$

If the incident radiation of frequency υ_0 interacts with the molecule then from Equation 1 and 2:

$$\mu = \alpha \varepsilon = \alpha \varepsilon^0 Cos 2\pi \upsilon_0 t \qquad \textbf{Equation 6}$$

Substitution of Equation 5 in Equation 6 yields:

$$\mu = \alpha^0 \varepsilon^0 \cos 2\pi \upsilon_0 t + \left(\frac{\partial \alpha}{\partial q_{vib}}\right)_0 \varepsilon^0 q_0 \cos 2\pi \upsilon_{vib} t \cos 2\pi \upsilon_0 t \quad \textbf{Equation 7}$$

This can also be written:

$$\mu = \alpha^0 \varepsilon^0 \cos 2\pi \upsilon_0 t + \left(\frac{\partial \alpha}{\partial q_{vib}}\right)_0 \frac{\varepsilon^0 q_0}{2} \left[\cos 2\pi (\upsilon_0 - \upsilon_{vib}) t + \cos 2\pi (\upsilon_0 - \upsilon_{vib}) t \right]$$

Equation 8

The first term describes Rayleigh scattering and the remaining terms describe Raman scattering.

Therefore for Raman scattering to occur there must be a change in the polarisability during any given vibration i.e.

$$\left(\frac{\partial \alpha}{\partial q_{vib}}\right)_0 \neq 0 \qquad \textbf{Equation 9}$$

2.2.2 Quantum Mechanical Theory

This approach recognises that the vibration energy of a molecule is quantised. Photons of light of frequency, υ, can be scattered by a molecule elastically or inelastically (Figure 2.2 shows an energy level diagram for Raman and Rayleigh scattering effects). Each vibration can be characterised by an energy, E_{vib}.

$$E_{vib} = h\nu(v + 1/2) \text{ (For a Simple Harmonic Oscillator)} \qquad \textbf{Equation 10}$$

Where v is the vibrational quantum number that can take values 0, 1, 2, 3....etc. During Raman scattering the molecule/crystal can gain or lose energy i.e. if the molecule gains energy ΔE, the photon will be scattered $h\nu - \Delta E$, and if the molecule loses energy the photon will be scattered with energy $h\nu + \Delta E$. Shown in diagram below (Figure 2.2).

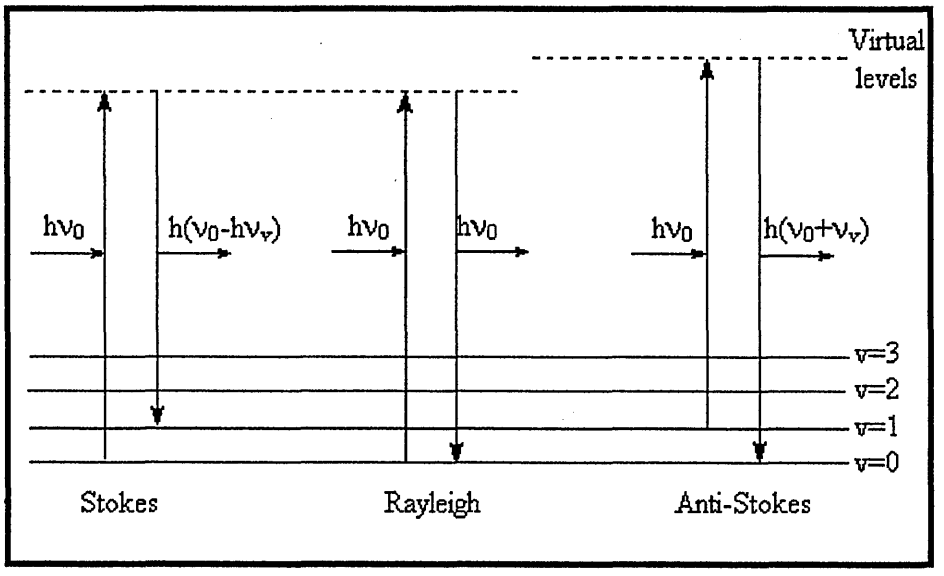

Figure 2.2 Energy level diagram for Raman and Rayleigh scattering effects according to quantum theory.

Stokes scattering is more intense than anti-Stokes scattering and is mainly used by today's vibrational spectroscopy research groups. The intensity difference is due to the population of energy states at thermal equilibrium i.e. Boltzman distribution. According to the Boltzman distribution law[7], the ratio of the number of molecules (N_i) in state i, having energy E_i, to the number molecules (N_j) in state j, having energy Ej, at thermal equilibrium, is given by:

$$\frac{N_j}{N_i} = \frac{g_j}{g_i} e^{-\left(\frac{Ej-Ei}{k_B T}\right)}$$ **Equation 11**

g_i and g_j are the degeneracies of the two states i and j.

At ambient temperature, from (Equation 11), the number of molecules in the ground state N_i will be much greater than that of the excited state N_j. For $E_j - E_i \rangle kT$, since the intensity of a transition is proportional to the number of molecules which are in the state corresponding to the starting point of the transition. Therefore, the incoming light has a greater probability of interacting with a molecule that is in the ground state.

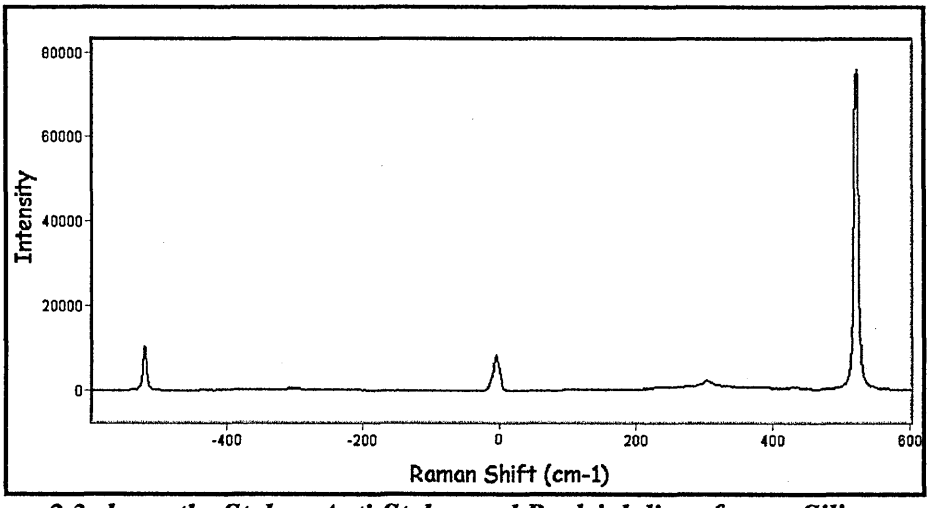

Figure 2.3 shows the Stokes, Anti-Stokes and Rayleigh lines from a Silicon wafer. The majority of the Rayleigh light filtered out by the holographic notch filters in the Raman system

2.2.3 Selection Rules and Intensities

There are 3N-6 normal modes of vibration for a non-linear molecule and 3N-5 for linear molecules. However, not all these vibrations will be Raman active. For a

vibration to be active there must be a change in the polarisability during the vibration (see Equation 9).

A Group theoretical treatment, in which the symmetry class of a particular molecule is analysed, is a reliable method for determining whether particular modes are Raman active[8].

It is often quoted that when a molecular vibration has a large $\frac{\delta \mu}{\delta q}$ (dipole, IR), $\frac{\delta \alpha}{\delta q}$ (the polarisability, Raman) is small and vice versa. Many vibrations are either strong in the infrared or Raman, but not both. Although this is not always the case due to some exceptions, it is still a good "rule of thumb". Due to these differences in the selection rules between Raman and IR it is important to acquire both an IR and Raman spectrum (where possible) to have complete vibrational information on the target species. Because of this Raman and IR are said to be complementary, not competitive, techniques.

2.2.4 Problems Associated With Raman Spectroscopy

2.2.4.1 Sensitivity

The Raman effect is intrinsically very weak, i.e. $\frac{\delta\alpha}{\delta q}$ (the $\delta\alpha$ term is a weak).

Because of this, energetic sources and sensitive detectors are necessary. These requirements have hindered the development of Raman spectroscopy over the years. It is not until relatively recently (late 80's) that technology has become available that has enabled Raman spectroscopy to come into its own and be developed as an

analytical tool of some merit. The optics (beam expander and Holographic Notch Filter (HNF)), and components, (Plasma Line Rejection Filter (PLRF)), in commercial Raman spectrometers available today still, however, reduce the overall throughput. Take perhaps the most important component; the holographic notch filters, which can be thought of as wavelength specific mirrors. These remove 99% of the Rayleigh scattered light but in addition also remove 5% of the Raman scattered light which reduces the overall S/N. The combined effect of all the optics within the instrument reduces the overall throughput to around 5-10%[9]. It is only the powerful/stable lasers and sensitive CCD cameras that allow Raman spectroscopy to be successfully employed. Enhancement techniques are available. These include Resonance Raman Spectroscopy, SERS (Surface Enhanced Raman Spectroscopy) and SERRS (Surface Enhanced Resonance Raman Spectroscopy); the latter able to boost Raman signals by up to 10^6 times. Resonance Raman Spectroscopy refers to a phenomenon in which Raman line intensities are greatly enhanced by excitation with wavelengths that closely approach that of an electronic absorption peak of an analyte. The peaks associated with the most symmetric vibrations are enhanced by a factor of 10^2 to 10^6[4]. Surface enhanced Raman involves obtaining the Raman spectra in the usual way on samples that are adsorbed on the surface of colloidal metal particles (usually silver, gold or copper) or on roughened surfaces of the aforementioned metals. For reasons that are still not fully understood, the Raman line intensities are often enhanced by a factor of 10^3 to 10^6. When surface enhancement is combined with the resonance enhancement (SERRS) the net increase in signal is roughly equal to the product of the intensity produced by each of the techniques[4]. Consequently, detection limits in the 10^{-9} to 10^{-12} M have been observed[4].

2.2.4.2 Fluorescence: The Bain of Raman Spectroscopists!

Fluorescence causes a high background in Raman spectra, which can be so strong as to completely mask Raman bands. Fluorescence is a phenomenon that is approximately 10^6-10^8 times more intense than Raman scattering and can be caused by small amounts of additives/trace impurities. Of course, the sample itself may be inherently fluorescent such as dyes and some iron containing species such as clays and minerals. Fluorescence occurs when the incident light source excites the species beyond the vibrational energy levels to actual excited electronic states. Decay then occurs by emission of photons in the visible region. These photons are collected/detected in the same way as the Raman scattered photons and generate a signal on the detector that resembles a high background in the Raman spectrum.

For some samples there is no remedy for fluorescence, but for others there are many ways to combat this and it is these difficult samples that Raman spectroscopists are required to use all their experience and skills to overcome. Below are some methods commonly adopted for reducing fluorescence:

1. Fluorescence "burn-out": This involves leaving the laser focused onto the sample for a length of time until the level of fluorescence recedes to an accepted/workable level. This can in itself cause problems which will be discussed in **2.2.4.3.**
2. Using different excitation wavelengths can reduce fluorescence. Using Ultra-Violet wavelengths moves away from exciting fluorescence as the Raman shifted light is always relative to the excitation wavelength, whereas the

fluorescence for a particular species is confined to a particular range of frequencies. Near infrared lasers also reduce fluorescence because the energy-per-photon of laser light is lower in energy so less likely to excite fluorescence (see point 7 (below) for the λ effect on Raman scattering).

3. Altering instrumental parameters such as simply reducing the laser power, using a lower magnification objective (larger spot, therefore reducing the power per-unit-area) and tailoring the acquisition time or accumulating (to prevent the detector saturating) can sometimes be all that is required to overcome small amounts of fluorescence.
4. Using fluorescence quenching agents or by adding a small amount of water, where possible, (to defocus the laser light, reduce heating effects and reduce the overall power density) has been known to reduce fluorescence levels.
5. When the background is not severe it is possible to subtract or base-line correct. These functions are found in many spectral interpretation packages like Grams 32. For baseline correction, points are placed on the data (i.e. the real baseline), which has the effect of removing the fluorescence background below the points. Care must be taken so as not to distort the Raman bands.

6 Using anti-Stokes Raman scattering as fluorescent scattered light undergoes a Stoke's shift (not always feasible, especially for low scattering cross-section samples).

7 Use Fourier-transform Raman instruments which use Nd/YAG 1064nm excitation (near-IR region). Higher-powered lasers are required (50mW) due to reduced Raman scattering (i.e. $I_{(scat)} \propto \frac{1}{\lambda 4}$). This is not a problem, as the near-IR radiation does not cause significant photodegradation. The MCT detectors used for FT-Raman instruments are not as sensitive as the CCD

detectors used in dispersive instruments but the Fellget advantage does apply i.e. the sampling time-per-wavelength is much longer than in comparison with dispersive instruments.

2.2.4.3 Sample Degradation

Localised sample heating is possible due to the high power confinement in the small laser focus/spot (2μm) and thermal degradation and/or polymorphic transitions can occur, however, carbonisation/degradation usually leaves a brown/black signature. This can easily be detected by taking an optical micrograph before sample laser irradiation and then one after and comparing. On the other hand, Witke et al[10] consider that the sensitivity of certain materials to laser-induced transformation can be an advantage and lead to additional information on otherwise unidentifiable amorphous phases that can then be interpreted with greater reliability. Biological samples are especially prone to laser damage where denaturation can occur with relative low laser powers[11]. With high powered lasers (where >10mW is at the sample) and when short wavelength (i.e. UV) lasers are used, additional measures may be needed for some samples, (especially ones with a dark colouration). Sample spinning[12] can be adopted so that the laser is not focussed onto one area for very long.

2.3 Raman Microscopy

2.3.1 History

In 1966, Delhaye and Migeon suggested that laser-excited Raman scattering could be used in the analysis of microscopic particles[13]. Hirschfield[14] then outlined some basic requirements for Raman microprobe spectrometers. The first results of practical Raman microscopy were presented at the IVth International Conference on Raman Spectroscopy in 1974[15,16].

2.3.2 Applications of Raman Microscopy

The coupling of a Raman spectrometer to a conventional optical microscope to yield a Raman microscope has provided the spectroscopist with a very powerful tool for the characterisation, study and mapping of materials using high spatial resolution. The utilisation of Raman microscopy in solid state physics and materials science was detailed nicely by Lucazeau and Abello[17] who described the study of heterogeneities in ceramics and thin films, micro-indentation on Si, the characterisation of Si-Ge layers and *in-situ* Raman spectra in plasma assisted CVD reactors[17]. Raman microscopy has also been used to characterise hard, wide-bandgap semiconductors (diamond films, GaN, $Al_xGa_{1-x}N$ alloys, AlN, and BN) to gain information on physical aspects such as stress, temperature and microstructure which was reviewed by Bergman and Nemanich[18]. The Raman microscopic analysis of carbonaceous materials also provides a good example of the molecular and structural information that Raman microscopic analysis can offer by the detailed analysis of the D (defect) band at ~1300cm^{-1} and the G (graphite) band at ~1550 cm^{-1}.

The Raman spectrum of carbon/graphite is well known [19-22] and the value of $I_{(D)}/I_{(total)}$ can give an idea of the amount of disorder[20] and the type of carbon material.

Raman microscopy has also been applied to some quite novel analyses, such as analysis of fluid inclusions in rock and minerals. In the geological context, analysis of this trapped material can provide vital information to understand the physical and chemical condition prevalent at the time of crystal growth[23]. Another example is the identification of gunshot residues[24] which can give information on the compounds within the residues, especially oxides, which in-turn can identify the gun and the ammunition type used[25].

2.3.3 Industrial Realisation of Raman Microscopy

Raman microscopy has been successfully applied to a wide range of analyses to identify contaminants, inhomogeneities and the properties of materials encountered in industrial production.

Examination of polymer films and fibres has resulted in the identification of inclusion particle which were picked up during the processing; for example, the identification of α -SiO_2 in polyethylene films[26]. In most cases the identification of these contaminants can result in providing the cause for mechanical failure and help improve processing.

The manufacture of microcircuits involves a large number of complicated chemical processing operations, during which there can be accidental contaminations that may impair the functioning of the circuit. Impurities in semi-conductor crystals and integrated circuits have been analysed[27], and thus has enabled the causes of contamination to be pin-pointed and eliminated.

The analysis of inclusions and deposits in glass, such as sodium sulphate, have been performed to yield valuable information about the refining mechanism or causes of unwanted bubble formation[26].

Raman microscopy has even been utilised for remote analysis utilising fibre optic probe technology. This means that samples such as DLC coatings for the hard disk industry[28], to ancient frescos in churches, to chemical and nuclear processes can be analysed off site. In fact, whatever sample cannot be brought to the laboratory can be sampled remotely. These systems are rugged, small and totally portable. A detailed evaluation of the portable DLC analyser[28] being utilised in industry is given in chapter 5.2.

2.4 The Renishaw Raman Microscope

The Raman microscopes used in this project were:

Renishaw Raman System 1000: Equipped with 782nm excitation from a laser diode: Used for analysis of fluorescent samples and samples which were prone to laser damage.

Renishaw Raman System 2000: Equipped with 514.5nm (Ar^+ - ion) and 632.8nm (HeNe) excitation. To enable relatively quick changeover from one source to the other, the holographic notch filters are "plug and play" i.e. they can quite easily be exchanged within the instrument. This instrument also has the facility to perform Raman imaging [29-31], a technique that continues to show promise. This system has an additional light path (called the imaging path) that has a collection of band pass filters. Instead of the laser being focussed by the objective to a 2μm spot (with x50 objective) the optics (especially the beam expander) are used to defocus the spot over a larger area ~200μm^2. The scattered light is then collected in the same way as for the system 1000 but a specific frequency range/band of the analyte in question has been chosen by the user and the band pass filter on the imaging path only allows Raman scattered light of those frequencies to be transmitted. The information is then processed to give an image e.g. black and white contrast.

Both systems can be operated in microprobe and confocal mode. The confocal mode is a method of improving the spatial resolution especially in the Z-direction which facilitates depth profiling; for example, of transparent polymer laminates[32].

2.4.1 Description of the Renishaw Raman Microscope

Figure 2.3(below) shows a schematic of the Renishaw Raman System 1000 with the important components/optics annotated.

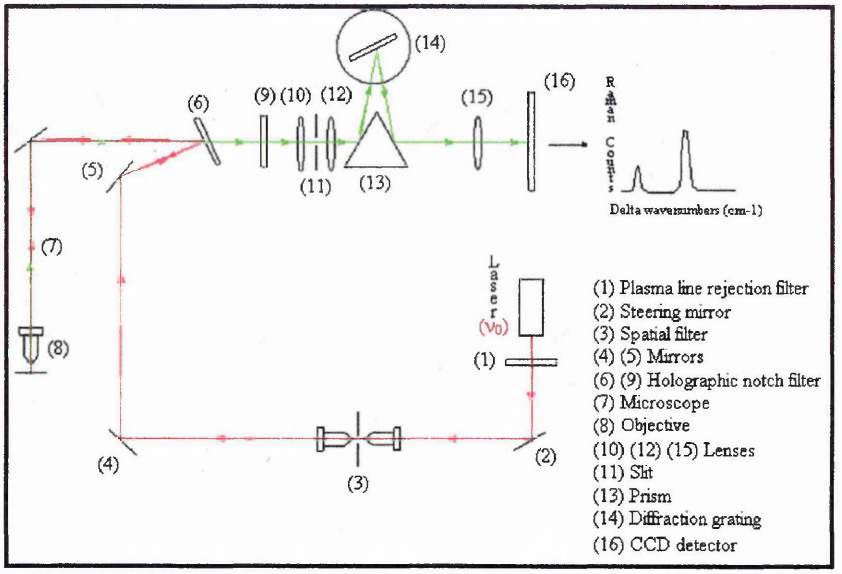

Figure 2.3 Renishaw Raman Microscope (System 1000)

On our system a visible laser i.e. either a 514.5nm Ar – ion or a 632.8nm HeNe gas laser provides the excitation light. A detailed list of all available excitation sources and wavelengths are given in Table 2.1.

SOURCE	WAVELENGTH (nm)
Argon ion	**488 or 514.5**
Krypton ion	**530.9 or 647.1**
Helium/Neon	**632.8**
Diode laser	**782 or 830**
Nd/YAG	**1064**

Table 2.1 List of available excitation sources for Raman microscopy

The initial optic within the system is a plasma line rejection filter (PLRF)(labelled 1 on diagram). The majority of gas lasers have strong lines, other than the lasing one. These need filtering out otherwise they would be detected and mistaken for Raman bands (unfortunately this filter can lead to a reduction in the intensity of ~50%[9]). The PLRF filter blocks the unwanted plasma lines from entering the spectrometer but transmits the main laser line. The first steering mirror (2) sends the monochromatic light through the beam expander/spatial filter (3) that consists of two objectives and an aperture. This has two effects: the first is to recollimate any stray laser light and the other is to expand the beam so that it is optimised to fit down the x50 objective lens. In microprobe mode, the x20 objective focuses the beam onto the pinhole (not essential) and then onto a second objective (x4) in order to produce a collimated beam. The expanded and collimated beam is deflected by mirrors (4 and 5) onto a holographic notch filter (6). This filter reflects the laser wavelength and the beam passes into the microscope (7) to be focussed onto the sample (8) using the objectives x10, x20 (also a x20 Ultra Long Working Distance lens is available), x50 and x100. The backscattered Raman light (180° configuration) is collected by the objective lens and returns into the microscope and arrives at the holographic notch filters (6) this reflects the strong unwanted Rayleigh light back through the instrument and away from the detection path but transmits the Raman scattered light. The second holographic notch filter (9) ensures that all the Rayleigh light is removed and transmits Raman shifted wavelengths. The scattered light arrives at the pre-slit lens (10) that focuses the Raman light through an adjustable entrance slit (microprobe mode 50 μm and confocal 10-15 μm open) (11). A second lens (12) recollimates the scattered light before a mirrored prism (13) deflects it onto a diffraction grating (14) that separates the beam into its component wavelengths. The prism deflects the

dispersed light through a lens (15) on to a CCD (charge coupled device) detector(16) (NB. The adjustable slit and the CCD detector are used to obtain the confocal set-up).

2.4.2. Optics/Components

2.4.2.1. Lasers

Three lasers having different wavelengths were available: helium/neon (632.8 nm), argon ion (514.5 nm) and a diode laser (782 nm). The lasers available have powers of 25mW that can be reduced to 50, 25, 10 and 1% using neutral density filters. It is possible to increase the Ar^+ ion laser power up to 40mW but is inadvisable, as this would dramatically reduce the lifetime of the laser. These lasers possess different polarisation (see below).

2.4.2.1.1 States of Polarisation: Monochromatic radiation

The plane wave that has been considered here propagates along the z-axis and has the electric vector parallel to the x-axis and the magnetic vector parallel to the y-axis. Such a wave, and the radiation associated with it, is often described as plane polarised, but this description is complete only if the plane is defined. Historically, the plane of polarisation was taken to be the plane containing the direction of propagation and the magnetic vector. The magnetic vector was then referred to as the direction of polarisation. A HeNe laser has a horizontal polarisation (resulting in a east-west orientation of the laser on the sample) since the Ar^+ and diode lasers have a vertical polarisation (resulting in a north-south orientation of the laser on the sample).

2.4.2.2. Holographic Notch Filters (HNFs)

These are expensive but essential components in the Raman microscope. The main function of the holographic notch filters (HNF) is to remove the Rayleigh and reflected light. The HNFs can be described as wavelength specific mirrors and they reflect light of a narrow band of wavelengths, with a high degree of efficiency. The result is a notch in the HNF transmission spectrum. The filters are of photosensitive organic material sandwiched between transparent substrates. A laser beam is used to write a hologram into the material to produce sinusoidal variation in the refractive index through the photosensitive material. The change in refractive index is necessary to diffract the light. The hologram can be written in order to reflect or reject a narrow band of wavelengths.

2.4.2.3. Diffraction Gratings

The diffraction grating disperses/separates spatially the incident polychromatic light into its constituent wavelengths. The surface of the diffraction grating is made of a series of, n, parallel lines or "grooves" spaced from each other by the same value, d. The greater number of grooves-per-millimetre the better the spectral resolution of the instrument will be. The gratings used in the Renishaw Raman instruments are 1200g/mm or 1800g/mm, but 2400g/mm are becoming increasingly used as technology in grating materials improves.

2.4.2.4 Charged Coupled Device Detectors (CCDs)

CCD devices/chips are composed of semi-conductor material that has a 2-dimensional array of pixels (576 x 384), each pixel is 22 x 22μm. The CCD detects the Raman scattered light by a "photogenerated charge mechanism". The continuous extended scanning technique has been clearly explained by Dyer and Smith[33] and the details are summarised below.

2.4.2.4.1 Static Exposure

In static mode the spectral "window" is calculated according to the wavelength, spectral dispersion, focal length and detector dimensions. The grating is rotated such that the wavelength corresponding to the centre wavenumber shift is positioned in the centre pixel. After choosing the exposure time, the shutter is opened, the chip is exposed, the shutter then closes and the charge read off the chip sequentially.

2.4.2.4.2 Continuous Extended Scanning (CES)

For CES the user determines the scan range limits. Usually the range depends on the material under investigation, such that, for example, 100-2100cm^{-1} is reasonable for inorganic and 400-3600cm^{-1} for organic materials. The desired scan range and exposure time are entered into the software, the grating is rotated such that the lower Raman shift limit will be incident in the pixel furthest from the output-register which is along short axis. The shutter is opened, and the grating begins to rotate continuously towards the higher angle i.e. larger shift and longer wavelength. When

this occurs, the charge begins to traverse the chip towards the output register. The time taken for the first wavelength to traverse the chip is equal to the exposure time. When the last wavelength has finally traversed the chip onto the readout register the camera shutter closes, the scan finishes and the results are then displayed. During the scan the grating is moved continuously, synchronised with detector readout. Since each wavelength in the full spectral range spends the set exposure time traversing the CCD, and since each wavelength only accrues readout noise once, the multi-channel advantage of the spectrograph is retained throughout a CE scan. The total exposure time (T_{tot}) is much larger than the exposure time (T_{ex}) and may be approximated by[33.]

$$T_{(tot)} \approx \left(1 + \frac{total\ scan\ range}{average\ spectral window length}\right) X\ T_{ex}$$

The CE scan method is superior to that found in alternative technologies because it overcomes the problems of limited spectral windows, optical misalignment (by not requiring grating changes or re-calibration) and the splicing of several static regions is not required which can result in generating severe errors in band shape for "step-n-stitch" technologies.

References

1 Brillouin L., Ann . Phys., 88 (1922) 17.

2 Smekal A., Naturwissenshaften, 11 (1923) 873

3 Raman C.V. and Krishnam K.S., Nature, 121 (1928) 50

4 Skoog, Holler and Nieman in, Principles of Instrumental Analysis (5^{th} Ed.), Saunders College Publishing, London, 429pp, (1999).

5 M. Delhaye and P.Dhamelincourt, J. Raman Spec. 3 (1975) 33.

6 D.J. Gardiner in, "Practical Raman Spectroscopy", (Eds D.J. Gardiner and P.R. Graves), Springer-Verlag, Berlin (1989)

7 Spectroscopy, volume 2. Eds. B.P.Straughan and S.Walker, Chapman and Hall London, 362 pp, (1976).

8 G. Davidson in, Group Theory for Chemist, McMillan Physical Science Series, Macmillan Education, London (1991).

9 Personal communication, Dr Ian Haywood, DLC carbon expert, Renishaw plc.

10 K. Witke, D. Klaffke, A Skoppe and J.P. Schreckenback, J. Raman Spectrosc 29 (1998) 411.

11 Modern Techniques in Applied Molecular Spectroscopy, Ed. F.M. Mirabella, Wiley Interscience, New York, pp 316, (1998).

12 Personal communication Mr Paul Whelan, Research Scientist, Materials Research Institute, Sheffield Hallam University, Sheffield.

13 Delhaye M and Migeon M, Compt. Rend. 262 (1966) 702.

14 T. Hirschfeld, J. Opt. Soc. Am., 63 (1973) 476.

15 Rosasco GJ., Etz ES. and Cassatt WA(1974) IV^{th} Internat. Conf. Raman Spectrosc., Brunswick, Me., USA.

16 Delhaye M and Dhamelincourt P (1974) IVth Internat. Conf. Raman Spectrosc., Brunswick, Me., USA.

17 G. Lucazeau and L. Abello, Analusis 23 (1995) 301-311.

18 L. Bergman and R.J. Nemanich, Annu. Rev. Mater. Sci., 26 (1996) 551-579.

19 A. Cuesta, P. Dhamalincourt, J. Laureyns, A. Martínez-Alonso and J.M.D. Tascón, Carbon, 32 (8) (1994) 1523-1532.

20 A. Cuesta, P. Dhamalincourt, J. Laureyns, A. Martínez-Alonso and J.M.D. Tascón, J. Mater. Chem., 8 (1998) 2875-2879.

21 F. Tuinstra and J.L. Koenig, J. Chem. Phys., 53(3) (1970) 1126-1130.

22 Y. Wang, D.C. Alsmeyer and R.L. McCreery, Chem. Mater. 2 (1990) 557-563.

23 S.Roberts and I.Beattie. In Microprobe Techniques in the Earth Sciences, Eds. P.J.Potts, J.F.W.Bowles, S.J.B.Reed and M.R.Cave, Chapman and Hall London, 387-408, (1995).

24 S. Stick, D. Bard, L. Gros, W. Wenz, J. Yarwood and K. Williams, J. Raman Spectrosc., 29 (1998) 787-790.

25 Sylvia Steffen, "Investigation of Gunshot Residues by Means of Raman Microscopy", Internship Placement Report, Sheffield Hallam University, Materials Research Institute (2000).

26 J.D. Louden Chapter 6 "Raman Microscopy" in Practical Raman Spectroscopy, Gardiner and Graves (Eds.) Springer-Verlag, Berlin 1989 pages 120-151.

27 Lang P, Katon J.E., Microbeam analysis, (1986) 47

28 http//.www.Renishaw.co.uk/spectroscopy/

29 D.N. Batchelder, C. Cheng and G.D. Pitt, Adv. Mater. 3(11) (1991) 566-568.

30 P.J. Treado and M.D. Morris, Appl. Spectrosc. Rev. 29(1) (1994) 1-38.

31 P.D. Wang, C. Cheng, C.M. Sotomayor Torres and D.N. Batchelder, J. Appl. Physics, 74(9) (1993) 5907-5909.

32 R. Tabaksblat, R.J. Meier and B.J. Kip, Appl. Spectrosc. 46(1) (1992) 60-68.

33 C. Dyer and B.J.E. Smith, J. Raman Spectrosc., 26 (1995) 777-785.

Chapter 3

Investigation of Spectral Origins

Chapter 3 Investigation of Spectral Origins

3.1 Crystals[1]

Metals and many non-metallic solids are crystalline, i.e. the constituent atoms are arranged in a pattern that repeats itself in three dimensions. The actual arrangement in the material is the crystal structure[1,2]. The crystal structures of most pure metals are simple; the three most common being body-centred cubic(bcc), face-centred cubic(fcc) and hexagonal closed packed(hcp) structures but, in contrast, the structures of alloys and non-metallic solids are quite complex.

A crystal is characterised by a primitive cell or unit cell, which is the smallest unit, repeated in three dimensions. The crystal is constructed by stacking identical unit cells face to face in perfect alignment in three dimensions. The position of the planes, directions, and point sites, in a lattice is described by reference to the unit cell and the three principal axes x, y and z (Figure 3.1: unit cell dimensions)

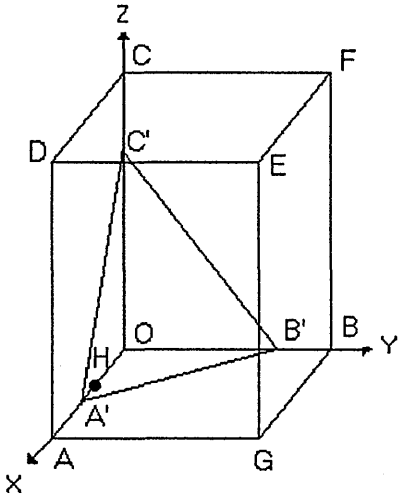

Cell Dimensions

OA = a
OB = b
OC = c
Lattice parameters

$\langle BOC = \alpha$
$\langle COA = \beta$
$\langle AOB = \gamma$
Defines size/shape

Any plane A'B'C' is defined by the intercepts OA', OB' and OC' with the three principal axes

Figure 3.1 Unit cell

The usual notation (Miller indices) defining crystal planes is to take the reciprocals of the ratios of the intercepts to the corresponding unit cell dimensions. Thus, A'B'C' is given by

$$\left(\frac{OA}{OA'}, \frac{OB}{OB'}, \frac{OC}{OC'}\right)$$

the planes ABC, ABE, CEA and CEB are (111), (11 $\bar{1}$), (1 $\bar{1}$ 1), and ($\bar{1}$ 11) respectively and are all planes of the same group/type {111}. Square brackets are used for direction vectors i.e. the directions CG, AF, DB and EO being [11 $\bar{1}$], [$\bar{1}$ 11], [$\bar{1}$ 1 $\bar{1}$] and [$\bar{1}$ $\bar{1}$ $\bar{1}$] respectively. Any point in a crystal is described by the fractional displacements of the point from the principal axes relative to the dimensions of the unit cell. Therefore the centre of the cell (Figure 3.1) is $\frac{1}{2}, \frac{1}{2}, \frac{1}{2}$, points F, E and H are 0,1,1; 1,1,1; $\frac{1}{2}$,0,0 respectively.

A face-centred cubic structure has atoms situated at the corners of the unit cell/cube and at the centres of all the cube faces. The atoms touch along the ⟨011⟩ close-packed directions. The lattice parameter, $a = 2r\sqrt{2}$. The atoms in the (111) planes are in the most close-packed arrangement possible and contain three close-packed directions 60° apart[1].

The chemical and physical properties of crystals depend on the structure of the atoms and the nature of the atomic binding. Perfect crystals, in which every atom site is filled and there are no disturbances in the regular arrangement of atoms, do not exist. All real crystals contain imperfections that may be point, line, surface or volume defects, which occur during the nucleation process. Knowledge of the structure of

defects and their properties is essential to fully understand all aspects of the properties of materials.

3.2 Defects in Crystals

3.2.1 Point Defects

All atoms in a perfect crystal/lattice are at specific atomic sites. In metallic like materials there are two types of point defects that are possible: vacant atomic sites or vacancy and an interstitial atom. Figure 3.2 shows these defects for a simple cubic structure.

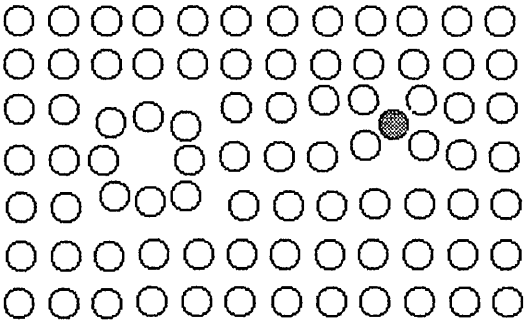

Figure 3.2 Vacancy and interstitial atom in a plane of a simple cubic lattice

The vacancy has formed by removal of an atom from an atomic site and the interstitial by the introduction of an atom into a non-atomic site. There is much evidence for these defects occurring during plastic deformation and high-energy particle bombardment (as happens during the PVD deposition technique). Also, a high-density of defects can be generated by rapid quenching from high temperature[1].

Impurity atoms in crystals can be considered as point defects and they play an important role in the physical and mechanical properties of all materials. Impurity atoms can take up two different types of site. (Figure 3.3 shows a substitutional impurity atom and interstitial impurity atom).

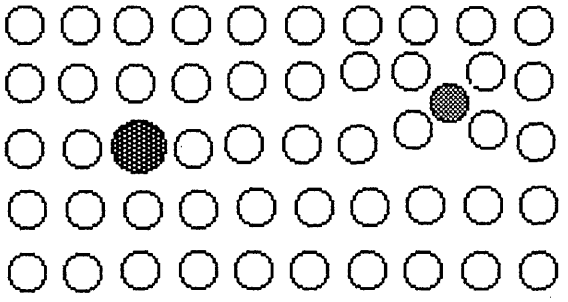

Figure 3.3 Point defects from impurity atoms

A substitutional defect is when impurity atoms replace atoms of the parent lattice lying in lattice sites, and an interstitial defect is when an impurity atom creates a defect at a non-atomic site. All point defects produce a local distortion in the lattice. The amount of distortion and hence the amount of additional energy in the lattice due to the defects depends on the amount of "space" between the atoms in the lattice and the size and number of the atoms introduced. Additional effects are important when the removal or addition of atoms changes the local electric charge in the lattice. This is unimportant in metallic crystals with metallic binding, but can be important in crystals in which the bonding is ionic, such as NaCl shown in Figure 3.4. N.B. the Cl atoms are larger than Na.

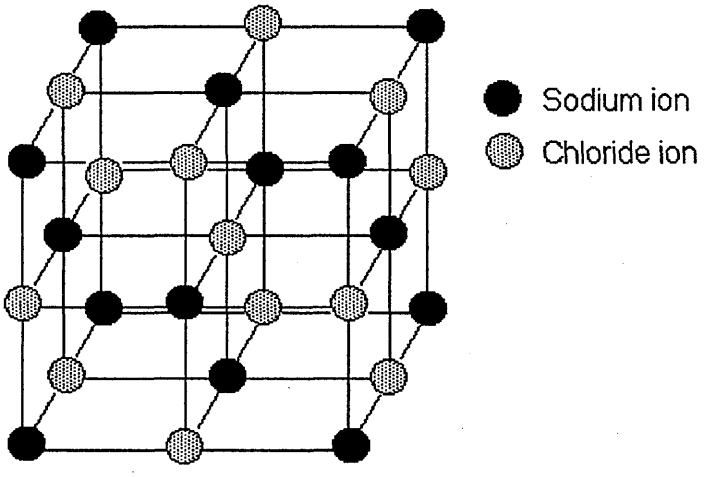

Figure 3.4 Sodium Chloride structure (Two interpenetrating fcc lattices)

Each negatively charged chloride ion is surrounded by six nearest neighbours, which are positively charged sodium ions, and vice versa. The removal of a sodium ion or a chloride ion produces a local positive or negative charge as well as creating a vacant lattice site.

3.2.2 Grain Boundaries

Crystalline solids usually consist of a large number of randomly oriented grains separated by grain boundaries. Each grain is a single crystal and contains defects. When the misorientation between the grains is small the boundary consists of an array of dislocations and is called a *low angle boundary*[1].

3.2.3 Defects in PVD Coatings

The Physical Vapour Deposition process results in all of the above-mentioned defects occurring. PVD coatings are dense polycrystalline materials that usually have

columnar grain morphology in which each column is a single crystal. Complex dislocations at the grain boundaries can result in holes/voids. However, with a sufficiently high enough bias voltage, which in turn controls the energy of the arriving atoms at the surface during crystal growth, their mobility on the surface and ability to find favourable lattice sites, these voids can nearly all but be eradicated. Figure 3.5 below shows (a) an SEM cross-sectional image of a PVD grown CrN coating and (b) an ESEM image of the column tops on a –75v bias grown TiAlN/VN coating. The columnar growth can easily be identified on both images.

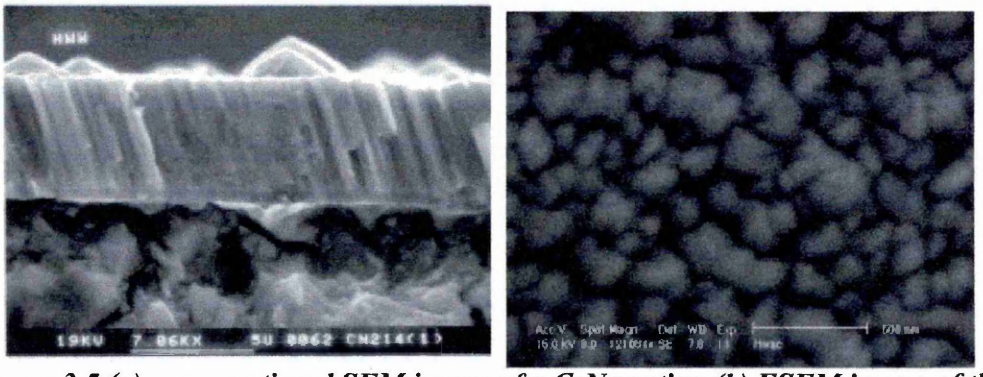

Figure 3.5 (a) cross-sectional SEM image of a CrN coating (b) ESEM image of the column tops on a TiAlN/VN coating (-75V bias).

In addition, there are also growth defects which stem from the macroparticles/droplets (see Chapter 1: Figure 1.2) that are intrinsic to the ion-etching process which is vital in generating PVD coatings with favourable properties. One of the most important of these is good adhesion to the substrate material.

3.3 Vibrations of Lattices[2]

Consider the elastic vibration of a crystal with one atom in the primitive cell. We want to find the frequency of a lattice wave in terms of the wavevector that describes the wave. The mathematical solution is simplest in the [100], [110], and [111]

propagation directions in cubic crystals. When a wave propagates along one of these directions, entire planes of atoms move in phase with displacements either parallel or perpendicular to the direction of the wavevector. We can describe with a single coordinate u_s the displacement of the plane from its equilibrium position (one dimensional). For each wavevector there are three modes, one of longitudinal polarisation (Figure 3.6 (a)) and two of transverse polarisation (Figure 3.6 (b)).

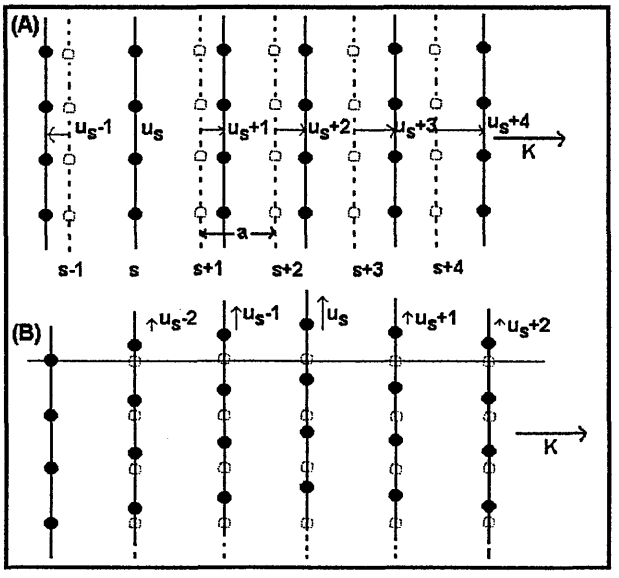

Figure 3.6 (A) Dashed lines are planes of atoms when in equilibrium and solid lines are planes of atoms when displaced as for a longitudinal wave. The coordinate u measures the displacement of the planes (B) Planes of atoms as displaced during a passage of a transverse wave (Source [2])

With crystals having more than one atom per primitive cell the vibrational spectrum shows new features. If we consider two atoms per primitive cell, as in the NaCl structure, for each polarisation mode in a given propagation direction the dispersion relation ω versus K develops two branches, known as acoustical and optical branches. There are longitudinal LA and transverse acoustical TA modes, and longitudinal LO and transverse TO modes. If there are p atoms in the primitive cell,

there will be 3p branches to the dispersion relation: 3 acoustical branches and 3p-3 optical branches. Thus NaCl will have six branches: one LA, one LO, two TA and two TO. The number of the branches follows from the number of degrees of freedom of the atoms. With p atoms in the primitive cell and N primitive cells, there are pN atoms. Each atom has three degrees of freedom, one for each of the x, y and z directions, making a total of 3pN degrees of freedom for the crystal. The number of allowed K values in a single branch is just N for one Brillouin zone. Thus the LA and the two TA branches have a total of 3N modes, thereby accounting for 3N of the total; degrees of freedom. The remaining (3p – 3)N degrees of freedom are accommodated by the optical branches. If we consider a cubic crystal where atoms M_1 lie on one set of planes and atoms of mass M_2 lie on planes interleaved between those of the first set (see Figure 3.7).

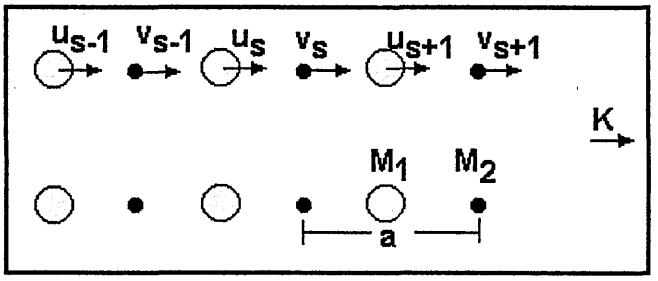

Figure 3.7 A diatomic crystal structure with masses M_1 and M_2 connected by force constant C between adjacent planes. The displacements of atoms M_1 are denoted by u_{s-1}, u_s, u_{s+1},and M_2 v_{s-1}, v_s, v_{s+1}. The repeat unit is a in the direction of the wavevector K. Atoms are shown in undisplaced positions.(Source[2])

$$\omega^2 \cong 2C\left(\frac{1}{M_1}+\frac{1}{M_2}\right) \qquad \text{Optical branch}$$

$$\omega^2 \cong \frac{2C}{M_1+M_2}K^2a^2 \qquad \text{Acoustical branch}$$

We assume that each plane only interacts with its nearest-neighbour planes. The particle displacements in the transverse acoustical (TA) and transverse optical (TO) branches are shown in Figure 3.8.

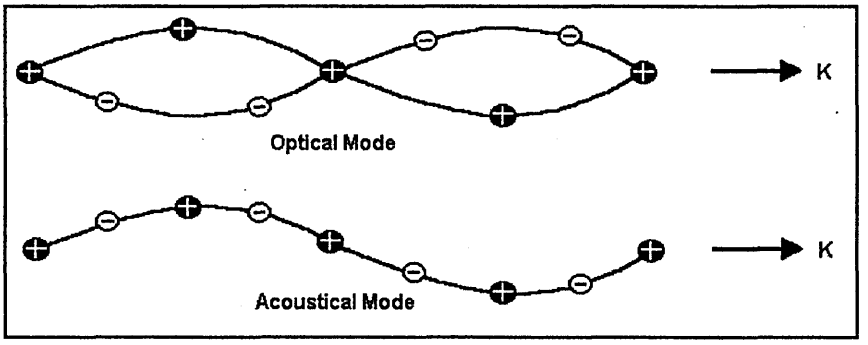

Figure 3.8 Transverse optical and transverse acoustical waves in a diatomic linear lattice (particle displacements for the two modes at the same wavelength).(source[2])

The atoms vibrate against each other, but their centre of mass is fixed. If two atoms carry opposite charges, we may excite a motion of this type with the electric field of a light wave, so the branch is called the optical branch. If the atoms (and their centre of mass) move together the branch is called the acoustical branch. The energy of a lattice vibration is quantised. The quantum of energy is called a phonon in analogy with the photon of the electromagnetic wave. Elastic waves in crystals are made up of phonons.

3.4 Raman Scattering in Crystals

The Raman effect stems from vibration-induced changes in the electronic polarisability of a molecular system. Vibrations involving the crystal lattice may not be ascribed to an individual molecule. Phonon modes are properties of the crystal lattice, often referred to as being delocalised, which may be visualised as collective states of the entire solid that lie lower in energy than the individual molecular internal

vibration states. When energy is deposited into the phonon modes of the crystal, equilibrium is maintained by the transfer of energy from the phonon modes to the internal vibrational modes. The site symmetry of a molecule in the crystalline state is, in general, lower than in the isolated molecule. This reduction in symmetry may split the degenerate vibrations. In addition, crystals can present lattice modes resulting from transverse and longitudinal motions (see Figure 3.6). However, these "external" modes give bands usually in the low frequency region or as combination bands with internal modes at higher frequency.

In Raman and Brillouin light scattering processes which involve lattice vibrations, the frequency of the scattered radiation differs from that of the incident radiation by the frequency of a normal mode of vibration – that of an optical vibration mode in the case of Raman scattering and that of an acoustical vibration mode in the case of Brillouin scattering[3]. Since the acoustic modes in all crystals, regardless of structure, can produce first-order changes in the electronic polarisability, all crystals can exhibit a first-order Brillouin scattering spectrum[3]. The Brillouin scattering spectrum of cubic crystals, for an arbitrary direction, will exhibit three frequency shifts corresponding to the LA and two TA modes. However, for [100] and [111] directions, the two TA modes are degenerate and only two frequency shifts will occur, one corresponding to the LA and one corresponding to the two degenerate TA modes[3].

3.5 Current State of Understanding on Raman Scattering in PVD Coatings

The current state of knowledge within the field of Raman microscopy of PVD ceramic coatings is very limited. Research has been mainly concentrated on binary coatings especially TiN but also ZrN has been studied[4-6]. There has been very little work (if any) performed on advanced multicomponent, multilayered or superlattice PVD hard coatings.

The majority of PVD deposited coatings have face-centred cubic NaCl-type structures, for example, TiN, ZrN, CrN, TiAlN, TiZrN etc. The selection rules dictate that first-order Raman spectra (optical phonons) are forbidden due to O_h symmetry. However, this does not mean that Raman scattering from face-centred cubic PVD coatings is not possible. Due to the relatively high percentage of defects in the coatings, such as, dislocations, crystal site vacancies, interstitials and residual stresses (which distort the crystal lattice (i.e. lattice parameter)), this allows a defect-induced first-order spectra to occur[4-7].

Unfortunately, this is not the only barrier to obtaining good microscopic Raman spectra from PVD coatings because there are other limiting factors for Raman scattering from materials with metallic properties:

1) Surface defects, such as droplets and pits (see Chapter 1: Figure 1.2). This can have a pronounced effect on focussing.
2) High reflectivity (which can result in reflecting 5% of the incident laser light)

3) Low penetration depth (d) of the incident light, which is due to high reflectivity, high density and dark/black coloration especially for TiAlN and derivatives. Although the resulting penetration depth (see equation below) is small for these coatings the spectra still arise from a spatial range corresponding to many unit cells. Unfortunately the absorption coefficients for these types of materials are not available in the literature and determination of these is non-trivial. Typical penetration depths (d) are thought to be in the range of 50 – 100 nm.

$d = \lambda / 4. \pi. k$ (where k denotes the absorption coefficient)[6]

Due to the above factors it is not surprising that Raman experiments have been confined to a small number of coating materials, especially TiN and ZrN.

The observed Raman spectra do, however, exhibit two pronounced groups of bands related to acoustical (150-300cm^{-1}) and the optical (400-650cm^{-1}) parts of the phonon spectrum. The phonon dispersion curves and the densities of states have been obtained in the past using inelastic neutron scattering[2] and these data agree well with Raman intensities in phonon spectra. Not only are there peaks associated with one phonon densities, there are also second order scattering (2A, 2O, A+O etc) (N.B. Second order transitions are not disallowed for fcc crystals). The Raman spectra provide the one-phonon density of states modified by the proper selection rules of the NaCl-structure (weighted density of states). Several authors[6,7] have made use of the optical properties of TiN which are favourable for Raman scattering in the frequency regime of the argon laser (514.5nm) due to resonant enhancement.

Raman spectroscopy is a good technique for studying perturbed lattice vibrations and induced first-order spectra give direct information about density of states associated with certain combinations of atomic displacements in the perturbed crystals. Papers have been published which describe first-order-Raman spectra of doped alkali halides NaCl:Ag^+ and NaCl : Tl^+ systems[8,9]. The perturbation was characterised by a mass change at the defect site and a change in the central-force constant between the impurity and its six-nearest-neighbour Cl^- ions. In a perfect alkali halide crystal every ion is at a site of inversion symmetry[10]. Consequently all first-order polarisability derivatives are identically zero, and there is no first-order Raman effect. When an impurity (colour centre) is substituted at a lattice site, the inversion symmetry is destroyed at the neighbouring sites, and certain atomic displacements of the neighbour atoms have non-zero first-order polarisability derivatives. The impurity also represents a departure from translational symmetry. It is also reasonable to assume that in the doped crystals the polarisability derivatives will be non-zero only in the neighbourhood of the impurity[8,9].

Work has also been performed on un-doped alkali-halides[10]. Second- or higher-order scattering is allowed as a result of combinations of phonons on the same or different branches. Second-order scattering will give a (more or less) continuous spectrum, as pairs of phonons from any point may combine. First-order scattering has been observed in pure KCl and KBr by applying a strong static electric field[11].

3.6 Development of a Spectral Acquisition Method for PVD Hard Coatings

3.6.1 Instrumental Parameters Affecting Spectral Quality

If high quality PVD ceramic coating spectra are to be collected it is imperative to have an understanding of how each individual instrument/software parameter will affect the spectra gained.

3.6.1.1 Laser Wavelength/Power

The throughput is a very important parameter and is defined as the power that reaches the sample surface. This is mostly dependent on the alignment of the instrument and laser power.

The excitation sources available for this work were, 514.5nm (Ar^+ - ion, *green*), 632.8nm (HeNe, *red*) and 782nm (laser diode, solid state laser, *Near Infrared*), which all had a maximum power of 25mW. What can immediately be noticed is the energy-per-photon of laser light diminishes on going from green through to near infrared, which will have an effect on the Raman scattering (there is a dependence of $\frac{1}{\lambda^4}$ on Raman scattering, where λ, is the wavelength of light). There will also be a difference in penetration depth due to the wavelength. The 782nm near IR laser, should in theory have a greater penetration depth than the Ar^+ - ion, although because these coatings are dense, hard and reflective this may not be the case. In addition to this there is a further resonance effect that can come into play. A good example of this is when a Raman spectrum of TiAlN is taken with 632.8nm (red) and 514.5nm (green) excitation (Figure 3.9 shows the overlaid spectra).

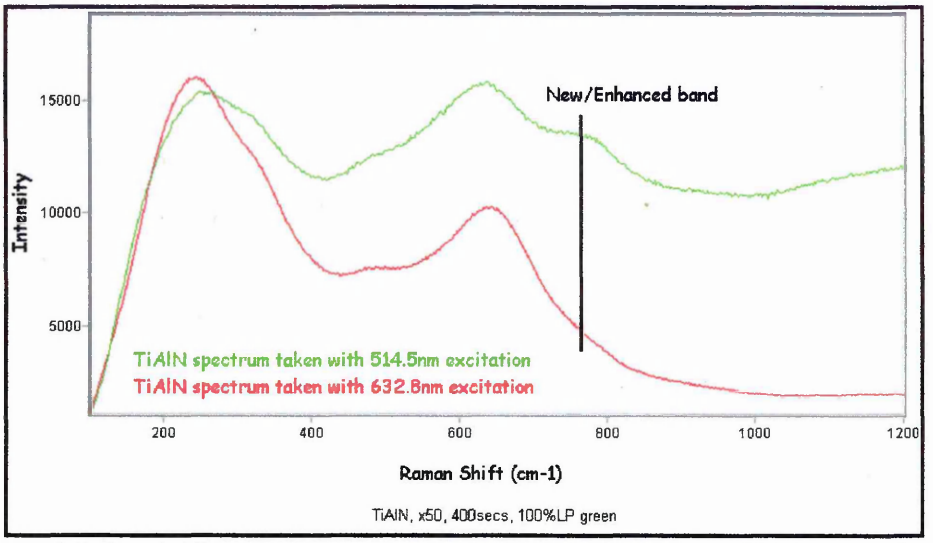

Figure 3.9 Overlaid spectra of TiAlN acquired with 514.5 and 632.8nm excitation

A band that can just be seen on the tail of the 640cm^{-1} TiAlN optic mode when the spectrum was acquired with 632.8nm becomes enhanced when the spectrum is taken using 514.5nm green laser light. This is firm evidence that there is resonance occurring for that particular mode when 514.5nm excitation is used. For the most part this is the only example of further information being obtained from using one particular wavelength of excitation over another. The spectra generally have the bands in almost the same position (an effect of penetration depth can be seen which results in a slightly changed band position due to a stress gradient within the coating; this will be discussed in Chapter 7).

A spectral database of PVD coatings was generated using the three- excitation wavelengths available. This was obtained so as to determine which laser resulted in the best spectra possible i.e. highest signal/noise, lowest fluorescence level and spectra that required the least manipulation. The spectra of all the coatings taken with the different excitation wavelengths are displayed at the end of this chapter in section 3.6. What is evident upon scrutinising the spectra taken with different wavelengths is

that the middle wavelength 632.8nm generated the best spectra. As a result of this the majority of the analyses subsequent to this discovery were performed utilising red 632.8nm laser light.

3.6.1.2 Microscope Objective

In Raman microscopy the laser beam is focussed onto the sample by a microscope objective and the Raman scattered light is collected by the same objective in 180° backscattered configuration. Focussing utilising a high NA objective lens increases the power-per-unit-area that results in increased Raman signals when compared with conventional Raman spectroscopy. The objectives lenses available are X10, X20, X20 U.L.W.D. (Ultra Long Working Distance), X50 and X100. Table 3.1 shows how the numerical aperture and collection angle differs for the objective lenses available. The numerical aperture of the focussing lens (objective) can be very high with X50 and X100. This means the light is focussed onto a small area, and collected over a wide angle which results in good collection efficiency.

Objective	NA	θ (°)
X 100	0.95	71.8
X50	0.80	53.13
X20 (U.L.W.D.)	0.40	23.58
X 10	0.30	17.46

Table 3.1 NA and resulting collection angle for the objective lenses available

Low NA objectives focus light onto a larger volume of material. This has implications on the information that is gained from the coating. The spectra arise from a greater number of unit cells, but with diminished power per-unit-area, and the collection efficiency is vastly reduced due to the reduced solid angle of collection (see Table 3.1). PVD coating spectra are inherently weak and this makes it impractical to use lower magnification/low NA objectives. Although it would appear from Table 3.1 that X100 is the objective of choice for many analyses, in reality it can lead to a diminished signal. This is because the Renishaw Raman systems are optimised for use with X50 objective lenses. The beam expander enlarges the beam so that it fits down the aperture of the X50 objective almost perfectly. When a X100 objective is used the input aperture is much smaller than for the X50, therefore there is a large amount of light that is wasted on the surrounding area within the objective. This results in a diminished power-per-unit-area incident on the sample, and thus a lower amount of Raman scattered light is collected and processed.

Empirical evidence has shown that the X50 objective gives the desired sampling volume (~2-3μm^3), collection efficiency and thus the best possible spectra for any given coating. Therefore subsequent spectra were acquired using the X50 objective, unless otherwise stated.

3.6.1.3 Exposure Time

The spectral range chosen is the main parameter that influences the sampling time. If only a specific band or small frequency range, i.e. for static exposures, is desired this can dramatically reduce the sampling time.

The choice of objective lens can vastly reduce the time necessary for a particular scan. As explained in section 3.6.1.2, a high numerical aperture corresponds to a large solid angle of collection and therefore for any given time a higher amount of scattered light will be collected than for low NA objectives. If the spectral range, objective lens and the focus are kept constant an increased exposure time will lead to a better Signal-to-Noise ratio (S/N) i.e. S/N $\propto$ (Exposure Time)$^{1/2}$.

PVD coatings are composed of transition metal nitrides. This meant that there was a big advantage as only a narrow spectral range of 100-1200cm^{-1} was required to obtain all the spectral information (including second order bands) when compared to organic compounds where a range of 400-3600cm^{-1} is routinely used. As a consequence of this a reduced sampling time was necessary which compensated slightly for the additional time required due to the coatings having a low scattering cross-section e.g. total scan time of ~5-10 minutes.

N.B All spectra featured in this thesis have a low frequency cut off/notch of ~150-200cm^{-1} that is as a consequence of the notch filter (see chapter 2; section 2.4.2.2). This meant that only spectral intensity from frequencies above ~150cm^{-1} was observed and bands that are near to this notch are distorted.

3.7 Spectral Database of PVD Hard Coatings

All coatings were grown using combined cathodic arc/unbalanced magnetron deposition. The PVD equipment used is described in Ref[12]. The Ti, Zr, Cr, Nb, V, Al, W and TiAl targets used were produced by vacuum casting whereas TiZr targets

consisted of small Ti and Zr segments which were bound on a backing plate. Typical deposition recipes are given in Ref.[13]. The coatings were deposited on High Speed Steel (HSS) and Stainless Steel (SS) and had a thickness of 2-3μm, deposited at 1-2 μmh^{-1}. Before analysis each coating surface was cleaned with ethanol to remove dirt and grease and samples were placed on a glass slide. A sampling area was chosen on the surface of each coating which was free from droplets/growth defects or blemishes of any nature and also from marks left by physical testing i.e. indentations, wear tracks and craters. In addition the sampling area from one laser wavelength analysis was noted and used again for the next analysis (although this was only an estimate). This was done because it is known empirically that there are subtle differences in the coating spectra (band position mainly) going from point-to-point. All spectra were acquired using a X50 objective, 400 seconds exposure-time and full laser power (unless otherwise stated). The throughputs of the different systems varied. The 780nm laser was attached to one Raman system and the 514.5 and 632.8nm lasers were used with another. On changing the lasers over from red to green excitation the resulting alignment differed also. A spectrum of silicon was always taken before any spectra were acquired. Silicon is a cubic crystal that has 3 phonons that have exactly the same frequency of $520cm^{-1}$[14]. This was used as a calibration for the Raman systems. If when a spectrum of silicon is taken and the resulting band did not have a position of $520cm^{-1}$, an offset correction was required within the software that recalibrates the grating to the correct position. This is performed routinely on a day-to-day basis.

The silicon band intensity is also a good method of assessing the alignment of a system (although certain orientations of the Si crystal with the laser beam can give a

more intense band this is dependent on the polarisation state of the specific laser being used). Therefore a spectrum of the silicon was acquired and the intensity noted as a way of compensating for the alignment differences between the systems and different laser wavelengths.

3.7.1 Binary Coatings

All the spectra are displayed by overlaying them. Thus, the x values of all the overlaid traces are set to the same value (the y-axis seen on the trace box is valid only for the current trace, all other traces are effectively "pulled-down" to the same y-axis scale i.e. normalised to the same scale. Therefore the intensities of traces cannot be compared. Binary coatings tend to have similar acoustic and optic band intensities. The Raman spectrum of the most well known of binary coatings TiN (Figure 3.10) is shown below along with ZrN (Figure 3.11) (N.B. both coatings are face-centred cubic[15], and are both composed of elements from group IV B of the transition metal series).

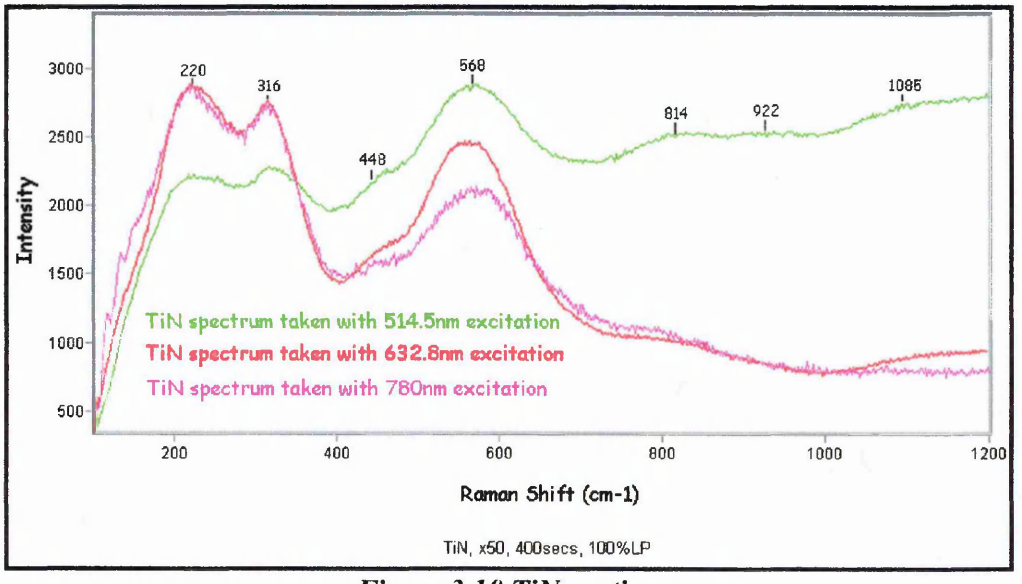

Figure 3.10 TiN coating

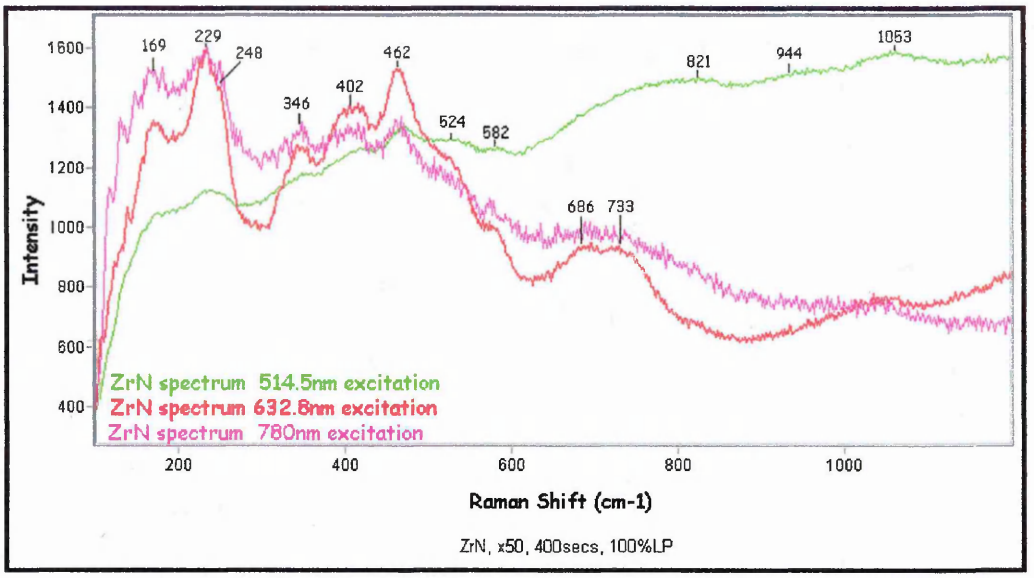

Figure 3.11 ZrN coating

When comparing the spectra of TiN and ZrN a similar pattern of bands arise although the ZrN spectrum shows a greater number of resolved bands in the optic mode region, which are much sharper than for TiN. The spectra above are both defect induced as they are fcc binary lattices and the similarity of the spectra also indicates that the coatings probably contain similar defects. The sharpness of the ZrN optic modes can be explained because the ZrN is more crystalline. What is also evident is that the ZrN bands are shifted relative to the TiN bands (see Table 3.2). This can be explained by the fact that Zr is a much heavier atom (RAM 91.22) than Ti (RAM 47.88). The lattice containing the Zr will thus have bands shifted to lower frequency. VN (figure 3.12) is also fcc but shows a different pattern and intensity of Raman bands. This may be explained by VN containing different and fewer defects than TiN and ZrN. As a consequence the first-order optical modes are weak (due to fewer defects within the lattice) but the acoustic modes are active and not dependent on the defect-density. Acoustic modes are always active even for fcc lattices (see section 3.4). AlN and MoS_2 (Figure 3.13 and 3.14 respectively) both have hexagonal structures with MoS_2

having sharper Raman bands. These Raman spectra are not dependent on a defect induced first-order Raman scattering mechanism.

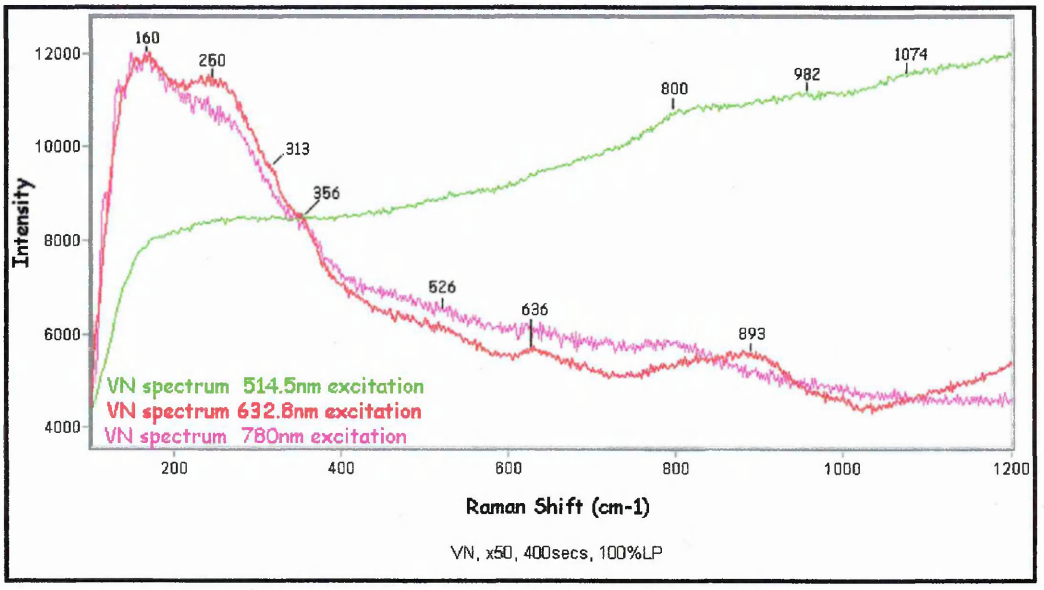

Figure 3.12 VN coating

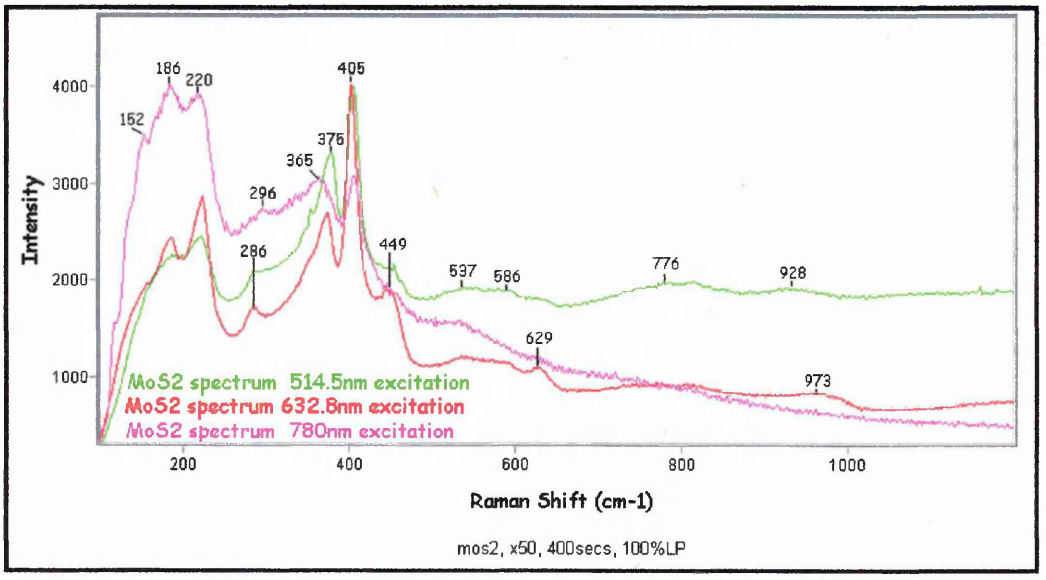

Figure 3.13 MoS_2 coating

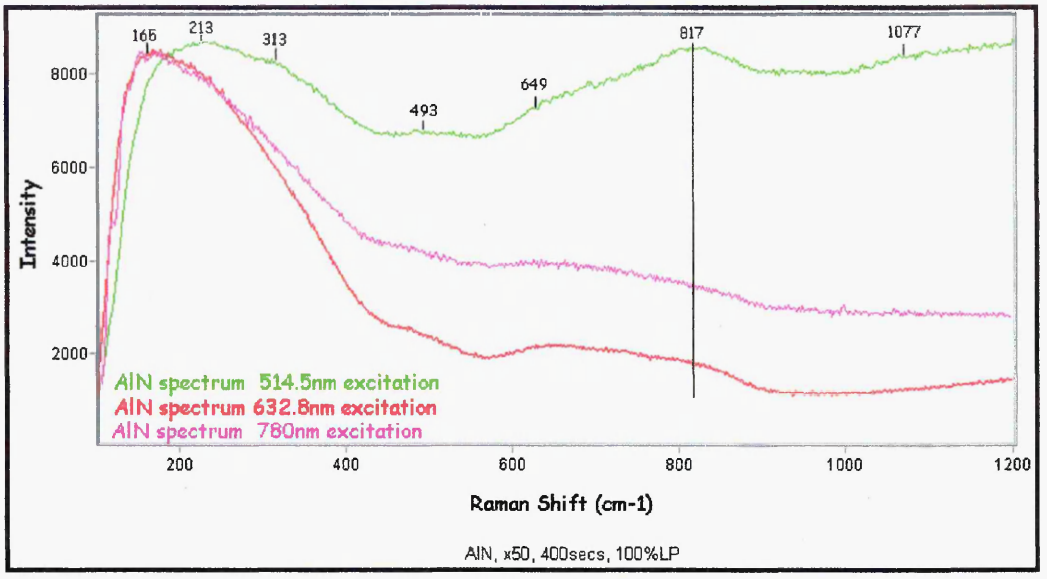

Figure 3.14 AlN coating

3.7.2 Multicomponent Coatings

Multicomponent coatings have additional elements within the TiN lattice. TiCN (Figure 3.15) has carbon introduced into the TiN lattice by CH_4 being bled into the coating chamber (in addition to N_2 and Ar). Since carbon is a small atom the only viable atomic sites are N sites. Hence the carbon atoms substituted for nitrogen at the N sites at random (this is again known from XRD data). TiCN still has a pattern of bands analogous to those of binary coatings. The carbon within the lattice will act as further defects/impurities thus reducing the symmetry and allowing first-order spectra to occur. For TiAlN Ti atoms of the TiN grid are partly substituted by Al atoms and the hardness increases by solid solution strengthening[16]. Due to the smaller atomic diameter of Al compared to Ti the coating structure deforms and this strengthens the grid structure[17].

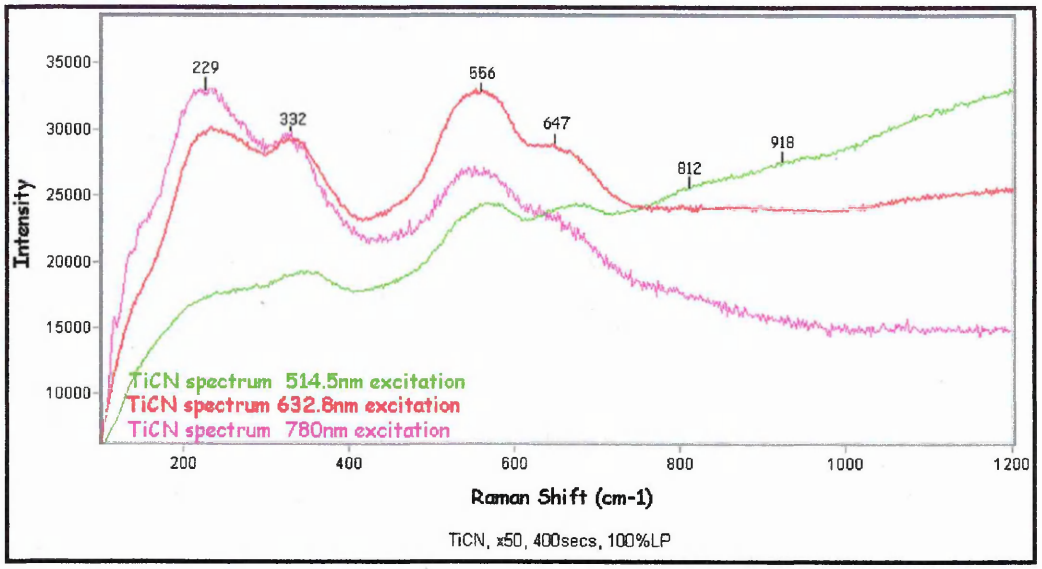

Figure 3.15 TiCN coating

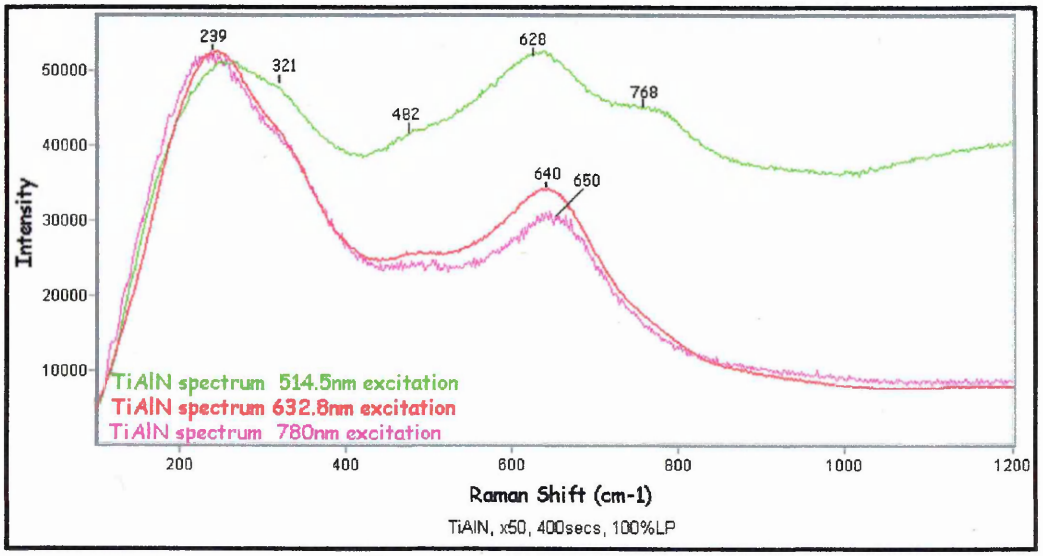

Figure 3.16 TiAlN coating

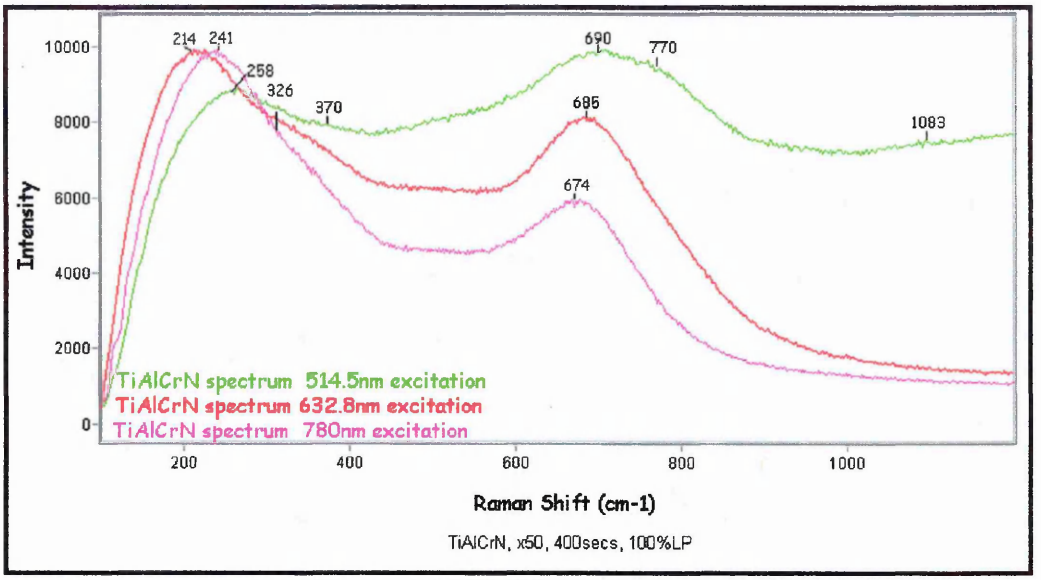

Figure 3.17 TiAlCr$_{(3at\%)}$N coating

The optic modes observed for the TiAlCrN appear to be less well resolved than for TiAlN. This is because the Cr atom is acting as a further defect thus resulting in a greater number of phonon relaxation mechanisms or additional bands. A further explanation is that a finer grain size[18] results when Cr is incorporated within the TiAlN lattice, again related to phonon relaxation mechanisms which can be regarded as defect induced band broadening.

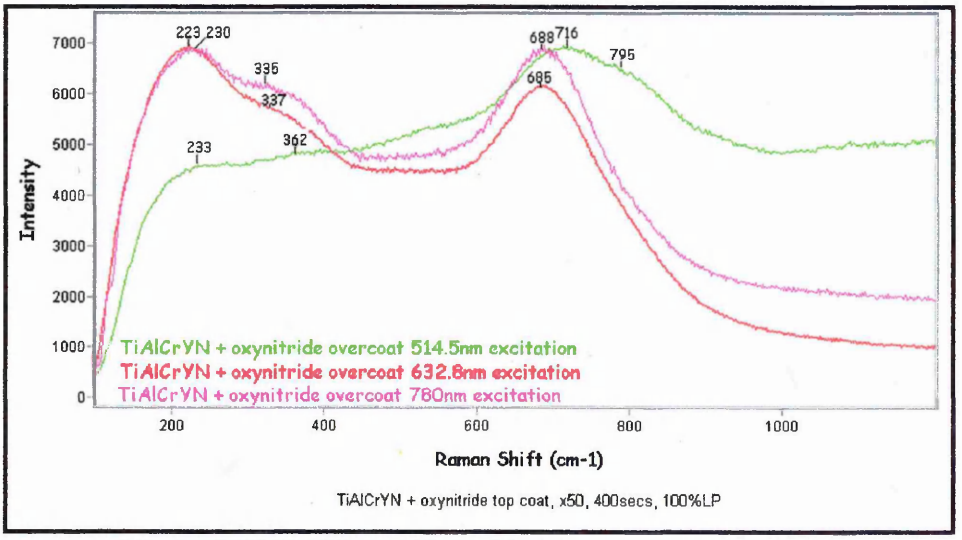

Figure 3.18 TiAlCr$_{(3at\%)}$Y$_{(2at\%)}$N with an oxynitride topcoat

The oxynitride topcoat (~0.1μm in thickness) has an glassy amorphous structure[19]. This may explain the absence of acoustic modes and the broader/shifted optic modes observed when the green laser is used. The green laser in theory should have the lowest penetration depth and therefore will have a greater contribution from the oxynitride layer within the Raman spectrum. The other wavelengths will also sample the underlying coating. The function of this topcoat is to reduce the friction coefficient during cutting.

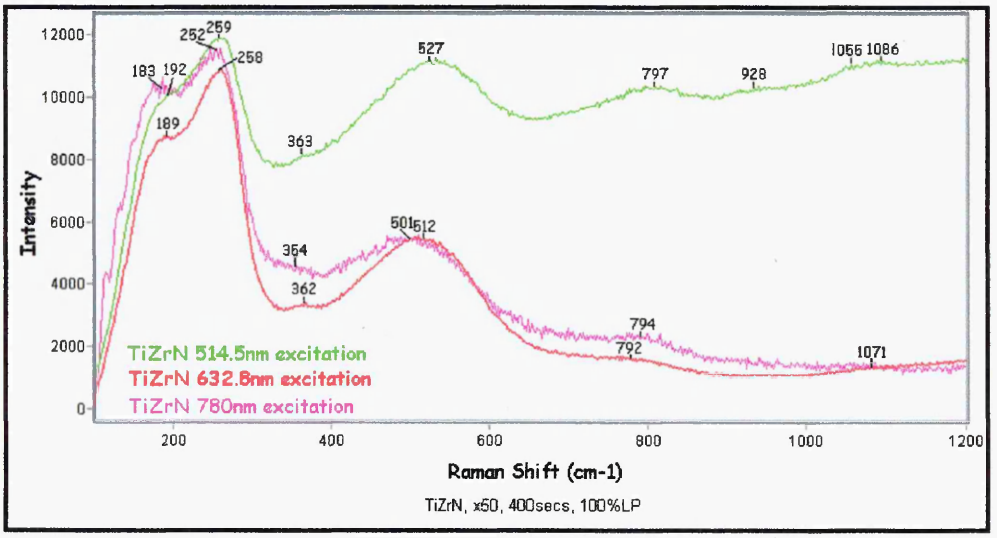

Figure 3.19 TiZrN coating

Because the Raman spectra are defect induced, the number of defects within the lattice will have a profound influence on the intensity of Raman bands. This is evident when the intensity of the main optical phonon modes are compared for TiN, TiCN and TiAlN (Figure 3.20 below). N.B. the traces are overlaid but the y-axis is now the actual intensity of bands and the scale is from the most intense spectrum i.e. TiAlN. All other traces are relative to it.

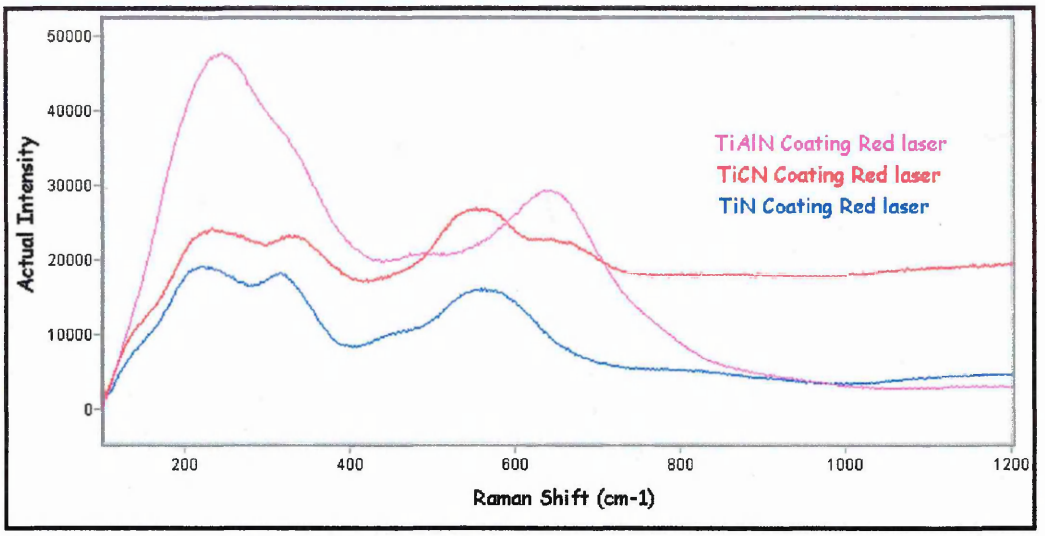

Figure 3.20 Overlaid multicomponent coating spectra demonstrating an increase in spectral intensity

It can be seen that when carbon is introduced into the TiN lattice the overall intensity is increased. The resulting Raman spectrum is very similar to TiN but a further optic band is visible at ~660cm^{-1}. This mode must be due to the carbon within the lattice. When aluminium is introduced into the lattice, (random substitution at some Ti sites), a further increase is observed. Due to the smaller atomic diameter of Al compared to Ti the coating structure is known to deform[17], therefore creating further defects. The acoustic modes for TiAlN are much more intense than for TiN and TiCN which agrees with the theory that the acoustical modes are mainly due to vibrations of the heavy metal atoms within the lattice and the optical modes are due to the Nitrogen/Carbon.

Multicomponent coatings tend to have fewer obvious bands than binary coatings but have more regions of spectral density. These spectra do not arise by a proper defect induced first order mechanism as for binary coatings because the added elements (Al, C, Zr, Cr etc.) which are known to occupy lattice positions at random, have the effect of being further defects and first-order phonon modes are observed.

3.7.3 Superlattice Coatings

These coating systems have alternating layers of two coating compositions (see chapter 1, section 1.3.3).

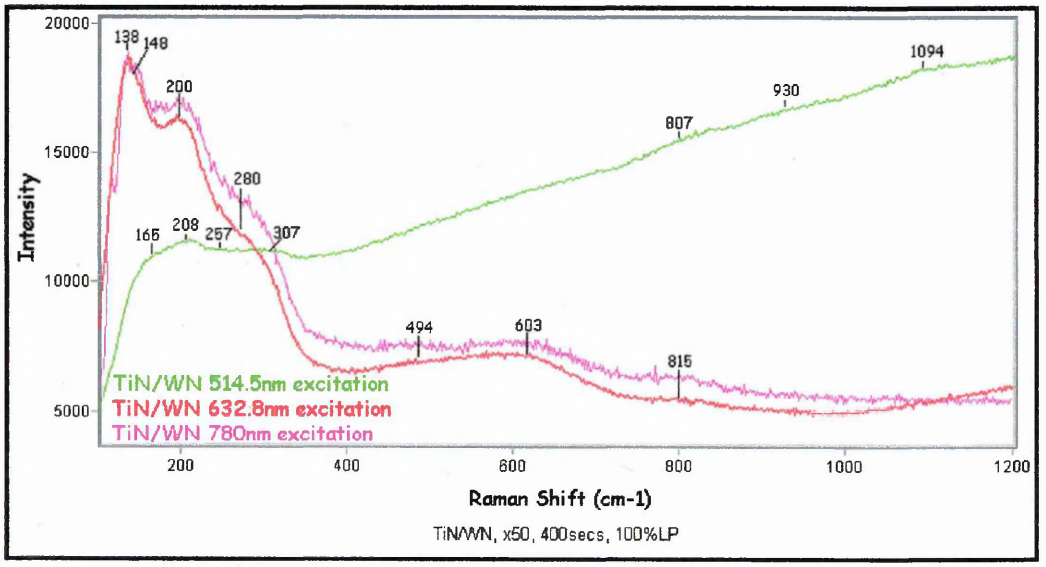

Figure 3.21TiN/WN coating

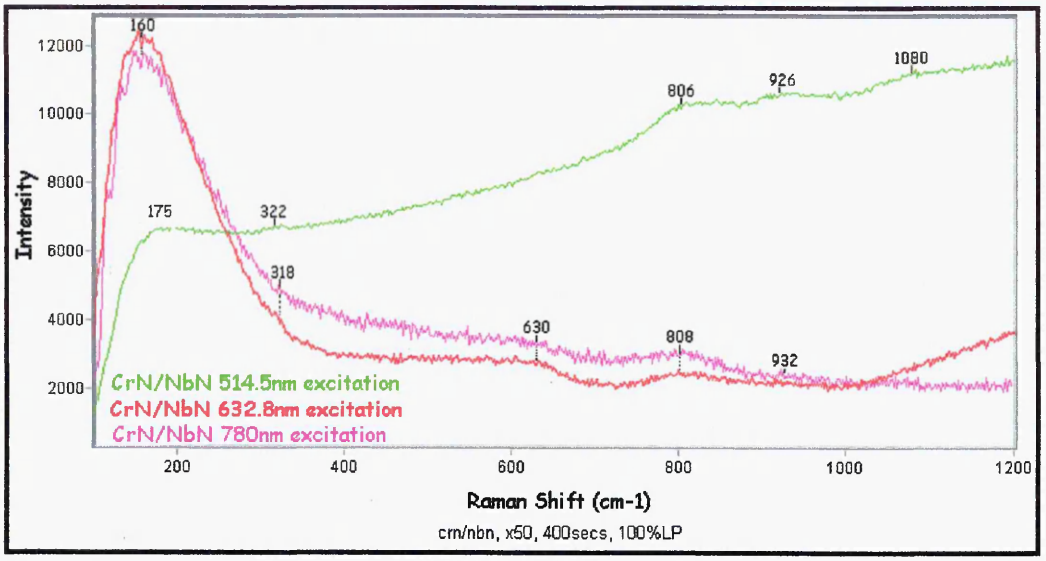

Figure 3.22 CrN/NbN coating

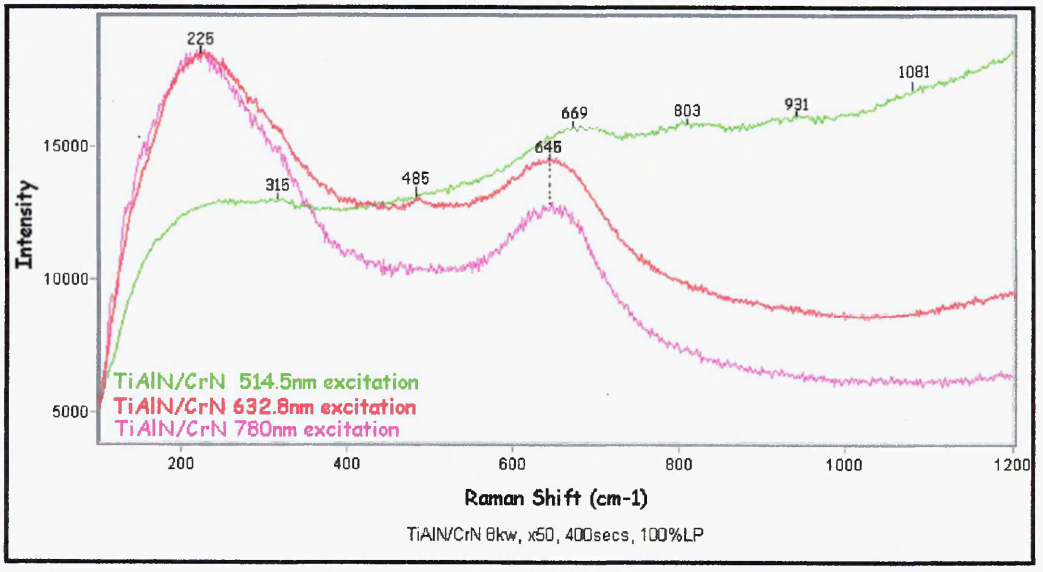

Figure 3.23 TiAlN/CrN coating

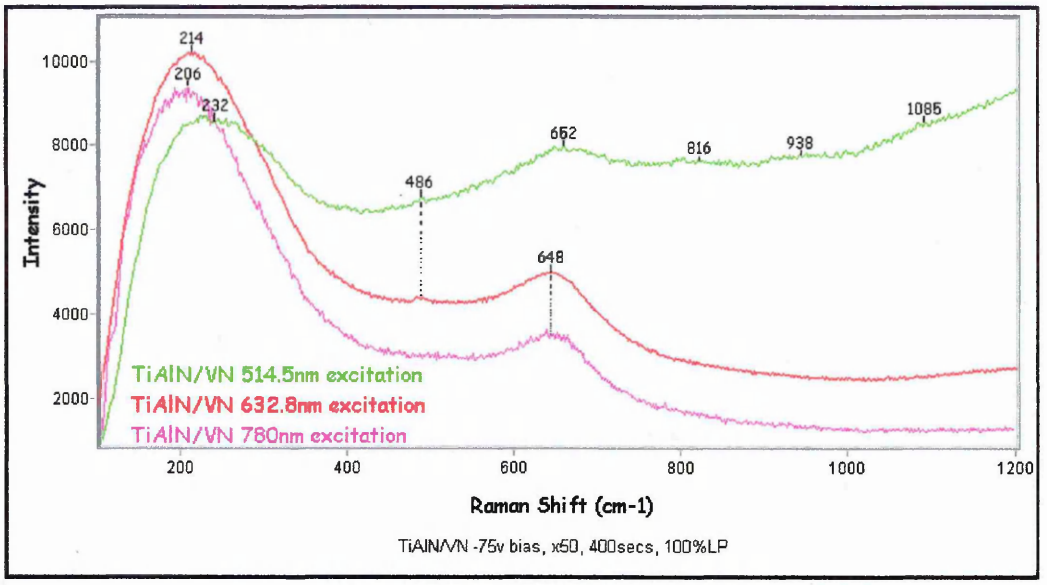

Figure 3.24 TiAlN/VN coating

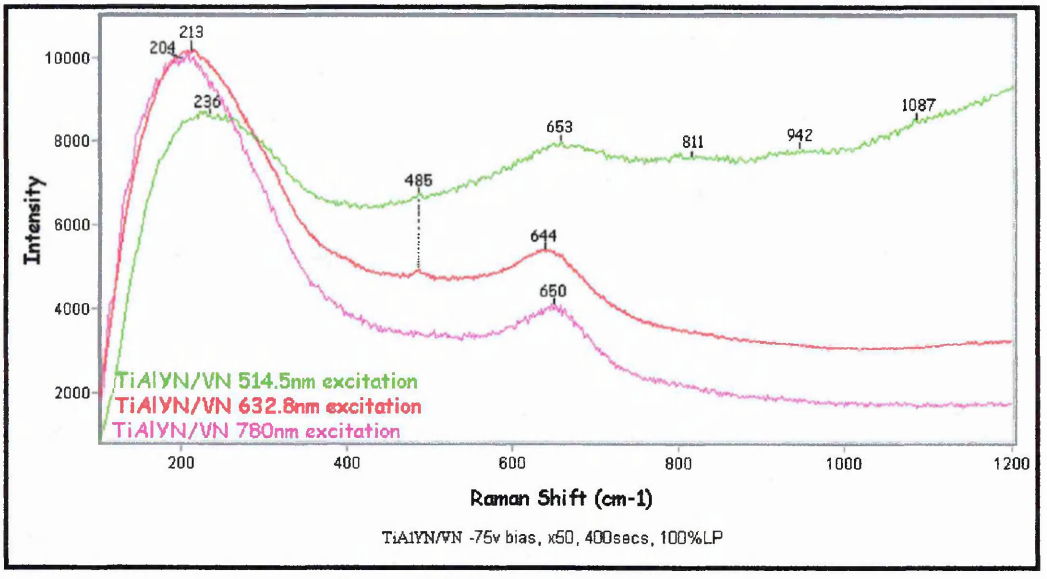

Figure 3.25 TiAlYN/VN coating

When 514.5nm (green) excitation is used to study the superlattice coatings there was a strange effect observed. The Raman spectra do not compare with the 632.8 and 780nm spectra, which for the most part resemble that of the multicomponent series of coatings. The most noticeable difference was that the acoustic modes were very weak

and the spectra were analogous to binary coatings i.e. the acoustic and optic modes have similar intensity. This could be due to the sampling depth of the 514.5nm laser which may be only sufficient to analyse the uppermost coating in the superlattice systems, therefore giving a spectrum indicative of a binary coating. In the case of TiN/WN and CrN/NbN which are both binary coatings systems, combined to produce a superlattice, we may expect the pattern and intensity of bands observed, indicating fewer defects within the lattices. For TiAlN/CrN, TiAlN/VN and TiAlYN/VN these are a binary and multicomponent combined system and the acoustic modes should, in theory, be more intense than optic modes. For TiAlN/CrN the CrN must be the uppermost coating layer and the laser must not be sampling the underlying coating, even though the superlattice period, (i.e. bi-layer thickness), is 3.8nm[20]. The spectra for the TiAlN/VN and TiAlYN/VN have spectra that resemble that of TiAlN i.e. acoustic modes which are much more intense than the optic modes. In addition the overtone and combination bands observed at higher frequencies are much more intense, indicating that a resonance enhancement may be taking place.

3.7.4 The Effect of Laser Wavelength on the Raman Spectra of PVD Coatings

There does not appear to be a marked difference in the Raman spectra when 632.8 and 780nm laser excitation is used. The spectra taken with 632.8nm laser excitation are, however, much more intense. However, when the 514.5nm laser was used the coating spectra showed three different phenomena, i) the spectra have an upward profile similar in nature to fluorescence, ii) the overtone and combination bands between 700-1100cm^{-1} are more readily observed indicating an enhancement of these

particular bands, and iii) most importantly further optic modes are observed in some cases. This is especially the case for TiAlN, TiAlCrN and AlN.

Additional bands/information was available for certain coating compositions when 514.5nm excitation was used. Unfortunately, however, the many undesirable spectral features far outweigh this (see below):

1) The upward profile of the spectra (fluorescence?). This could be due to possible surface contamination; for example, absorbed oils and dirt, having a larger contribution to the spectrum than for the Red and near infrared lasers.
2) lower penetration/sampling depth, (which can result in information being lost especially for superlattice coatings).
3) Poorer signal-to-noise when compared to spectra taken with a 632.8nm laser.

The 632.8nm laser therefore gives spectra with desirable features, the biggest bonus being that the spectra require very little/if any post analysis manipulation most notably base-line correction, which is known to generate distortions in spectra.

Therefore the majority of analyses subsequent to these findings were performed using the 632.8nm red laser.

3.8 Information Obtained From the Raman Spectral Lines

It has been seen that PVD coatings give Raman spectra which show lattice modes in the region 100-1200cm^{-1} in which there are two pronounced groups of bands related to acoustical (150-300cm^{-1}) and to the optical (400-650cm^{-1}) parts of the phonon spectrum. Table 3.2 (below) shows a summary of assignments for the optical and acoustical phonon modes for the coating systems investigated (for spectra acquired with 632.8nm laser).

Mode	TA / LA	TO / LO	2A	A+O	2O
TiN (fcc)	220, 316	560-700	448	814	1185
(Fig. 3.10)					
Literature [4-7]	200, 340	520-590	400-500	~800	~1100
ZrN (fcc)	169, 229-248	462-580	346, 402	686, 733	1041
(Fig. 3.11)					
Literature [4]	160, 260	460-560	325-525	~710	~1025
VN (fcc)	160, 250	526, 636	313, 356	740-1000	1074
(Fig. 3.12)					
MoS_2 (fcc)	186, 220	375, 405	449	500-670	750-870
(Fig. 3.13)					
AlN (hcp)	160-450	575-700	493	700-900	----------
(Fig. 3.14)					
TiCN (fcc)	229, 332	556, 647	---------	812	1100
(Fig. 3.15)					
TiAlN (fcc)	239, 315	640	482	----------	----------
(Fig. 3.16)					
TiAlCrN (fcc)	214, 326	685	370	----------	----------
(Fig. 3.17)					
TiAlCrYN (fcc)	223, 335	685	----------	----------	----------
(Fig. 3.18)					
TiZrN (fcc)	189, 258	512	362	792	1071
(Fig. 3.19.)					
TiN/WN (fcc)	138-148, 200	603	280	815	~1100
(Fig. 3.21)					
CrN/NbN (fcc)	160	630	318	808	~1100
(Fig. 3.22)					
TiAlN/CrN (fcc)	225	645	485	----------	----------
(Fig. 3.23)					
TiAlN/VN (fcc)	214	648	486	----------	----------
(Fig. 3.24)					
TiAlYN/VN (fcc)	213	644	485	----------	----------
(Fig. 3.25)					

N.B. There is a high probability of strong overlap (especially between optic modes of the crystal lattice and second order acoustic modes).

There has been additional evidence gathered to support the theory that the optic modes are mainly due to the vibrations of the lighter elements and the acoustic modes due to the vibrations of the heavier elements within the lattice as there are patterns of bands observed for each class of coating. Binary coatings tend to have optic and acoustic modes that are approximately the same intensity. Multicomponent coatings, with an additional metallic element within the lattice, have acoustic modes that are far greater in intensity than optic modes. Superlattice spectra have bands that most resemble multicomponent coatings. In addition, higher frequency bands that are combinations and overtones are also observed but do not give any additional valuable information. All these Raman bands are quite low in intensity and are usually very broad (FWHM 100-150cm^{-1}).

The spectra that result from each coating whether it be binary, multicomponent, superlattice is unique i.e. a fingerprint. The Raman spectra are dependent on the atoms that make up the lattice, the crystallinity/order, residual stress and defect density.

Band widths will increase with temperature, doping crystallite size, i.e. TiAlN should have narrower bands than TiZrN due to the size of Zr relative to Al (if all other contributions are kept equal), and structural defects i.e. point defects such as vacancies and interstitials resulting in an increased number phonon relaxation mechanisms. Band widths should also increase with a decrease in crystallite size/grain size, also a result of such relaxation mechanisms. Chapter 7 describes how deposition parameters can affect these spectral features.

The band positions will shift to low frequency with tensile strain/stress and shift to higher frequency with compressive strain/stress[21] and this is the case for both residual and induced stresses (also detailed in chapter 7). The positions of the phonon bands also depend on the atomic weight of the atoms that make up the lattice.

References

1 D. Hull in "Introduction to dislocations", Pergomon press, London, 1965 pp1-12.

2 C. Kittel, in Introduction to Solid State Physics (5^{th} Ed.), John Willey & Sons New York 1976.

3 Inelastic light scattering: proceedings of the 1979 US-Japan Seminar held at Santa Monica, California, USA, 22-25 January, 1979 ; editors, E. Burstein and H. Kawamura, Oxford: Pergamon Press,1980 Notes.

4 W. Spengler and R. Kaiser, Solid State Communications. 18, (1976) 881.

5 W. Spengler, R. Kaiser and H. Bilz, Solid State Communications 17, (1975) 19.

6 C.C. Chen, N.T. Liang, W.S. Tse, I.Y. Chen and J.G. Duh, Chinese Journal of Physics 32(2), (1994) 205.

7 W. Spengler, R. Kaiser, A.N. Christensen and G. Muller-Vogt, Phys. Rev. B 17(3) 1095-1101 (1978).

8 G.P. Montgomery, Jr., M.V. Klein, B.N. Ganguly and R.F. Wood, Phys. Rev. B 6(10), (1972) 4047.

9 R.T. Harley, J.B. Page, Jr. and C.T. Walker, Phys. Rev.B 3(4), (1971) 1365.

10 C. Raptis, Phys. Rev. B, 33(2), (1986) 1350.

11 M. Krantz and F. Luty, Phys. Rev. B, 31 (1985) 2599

12 W.-D. Münz, D. Schulze and F.J.M Hauzer, Surface and Coatings Technology, 50 (1992) 169.

13 I. Petrov, P. Losbichler, D. Bergstrom, J.E. Greene, W.-D. Münz, T. Hurkmans and T. Trinh, Thin Solid Films, 302 (1997) 179.

14 I. De Wolf, G. Pozzat, K. Pinardi, D.J. Howard, M. Ignat , S.C. Jain and H.E. Maes, Microelectron. Reliab., 36(11/12) (1996) 1751-1754.

15 L.A. Donohue, J. Cawley and J.S. Brooks, Surface and Coatings Technology 72(1-2), (1995) 128.

16 H.K. Tonshoff, B. Karpuschewski, A. Mohlfeld and H. Seegers, Surf. Coat. Technol. 116-119 (1999) 524-529.

17 O. Knotek, M. Bohmer, T. Leydecker, J. Vac. Sci. Technol. A 4 (1986) 2695-2700.

18 D.B. Lewis, L.A. Donohue, M. Lemke, W.-D. Münz, R. Kuzel Jr., V. Valvoda and C.J. Blomfield, Surf. Coat. Technol. 114 (1999) 187-199.

19 M. Lembke, D.B. Lewis, W.-D. Münz, J.M. Titchmarsh, Surface Engineer (submitted 2000).

20 W.-D. Münz, L.A. Donohue, P.Eh. Hovsepian, Surf. Coat. Technol. 125 (2000) 269-277.

21 N. Muraki, V. Sergo, G. Pezzotti, G. Katagiri, S. Meriani and T. Nishida, Applied Spectroscopy, 51(11) (1997) 1761-1765.

22 G. Pezzotti, Comp. Sci. Technol., 59 (1999) 821-831.

Chapter 4

Studies of Mechanically Induced Deformation of PVD Coatings

Chapter 4 Studies of Mechanically Induced Deformation of PVD Coatings

4.1 Previous Roles of Raman Microscopic Analysis in the Field of Deformation Analysis

It appears from the literature that Raman microscopy has not been used previously for the study of deformation of PVD coatings. The CSEM Instruments: Advanced Mechanical Surface Testing Application Bulletin does however mention that Raman mapping of scratched regions can provide additional information on the local stress and strain distribution, together with the molecular composition of any tribochemically produced residues[1]. This clearly sends out a message that Raman microscopy is an ideal method for gaining this type of information but neglects to provide references on this point. Raman has, however, been used to study deformation processes of other materials:

1) Nanocrystalline germanium samples processed by severe plastic deformation under high pressure, 6 Gpa were investigated by TEM, X-ray diffraction and Raman spectroscopy[2]. XRD showed decreasing peak intensities and peak broadening. Raman revealed decreasing band intensities, a peak shift to lower frequencies, peak broadening, asymmetry of the peaks and new Raman spectral bands. This was attributed to two areas of the NC Ge: the interior with a near perfect crystal lattice and the grain boundary defect structure associated with high levels of elastic strains and distortions of the crystal lattice[2].

2) Studies of particle beam damage in SiC have been studied[3] in order to understand crystal growth mechanisms. It was found that the damage layer depends on the kind and energy of the bombarding ions (heavier ions such as Ar^+ resulted in

severe damage). The lattice distortions produced by the ions have to be annealed by a subsequent thermal treatment but irreversible structural changes do occur[3]. Raman spectroscopy was used to monitor transformation between crystalline and amorphous state and detect different types of damage[3]. In addition, it was able to give details on the composition of damaged layers and showed chemical rearrangement for heavily damaged layers. It was concluded that Raman spectroscopy was able to discriminate between different degrees of material distortion. Broader bands resulted due to the lack of translational long-range order, resulting in loss of wavevector conservation and a breakdown of the Raman selection rules. The density-of-state functions for the relevant wavevector components showed[3] a broad distribution with maxima in the neighbourhood of the acoustic and optic modes near the centre of the Brillouin zone.

3) Diamond has also been studied after ion-implantation, to understand the processes by which defects affect the electrical conductivity of diamond. Understanding the nature of defects and their removal would facilitate the doping of diamond by ion-implantation. Previous work[4] has shown that there is a critical point after which the diamond structure cannot be restored by annealing. Raman spectroscopy was used to study the density of defects, i.e. implantation dose, and annealing, since Raman spectroscopy is able to distinguish between the allotropes of carbon. Sample irradiation above the critical irradiation dose results in an amorphous carbon layer. The annealing behaviour[5] of the Raman peaks from this layer gave important clues as to the defect origin and kinetics.

Pezzotti performed work on micro-mechanical analysis of fracture and deformation phenomena in polycrystalline ceramics[6] that relates quite nicely to work presented

in this chapter. He discusses how the utilisation of micrometer scale resolution provided by Raman microscopy enables the micro-mechanical features of the fracture and deformation behaviour of ceramics to be investigated. (1) The local analysis of internal residual stresses in monolithic and composite ceramics, resulting from thermal and elastic anisotropy; (2) the quantitative assessment of crack-face closure stresses (so called bridging stresses) and (3) the mapping of residual stresses stored in the neighbourhood of an indentation process which is the most applicable to this work. For ceramics, besides the work dissipated in plastic deformation, a non-negligible amount of the overall work applied by the indenter on the specimen surface may be transformed in elastic energy that remains stored around the indentation impression. A direct evaluation of the elastic strain energy associated with a Vickers indentation impression was measured using microprobe piezo-spectroscopy[6]. High compressive stress values resulted from the centre of the indentation toward the edge. Out from the impression, the stress tended to relax over a distance between 150 –200 μm. Along the diagonal, the stress relaxation occurred over a shorter distance than for the other directions due to the stress release effect arising from surface cracking. The Raman spectrum also provided immediate practical information regarding the structural damage of the material on the crystal lattice scale. The higher the local indentation pressure the larger was the observed peak width. The long-range crystalline order was clearly increasingly disrupted moving towards the indentation centre, which was the highest stress concentration during the indentation process. The disruption of the crystallinity was likely due to a high dislocation density beneath the indentation impression. Due to the low dislocation mobility in non-oxide ceramics a partial amorphisation was not ruled out. In principle Raman analysis of peak width,

similar to X-ray analysis, can enable one to get direct information on the local plastic deformation of the crystal[6].

The development of a scanning near field optical microscope (SNOM) coupled to a Raman spectrometer has enabled Raman mapping with a spatial resolution of ~150nm[7]. This has been used to gain a high-resolution map of the region surrounding a scratch on a single crystal silicon wafer. Raman measurements indicated that the silicon had undergone a phase change during the scratching process[7]. Shifts to higher frequncy were observed in the 520cm^{-1}silicon band indicating compressive stresses[7]. In addition they mentioned that previous theoretical studies of the response of solids to plastic-elastic deformation suggested that the greatest residual compressive stress was expected to be located at the plastic-elastic deformation interface[7].

4.2 Physical Methods Adopted for Wear/Deformation Studies

4.2.1 Pin-on-Disk Tribometry

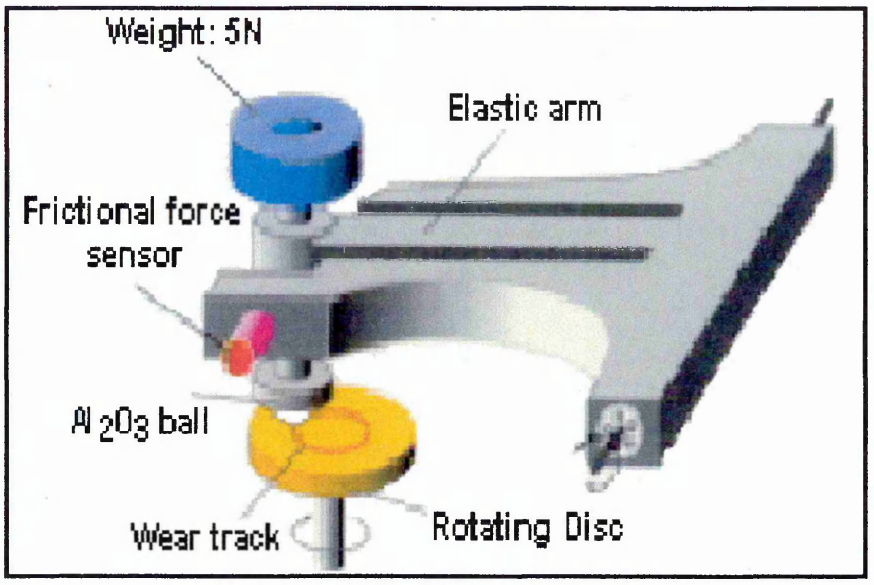

Figure 4.1 Schematic representation of a Pin-on-Disk (CSEM tribometer)

In pin-on-disk tribometry, a flat or sphere shaped contact ("pin") is loaded onto the test sample ("disk") with a precisely known weight (governed by the normal load which is placed as a dead weight on top of the disk). The pin is mounted on a stiff lever, designed as a frictionless force transducer. As the disk is rotated with a known velocity (or sliding speed), the resulting frictional forces acting between the pin and the disk are measured by very small deflections of the lever. This results in a trace of friction coefficient vs. sliding distance in which an average coefficient of friction can be gained. Wear coefficients for both the pin and disk material are calculated from the volume of material lost during a specific test run. This simple method enables the determination of friction and wear behaviour of almost any solid-state material combination.

The Bodycote - SHU standard conditions for Pin-on-Disk testing are:

1) The CSEM Tribometer test rig is used under ambient laboratory conditions with no strict temperature or humidity control (~20-25°C and a measured relative humidity of between 30 to 35%).
2) Corundum (Al_2O_3) polycrystalline 6 mm diameter balls (Saphirwerk, Industrieprodukte AG) with a hardness of 1900 HVN and a surface quality R_a 0.2 μm are used as counterbodies.
3) Normal load of 5 N
4) Sliding speed of 10 cm/s

4.2.1.1 The Sliding Surface

Surfaces are far from perfectly clean. Even if at one time they were very clean (i.e. when both the coating and Al_2O_3 ball are cleaned with ethanol before the experiment is started), they inevitably become "contaminated" from the atmosphere around them. They can also become contaminated from other sources such as the storage container (plastic bags). Plasticisers, unreacted monomer and other additives seem to have an affinity for the surface of the coatings. It has been observed that if these coating are kept in these bags there is a visible layer on the surface that must be cleaned off before an experiment. Paper envelopes and tissue paper should be used as storage media instead.

The definition of standard conditions for sliding, for the three classes of materials (metal, polymers and ceramics) are as follows:

i) Metals will usually be covered with a film of oxide, which is covered by a second film of adsorbed gases and hydrocarbons (oils).

ii) Polymer surfaces may contain adsorbed water and plasticisers, and will likely be covered with biocides, absorbed gases, and oils.

iii) Ceramics materials will also be covered with adsorbed gases and oil; in addition, the non-oxide ceramics may oxidise and be covered by a thin layer of native oxide.

The thickness of the above mentioned adsorbed layers and coatings are in the order of 10 nm. The presence of these thin films must be taken into account as they can significantly affect the sliding wear characteristics and result in wear variations.

4.2.1.2 Friction

Friction may be defined as the resisting force tangential to the common boundary between two bodies when, under the action of an external force, one body moves relative to the surface of the other. It is necessary to distinguish between rolling and sliding contact. Sliding is the dominant frictional movement that will be described exclusively in this chapter.

The magnitude of the frictional force is described by the value of the coefficient of friction, which can vary over a wide range: from 0.001 in a lightly loaded rolling contact to greater than 10 for clean metals sliding against themselves in vacuum[8,9]. However, for most materials sliding in air the coefficient of friction lies between 0.1 and 1[8]. Equation 4.1 shows the mathematical relationship of friction associated

with sliding wear processes, where μ is the coefficient of friction, F_f, is the frictional force tangential to the sliding direction and F_n is the normal load.

$$\mu = \frac{F_f}{F_n} \qquad \textbf{Equation 4.1}$$

A model developed by Bowden and Tabor[10] assumed that the frictional force which arose was mainly from two sources: an adhesive force developed at the real areas of contact (asperity junctions) and a deformation force required to plough the asperities of the harder surface material through the softer materials. Thus:

$$\mu = \mu_{adhesion} + \mu_{deformation} \qquad \textbf{Equation 4.2}$$

There have been many models used to predict the value of the coefficient of friction [8,9,10]. Some, which may be valid for special applications, make broad assumptions which relate to a broad range of materials and applications. Generally there are too many interactions that occur during sliding of two counterparts in an ambient atmosphere to allow the development of effective models for predicting friction characteristics of materials. However, important pointers can be derived from some models[8,9,10]:

i) There is a tendency of materials to react with compounds/elements in the surrounding environment, resulting in e.g. an oxide transfer layer, which can support the loads encountered during sliding to a certain extent (Figure 4.2 (a)). In addition, the tribo-chemical reactivity of certain materials can produce hard stable oxides (e.g.Al_2O_3), as wear debris which may be

caught in between the two contacting bodies, resulting in third-body abrasive wear which can result in wear grooves[8], (see Figure 4.2(b)). Figure 4.2 shows ESEM (Environmental Scanning Electron Microscopy) images of wear tracks resulting from Pin-on-Disk tests on TiAlN/VN superlattice coatings.

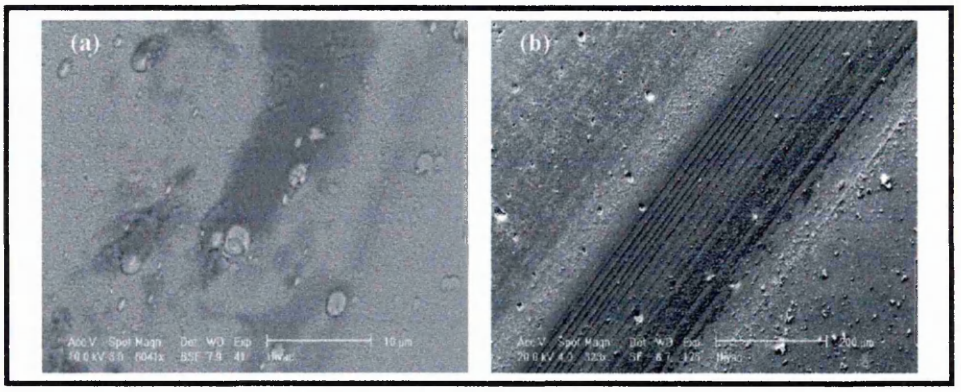

Figure 4.2 ESEM images of worn surfaces (a) transfer layers within the wear track when an Al_2O_3 ball is used (b) wear grooves observed when a WC ball is used i.e. third-body abrasive wear (N.B. All other sliding conditions were kept constant.)

ii) The solubility of the counterparts has a major influence on the adhesive friction forces. This mainly affects inert materials in inert atmospheres OR in vacuum when no oxide or adhesion layers are present to keep the clean surfaces apart. An example is the exceptionally high friction coefficient observed from metals sliding in a vacuum[8,9].

iii) Mechanical properties of the counterparts such as hardness, toughness, internal stresses, which affect mainly plastic deformation in the asperities or the cracking and spallation behaviour of a material. The standard counterbody used for these sliding tests are 6mm-diameter polycrystalline corundum (Al_2O_3) balls. Corundum is also chemically inert and reduces

the possibility of reaction products occurring from the ball with the coating under investigation.

(i), (ii) and (iii) are issues or physical processes which might be included in a model for friction.

4.2.1.3 Wear

Wear is the removal of material from a solid surface as a result of mechanical action[9]. This term covers a broad range of mechanisms; namely abrasive, adhesive, erosive, fatigue and oxidative wear. For ceramics, the amount of material removed is usually small, especially from the mechanisms that occur for PVD coating systems in sliding contact with corundum. The removed material or wear debris analysis will be discussed in chapter 6.

4.2.1.4 Simple Theory of Sliding Wear: The Archard Wear Equation

When two surfaces in contact slide over each other, one or both of the surfaces will suffer wear. Holm and Archard originated a simple theoretical analysis of this type of wear. It highlights the main variables that influence sliding wear; it also yields a valuable method of describing the severity of wear, by means of the wear coefficient k. Although this method was originally developed for metals it can be applied to other similar materials as well. The starting point for the model is the assumption that contact between the two surfaces will occur where the asperities touch, and the real area of contact will be equal to the sum of the individual asperity contact areas. This

area will be closely proportional to the applied normal load, and it can be assumed that, for metals and metallic-like materials, the deformation of the asperities will be plastic. Figure 4.3, shows a single asperity contact assumed to be circular with radius a, at various stages of evolution during sliding.

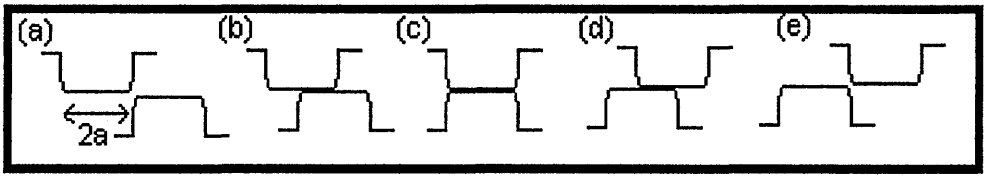

Figure 4.3 Single asperitiy contacts during sliding

It has reached its maximum size at (c), and the normal load supported by it, ∂W, is given by.

$$\partial W = P\pi a^2 \qquad \textbf{Equation 4.3}$$

Where P is the yield pressure for the plastically deforming asperity. As sliding proceeds, the two surfaces become displaced (shown by Figure 4.3) (d) and (e) and the load/pressure originally borne by the asperity is transferred to other asperity junctions which are in the process of forming elsewhere on the surfaces. Continuous sliding results in the continuous formation and destruction of these asperity contacts. Wear is associated with the detachment of fragments of material from the asperities, and the volume of each wear fragment will depend on the size of the asperity junction from which it originated. The analysis of wear debris/fragments utilising Raman microscopy will be discussed in detail in Chapter 6.

The constant K termed the wear coefficient is dimensionless and always less than unity. This provides a valuable means of comparing the severity of wear processes in different systems. However, for engineering applications the quantity K/H is often more useful. This is given the symbol k and called the dimensional wear coefficient. k is usually quoted in units of m^2/N, and represents the volume of material removed by wear (in mm^3) per unit distance slid (in metres), per unit normal load on the contact (in Newtons).

It has been found experimentally that for many systems the volume of material removed is indeed proportional to the sliding distance. A transient behaviour is often observed at the start of sliding, until equilibrium surface conditions have become established; the wear rate during this initial *running-in* period may be either higher or lower than the corresponding steady-state wear rate. Table 4.1 (below), shows the friction and wear characteristic plus other important parameters for some current coating compositions.

SAMPLE	THICK.	STRESS	ROUGHN.	SLIDING WEAR			ABRAS. WEAR	ADHESION		HARDNESS		YOUNG'S
				friction	wear resist	K	K_c	Rockw-C	Scratcht.	HP	HK	modulus
	μm	GPa	μm		m^3/m	m^2/N	m^2/N	test	$[L_c]$= N	(50mN) GPa	(25g)	1/(1-vsqd)
CrN/NbN 4-23 (-75V)	5.0	1.8	0.072	0.69	3.6E-15	2.1E-15	6.10E-13	1	50	42	3500	423
CrN/NbN 4-29 (-105V)	3.5	3.5	-----	0.80	-----	-----	7.49E-13	1	50	43	3255	364
CrN/NbN 4-22 (-120V)	4.5	6.5	0.033	0.90	5.0E-15	5.0E-15	6.60E-13	1	62	56	3800	458
CrN/NbN 4-25 (-150V)	4.1	7.1	0.026	0.89	2.0E-14	3.9E-15	7.489E-13	1	52	48	3650	425
TiAlYN/VN (-75V)	3.8	5.6	0.189	0.60	4.4E-15	4.0E-16	1.90E-13	2	30	45	3250	443
TiAlYN/VN (-95V)	4.0	8.5	0.162	0.65	4.5E-15	4.5E-16	9.92E-14	3-4	39	60	4430	518
TiAlYN/VN (-105V)	4.5	-----	0.104	0.62	2.0E-15	3.9E-16	1.49E-13	3	34	38	3565	500
TiAlN/VN (-75V)	4.2	3	0.098	0.58	3.07E-16	6.0E-17	2.27E-13	2	47	29	3020	428
TiAlN/VN (-95V)	4.2	7.7	0.139	0.56	2.51E-16	5.0E-17	2.83E-13	2	49	36	3940	449
TiAlN/VN (-125V)	4.1	9	0.159	0.50	3.3E-16	5.1E-17	2.99E-13	2	44	34	4045	416
TiAlN/CrN (-75)	4.5	5.1	-----	-----	-----	2.4E-16	1.901E-13	1	50	55	3195	453
TiAlN/CrN (-85)	4.1	7.4	-----	-----	-----	-----	-----	2	47	53	4445	465
TiAlN/CrN (-95)	4.1	9.2	-----	-----	-----	3.1E-15	1.055E-13	1	52	60	4145	515
TiAlCrYN (SC 11)	3.8	-----	0.15	0.65	4.1E-16	1.0E-16	1.49E-13	1-2	53	46	2700	452

Table 4.1: Friction, wear and other important parameters for current coating systems

4.2.1.5 Wear of Ceramic Hard Coatings

Oxidative wear is the dominant wear mechanism for ceramics whereby the energy produced in the asperities (the real area of contact) is high enough to oxidise the materials as sliding occurs (see Figure 4.4 (formation of transfer particles; source Ref:11)). These oxide particles are sometimes hard depending on the tribo-couple and can induce a second mechanism of abrasive third-body wear. The high hardness of PVD coatings results in very small asperities in the point of contact. This means that the frictional force is concentrated into a small area, which leads to high temperatures in the asperities[8]. These temperatures are termed flash temperatures and can be over 1000°C, at spots where asperities collide. Attempts to quantify these flash temperatures have led to the development of models[12,13]. These, however,

are restricted by uncertainties, namely (i) real area of contact (area of asperity contacts); (ii) time of heat source exposure; and (iii) consistency of material properties. Cowan and Winer[12] proposed that for a stationary ball in elastic contact with a rotating disk, the flash temperature is dependent on the sliding speed. This statement has been reinforced by Vancoille et al[14] with sliding wear tests on TiN performed at low, medium and high sliding speeds. The ratio of anatase-to-rutile TiO_2 was dependent on the sliding speed. They concluded that at sufficiently high sliding speeds, and thus correspondingly high temperature, only rutile was formed in the tribo-contact.

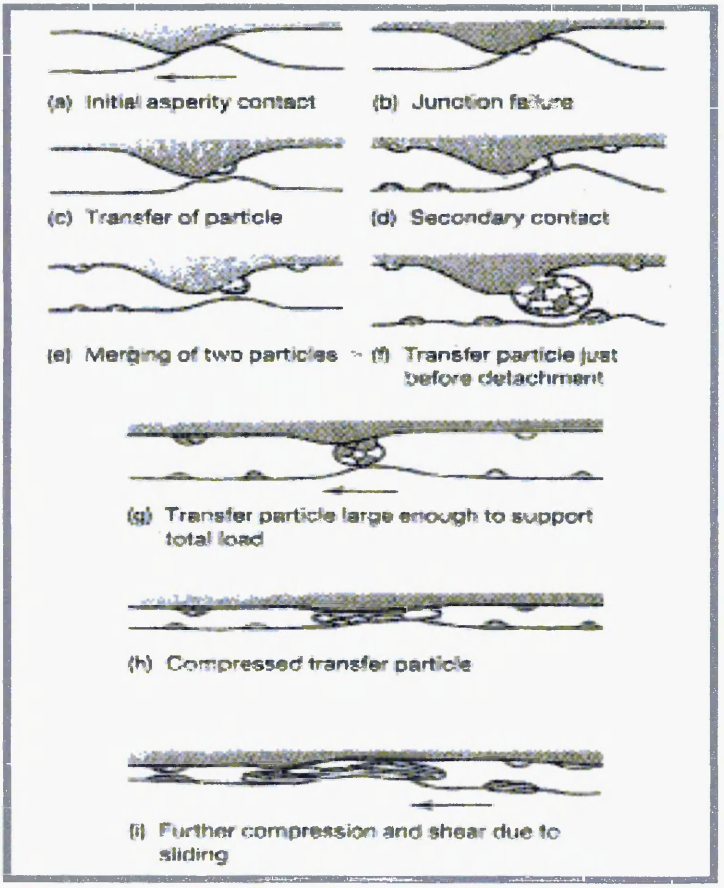

Figure 4.4 Formation of a transfer particle by asperity rupture and aggregation[Ref. 11]

4.2.1.6 Wear of Cutting Tools

The wear of cutting tools is discussed in detail in chapter 5. At this point it must be mentioned that the Pin-on-Disk sliding wear tests do not simulate all the wear mechanisms encountered during real cutting operations, especially dry high-speed cutting. The Pin-on-Disk test is a standard test in which all coatings are evaluated and their friction and wear properties recorded. It is true that the lower the friction coefficient measured in Pin-on-Disk for a particular coating system, should and usually does, result in better performance in a high-speed cutting environment. This is due to a reduced wear rate by a lowering of the cutting temperature. High-speed cutting is a much more complicated wear environment than Pin-on-Disk sliding wear and therefore there is no guarantee that a coating which performs well in a Pin-on-Disk test then goes on to perform well in real cutting operations. Table 4.2, compares the friction/wear environments of sliding and cutting wear with particular focus on the similarities and differences.

Similarities	Differences
High contact temperatures	Wear coefficients easy to obtain with Pin-on-Disk
Oxides produced which can give an idea of the temperature reached during the wear process	Un-even wear with cutting tests i.e. crater wear, also wear/temperature gradient on the tools going from the axis point round the ball nose to the fastest point
Friction is important as mechanical engagement occurs	Cutting is more abrasive environment, i.e. impacts with the work-piece and chip impacts
Non-equilibrium tribo-oxidation reactions occur	Short-lived flash temperatures occur when asperities collide in Pin-on-Disk. A more constant temperature results from cutting.
Debris easy to collect i.e. it gathers at the edge of the wear track and swarf collects on top of the work-piece in cutting tests	Difficult geometry of the cutting tools for analysis
Both non-lubricated	Cutting tests are much quicker than Pin-on-Disk
	Different contact areas i.e. 6mm ball and the contact of the cutting face with the work-piece

Table 4.2 Similarities and differences of sliding wear and cutting wear environments

Raman mapping of real worn cutting tools, flank wear measurements using optical methods and swarf analysis are discussed in chapter 5.

4.2.2 Ball Cratering

This technique is quick, has high accuracy, and is a low cost method of determining the thickness of thin layers. The thickness range which is covered by the ball cratering method is 0.3 – 30μm.

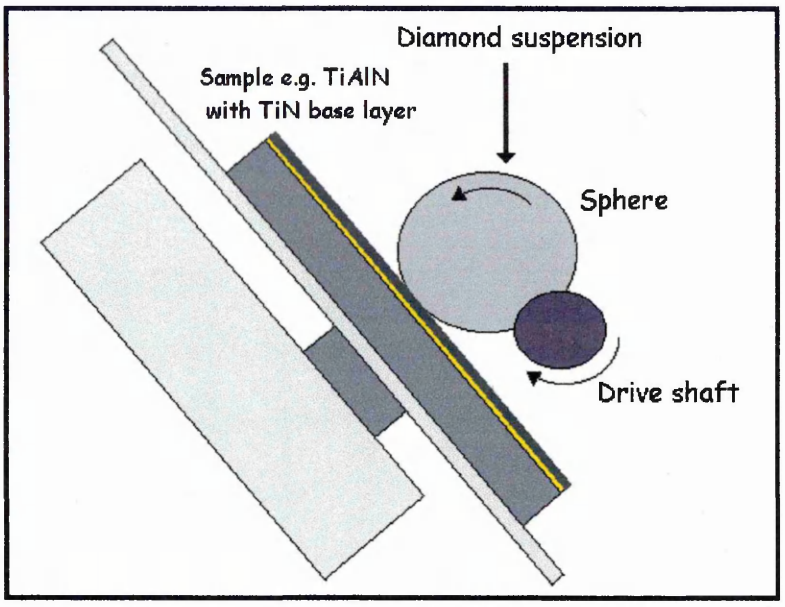

Figure 4.5 shows a schematic of the ball cratering technique

It can be applied to a wide variety of coating/substrate systems. Also, because of the very small crater depths and cratering area it is considered a virtually non-destructive method.

A ball crater is formed on the coating surface by rotating a sphere in combination with a diamond suspension as the abrasive medium. The crater formed is shown schematically below.

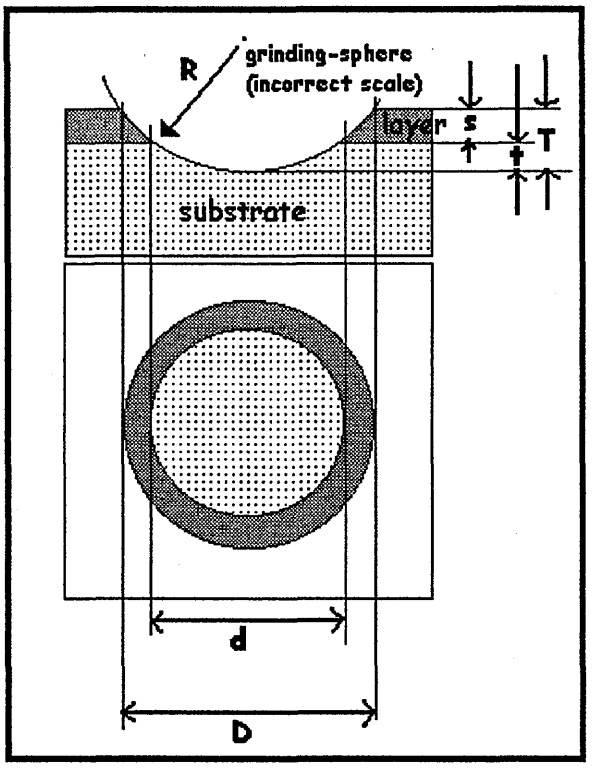

Total indentation depth is given by:

$$T = R - \sqrt{R^2 - \frac{D^2}{4}} \quad \text{(Eq. 1)}$$

R = radius of grinding sphere
D = crater-diameter
T = indentation depth

layer thickness $s = T - t$ (Eq. 2)

Substituting T and t in equation 1:

$$T = R - \frac{1}{2}\sqrt{4R^2 - D^2} \quad \text{(Eq. 3)}$$

$$t = R - \frac{1}{2}\sqrt{4R^2 - d^2} \quad \text{(Eq. 4)}$$

$$s = \frac{1}{2}\left(\sqrt{4R^2 - d^2} - \sqrt{4R^2 - D^2}\right) \quad \text{(Eq. 5)}$$

Figure 4.6 Schematic representation of the geometry of the formed crater

Ball cratering or Calotest can be performed on multilayer structured coatings that are made up of many layers. A layer thickness of approximately 200nm can be measured accurately with this method[1]. Trials with finer particle size diamond paste with sizes ~1μm gave a net improvement in the quality of the craters produced by the calotest[1].

Although ball cratering is primarily used for coating thickness measurements it can be implemented in other ways due to its unique way of removing coating. For this project ball cratering has not been used just for its intended use, (i.e. thickness measurements), but for simulated wear experiments in which upper coating layers can be removed easily revealing lower layers as would happen during real wear situations. Figure 4.5 illustrates this by giving a TiAlN/TiN coating system as an example, in

which it is possible to remove the uppermost TiAlN layer to reveal the base-layer of TiN beneath. This has been of paramount importance when studying wear using idealised coating models in the quest for developing a Raman based wear detection method. This will be discussed further in chapter 5.

4.2.3 Scratch Testing

One of the primary requirements of PVD coatings is an adequate adhesion of the coating to the substrate, a state that may be defined in which interfacial forces hold two surfaces tightly together. The most commonly used method to measure the adhesion of coating systems is a mechanical scratch tester (Figure 4.7).

Scratch testing is primarily concerned with introducing stresses at the interface between the coating and substrate. A smoothly rounded chrome-steel stylus with a tungsten carbide or Rockwell C diamond tip (in the form of 120° cone with a hemispherical tip of 0.22 mm radius) is drawn across the coating surface, and a vertical load (or normal load F_N) is applied to the point either step-wise or a linearly increasing load. As the sample is displaced at constant speed (for linearly increasing load), the resulting stresses at the interface cause flaking or chipping or complete removal of the coating. The minimum load at which a specific failure event is recorded is called the critical load (L_C). There are a range of different failure modes active during scratch testing, as observed on the coating after the indentation passage. The mechanism of coating removal is important as this reflects the adhesion strength but other failure modes, such as transverse cracking that occurs while the coating is still adhered to the substrate are also important.

The scratch test applies deformation in an elastic and plastic form until the coating and substrate are separated. Burnett and Rickerby[15] have shown that the deformation, strain energy and frictional forces generate a combination of two effects; i) a stress field due to ploughing, and ii) a stress field due to friction. The main contribution to coating removal comes from the ploughing stress field. The internal stresses in the coating can have a significant effect on the interface failure[9]. The general rule is that the higher the internal/residual stress, the lower the adhesion strength of the coating to the substrate (residual/internal stresses will be discussed in Chapter 7). Figure 4.7(b) below, demonstrates that the material response due to the indenter scratching falls into three distinct regions.

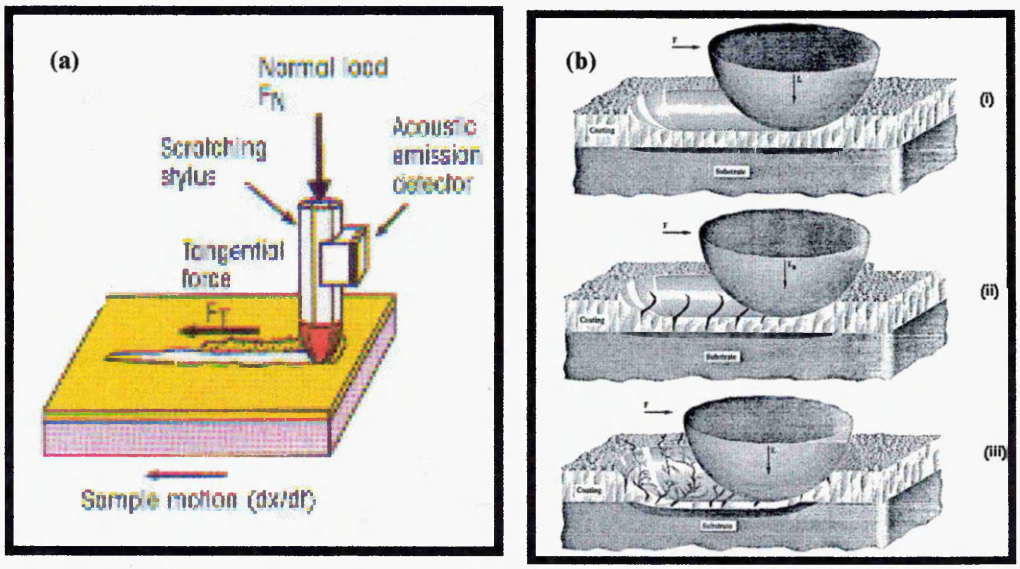

Figure 4.7(a) Schematic of the scratch testing technique[1] (b) Material response due to the indenter scratching is classified into three distinct regions[16]

(i) The indenter moves on top of the coating and only mild plastic deformation occurs in the coating with no or few cracks observed. In this region the coefficient of friction is low.

(ii) A transition region in which the indenter penetrates into the coating, regular transverse cracking is observed in the coating which develops into

an irregular crack pattern just before coating removal at the critical load. The coefficient of friction increases rapidly owing to the fracture energy absorbed in the cracking of the coating and the plastic energy absorbed in the substrate as the indenter ploughs.

(iii) The indenter comes into contact with the substrate and there is no further increase in the coefficient of friction as it is essentially controlled by the plastic deformation of the substrate. When adhesion is good the applied mechanical energy is absorbed by the extensive transverse cracking instead of flaking.

The scratch testing technique gives a rather subjective measure of practical adhesion (critical load, L_c). The critical load is determined routinely by optical microscopy. The user examines the scratch, both within and at the edges, to determine if flaking or chipping has occurred. This is a sign of adhesion being compromised. Alternatively, the acoustic emission is monitored, i.e. monitoring the sound from the cracking and chipping during failure, as an indicator when the critical load had been reached. This is not a good method as the trace is subject to other outside effects such as vibration and sound from other sources. It is generally unreliable and is not used a great deal.

In this work, the scratch testing technique, as for ball cratering, has not just been used for its intended purpose but has been extensively used for deliberately applying deformation and stresses into coatings. Raman measurements have then been performed on scratches to assess the spectroscopic changes due to the damage/disorder and stresses that are introduced into the coating.

4.3 Studies of Mechanically Induced Deformation

The following work has been performed to ascertain the spectral response to externally applied deformation/strain. This was done to further aid in the understanding of wear processes, especially from abrasion where scratching/scoring is known to occur. TiAlN was chosen as the coating of study because of its use as the main component of many current tool coatings.

4.3.1 Raman Analysis of Scratches

Figure 4.8 below, is an optical micrograph of a TiAlN coating that has been scratched.

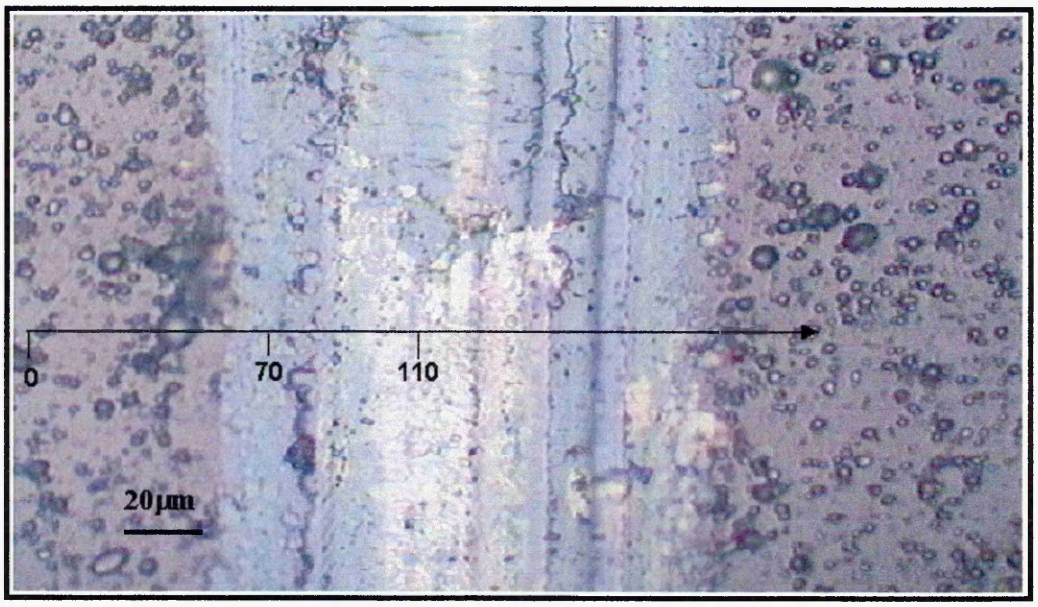

Figure 4.8 Optical micrograph of a scratched surface on a TiAlN coating (N.B. Cracks and removed droplets within the scratch)

When Raman spectra were taken on the scratched surface a modified/changed spectrum resulted, the most noticeable change was a much broader optical mode at ~650cm^{-1} when compared to the undamaged/as-deposited coating (Figure 4.9

compares spectra that were taken at 0, 70 and 110μm positions along the line indicated on the above optical micrograph, Figure 4.8).

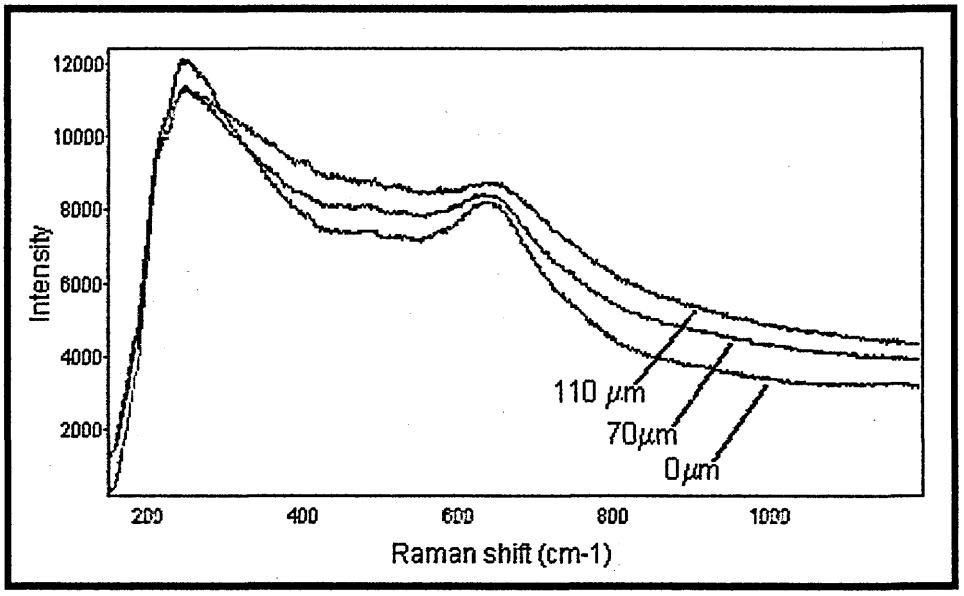

Figure 4.9 Overlaid spectra showing a bandwidth increase when on scratched/damaged areas

Raman point mapping from this initial observation was adopted for further study of deformation due to scratching, i.e. line mapping. Figure 4.10 below shows a schematic representation of Raman line mapping of a scratched region.

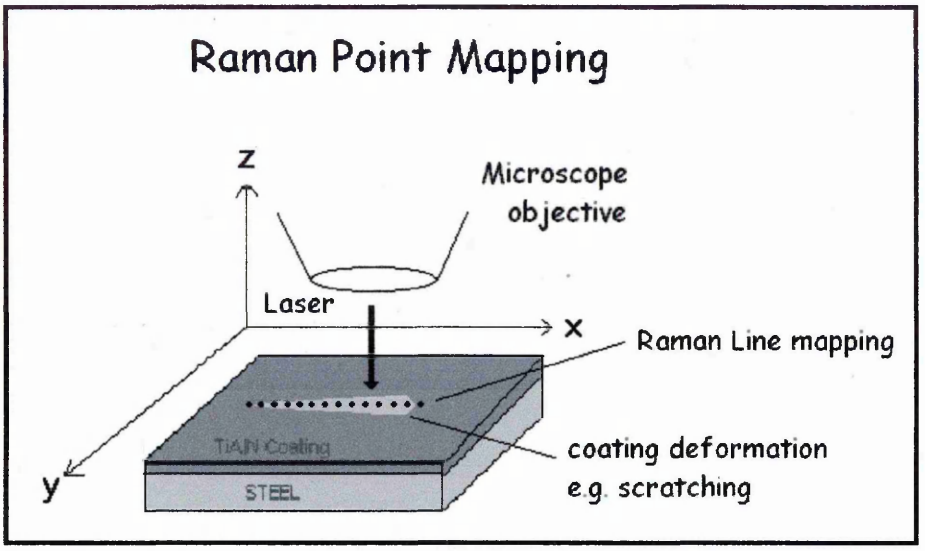

Figure 4.10 Schematic representation of Raman point mapping

The very accurate movement of an automated stage (Prior instruments, precision of movement ~0.5μm) facilitates systematic movement of the laser beam. This is a good method of sampling lines/areas of materials in a controlled and accurate manner. The user sets (in the software) a distance of travel in the x- and y-axis, (i.e. if a line map were to be performed one of the axis would be set to zero), and a step-size (μm) i.e. distance between sampling points. The stage is then moved to the start position and the experiment initiated. Unfortunately even though the stage movement is automated the focus of the laser beam from one point to the next is not for uneven samples, therefore the laser needs to be refocused at each point requiring the use of a 'dwell time' for refocussing purposes. More recent mapping stages have an auto-focus facility that is placed on the microscope's course and fine focus that is able to adjust the microscope height to find the best laser focus from one point to the next.

4.3.2 Raman Mapping Across Scratches (TiAlN Coating)

This enabled information about the disordering process during scratching to be analysed. A line map was started before the scratch, i.e. as-deposited area, and was finished on the undamaged coating after the scratch, a 20μm step-size was chosen between each measurement (the line- map region is highlighted in Figure 4.8).

The main optical phonon mode at ~650cm^{-1} of TiAlN was band fitted at each sampling point using Gaussian-Lorentzian peak shapes using Grams 32 software. A typical band fitting, comparing the fit arising from an as-deposited coating spectrum to one from a scratched region is shown in Figure 4.11 below .

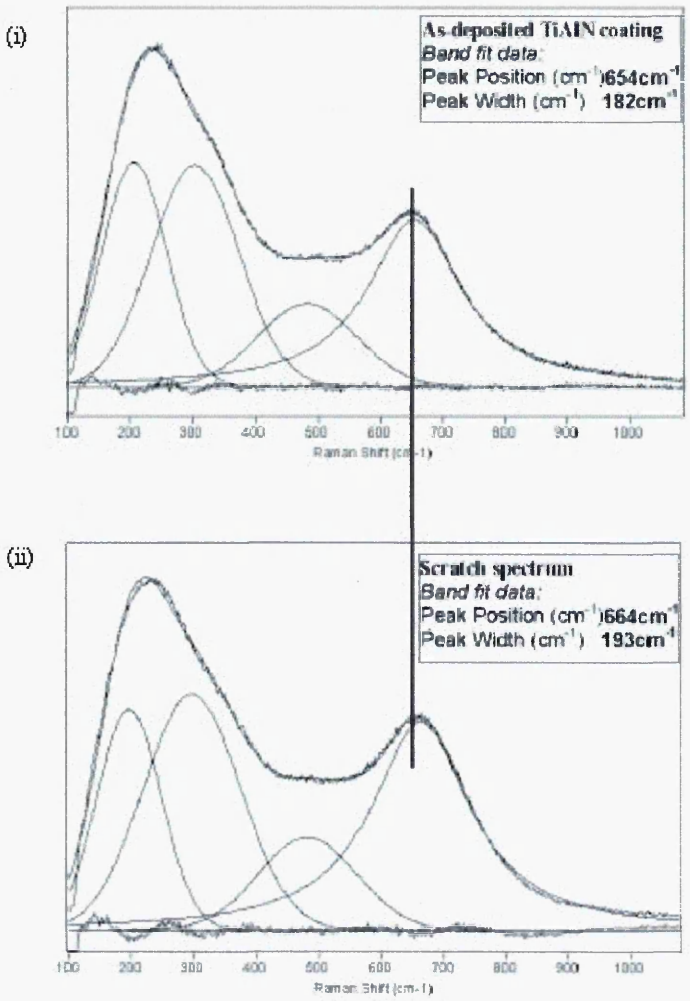

Figure 4.11 Typical band fitting (i) As-deposited (ii) Scratch spectrum (vertical line highlighting the shift in the main optical phonon at ca. 660cm^{-1})

The band width was plotted against distance (μm) travelled over the scratch. The graph below, (Figure 4.12), shows the Raman line-map and demonstrates how the width of the main optical phonon mode of TiAlN can be influenced by the state of disorder and hence can be used as a quantitative measure of the extent of coating deformation.

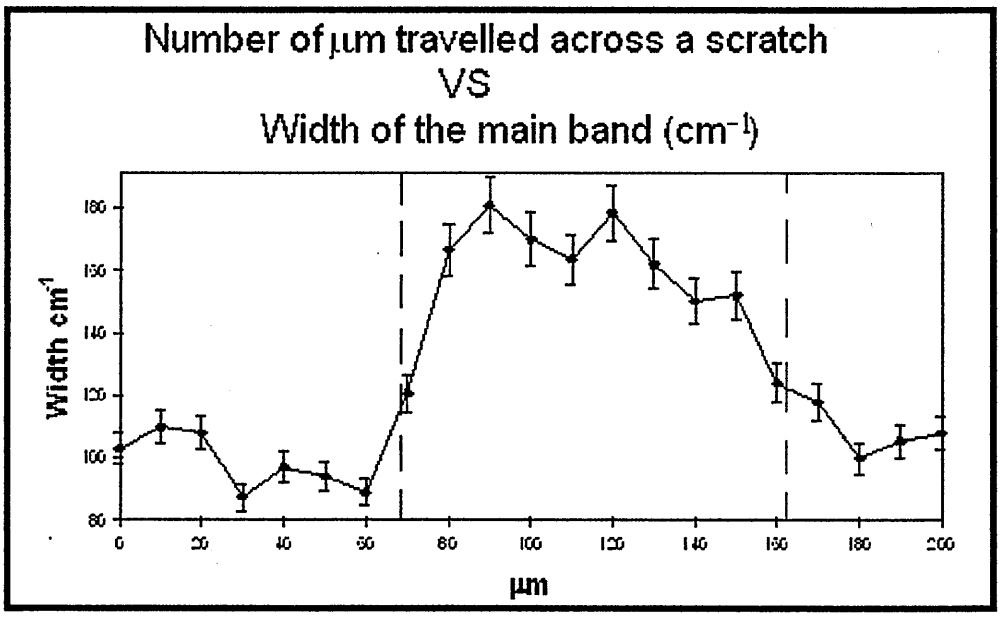

Figure 4.12 Band width vs. distance for mapping across a scratch (Dashed lines show the region when measurements were taken on the scratch)

There was a maximum increase of ~80cm^{-1} in band width when compared to the as-deposited coating which is a significant increase.

4.3.3 Raman Mapping Along Scratches (TiAlN)

We have employed the scratch tester in the "linear increase in load" configuration to correlate the normal load (N) applied by the scratch tester, with the width of the main 650cm^{-1}phonon band of a TiAlN coating. An initial load of 5N and a final load of 70N were used as parameters in the scratch tester. The diamond stylus was then drawn along the surface of the coating with a constant speed, with a distance - load relationship of 1mm = 10N. Therefore the scratch had a fixed length and had increasing damage and depth in the direction of increasing load. Raman mapping was performed along the scratch (~ in the centre) in the direction of increasing load, the

line-map was initiated 200μm before the scratch and ended beyond the scratch (i.e. 0 – 7200μm, with 200μm step size). Figure 4.13, shows optical micrographs of, (a) start point, (b) first measurement on the scratch (5N position), (c) 6800μm position and (d) final measurement beyond the scratch.

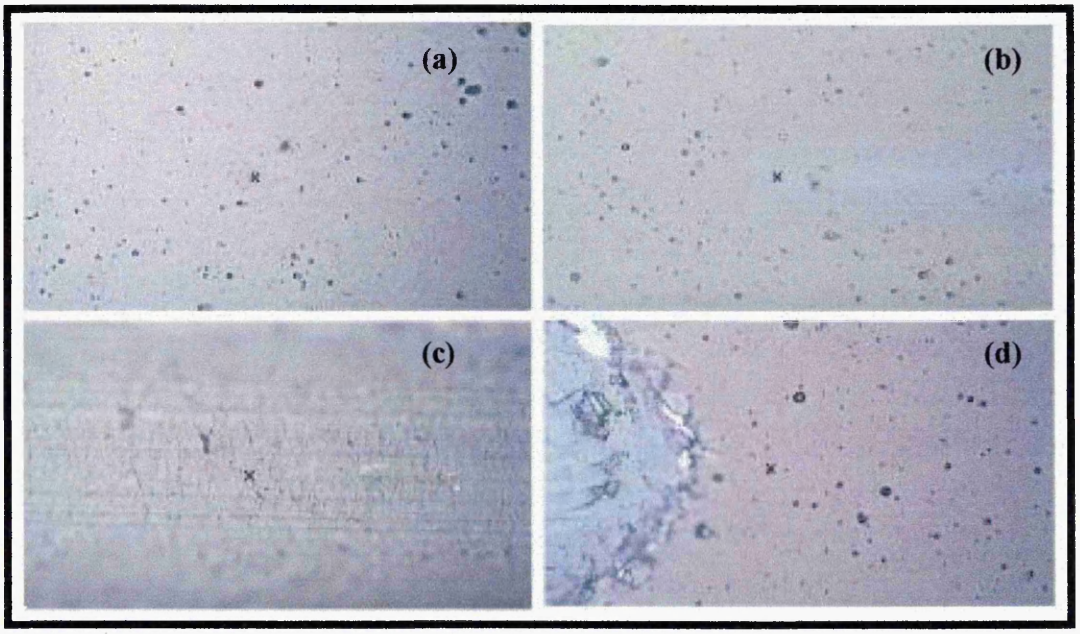

Figure 4.13 Optical micrographs of significant points along the line map

The graph in Figure 4.14 (below) demonstrates the material response i.e. to deform/crack with increasing load on the indenter. Band fitting was performed as for previous analyses.

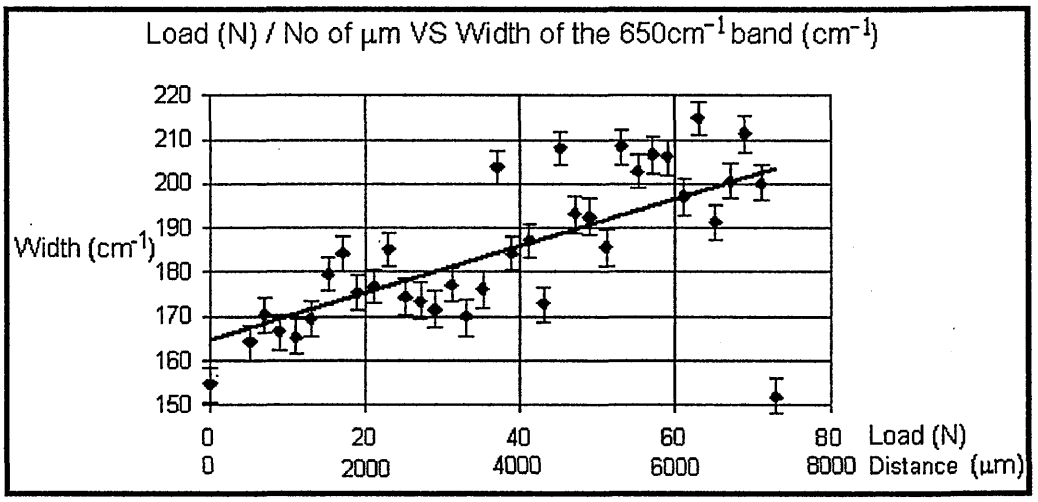

Figure 4.14 Load – Band Width relationship for coating deformation

A gradual increase in the width of the optic mode was observed when the load on the diamond indenter was linearly increased. This can be explained by the coating becoming more disordered as the load on the indenter was increased, as a result of more and more damage to the coating. As a response to the applied stresses, the coating cracks. This leads to new phonon relaxation mechanisms and prevents the lattice modes from propagating across a large number of unit cells. This results in band broadening. Raman signals from PVD coatings can thus "detect" changes due to damage/disorder.

What is also evident from the above graph is that the scatter in the data after the critical load (L_C) has been reached at ~40N is greatly increased. This again is believed to be due to extensive cracking. Cracks in the coating can internally reflect and enhance signals[17], thus the Raman spectrum taken on or near a crack, whether visible or beneath the surface, will be dramatically different to when the laser is focussed onto areas away from cracks. The Raman spectrum will also "detect" more disorder when focussed onto a crack and the optic mode will be broader. The scatter in the Raman data after the coating-substrate adhesion has been compromised could

be used as an indicator that the critical load has been reached. This would have an advantage over normal optical methods, as cracks are not always observed optically. The Raman spectra will detect sub-surface cracks (via band broadening) that are not obvious by optical means.

There appear to be three distinct areas in the graph, i) an almost linear increase in the band width up to 17N, ii) 19 – 35N a decrease in band width (i.e. appearing to become more ordered) and small amount of scatter and iii) >35N a large amount of scatter. This would appear to be consistent with the three stages predicted by Attar and Johannesson[16] i.e. i) mild plastic deformation with few or no cracks, ii) a transition region in which the indenter penetrates and regular transverse cracking is observed, iii) the critical load is breached and transverse cracking develops into an irregular crack pattern and the indenter comes into contact with the substrate.

The band position was also measured at each point along the scratch (Figure 4.15 below). The graph demonstrates that the indenter has induced strain/stresses in the coating, evident via observed band shifts. At the start of the scratch where the damage is slight (like case (i)) the small ~3 or 4cm^{-1} shift indicates compressive stresses, as expected from an indentation process[6]. This has been observed previously by Gardiner et al [17], who has shown that compressive stresses propagate out until cracks occur. It appears that the initial stages of damage caused by the indenter can be thought of as a simple static indentation process with low load. At 9N load the 'shift' becomes tensile (i.e. negative frequency shift) thus the indenter must be inducing tensile stresses into the coating, as it is drawn/ploughed through the coating. This may be explained by a plastic flow mechanism as the coating is

ploughed; as in case (ii), and at 19N the band position gradually increases towards the as-deposited coating value at 29N. This may be explained by small cracks occurring which are relieving the stresses. It appears that the band position is an even more sensitive measure of disorder/stress, as the scatter becomes quite marked above 30N, indicating that irregular cracks have occurred (as in case (iii)). The Raman band position above this point becomes dependent on the sampling point i.e. on the stress fields that surround the cracks.

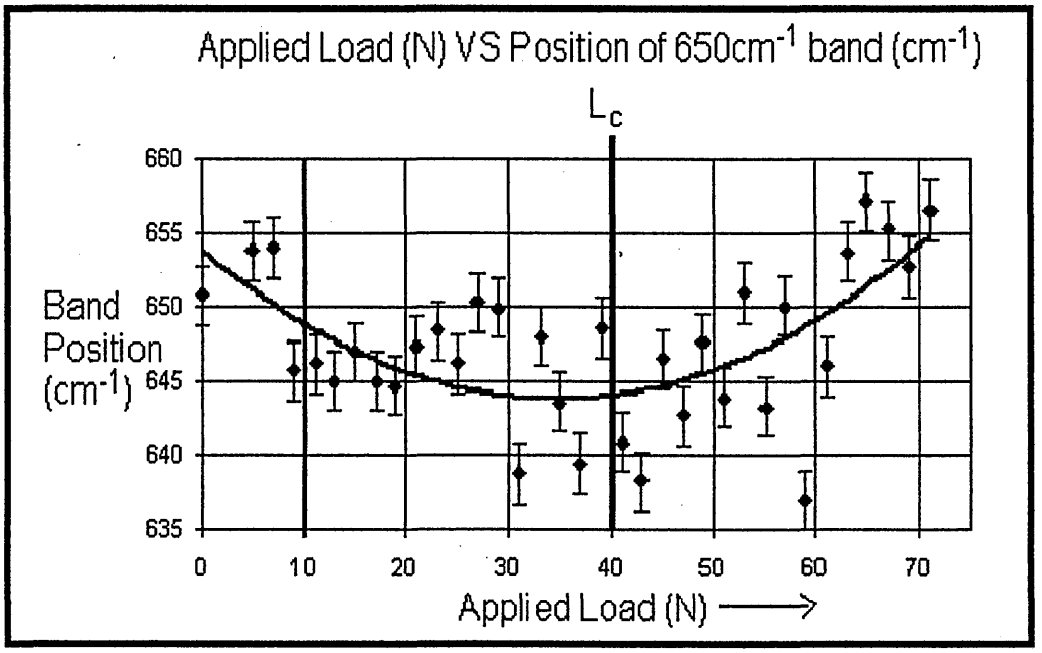

Figure 4.15 Load – Band Position dependence during a scratch test (Spectral shifts due to stresses imparted by the scratch indenter)

4.3.4 Other Coating Systems Studied

A continuation of the scratch experiments was performed on a TiZrN coating to ascertain if the same phenomenon observed for TiAlN could be replicated for another similar system.

4.3.4.1 Raman Mapping Across a Scratch (TiZrN)

TiZrN has essentially the same structure as TiAlN (i.e. fcc), except a larger element, Zr, has been incorporated into the lattice. This will have a pronounced effect on the residual stress within the coating as a result of the distortion of the lattice parameter caused by Zr a large metal atom, the residual compressive stress/dislocation density will be greater for TiZrN.

An optical micrograph of the scratched surface (Figure 4.16) was taken and annotated with + marks to indicate the beginning (at the right hand side) and end of the mapping measurements.

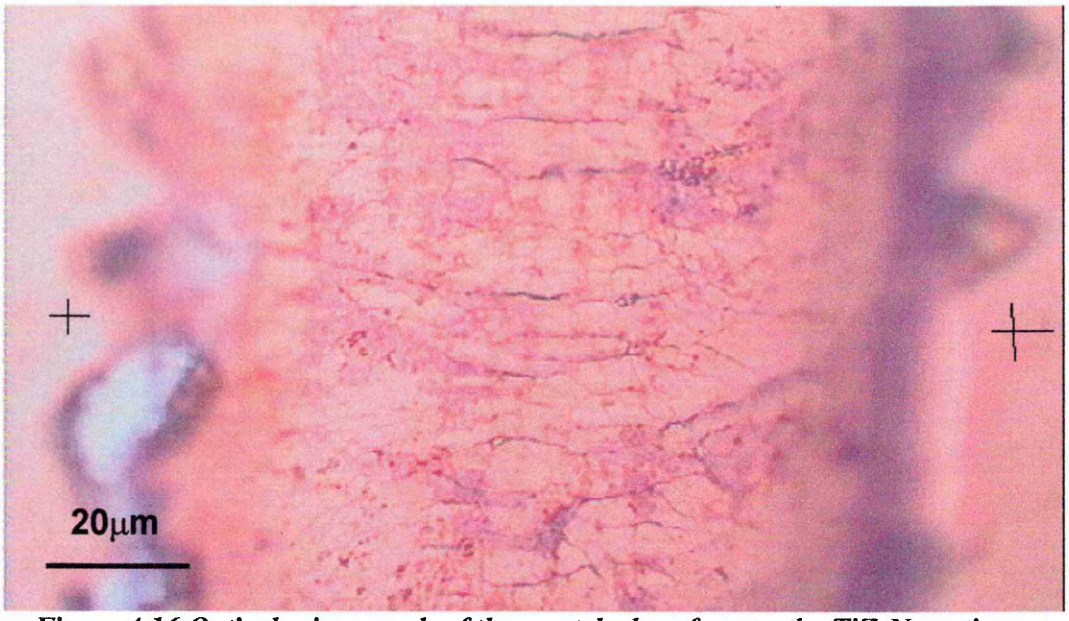

Figure 4.16 Optical micrograph of the scratched surface on the TiZrN coating (sampling start and finish points are indicated on the image, regular transverse cracking can be seen in the deformed surface)

The optical micrograph shows the coating had undergone spallation (or chipping) at the edges of the scratch, most visible at the bottom left of the image. This indicates that the sampling line chosen is very close to the critical load for this coating system. Figure 4.17 (below) shows a graph of band width against distance (μm) mapped for TiZrN. Quantification of the band width and band position was determined using band fitting (as done previously) but this time the main optic mode at ~510cm^{-1} was monitored to assess the amount of damage to the coating structure.

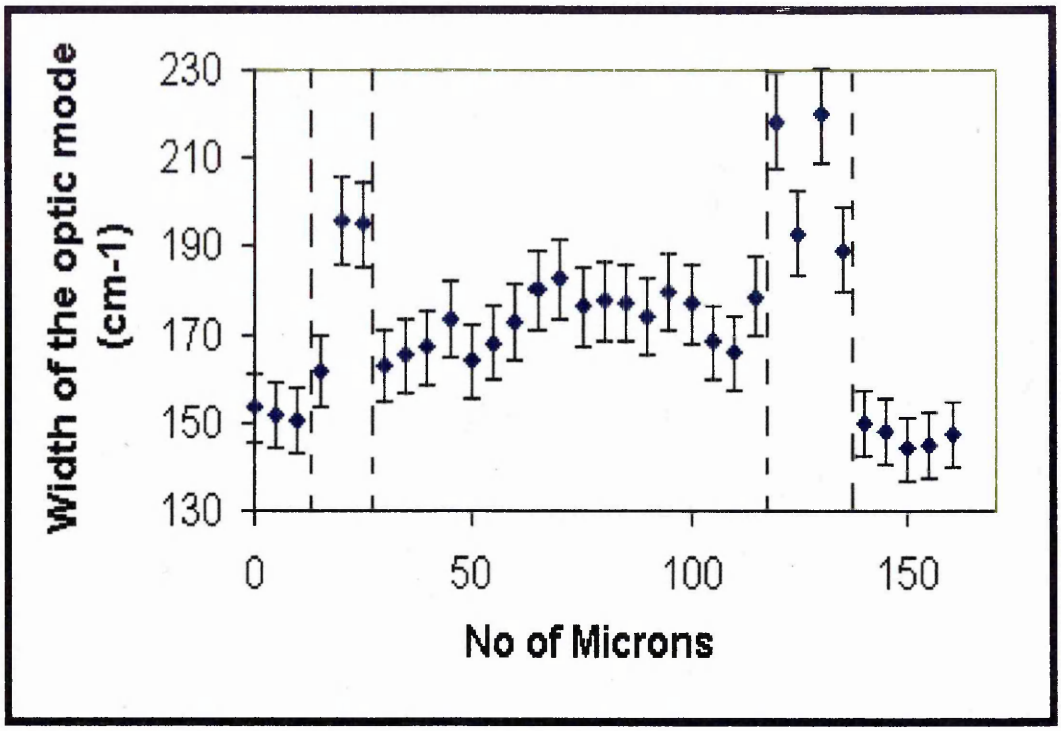

Figure 4.17 Graph of Band width vs. distance for mapping across a scratch on a TiZrN coating
(dashed lines signify the scratch edge regions)

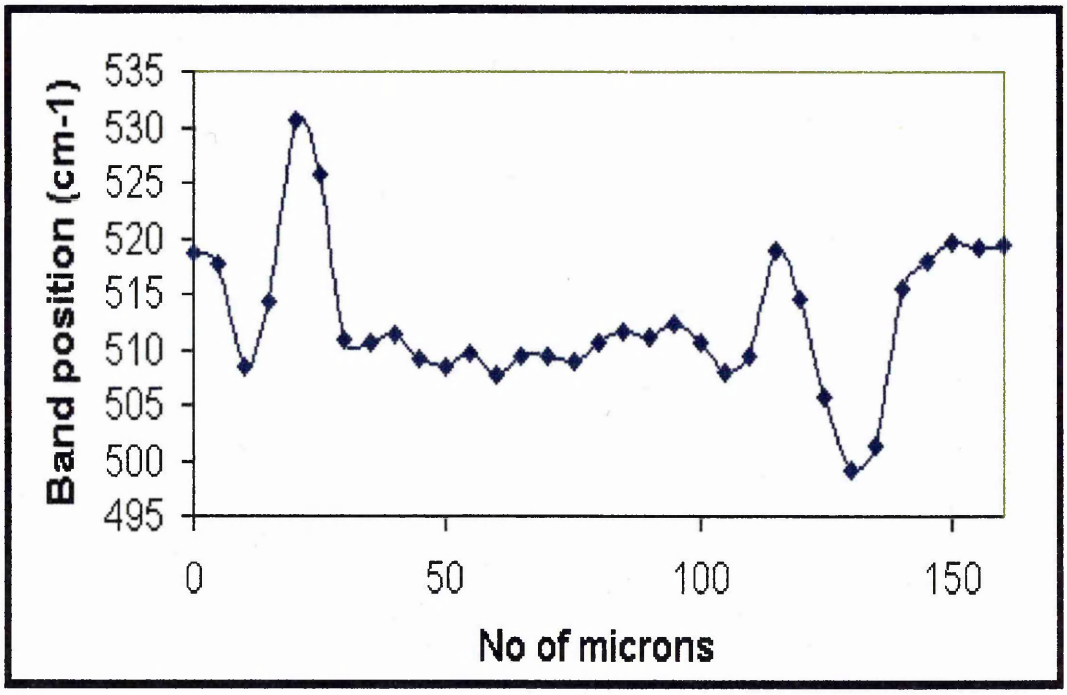

Figure 4.18 Graph of Band position vs. distance for mapping across a scratch (TiZrN coating)

Larger band widths were indeed measured when spectra were taken on the damaged surface, as observed for TiAlN. The step-size chosen for this analysis was 5μm, which enabled the edges of the scratch to be sampled, i.e. at 20, 25 and 120-140μm positions. A massive increase in band width was observed when measurements were taken on the edges, implying that the TiZrN coating was much more disordered. In addition, the stresses at the edges of the scratch were increased (Figure 4.18). It appeared that measurements taken at the LHS edge had increased compressive stresses and the RHS edge had an increase in tensile stresses (or a reduction of the overall residual compressive stress). This correlates well as spallation/chipping is always observed at the edges of scratches close to the critical load. However, sampling positions within the scratch only showed a maximum band width increase of ~25cm^{-1} which is substantially less than for TiAlN where an increase of ~80cm^{-1} was observed. Due to the incorporation of a heavier atom within the lattice and subsequent increase in dislocation density and increased hardness may have resulted in a coating composition that was more resistant to deformation than TiAlN.

4.3.4.2 Raman Mapping Along a Scratch (TiZrN)

The Raman line-map was started just before the beginning of the scratch and then all subsequent measurements were along the scratch in the direction of increasing load, the final measurement was positioned on the end of the scratch. A step-size 250μm was chosen. The graph of band width vs distance is displayed below (Figure 4.19).

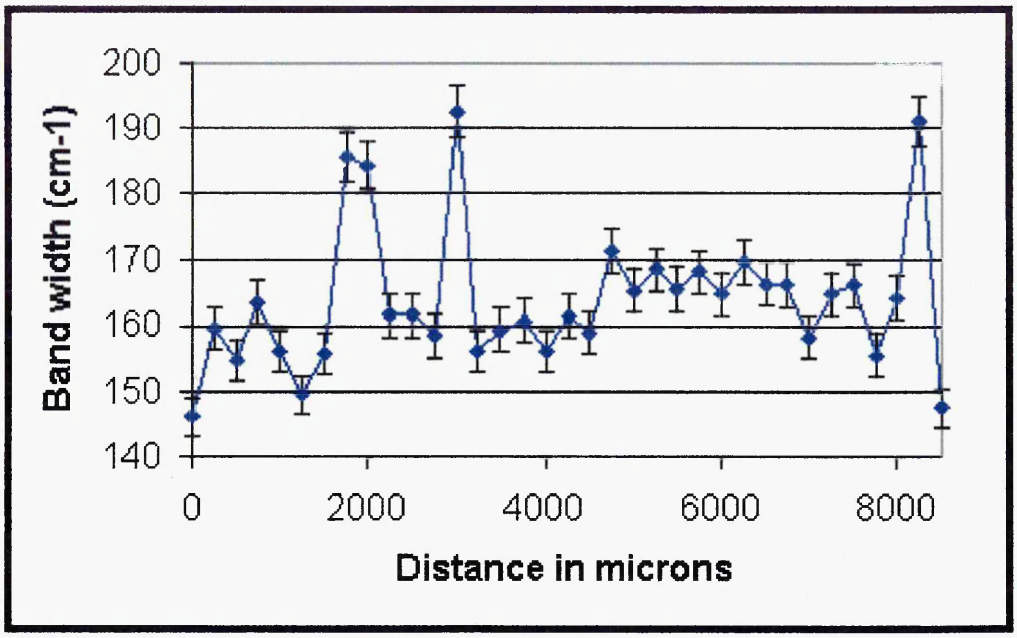

Figure 4.19 Graph of Band width vs. distance for mapping along a scratch TiZrN

The band at ca. 510cm^{-1} was plotted and showed a similar shape consistent with the same phenomenon as TiAlN i.e. disordering due to the action of scratching.

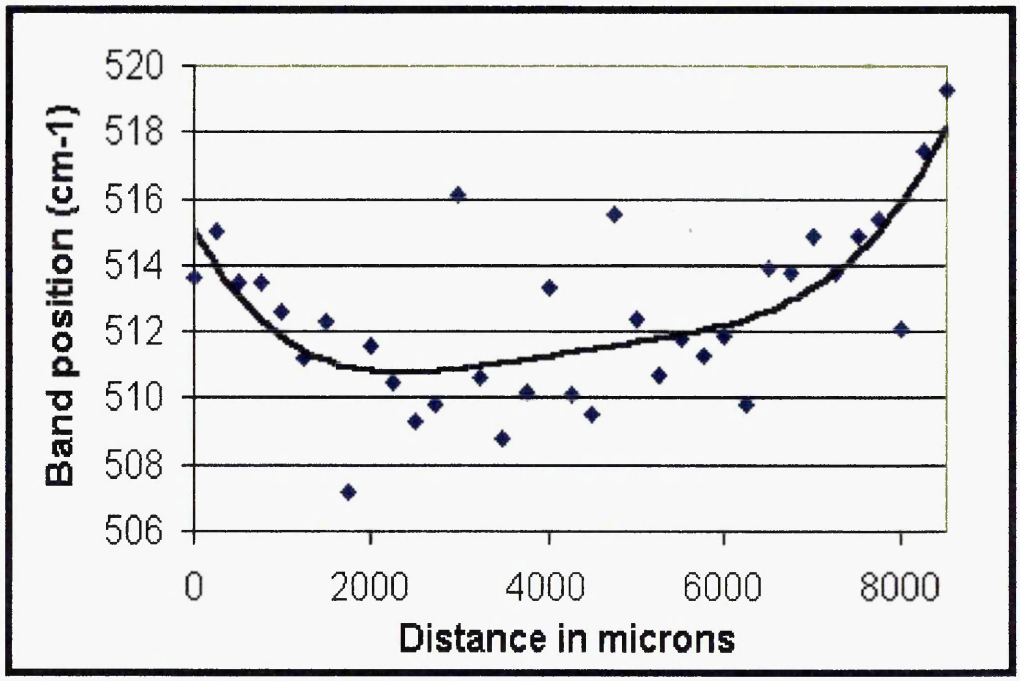

Figure 4.20 Graph of Band position vs. distance for mapping along a scratch

4.4 Raman Mapping of Other Mechanically Induced Deformation

The focus was then changed from monitoring the spectral changes due to the deformation/damaging process of scratching to the effects of the sliding wear on the spectral bands of PVD coatings.

4.4.1 Mapping of a Wear Track Present on a TiAlN/VN Superlattice Coating

Much of the previous work was centred on TiAlN, but for this analysis the focus was changed to a TiAlN containing commercially available coating composition. That was TiAlN/VN (Supercote-33), a superlattice coating with a bi-layer thickness in the range 2-3nm. The Raman spectrum of this coating was very similar to TiAlN the only difference being a slight shift in the frequency of the main optic mode at ~650cm^{-1} (see Chapter 3 for coating spectra). Standard conditions for the Pin-on-Disk tribotest were used: 5N normal load, 10cm/s sliding velocity, 10mm sliding radius and a corundum ball. An area clear of debris and tribo-chemically deposited transfer layers was chosen. A 20μm step size was utilised to sample across the wear zone, i.e. the track, starting the analysis before the worn area (i.e. as-deposited area) and finishing beyond the scratch on un-worn coating. The position and width of the main optic mode was again ascertained via band fitting. Figure 4.21 highlights the shift in the main optic mode at ~650cm^{-1} when measurements were taken on the wear track.

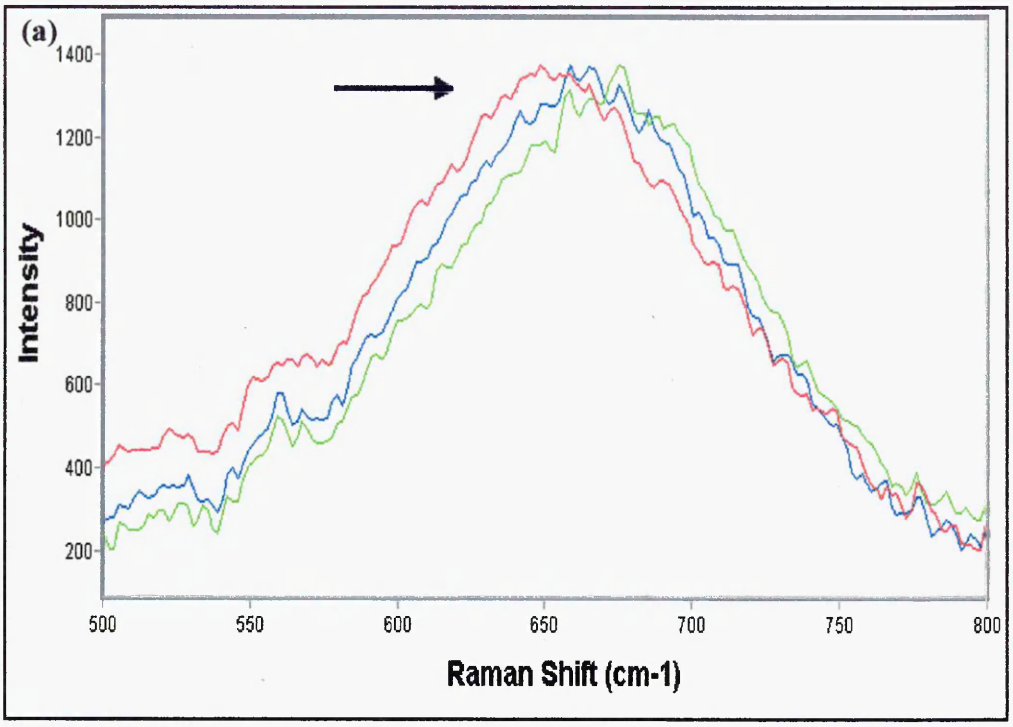

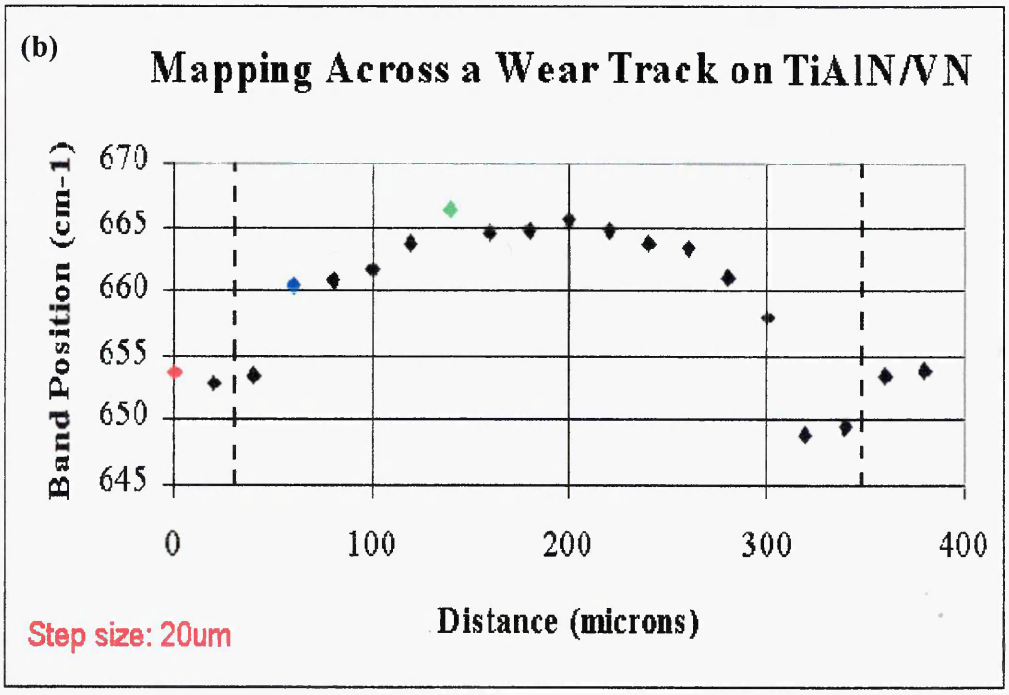

Figure 4.21 (a) Band shifts due to the stress imparted by the sliding action/ indentation of the ball into the coating during the wear process (b) Band shift of the main optic mode when measurements were taken on the worn surface (red, blue and green points from overlaid spectra above)

The band width of the optic mode did not change when measurements were taken on to the wear track. This may be explained by the fact that no cracks or severe deformation were observed within the tracks. The wear process observed for this coating was polishing wear. Figure 4.22 shows ESEM images of the worn surface (a) low magnification of wear track and (b) high magnification image of the worn surface (after 40,000 cycles using the standard conditions) (c) oxide crystals formed during the high contact temperatures (d) elongation, erosion and squashing of droplets within the track.

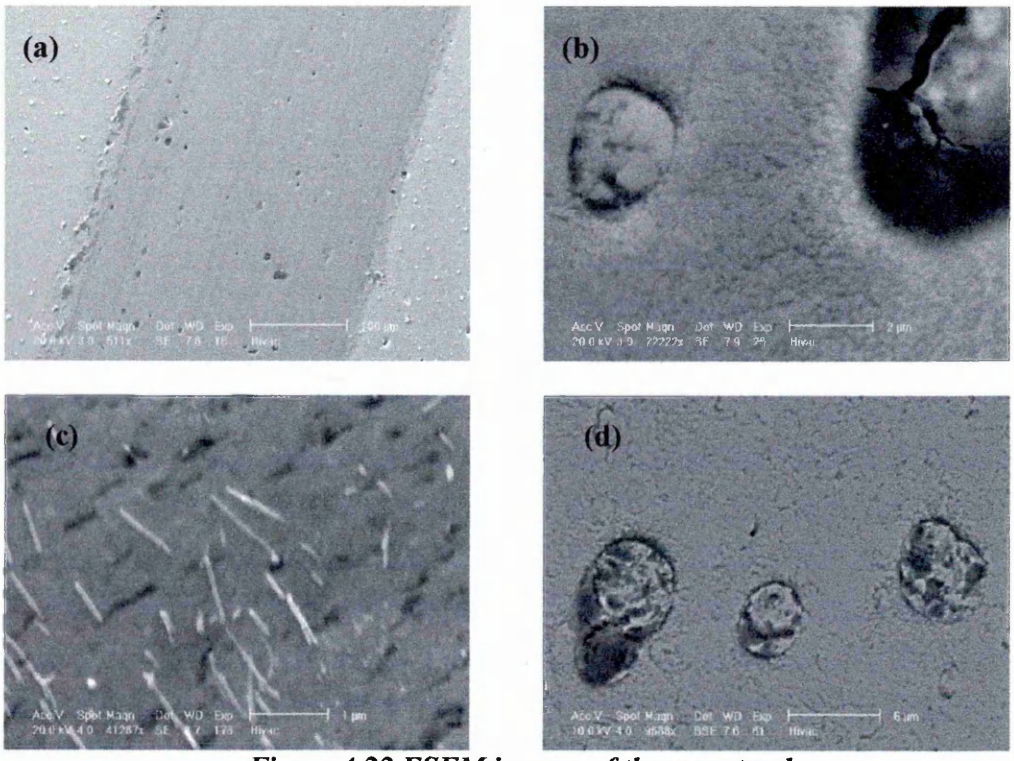

Figure 4.22 ESEM images of the wear track

The majority of damage to the coating occurred when 'droplets' were detached/removed from the coating due to the forces imparted during sliding (see Fig. 22(a and b)). This damage only caused local deformation in and around the droplet region where cracks can be seen within the pit left behind by a removed droplet (see Fig. 22(b)). One might predict that spectral changes due to deformation would only

be seen if a Raman measurement was taken on or very near to a removed droplet. The growth columns that occur for these polycrystalline coatings during deposition were polished flat by the sliding wear and also droplets that remained were gradually worn flat, with the removed material going as wear debris. Initially, when there was contact between the ball and a droplet, the defective coating that is known to grow on top of these macro-particles was removed revealing the pure vanadium droplet beneath. When this occurred the dislocations and coating - droplet interactions (in addition droplet-substrate adhesion) within the bulk of the coating will determine whether the droplet will subsequently be dislodged and removed. It is possible that the removed droplets may get caught beneath the ball and result in a deposition layer within the track.

The compressive stress increase when measurements were taken within the wear zone can be explained by the pressure of the indentation between the ball and the coating as sliding occurs. The largest shift was observed when measurements were taken in the centre of the track where the pressure from the contact between the ball and coating was the highest.

4.5 Mapping of Other Defect Structures

The major defects on the surface of the coating are droplets/macroparticles. It is highly possible that if a non-microscope system were to be used the user could easily focus onto a droplet. The spectral changes that occur when measurements are taken onto droplet needs to be investigated. In addition the possibility of measuring the quantity of droplets on the surface by Raman area mapping is investigated.

4.5.1 Mapping of a Droplet (TiAlN)

Optical micrograph of the droplet taken with a 50X microscope objective

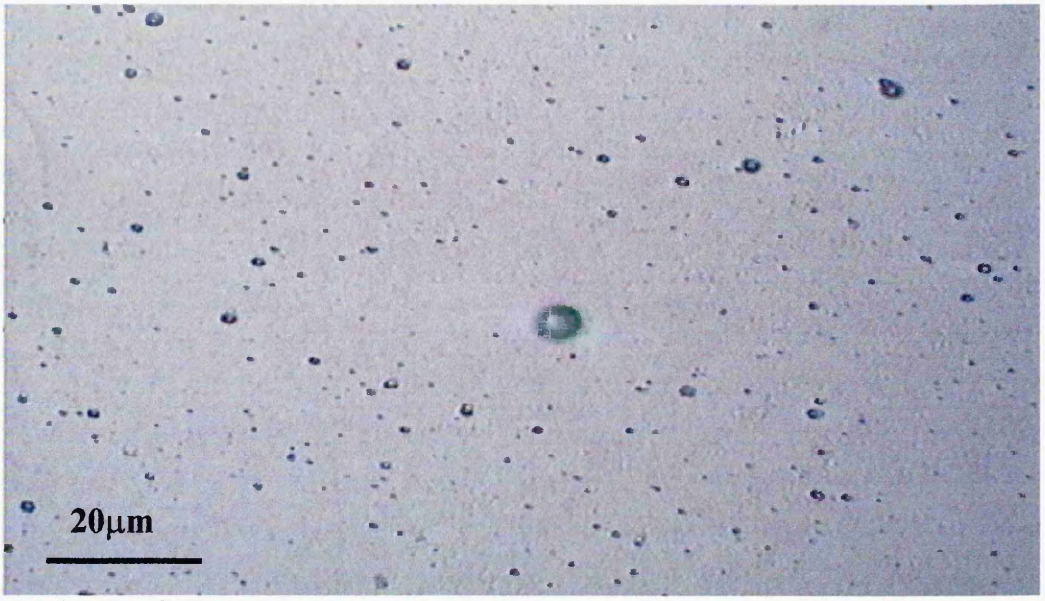

Figure 4.23 Optical micrograph of a large droplet present on a TiAlN coating (Diameter of the droplet in the X direction was ~6.5μm)

The Raman mapping was performed in the x-direction (from left to right on the micrograph) and was started before the droplet and finished ~5μm after the droplet, a step size of 1μm was chosen for the analysis.

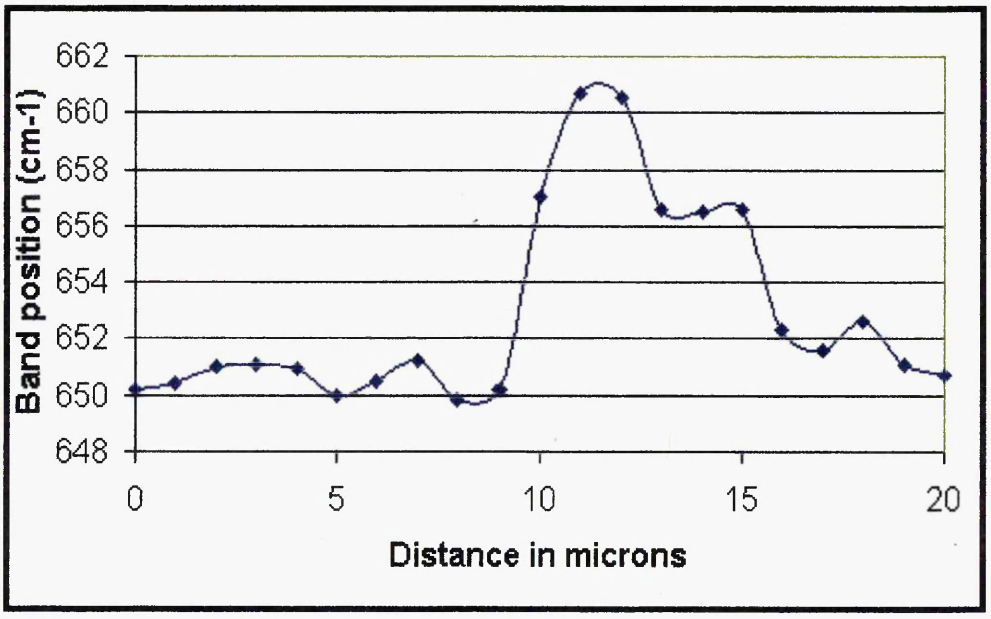

Figure 4.24 shows the band position as mapping was performed across the droplet.

There was an increase in compressive stress when measurements were taken on the droplet, where a maximum shift of ~10cm^{-1} was observed. It also appeared that the presence of the droplet affected the surrounding area, i.e., it increased the stress in the neighbouring area. This can be seen as scatter in the data before and after the droplet i.e. 0-5 and 14-20μm. The value for the width of the band in an as-deposited coating (away from scratches and droplets) for this particular coating was 120cm^{-1}.

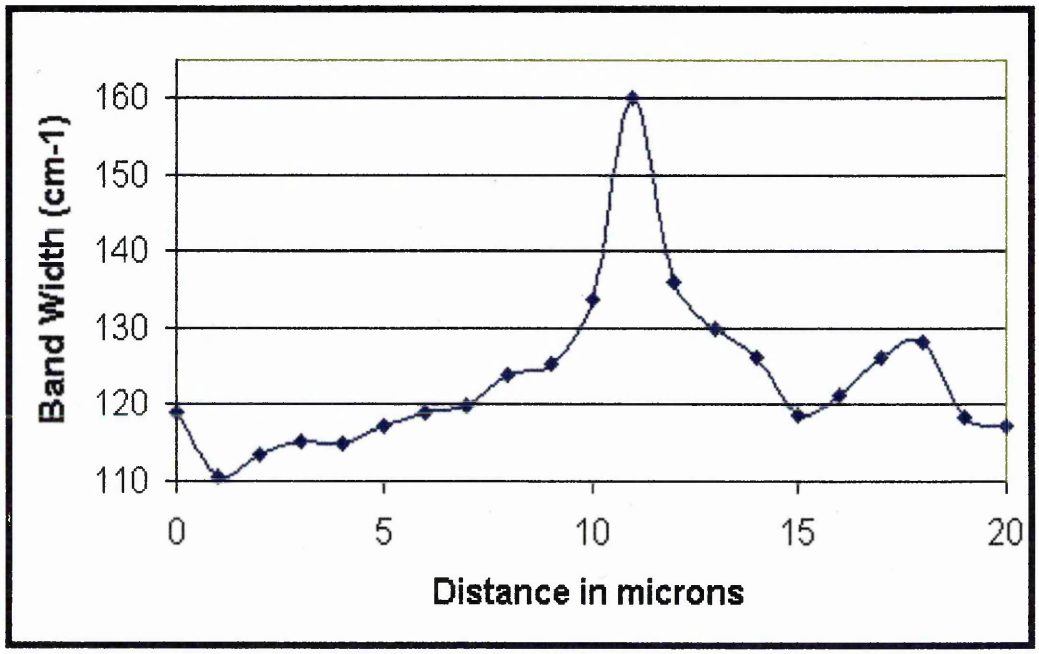

Figure 4.25 Band width increase when on a droplet

The coating that was present on top of the droplet was highly disordered (see Figure 4.25 (above) shown by a band width increase of ~40cm^{-1}when measurements were taken on the droplet. The geometry of the droplet must be taken into account as this may affect the observed spectrum.

4.6 Explanation of Observed Spectroscopic Effects

The band shifts observed for the mechanically induced deformation of the coating systems investigated may be explained quite easily as piezo-spectroscopic effects. That is, by the spectral shifts induced by stress. The physical origin of the effect is that any applied or residual strain/stress changes the vibrational and electronic levels of the material under investigation inducing frequency shifts[18]. However, the physical origin of the band broadening is more complicated. Optical phonons broaden when there are imperfections in the crystal that is under investigation[19]. The PVD coatings are polycrystalline, and far from perfect, since they are made up of many crystal grains in which there are point defects, dislocations and crystallite boundaries and pores. The additional effect of mechanical disordering will be superimposed on top of the aforementioned imperfections, thus increasing the band width even further.

Usually the natural line width of Raman phonons is mainly determined by the decay of an optical phonon into two phonons of opposite wavevectors[19]. The feature of the optic-phonon scattering by static imperfections is connected with the phonon DOS (Density of States) singularity[19]. Another important parameter is the size of the region where the phonon interacts with an imperfection. This is because the line shape asymmetry induced by imperfections is much more pronounced in the case of the short-range disorder, when a phonon changes its momentum in the scattering process by imperfections. The line shape asymmetry is thus sensitive to the dimensions of the imperfection. The damage caused by the mechanical disordering processes will increase the number of crystal imperfections/defects per unit volume

and also increase the size of the imperfections. The contribution of defects is proportional to their concentration for line defects[19]. The disordering process will increase the number of dislocations by breaking up grains and resulting in a larger proportion of grain boundaries per unit volume sampled by the laser beam.

References

1 CSEM instruments Advanced Mechanical Surface Testing "Application Bulletin; Advances in Surface Mechanical Properties Characterisation", ed. N. Randall, Switzerland, autumn 1996.

2 R.K. Islamgaliev, R. Kuzel, E.D. Orbraztsova, J. Burianek, F. Chmelik and R.Z. Valiev, Mater. Sci. Eng. A249 (1998) 152-157.

3 H. Hobert, H. Dunken, R. Menzel, T. Bachmann and W. Wesch, J. Non-Cryst. Solids, 220 (1997) 187-194.

4 C. Uzan-Saguy, C Cytermann, R. Brener, V. Richter, M shaanan, R. Kalish, Appl. Phys. Lett. 67 (1995) 1194.

5 R. Kalish, A. Reznik, K.W. Nugent and S. Prawer, Nuc. Instr. Meth. Phys. Res. B 148 (1999) 626-633.

6 G. Pezzotti, Comp. Sci. Technol. 59 (1999) 821-831.

7 S. Webster, D.A. Smith, D.N. Batchelder and S. Karlin, Synthetic metals 102 (1999) 1425-1427.

8 I.M. Hutchings in "Tribology – Friction and Wear of Engineering Materials", Hodder Headline plc, London 1992.

9 E. Rabbinowicz in "Friction and Wear of Materials", 2nd ed, John Wiley and Sons inc., London 1995.

10 F.P. Bowden and D. Tabor, Proceedings of the Institution of Mechanical Engineers International Conference: Tribology - Friction, Lubrication and Wear; Fifty Years On, London, (1987), p 157-172.

11 H. Mishina and T. Sasada, "Mechanism of Seizure in Sliding Surfaces", The Japan Congress on Materials Research, Kyoto, Japan (1983), p 154-159.

12 R.S. Cowan and W.O. Winer, in ASM Handbook, Friction, Lubrication and wear Technology, edited by P. Blau (ASM, Materials Park, OH, 1992), vol. 18, p.39.

13 D. Kuhlmann-Wilsdorf, Mater. Sci. Eng., 93 (1987) 107.

14 B. Blainpain, M. Franck, H. Mohrbacher, E. Vancoille, J.-P. Celis and J.R. Roos, in Thin Films in Tribology: Micro-Raman spectroscopy for the characterisation of wear induced surface modifications on hard coatings, D. Dowson et al, (ed.) Elsevier, Amsterdam, 1993, p 623.

15 P.J. Burnett and D.S. Rickerby, Thin Solid Films, 154 (1987) 403.

16 F. Attar and T. Johannesson, Surf. Coat. Technol. 78 (1996) 87-102.

17 M. Bowden and D.J. Gardiner, Applied Spectroscopy 51(9) (1997) 1405-1409.

18 N. Muraki, V. Sergo, G. Pezzotti, G. Katagiri,S. Meriani and T. Nishida, Applied Spectroscopy 51(11) (1997) 1761-1765.

19 L.A. Falkovsky and J. Camassel, Physica B 284-288 (2000) 1145-1146.

Chapter 5

Development of a Raman Based Method

for Wear Analysis of Cutting Tools

Chapter 5 Development of a Raman Based Method for Wear Analysis of Cutting Tools

A large proportion of this project has been dedicated to creating a Raman microscopy based method for the quantification of real wear on PVD coated cutting tools which would eventually lead to a prototype test unit. The strategy for fulfilment of this goal is described in this chapter.

5.1 Previous Wear Test Studies Utilising Raman Microscopy

The majority of wear analysis has been concentrated on the study of TiN coating wear by sliding/fretting against various pin materials, chromium steel[1,2], and corundum[3] and silicon nitride[4] ceramics. We have been especially concerned with the detection of reaction/transfer layers[2], surface modifications[6] and characterisation of wear debris[3,5,7]. Diamond-like-carbon and diamond films have also received much attention over the past decade. Schouterden et al[8] demonstrated using Raman spectroscopy that, under fretting wear against Al_2O_3 (without lubrication), the amorphous structure of DLC underwent partial graphitisation with an increase in the intensity of the G-band and further separation of the D and G-band, indicating a larger crystallite size. Under the same testing conditions, TiN showed evidence for a tribo-oxidation reaction occurring in the contact by observation of anatase TiO_2 at low amplitudes and speeds that transformed to rutile for higher speeds. The fretting wear of CVD diamond against diamond coated Si_3N_4 counter-bodies studied using Raman microscopy[6] (in which a lower intensity of the diamond peak was observed at the centre of the wear zone) was associated with reduced

coating thickness due to wear. A peak shift in the worn area was smaller than for the as-deposited film indicating that there was also a reduction in the residual compressive stresses due to the wear. When the same diamond coating was tested against WC-Co a transfer layer was formed on top of the coating. A Raman spectrum of the transfer layer showed characteristic peaks from the as-deposited diamond coating and in addition 4 peaks due to WO_3. Erdemir et al[9] showed, for steel sliding against DLC films in dry nitrogen, that a black deposit and transfer layer resulted which essentially matched those of graphite (via comparison with a standard) the line shapes were broader which was attributed to a phonon damping mechanism related to structural disorder of the graphitic precursors. In addition Liu et al[10] studied the wear mechanism of DLC carbon films utilising Raman microscopy and found that there was a change from diamond-like - graphite in the wear track. They predicted that, besides a friction-induced annealing, a sliding-induced strain energy involved in the surface layer helped further assist the transformation to graphite-like carbon.

Friction and wear studies of carbonaceous layers deposited on top of PVD coating have also been studied[11-13]. PVD deposited TiN was irradiated with a flux of 80-KeV carbon ions[11]. Depth profiling using Rutherford Backscattering spectrometry (RBS) showed a pure carbon layer on top and a Gaussian distribution of carbon buried inside. Raman spectroscopy was used to investigate this carbonaceous surface layer and found features typical of DLC. Subsequent fretting analysis (against corundum) of the as-deposited and carbon implanted TiN found that the coefficient of friction for the TiN implanted with C^+ ions to be lower (0.1), compared with an as-deposited TiN value of 0.4. The resultant wear rate was also lower. Wanstrand et al[12], described the current strategy of PVD coating developers to incorporate large amounts of carbon

into metal-based coating materials and discussed their resultant characteristics of low friction and high wear resistance for applications such as cutting and machining parts. Several nitrides and carbides of Ti and Cr were discussed. Nano-tribological investigations of carbon overcoats on magnetic recording disks has been performed[13]. They described how a relation between the Raman spectrum and the mechanical properties of carbon overcoats exists. Thus, described how a high sp^3 / sp^2 bonding ratio correlated well with a shift in the G-band to lower frequency and an increase in diamond-like nature increased the wear resistance.

A recent collaborative paper between CSEM instruments (Switzerland) and Sheffield Hallam University discusses how the incorporation of Cr and Y influences the wear performance of TiAlN at elevated temperatures[14]. This paper has much significance since TiAlCr(Y)N is the major constituent of commercially deposited tool coatings grown at Bodycote – SHU coatings (discussed in detail in sections 5.5). The tribological properties of $Ti_{0.5}Al_{0.5}N$, $Ti_{0.43}Al_{0.53}Cr_{0.02}Y_{0.02}N$[15] and TiAlN/CrN are discussed. The coatings show similar hardness values and were grown using combined cathodic arc/unbalanced magnetron sputtering. The hard coatings were compared against the wear performance of commercially available TiN and TiAlN coatings. The hard coatings investigated differed considerably in their microstructure in that TiN and TiAlN exhibited typical columnar microstructure, whereas TiAlCrYN exhibited a fine, nearly equiaxed type of grain structure[15]. TiAlN/CrN showed the typical layered structure with competitive columnar growth. Oscillatory sliding tests were performed in the temperature range 400-900°C and evaluated in terms of friction coefficients and wear depth. Uncoated and TiN coated cemented carbide showed a systematic increase in wear as a function of temperature. The TiAlN film showed

progressively increasing wear as a function of temperature. The wear behaviour of the TiAlN/CrN superlattice was only performed at the highest measurement temperature of 900°C but it still showed the lowest wear track depth of the coatings investigated. This was attributed to higher toughness and lower oxidation rate in comparison with TiAlN. The Yttrium containing coating has high residual stress (-7 Gpa)[16] and showed interesting behaviour, in that between 400 and 600°C there was a sharp increase in wear track depth. However, beyond 600°C an inverse relationship of decreasing wear rate with increasing temperature combined with lower stress ~ -3.5GPa at 900°C was apparent. The results were particularly interesting when compared to recent dry cutting tests performed at Bodycote-SHU. It has been found that a sequential increase in cutting temperature of the TiAlCrYN coatings typically demonstrate systematic improvements over conventional TiAlN films. J.P.Celis[17] described how pin-on-disk laboratory testing of ceramic coatings on cutting tools can help give a materials-oriented approach, making use of tribo-chemistry, and give an understanding of surface layer formation and the estimation of contact conditions.

5.2 A Commercially Available Example of Raman Spectroscopy Being Utilised in Industry - The Diamond-Like-Carbon Analyser[18]

The DLC system is a quality control system for diamond-like-carbon coatings. DLC has become vastly popular as a coating to protect the platters of computer hard disk drives against damage from contact with the read-write heads. DLC coatings were chosen for this purpose because of their physical properties, which are smoothness and wear resistance. These coatings were initially evaluated using wear and scratch testing which are destructive techniques. A method of non-destructive rapid analysis

was required and the Renishaw DLC analyser was developed for this purpose. This can determine rapidly a range of important parameters of DLC films, such as, film thickness, hydrogen and nitrogen content, and chemical bonding of the carbon. These samples can be analysed in air, with no sample preparation, for coatings on a wide range of substrates (e.g. aluminium, ceramic, glass), on samples ranging in size from 1 μm to over 150 mm. There is no sample damage and a typical data acquisition time of 10 seconds is achieved. A simple pass/fail message results, and this enables quick and easy quality control as the coated sample comes off of the process.

5.3 Strategy

It has already been established in Chapter 3 that characteristic spectra result from PVD coatings, therefore idealised coating models were used to investigate whether suitable spectral differences could be discerned from layered coating models. Then real tools, coated with a commercially available coating were worn and analysed to investigate what species were present on the tool surface after wear and also to determine spectral changes due to wear. Figure 5.1 (below) show a basic schematic of a proposed portable Raman system implementing a fibre optic probe for analysis of worn tools.

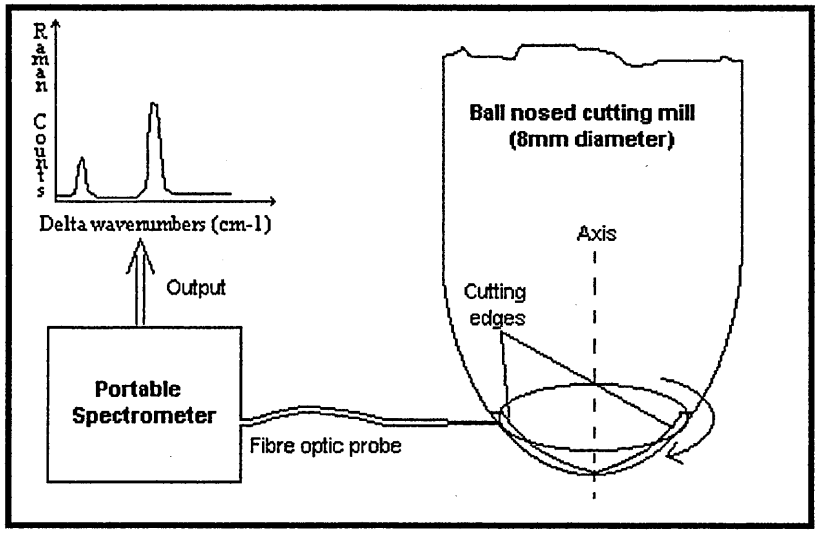

Figure 5.1 Schematic of a fibre optic probe Raman system for wear analysis (Patent: Tool Condition Monitoring)

Raman microscopy has not to date been utilised for the study of worn PVD coated cutting tools. This is perhaps because of the difficult geometry of the tools or that other research groups may not have realised the potential of Raman spectroscopy in wear test studies.

Initially, an *in-situ* method was thought to be of greatest value within the machine shop. A fibre optic probe would focus onto the cutting edge of the tool while rotating, and spectral analysis would instruct the operator when a new tool is required (or give an approximate cutting time left on the current tool). The operator would probably perform this after a period of time-in-cut or after a certain number of components had been machined. The tool might need to be withdrawn from the work-piece and for example docked in a certain position (still rotating, probably at a lower speed i.e. idling).

5.3.1 Difficulties in Achieving an On-Line Method of Wear Quantification

There are many reasons why this type of system would be very difficult to implement. For example:

1) As the tool rotates (5000 – 20000 rpm) the cutting edge, the most important aspect of any cutting tool, and the worst wear region, would only be in focus periodically during the analysis. In addition, spectral intensity from other areas of the tool that are not representative of the wear would almost certainly be included in the resultant spectrum. The amount of time that the cutting edge region would be in focus would be dependent on the speed of rotation, the acquisition time and the spot size of the laser beam. Below is a calculation of the amount of time the cutting edge region would be sampled for a tool rotating at 1000rpm for a 10 second acquisition time.

Calculation

It was thought that an acquisition time of 10 seconds would be acceptable in industry. A tool that rotates at 1000rpm will have rotated 167 times in 10 seconds and a single revolution of the tool takes ~0.06 seconds.

The size of the cutting edge region required for analysis is ~100μm (therefore, 200 μm for both cutting edges as the tool is symmetrical; assuming that each edge has been subjected to the same wear amount).

The circumference of the tool is 25.136mm, therefore the proportion that incorporates the cutting edges is 0.2mm / 25.136mm which is equivalent to $1/126^{th}$ of the total surface.

Therefore the amount of time the cutting edges are in focus for 1 revolution is $0.06 / 126 = 4.8 \times 10^{-4}$ seconds. The total time in which both cutting edges are in focus: $4.8 \times 10^{-4} \times 167 =$ **0.08 seconds**

[For a tool rotating at 19, 000rpm (3167 revs. in 10secs) the edges would be in focus for much longer i.e. 1.52 seconds. Still not a reasonable exposure time].

The result of this calculation demonstrates that a reasonable spectrum can not be acquired with a 10 second exposure time, as the cutting edges are sampled for only 0.08 seconds in that total time. This is also a "best-case" scenario as the geometry of tool in the calculation has been assumed to be circular (this is not the case in reality as the geometry of cutting tools are very complex). This would mean that an acquisition time of 10 / 0.08 = 125 seconds, would be required to obtain a spectrum with the equivalent time of 10 seconds spent analysing the cutting edge region. But, in addition to extra analysis time required to sample the wear zones (cutting edges), the remainder of the exposure time (i.e. when the laser is not focussed on to the desired region) is focussed periodically in air and onto areas of the tool that have not been subject to the same wear environment. Safety issues may also arise due to the surfaces of the tools causing specular reflections of the laser light (goggles would need to be worn). This further demonstrates that a static analysis method would be more viable.

2) The ability to focus onto a rotating object brings into question the reproducibility of the geometry of tools.

3) The ability to hold the fibre optic in the desired position during analysis and, most importantly, not damage the fibre optic via collisions with the rotating tool.

4) There is the question of whether tools require cleaning prior to analysis to remove dirt and grease and built-up-edge (described within section 5.6). Contamination would surely affect the measurements, most notably due to the fluorescence level. This would essentially control the spectral quality.

The ability to gain a spectrum from a rotating tool was thought to be beyond the capabilities of the technique. Therefore a second proposal was to analyse the tools in a stationary position.

5.3.2 Stationary Method of Analysing Worn Tools

This would be a much simpler system to implement and construct, and would allow the tool to be cleaned easily and safely before each analysis. The static system may not be as valuable a proposition to the end user as an on-line system but has many practical advantages:

1) It would be cheaper to build by removing the need for integration with the cutting machinery and software. There are also many different commercially available cutting centres/equipment and the on-line system would need to cater and be adapted for each. This would certainly increase development costs.

2) The static system would be capable of analysing a large number of tools, via a sampling carousel that would ideally be automated. The tool complete with chuck could be placed into a sample holder that would ideally clasp the tool/chuck at the right position to enable the fibre optic to sample the cutting edge. The on-line system would also be limited to one piece of cutting equipment whereas the static system could be used for all the tools in a particular machine shop, as it would not be confined to one cutting machine.

5.4 Idealised Coating Models

To enable wear (the gradual removal of material due to mechanical contact), to be investigated idealised coating models were formulated. These were layered coating systems that were acceptable in terms of functionality (hardness, adhesion, stress, wear resistance etc.), which did not require a large deviation from the already established coating deposition methods/recipes and which were economically viable.

The Initial Ideas Were:

i) A coating system that incorporated a base layer of one coating composition and a top-working layer of another composition. This system required that the two chosen coatings would have very different Raman spectra. A strong band from the base-layer could be monitored, most desirably without interference from the uppermost layer. This method could also be successful if a strong band from the uppermost layer could be monitored as it disappeared i.e. as the coating was worn away. This would leave a thin base-layer, (e.g. 1 μm) as a "safeguard" before the substrate was reached. In

theory this would enable the operator to replace the tool and allow the worn tool to be reground and recoated before any real damage to the underlying base material occurred. This is a common practice, implemented by many companies, especially for cutting operations where expensive tools (£100 - £500) and expensive components are being generated and/or where the surface finish and tolerances are crucial.

ii) An additional idea was to incorporate a marker layer. This marker layer would ideally have a high scattering cross section such that only a short exposure time would be required to detect its presence. Unfortunately the constraints imposed by the deposition process did not allow this to be a viable option. The main reasons being that the prime marker candidates (strong scatters like metal oxides, especially Al_2O_3, graphitic carbon) would compromise the coating-substrate adhesion. A base-layer is required to give a transition of hardness from the substrate to the coating. A marker layer would certainly compromise this process. In addition, this method would also require a further pre-process step that would almost certainly add to the cost of production of the tools and be unacceptable. This method was deemed to be a non-starter.

5.4.1 Model System 1

A coating system composed of a TiN base layer and TiAlCrYN working layer (Cr and Y present, to generate good oxidation characteristics) was chosen for analysis. It has already been established (see in chapter 3) that the incorporation of Cr and Y does not have a profound effect on the Raman spectrum of TiAlN and even increases the total

intensity. Cr and Y do have a big role to play in increasing oxidation/wear resistance and are therefore crucial for functionality.

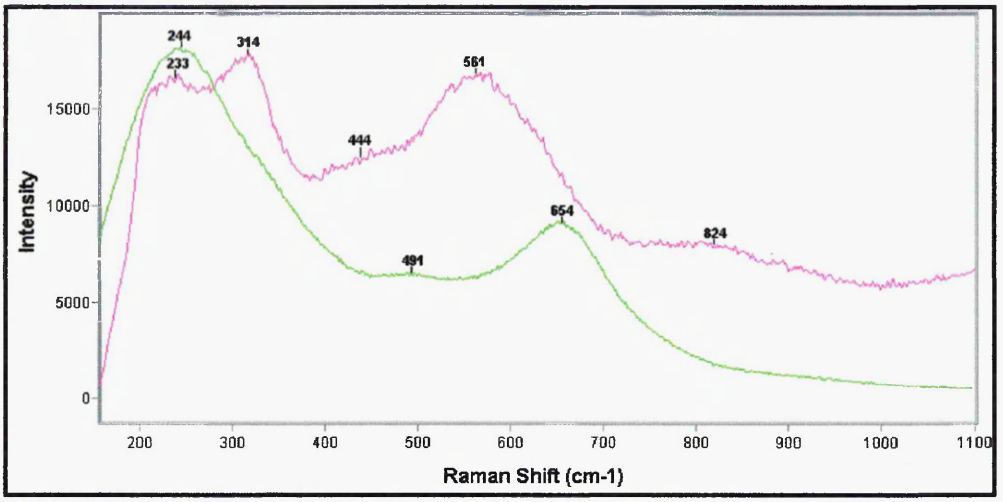

Figure 5.2 Overlaid spectra of TiN (violet) and TiAlCrYN (green) (Model 1)

Model 1 has much potential as an acoustic mode observed at 314cm^{-1} as well as the main optic mode at 561cm^{-1} could be monitored as the TiAlCrYN top layer is worn away. In addition, the strong 654cm^{-1} optic mode of TiAlCrYN could be monitored as it diminished. This could lead to only a narrow spectral range being required in order to differentiate between the two compositions. The TiAlCrYN spectrum is much more intense than TiN, this is because of the defect induced first order Raman scattering mechanism (discussed in Chapter 3), whereby the additional atoms within the TiN lattice, that is Al, Cr and Y act as further defects in the crystal lattice. This has a consequence in that to acquire a reasonable spectrum for TiAlCrYN takes far less time than for TiN.

5.4.2 Ball Cratering of Model Coating Composition 1

Ball cratering (described in Chapter 4) is an ideal method of simulating wear or to depth profile coating structures. Model 1 was composed of a TiAlN working layer which was a $TiAlCr_{(0.03)}Y_{(0.02)}N$ with a 0.1μm oxynitride top coat (1.5μm thickness). The base layer was composed of a 2μm TiN layer deposited on to a HSS substrate.

Ball Cratering Conditions:

30mm diameter ball (chromium alloy steel; 100chrome6), 1μm diamond suspension, depth of crater determined by varying the times: initial craters were done in 0.1 seconds increments. After the TiN base layer became prominent, additional craters were performed using 1 second intervals. Craters of increasing depth were worn into the coating. The coating surface and craters were cleaned using ethanol before Raman analysis.

Raman Microscopy:

Measurements were taken at the centre of each crater to represent the deepest point. Raman instrumental parameters utilised were a X50 objective lens, 150 seconds acquisition time and a 100-1800cm^{-1} spectral window. 100% laser power was utilised from a 633nm HeNe laser.

Results:

as-deposited coating: Oxynitride top coat

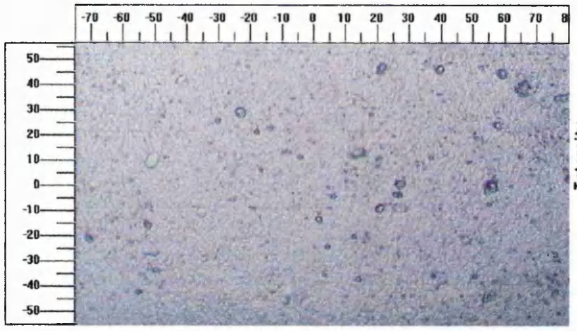

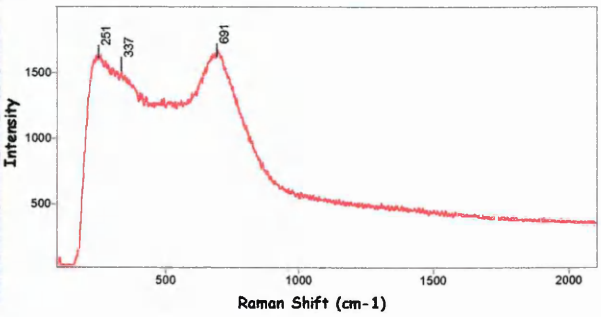

0.1 second crater: TiAlCrYN i.e >0.1µm of coating material was removed

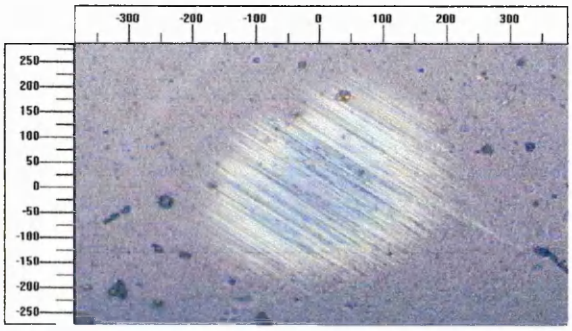

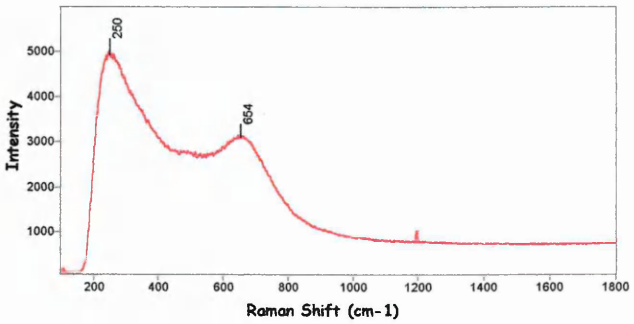

0.2 second crater: TiAlCrYN

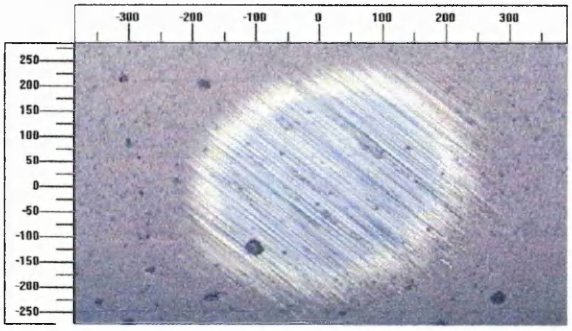

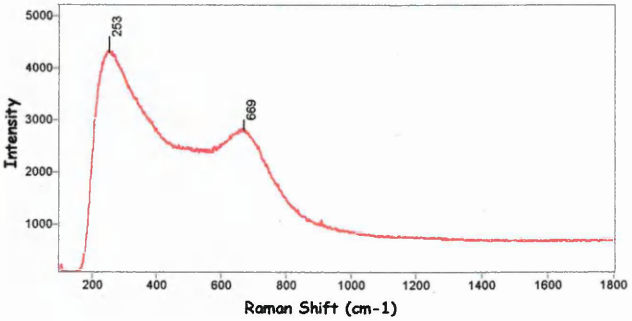

0.3 second crater: TiAlCrYN

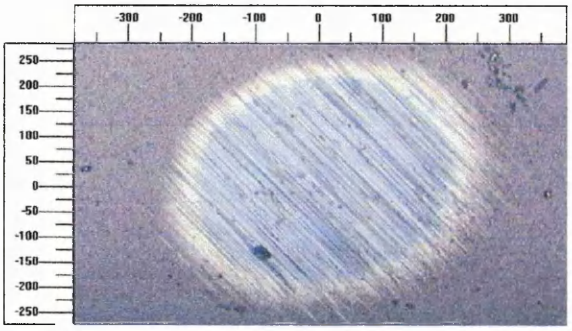

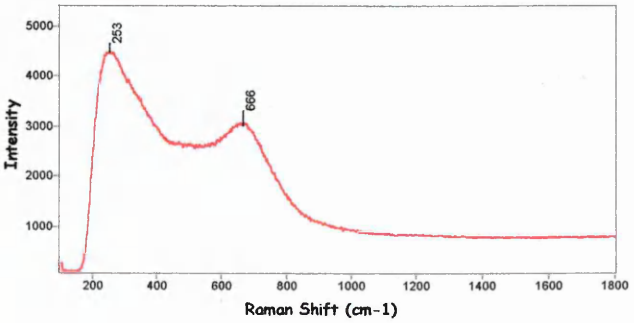

0.4 second crater: TiAlCrYN

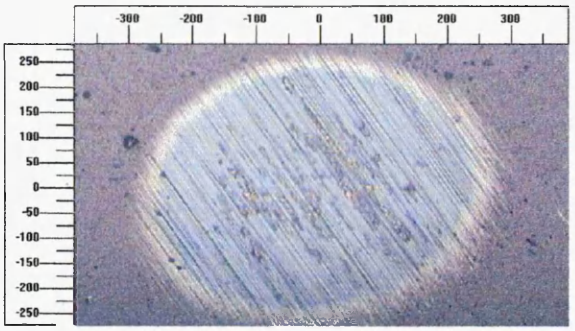

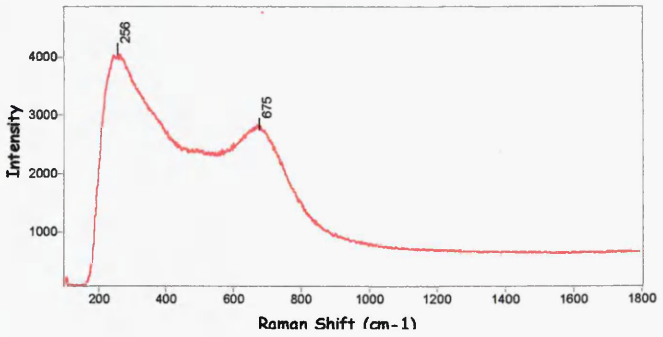

Focussed on golden area:

Evidence that the wear process had reached the TiN base layer

(Golden areas observed in the optical micrograph, Raman spectrum displayed to the right)

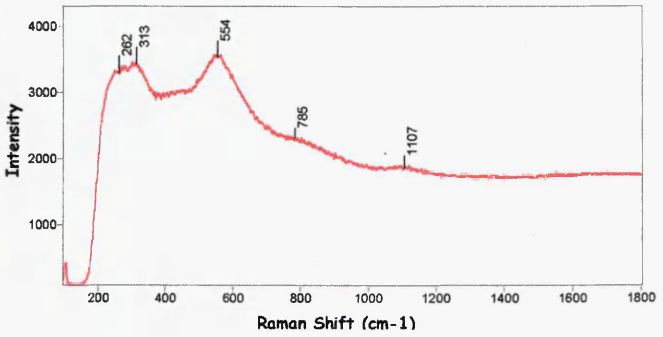

0.5 second crater: As above

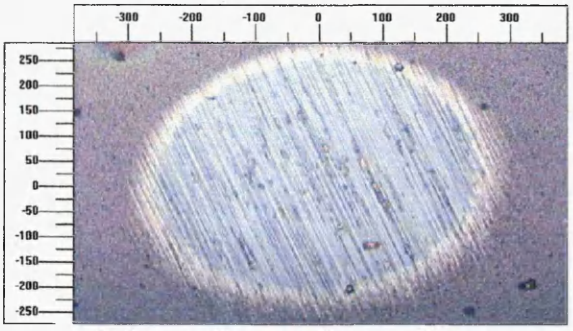

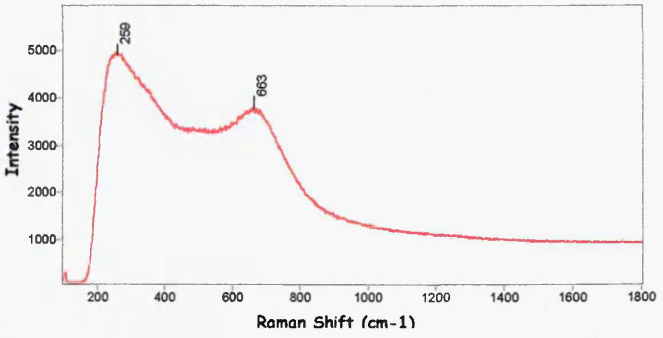

0.6 second crater: Intermediate spectrum

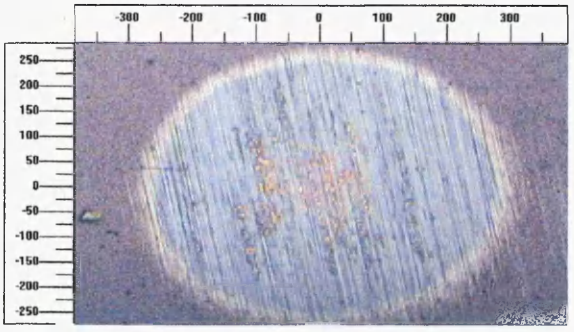

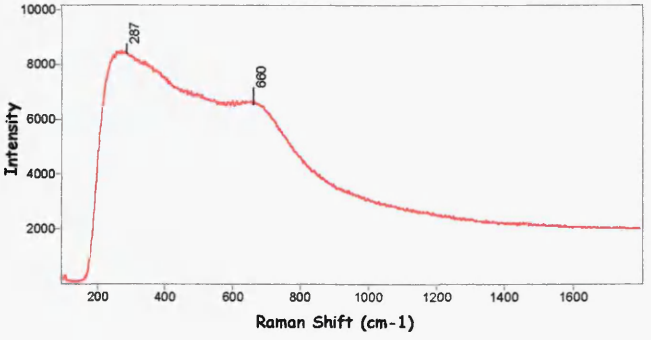

0.8 second crater:

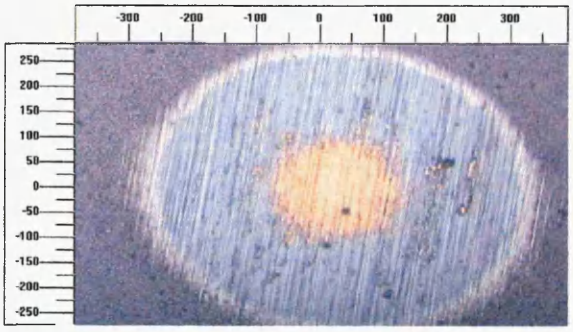

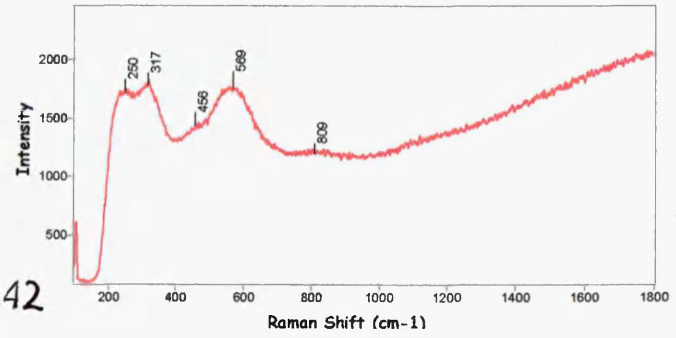

1.0 second crater: TiN layer very visible

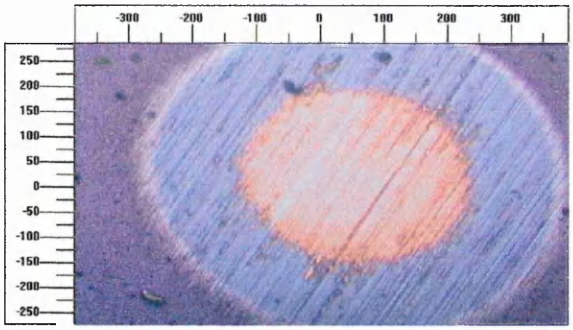

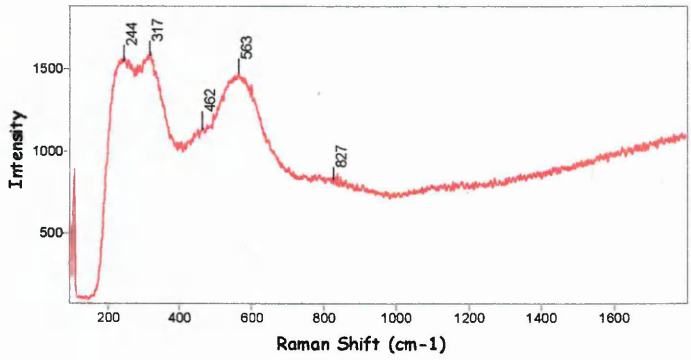

10.0 second crater: TiN

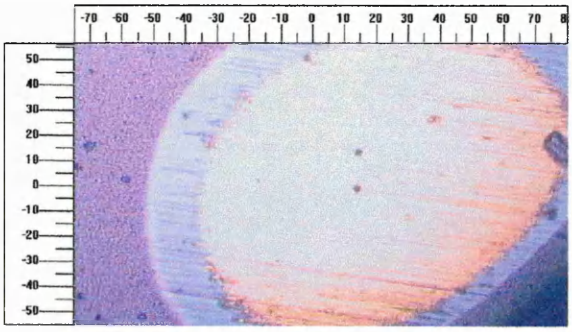

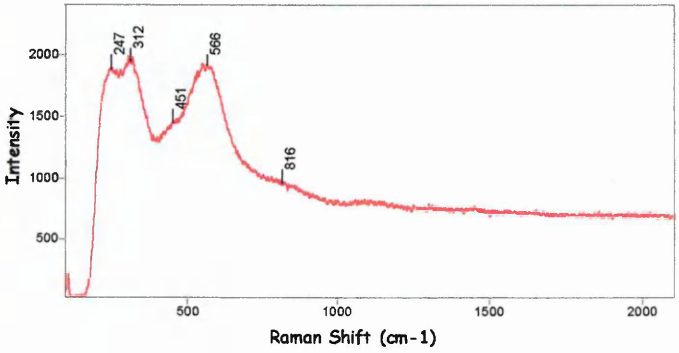

12 second crater:

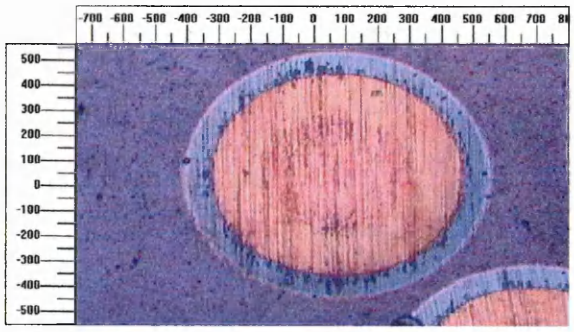

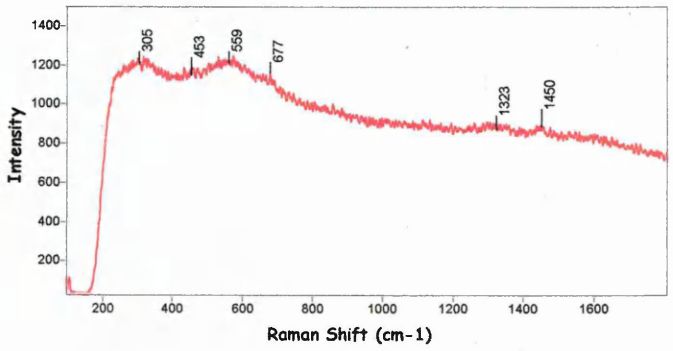

14 second crater: HSS substrate (diamond particle from cratering suspension detected in the crater)

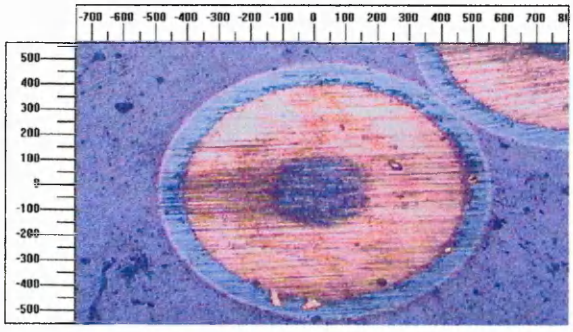

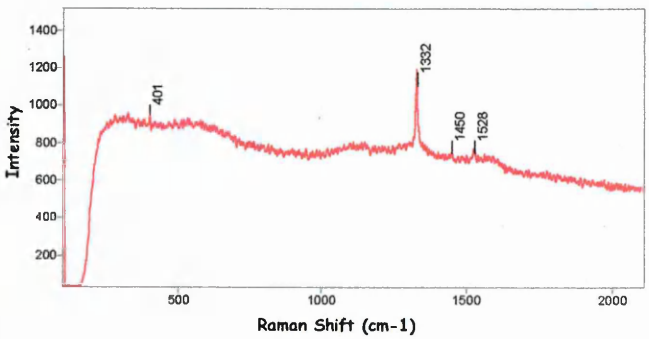

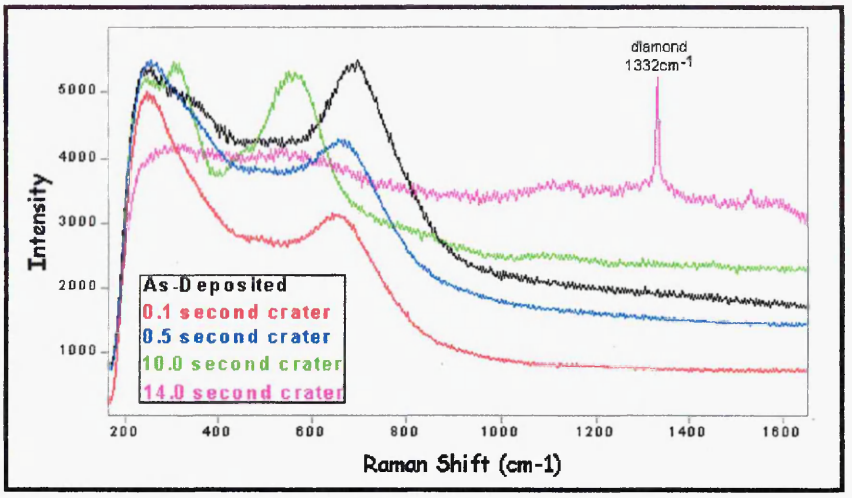

Figure 5.3 Overlaid spectra from the ball cratering experiment on model system 1

Figure 5.3 demonstrated the changes in the Raman spectra as the laser probed deeper into the coating structure. Initially when the laser was focussed onto the uppermost surface a spectrum typical of oxynitride was observed. After a short cratering time of 0.1 seconds, a spectrum of TiAlCrYN is seen (the oxynitride is thin and is quicky worn away). After 0.5 seconds the resultant spectrum started to change i.e. the low frequency acoustic modes diminished to resemble a spectrum more typical of a binary coating indicating that only a thin layer of TiAlCrYN remained. After 1.0 second cratering, the TiN base layer was fully revealed and after 14 seconds all the coating had been removed to leave the HSS substrate exposed. This appeared to show a low intensity spectrum, probably from the carbides that are contained within the steel. In addition a particle of diamond suspension was detected at $1332cm^{-1}$.

5.4.3 Model System 2

A second model system comprised a TiAlCrYN (~1μm) top layer and a bottom (base) layer of CrN (~0.2μm). The spectra of TiAlCrYN and CrN are very different, CrN is even less intense when compared to TiN (base layer model 1) and it was chosen for this reason. The Raman bands indicative of TiAlCrYN could then be monitored as they diminished and in theory there would still be a small thickness of the base layer remaining.

Ball Cratering Parameters:

A 30mm diameter ball, 0.1μm particle size diamond suspension and cratering times 0.4 – 19.6 seconds were implemented. A series of craters were worn in to the coating. The time regime for the cratering was performed in such a way as to result in an even cratering rate.

Raman Parameters:

Measurements were taken at the centre of each crater to represent the deepest point. Raman instrumental parameters utilised were 514.5nm excitation, a X50 objective lens, 150 seconds acquisition time and a 100-1800cm^{-1} spectral window.

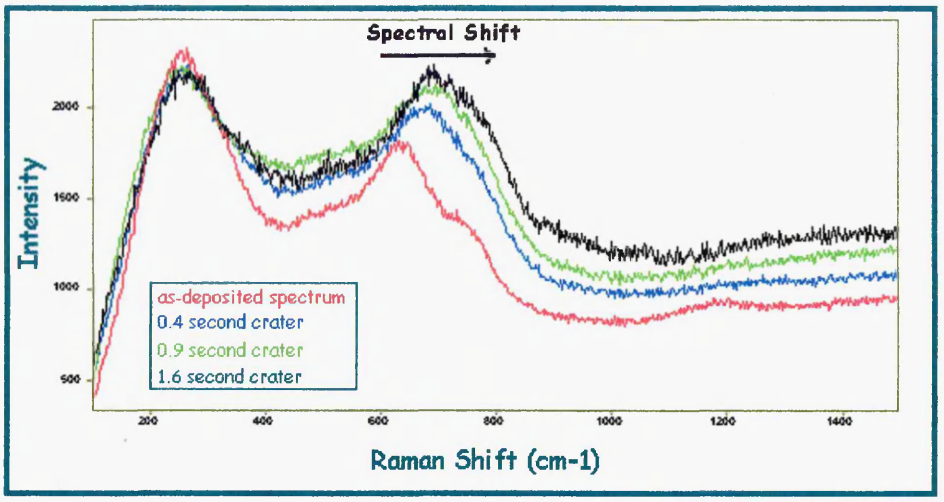

Figure 5.5 Overlaid spectra after 1.6 seconds cratering (TiAlCrYN coating still observed)

When 514.5nm laser excitation was used two overlapping bands were observed for TiAlCrYN (see chapter 3). There was a spectral shift to higher frequency of the main optic modes which appeared to be proportional to cratering time (indicated on Figure 5.5). This indicated that there was an increase in compressive stress due to wearing or that additional spectral features, such as band broadening, are occurring due to the disordering process.

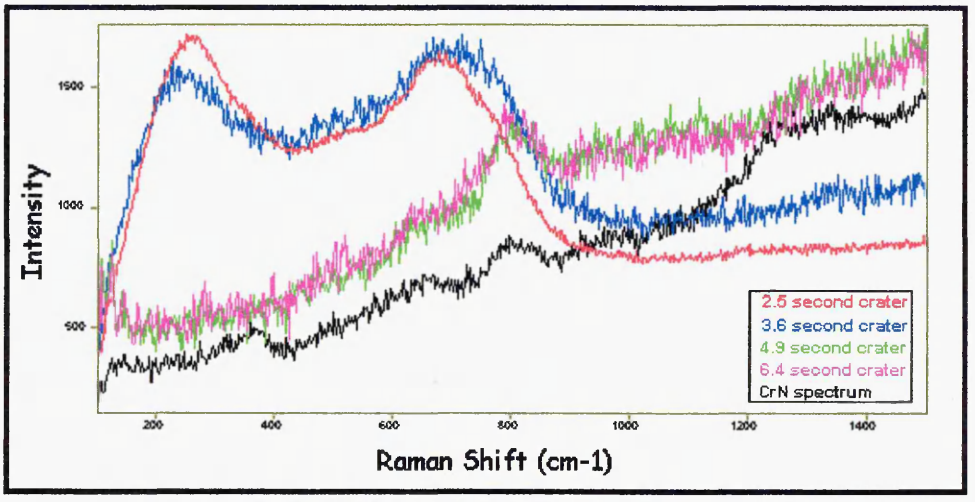

Figure 5.6 Overlaid spectra after 6.4 seconds cratering

Figure 5.6 above demonstrates that after 3.6 seconds cratering time the TiAlCrYN coating spectrum began to become less intense (lower S/N) i.e. indicating that probably only a very thin layer was remaining. Subsequent craters to this show that the CrN base layer has been reached as the bands associated with TiAlCrYN are no longer observed and a very weak intensity spectrum from CrN was apparent.

5.4.4 Overall Conclusions From Ball Cratering of Idealised Models

The wearing procedure utilised to remove layers of coating revealing further underlying indicator layers, was shown to be a good technique for simulating wear. However control of the abrasive wear mechanism was not easy and did not allow the experiment to be stopped just prior to reaching underlying base layers. Nevertheless the utilisation of these coating systems has shown Raman microscopy to be good method of deducing the amount of removed material via engineered base layers. The question then arose as to whether already established commercially available layered coating compositions, could be studied in the same manner without the need for additional base layers. Supercote-02, a highly popular commercial coating, designed to be an all-purpose coating for cutting applications was chosen for subsequent cratering and wear analysis.

5.5 Examination of Supercote-02 (The General Purpose Coating)

5.5.1 Coating Specifications

Cr Stabilised TiAlN	**: $Ti_{(0.44)}Al_{(0.53)}Cr_{(0.03)}N$**
Thickness	**: $3 \pm 0.5\mu m$**
Coating deposition temp.	**: $450^{o}C$**
Hardness HK(0.025N)	**: 2500**
Hardness HP1 (30mN)	**: 42 Gpa**
Youngs Modulus	**: 431Gpa**
Coefficient of Friction (Al_2O_3)	**: 0.7**
Roughness (Ra)	**: $0.04\mu m$**
Max. Working Temperature	**: $700^{o}C$**

The deposition process for Supercote-02 is such that TiAlCrN is deposited approximately 2.8 μm thick. The Cr target power is then "ramped up" to form a gradually increasing superlattice period of TiAlN/CrN. Oxygen is then gradually introduced and the power on the Cr target is reduced to form an oxy-nitride layer. The TiAlN/CrN and the oxy-nitride layers together are 0.1 - 0.2 μm (only 20 minutes of the whole four hour deposition process). The purpose of the oxy-nitride and superlattice layers is to have a low friction hard initial surface so that it does not require "wearing-in" as other coatings do. Figure 5.7 (below) shows the Supercote-02 coating architecture.

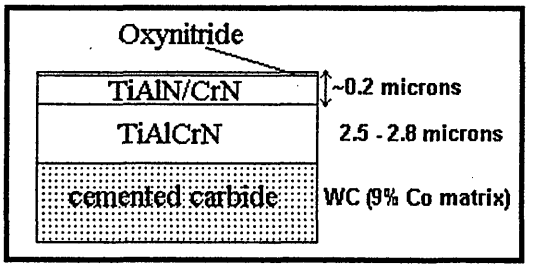

Figure 5.7 Supercote-02 coating architecture

5.5.2 Ball Cratering Analysis of Supercote 02

Ball cratering was performed in the same manner as previous analyses. The Raman spectra for the individual layers were obtained using a 632.8nm HeNe laser, 400 second acquisition time, x50 microscope objective and 100% laser power (~5mW at the sample). Figure 5.8 shows the individual coating spectra. It may be seen that the spectra are very much alike. This was not surprising since all three layers are composed of Ti, Al, Cr and N arranged in a polycrystalline fcc crystal network. A machine shop worker would find it difficult to distinguish between these three coating layer spectra. Chemometrics will be discussed in the later part of this chapter as a way of separating out and distinguishing between the coating layers and gleaning more information from the wear analysis.

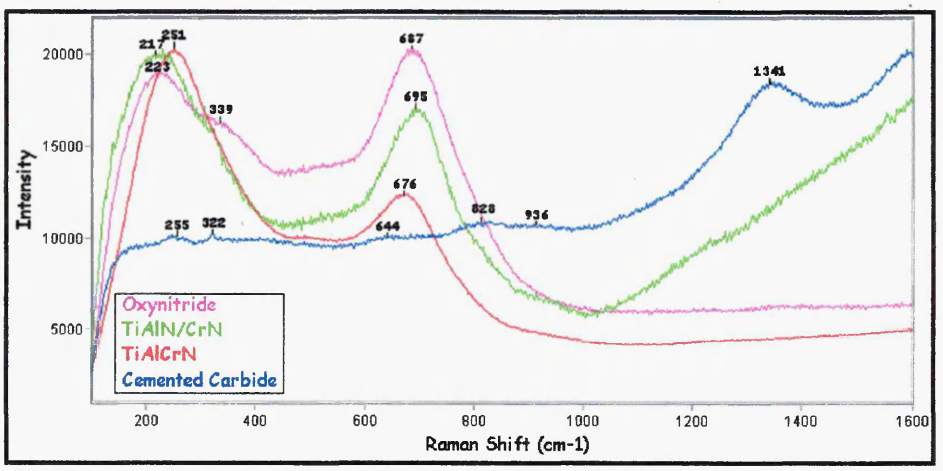

Figure 5.8 Spectra of coating layers in Supercote-02

The substrate material for this system was cemented carbide (i.e. it is tungsten carbide within a 9% cobalt matrix), and was chosen because of its use as the material for high-speed cutting tools. Small bands at low frequency, broad optic modes around 600 - 900cm^{-1} and a large D-band at 1341cm^{-1}typical for amorphous free carbon were

detected for the cemented carbide material. The G-band was (also) just observed at ~1600cm^{-1}. These carbon bands could possibly be used as an indicator of when the base material had been reached during a cutting operation. However, this would unfortunately be too late, as substrate damage may have occurred in some other region of the cutting edge prior to detecting the carbon. In addition, the cleanliness of machine shops is such that these bands could easily be mistaken for dirt/grease on the surface of the coating, especially if a restricted spectral region (for rapid analysis), for example 1200-1700cm^{-1}, were taken as an indicator as there are no other coating bands within that region.

5.6 Introduction to Cutting Tools[19]

Cutting tools are used extensively in the automotive and engineering industries to generate certain components. These tools vary from drills, end mills, taps, reamers etc. The cutting can be performed in a lubricated environment, where the fluids act as lubricant and coolants, and give the tool increased life. These coolants are usually plant-wide distribution systems served from a common re-circulation and cleaning system. The system should maintain a level of cleanliness that is consistent with accepted health standards for the industry. The cleaning of the re-circulated cutting fluid is very important. Tramp oil from the machinery and metal chips must be removed as well as much finer contaminants. Contaminants can come from the cutting process or from the plumbing of the circulation system. They can even exist as microbes that grow in such harsh environments. All must be removed and the chemistry adjusted back to a specified level. Finally the chips and other contaminants must be disposed of safely.

All these aforementioned prerequisites of cutting fluid use cost vast amounts of money to maintain. Many of the fluids and other contaminants pose a health risk to the machine workers and others within the local proximity, especially when fine mists of these fluids enter the atmosphere and are inhaled. There is therefore a massive economic and health "premium" if dry machining can be implemented. Consequently there is a big "push" to move to protective coatings and tool materials which allow cutting without the need for hazardous fluids, so called "green" manufacturing processes.

Tool materials need to be wear resistant, tough, and have a characteristic referred to as "hot hardness". Because the type of active wear mechanism varies with wear environment, tool manufacturers have a broad range of materials available that are wear resistant when used for different cutting conditions. The common tool categories are high-speed steels (HSS), cast cobalt alloys, micro-grain (powder metallurgy) high-speed steels, and various grades of carbides, ceramics, polycrystalline diamond (PCD), or cubic boron nitride (CBN). To further increase the hardness of these materials they can be coated with CVD (chemical vapour deposited) or PVD coatings, such as, TiN, TiCN, TiAlN etc.

Alumina-based tools exhibit high hardness and very good chemical stability and thus offer advantages over cemented carbides with respect to wear behaviour in many cutting applications. But, these ceramic tools have relatively low strength and toughness and have susceptibility to thermal cracking[20]. Tough materials can absorb energy and resist plastic deformation without fracturing. With increasing hardness, there is generally a decrease in toughness, which is also applicable to

coatings. Hot hardness is also another important characteristic for cutting tools, and is defined as the ability of the material to maintain hardness at elevated temperatures.

5.6.1 Wear Characteristics of Cutting Tools in High Speed Cutting Applications

Cutting tools wear because normal loads on the wear surface are high and the cutting chips and work-piece that apply these loads are moving rapidly over the tools wear surfaces[19]. The cutting action and related friction at these contact surfaces increase with temperature, which further accelerates the physical and chemical processes associated with tool wear.

In order to cut/remove the material as chips, and form the desired component, tool wear is an economic penalty that must be accounted for in order to machine the part. The magnitude of this economic penalty is minimised if the cutting process is planned and controlled based on sound knowledge of the wear process and it dependency on the selected cutting conditions. Cutting conditions are frequently referred to as depth of cut, cutting velocity, and feed rate. During the process planning stage, an assessment must be made into the how difficult the material is to machine. To make these choices, the wear environment in metal cutting must be understood to enable the correct choice of tool and tool material and/or coating.

Cutting tool wear occurs along the cutting edge and on adjacent surfaces. Figure 5.9 Shows a view of the cutting process where the rake and clearance surface intersect to define the cutting edge.

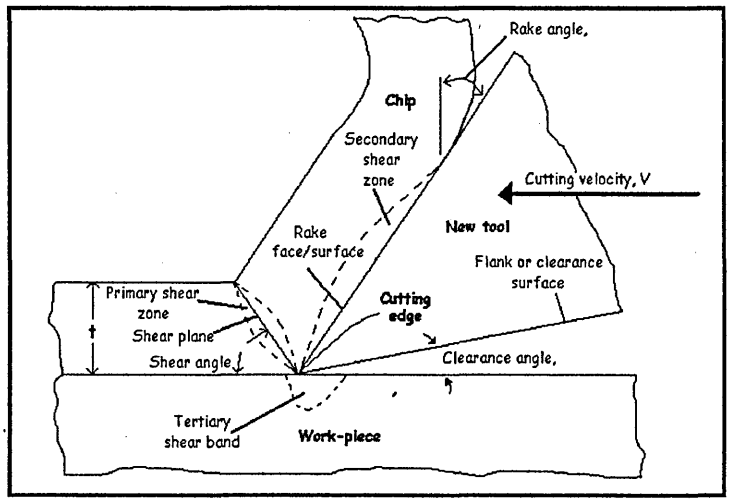

Figure 5.9 Chip, work-piece, and tool relationship(Ref 19)

Figure 5.10 (below) adds the stress and strain states that are present in the material and the chip.

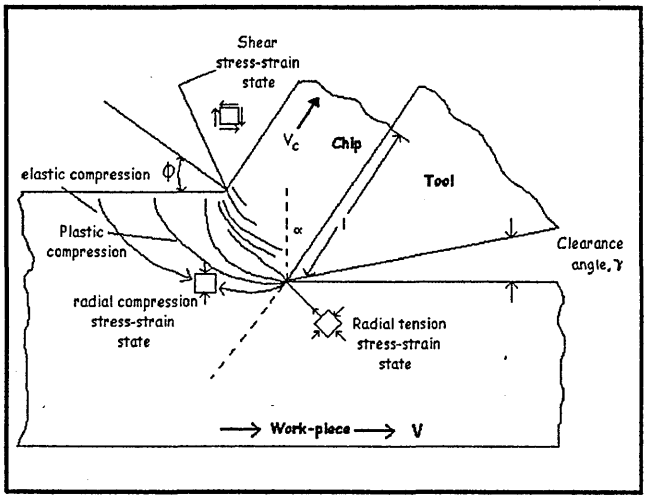

Figure 5.10 Stress and strain states in cutting edge region, source Ref 19

The tool engages the material to depth, t, and the resultant force vector creates a component force, F_s, that shears the material along the shear plane area, A_s, to form a chip having thickness t_c. The direction of the chip motion is controlled by the rake angle, α. The magnitude of chip velocity, V_c, is a function of the cutting velocity, V, the rake angle, and the shear angle, φ.

Cutting tool wear is localised on specific surfaces where stress, strain, velocity, and temperature are above critical levels. It is imperative that these critical conditions are understood.

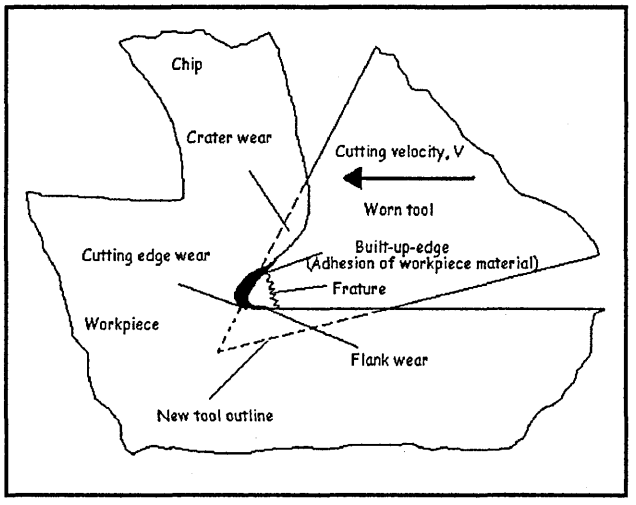

Figure 5.11 Tool wear due to the velocities and forces, source Ref 19.

Along the rake surface, the chip motion, V_c, and high normal stresses have produced a wear scar called crater wear. Along the clearance surface, the tool motion, V, and high normal stresses due to force F_t have increased the area of contact between the tool and work-piece, producing flank wear. Cutting edge wear has increased the radius of the tool and is caused by the combined affect of these component forces localised to the cutting edge region. The wear process changes the geometry of cutting tools. Flank wear decreases the diameter of the end mill; these changes to the geometry of the tool produce out-of-tolerance dimensions on machined parts. The edge wear and crater wear on the rake surface alter the state of stress and strain in the cutting region, thus changing cutting forces and the mechanics associated with the chip making process. Severe geometric changes due to crater and flank wear weaken the tool so that the edge may suddenly fracture (Figure 5.12, stresses on tool wear surfaces).

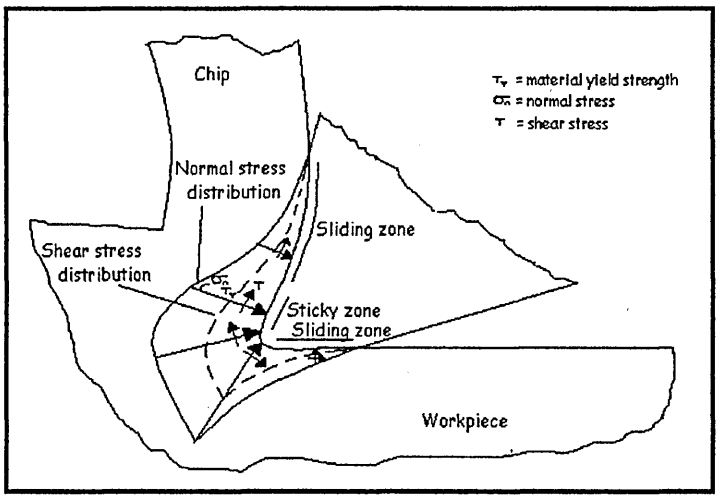

Figure 5.12 Wear surface stresses

Figure 5.12 shows the approximate distribution of normal and shear stresses on the tools wear surfaces. The normal stress, σ_n, are caused by the normal force acting along the rake surface, the cutting edge surface, and the clearance surface. The shear stresses, τ, that act along the surface of the tool and that are associated with sticking and sliding shear processes. For the sticky zone, the normal force has a magnitude that results in shear stress component that equal the shear yield strength, τ_y, of the strain-hardened workpiece material. Rather than sliding along the surface, the chip tends to adhere and periodically separate along the shear fracture planes within the material, leaving adhered material to the tool, which subsequently causes tool wear. A sizable amount of material may adhere for extended periods of time. Stable masses of adhered material are known as "built-up-edge" and alter the geometry of the cutting edge. The sliding zones have friction forces and associated surface shear stresses that vary according to the normal force and coefficient of friction. Tool surface roughness and lubrication conditions affect the magnitude of these surface shear stresses. The state of stress created by the shear loads in the sticky and sliding zones along the rake surface produce the secondary shear zone (see Figure 5.9).

The primary shear zone extends from the cutting edge to the work surface; it is the zone where the work material is plastically deformed and sheared to form the chip. The conflict between chip motion strain and stationary workpiece strain produces a ploughing action by the cutting edge. Normal stresses can become very high and exceed the strength of the tool material, causing plastic deformation or fracture of the cutting edge. A sticky zone may not always occur for certain cutting conditions. However, the ploughing action along the cutting edge will always exist to some degree because it is impossible to create a cutting edge with no radius and a primary shear zone that is a perfect plane. The magnitude of the stress in the cutting region also varies with time, and the associated load variations may create a fatigue failure environment for the tool.

5.6.2 Increased Productivity

One way to increase machining productivity is to increase the chip removal rate, which is a function of the engagement area of the tool with the work material and the velocity at which the tool moves through uncut material. Therefore, one option is to increase the cutting velocity. The productivity gain must be balanced against increased tool wear caused by higher cutting velocities (see figure 5.31 a real case). The magnitude of the velocity and the related shear stresses at these interfaces determines the amount of thermal energy released per unit of contact area. These thermal energy releases cause the temperature of the workpiece, cutting tool, and chip to increase. The productivity gain from increasing the cutting velocity proportionately increases the wear surface velocities, strain rates, and the release of thermal energy, thus increasing the wear environment temperature.

5.6.3 Temperatures During Cutting

The difference between the thermal-energy release rate and the thermal-energy dissipation rate determines the temperature of the material and tool in these wear zones. Thermal-energy dissipation is a function of the thermal conductivity properties of the tool material and the workpiece material. The chip/swarf carries some of this thermal energy away from the tool (see section 5.9) and work material. Additionally the workpiece size and specific heat determines the workpiece heat capacity, and, to a lesser extent, the surface area plays a role in convective and radiative heat transfer to the surrounding air. Even with the best of tools their hardness, toughness, and chemical stability properties eventually adversely change with increasing temperatures. Average temperature conditions are approximated using the following type of relationship.

$$T = u\left(\frac{Vt}{Kpc}\right)$$

Where T is the mean temperature of the tool-chip interface, u is the specific cutting energy (which is the energy used per-unit-volume of material removed), V is the cutting speed, t, is the un-deformed chip thickness and k, p, and c are the conductivity, density, and specific heat, respectively of the workpiece material.

The temperature distribution in the cutting region can cause portions of the tool to be at dangerously high temperature levels (i.e. hot spots), well above the mean predicted temperature. The mean temperature relationship given above does not identify all the important variables and how they affect temperature. "Combining these temperature effects with the state of stress, strain rates, and material motion makes the wear zones

of the tool a complex 'battle-ground' in which these conditions interact to trigger the mechanisms that cause wear"[19].

5.6.4 Wear Mechanisms

A particular wear mechanism is dependent upon the contact stress, relative velocities at the wear interface, temperature, and physical and chemical properties of the contacting materials. Figure 5.14 (below) shows a generalised temperature distribution in the cutting region (when the contacting zone remains constant).

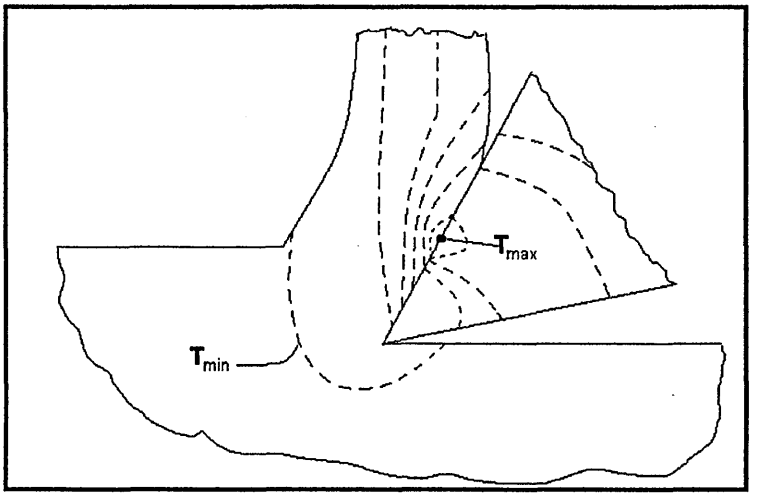

Figure 5.13 Temperature distribution in the cutting region

Temperature, a variable that is dependent upon the pressure (normal stress), velocity, and size of the wear surface. There are four broad classes of mechanism:

i) Seizure

ii) Melt wear

iii) Oxidation/diffusion-dominated wear

iv) Plasticity-dominated wear

(In addition to producing temperature maps, cutting tool research has developed similar maps for feed rate, which is related to pressure for a given engagement condition, and velocity (see Figure 5.14)).

5.6.4.1 Initial Wear Mechanisms

Materials in contact have surface roughness irregularities in the form of protrusions or asperities (see chapter 4 section 4.2.). At the interface, asperities from the two contacting materials touch, defining tiny contact areas. The total area from these contact points is a fraction of the projected area of the contact surface. The stresses and heat are intensified in the asperities, and partial removal may occur due to the seizure accompanied by fracture of the asperity or melting in the asperity. As these asperities are removed, the initial surface roughness is altered and the contact area increases. If the force conditions remain unchanged, pressure decreases and the active wear mechanism changes to plasticity and/or oxidational/diffusion-dominated wear. This initial wear period will create small visible wear surfaces.

5.6.4.2 Steady-State Wear Mechanism

If conditions of high velocity and normal stress are implemented this would result in seizure and melt mechanisms and cause rapid failure of the cutting tool and should be avoided. Assuming that such conditions do not exist, the wear surfaces get progressively larger.

Plasticity dominated wear results in small particles of material being deformed and being fractured from the wear surface. This is termed abrasion and can occur for any of the wear surfaces. It is most common wear process along the clearance or flank surfaces of most tools. Because normal stress and temperature vary over the wear surfaces of the tool a plasticity dominated wear mechanism that dominates in one wear zone may not dominate in another. Figure 5.13 Indicates that the maximum tool surface temperature occurs on the rake surface a small distance from the cutting edge when cutting most materials. This is where the crater wear condition occurs; diffusion wear is often the dominant mechanism[20]. The high temperatures and pressure cause atoms to move between the contacting materials, and this diffusion process locally aids in the removal of material to form the crater. In very hard cutting tool materials, such as ceramics and hard coatings, where high cutting velocities are commonly used, these oxidation and diffusion mechanisms may be responsible for a majority of the wear. This mechanism will presumably be accelerated when the coating has worn to leave the underlying substrate exposed.

Figure 5.14 shows wear mechanism maps and safe operating region for cutting tools[21].

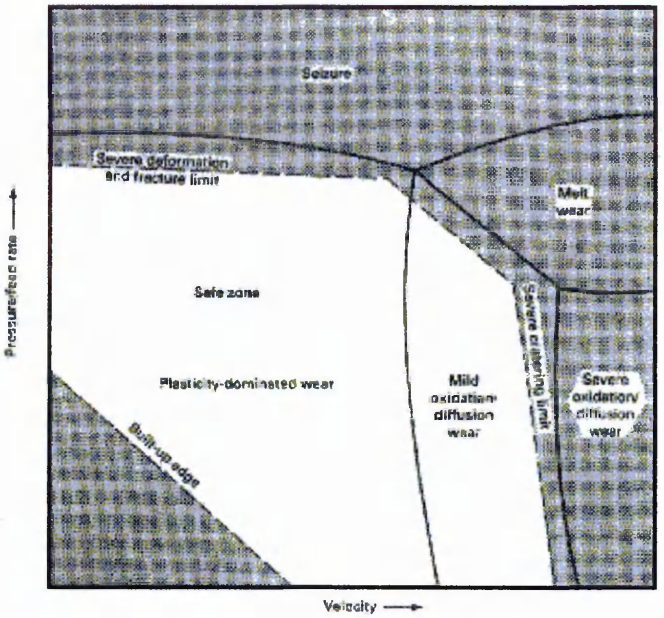

Figure 5.14 Wear mechanism map (Ref. 19)

The dashed line in the lower left corner of Fig 5.14 identifies a built-up-edge (BUE) condition that affects the process in two ways. Near the cutting edge, the higher pressures cause particles of work material to adhere to the cutting tool in the sticky zone. If the shear forces due to chip movement are high enough, the bond will be temporary and the adhered material will fracture away from the tool surface. When it fractures small particles of tool/coating will be removed also (this has indeed been observed see section 5.9). This then is a wear process and is associated with conditions in the so called "safe zone". The second effect on the process occurs when the BUE is not fractured away by the chip motion and remains adhered. This alters the geometry of the cutting tool; it changes the shear angle, causing instabilities in the chip-forming process plus damage to the machined surface. For rough cuts, this BUE can be beneficial in that it provides an intermediate protective layer between the tool surface and the work material.

Wear can also occur as chipping along the cutting edge. Such chipping commonly occurs when the cutting edge intermittently removes chips. This results in cyclic impact and thermal loading of the cutting edge. These two cyclic loading states can initiate small cracks and then cause these cracks or other residual cracks to propagate, leading to tool chipping. These abrasion, oxidation, diffusion, and chipping mechanisms that occur in operating conditions within the safe-zone, shown in Figure 5.14, cause the initial wear surfaces to gradually enlarge over time. This surface life period is often referred to as the steady-state wear period. Figure 5.15 (below) shows these three stages of tool wear for five different cutting velocities.

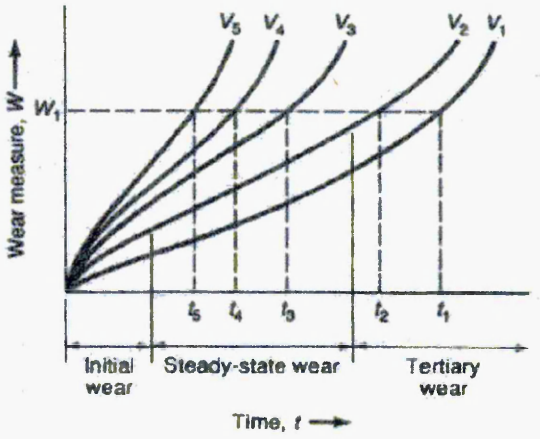

Figure 5.15 Tool wear curves for different cutting velocities

5.6.4.3 Tertiary Mechanisms

The steady state wear will eventually enlarge the wear surfaces to a critical size that will trigger accelerated wear. The pressures and velocities on these enlarged surfaces begin increasing the temperature such that the rapid oxidation/diffusion and local seizure or melting conditions cause rapid destruction of the tool. In tools that have a hard, wear resistant coating such as titanium nitride, wear through this coating or separation of small volumes of the coating from the base material will expose the less-

resistant core material to these same rapid wear conditions. A tool change must be made before this point is reached. To further complicate the understanding of cutting tool wear mechanisms, there is a growing trend toward higher and higher speed machining. This means using cutting velocities 5 to 10 times the normal speed. New tool materials and machine tool designs have made this possible; but such changes alter the wear environment. Proportionally more thermal energy is removed with the chip due to the decrease in contact time between the tool and the chip; however the higher velocities will increase absolute temperatures on the tool wear surfaces. Under such conditions, abrasive wear may become less important and the diffusion and oxidation processes could be dominant in creating and enlarging the wear surfaces.

5.6.5 Machine, Cutting Tool and Tool Wear Interactions

The cutting tool is only one element of the machining system. It is a complex system comprising of the workpiece, the workpiece holding fixture, the tool holder and the machine tool. Before configuring a machining system, the selection process starts by obtaining knowledge about the type and quality of the surfaces to be machined. The geometry of these surfaces will determine the types of cutters that are required. If we consider a single type of surface is being machined to a given quality level (that is, tolerance and surface finish). The selection of the machine tool, the type of cutting tool, the type of cutting tool material, the feed rate, the cutting velocity, and the depth of cut defines one operating state for the machine system. This state will establish the wear environment at the cutting edges of the tool. How rapidly this wear environment degrades the tool will determine how frequently the tool will have to be changed. A tool change interrupts the machining process, which subsequently decreases the

production rate and adds a cost that is associated with the interruption, the tool change expense, and the replacement tool cost. Trying to reduce this cost by lengthening the intervals between changes will eventually lead to the cost to rise again. This rise occurs when the wear process has progressed to induce tertiary wear mechanisms and accelerated wear of the cutting edge. The accelerated wear damages the surface, necessitating repair expense or cost associated with a scrapped part. Even if the tool-changing interval keeps the wear process within the steady-state wear zone, this is finite probability that the tool may fail unexpectedly before a scheduled replacement and cause damage that requires repair or scrapping of the part. How probable such an event is dependent upon the workpiece material characteristics, the nature of the cutting loads on the tool and the quality of the cutting tool (including the quality of any coatings).

5.6.6 Tool Material Choice

Wear resistance is the ability of the material to have a useful life when subjected to the types of wear mechanism already discussed. The common tool materials categories are high-speed-steel (HSS), cast cobalt alloys, micrograin (powder metallurgy) HSS, various grades of carbides, ceramics, polycrystalline diamond (PCD), or cubic boron nitrides (CBN). Some of these materials are routinely coated with a harder material such as TiN, TiC, or Al_2O_3 etc.

Cutting tool manufacturers have developed elaborate systems to specifically classify their cutting tools materials; however, their systems are often based on some logical trade-off between wear resistance and toughness for different levels of tool loading

caused by different cutting edge engagements, feed rates, and cutting speeds. Table 5.1 relates these trade-offs to cutting tool wear mechanisms.

Heavy roughing	Roughing	Semifinishing	Finishing
	Chipping		
Fracture	Deformation	Wear land	Deformation
Chipping	Cracking	Deformation	Crater
Deformation	Crater	Crater	Wear land

Increasing feed **Increasing speed**

5.6.6.1 Cemented Carbides

Cemented carbides are the choice for high-speed machine tool base materials. A variety of carbide materials are available in fine powder form and can be produced using P/M processing into a coherent, hard material using binders such as cobalt. The development of coated carbides has lead to an increased range of application. The type of powder, binder, and powder particle size determine the final properties. Cemented carbide cutting tool suppliers provide a broad range of grades, from those suitable for finished surfaces using high cutting speeds and small depths of cut, to tougher grades more suitable for lower cutting speeds and heavy tool loads found in rough cuts. For certain work materials, temperature conditions, and cutting surface pressures, diffusion and oxidation wear processes very rapidly degrade the cutting edge.

5.7 Raman Analysis of Worn Tools

Supercote-02 was deposited onto 8mm diameter Marwin whisper mills (ball nosed). Cutting tests were then performed in parallel with Raman measurements. The tools were tested cutting into EN 24 steel (approximate analysis: C $_{(0.4)}$ Mn $_{(0.6)}$ Ni $_{(1.5)}$ Cr $_{(1.1)}$ Mo $_{(0.30)}$) and a hardness of 35 Rc[22]. An automated Mazak cutting centre was used utilising the following cutting conditions.

Cutting Conditions

RPM speed:	**15000**
Linear speed:	**385 m/min**
Feed:	**0.2 mm/rev**
Depth of cut:	**4 mm**
Radial cut:	**1 mm**

5.7.1 Initial Measurements

Raman mapping was implemented to systematically sample an area of the worn rake face and cutting edge. These were performed with X: 200μm Y: 500μm, and a 100μm step size (18 spectra per map). Figure 5.16 shows a schematic of the area mapped (with 1 - 18 representing where the points were taken).

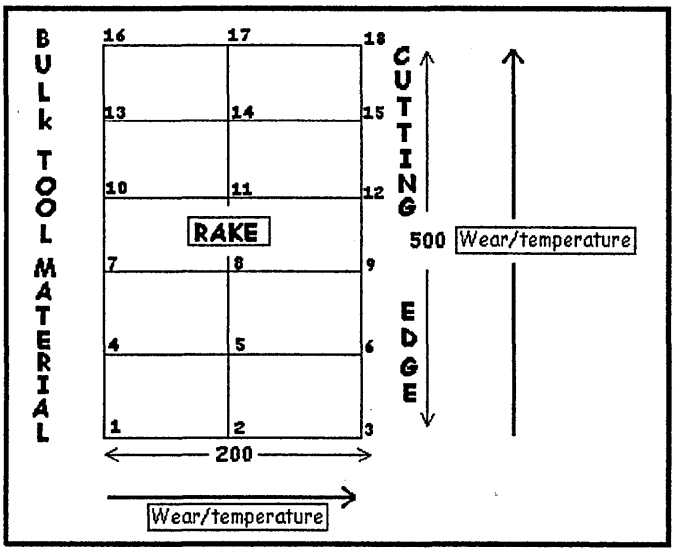

Figure 5.16 Raman mapping area and associated phenomena (distances in μm)

The maps were taken at this position on the tool because it allowed automated measurements to be permitted, as it was a reasonably flat surface. Other areas of the rake surface had a higher curvature. A schematic representation of the cutting tool is shown in Figure 5.17; this indicates that the wear region spans from the axis point at zero speed around the radius (ball-nose) of the tool to the fastest speed, which is at the depth of cut, which for these measurement was 4.0 mm (the radial cut was 1mm; 1mm would be shaved off on each pass of the tool and the depth to which the tool engages the material is termed the depth of cut which was at 4 mm for this cutting test, the resultant chip of removed material would have dimensions of 1 by 4 mm).

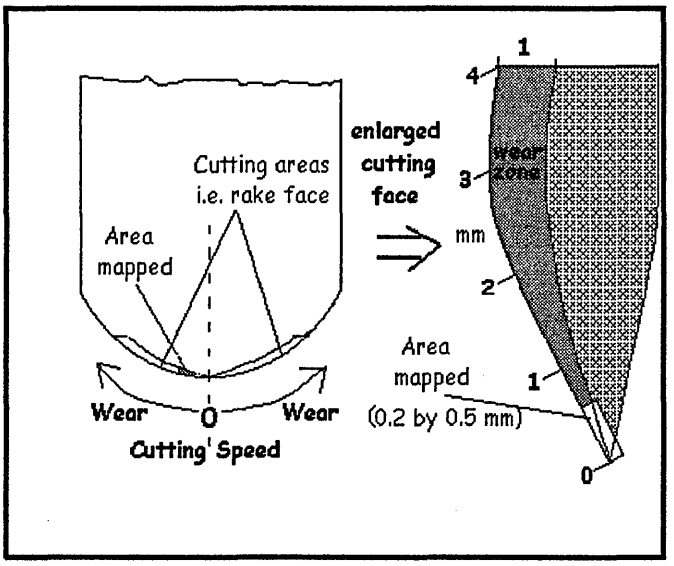

Figure 5.17 Schematic showing cutting speed dependence on cutting face/edge (Enlarged region showing Raman area map which directly relates to figure 5.16)

The cutting speed increases as one goes round the ball nose; the temperature and amount of wear also do (as shown). These are harsh conditions that are more typical for roughing applications (that is large amounts of material was removed to result in the approximate shape of the desired component (the tolerances/surface finish do not matter). A finishing cut would then be used to remove a small amount of material to gain the actual component. The surface finish and tolerances are of paramount importance for finishing cuts.

5.7.2 Raman Mapping of Wear Scars on Coated Cutting Tools

The times-in-cut measured were 3, 6, 12, 64, 120, 130 minutes.

Raman Microscopic Parameters: x20 (ULWD) objective lens to enable focussing to be achieved on the difficult geometry tool, 125 second acquisition time, 100% power (25mW with ~5mW at the sample) using 632.8nm laser light.

0 minutes (Unworn spectrum):

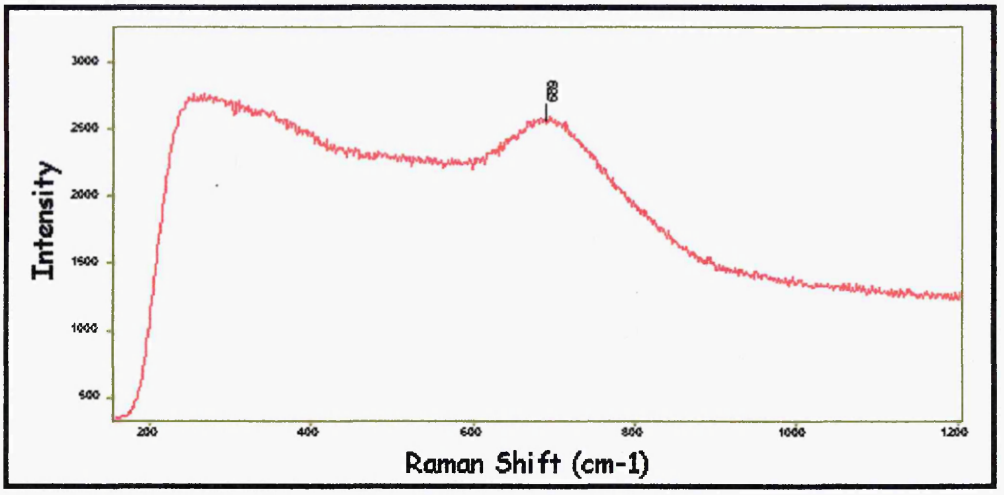

Figure 5.18 Unworn surface of a supercote-02 coated tool

Low frequency acoustic modes between 200 - 425cm^{-1} and a main broad optic mode at ~690cm^{-1} were observed.

5.7.2.1 3 Minutes Wear

Figure 5.19 (below) shows the wear of (a) an uncoated tool (WC - Co) and (b) coated tool (WC - Co coated with Supercote-02) both after 3 minutes-in-cut.

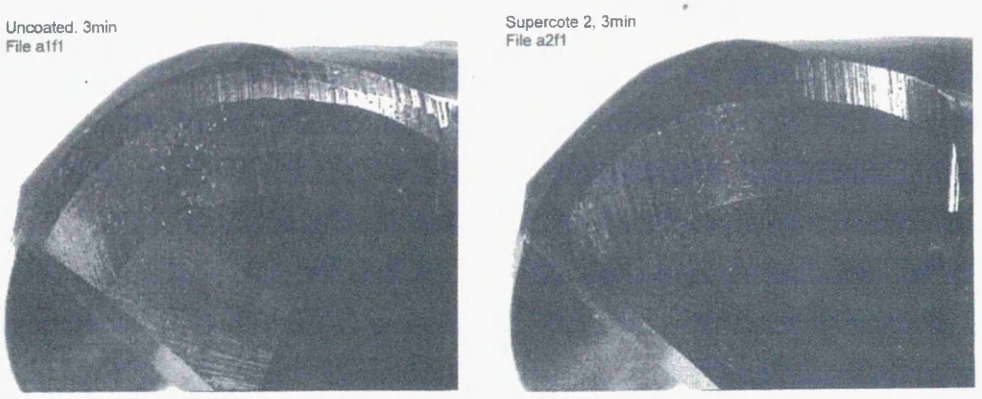

Figure 5.19 (a) un-coated WC-Co and (b) coated with Supercote-02

To enable the wear state to be viewed the cutting tools were placed on their side with their flank surface showing. The 3 minute-in-cut uncoated tool showed vast amounts of wear virtually all around the flank of the tool. This would lead to out-of-tolerance machined parts and the tool could critically fail if used for further time due to increased cutting stresses because of the distorted geometry of the tool. The coated tool showed very little wear although a small wear crater was observed (top right of the image). This confirms that the mechanisms of wear of uncoated and coated tools are very different, and further emphasises the economical gains from coating cutting tools for prolonged tool life. The uncoated WC-Co tool gradually began to glow red-hot as time progressed and caused severe oxidative wear which lead to rapid deterioration of the cutting surface.

From the Raman area maps performed for the wear analysis, positions 12, 15 and 18 appeared to be most representative for the overall wear i.e. on the cutting edge. Other positions within the map tended to be subject to a graded wear situation, as indicated on Figure 5.16. The majority of wear occurs on the cutting edge of tools and a reduction in the observed wear is observed as one goes out from that edge onto the rake surface into the bulk of the tool. The measurements at these other position would lead to a misleading indication of wear i.e. under-estimation.

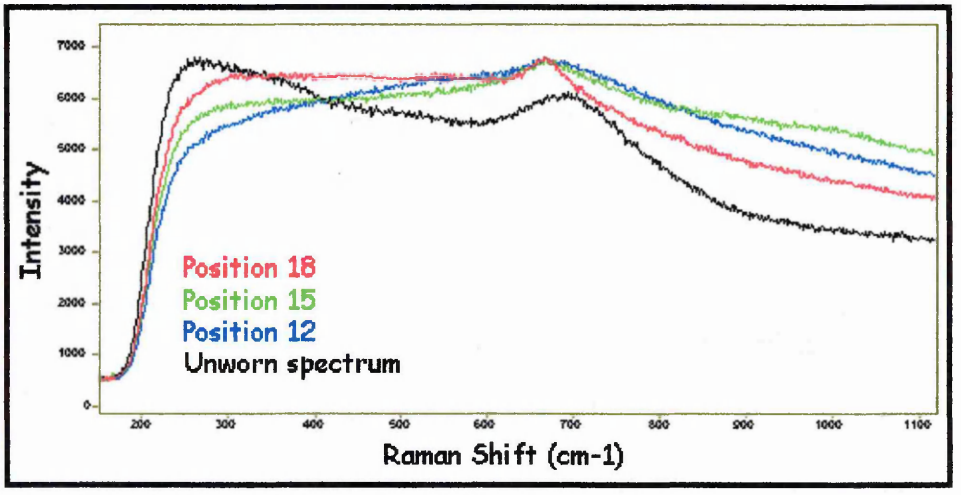

Figure 5.20 Spectra from the rake face of a tool worn for 3 minutes

The optic mode typical for the oxynitride (~680cm^{-1}) was observed for positions 12 and 15 i.e. 300 and 400 μm round from the axis point of the tool. The acoustic modes appeared to be diminished. The Raman spectrum resulting from position 18, the position representative of the most wear in the map region resulted in a band that was centred at 670cm^{-1}. Although this band was still broad, it was considerably sharper than the oxynitride optic mode or any other bands resulting from the coating components (see Figure 5.8 (coating layer spectra)). The band was also shifted to lower frequency. The initial theory was that the sharpening of this band was a function of the wear process, although this did not seem logical, as other

measurements have shown that the damage/disorder to PVD coatings leads to broader bands. At position 9 in the Raman area map (Figure 5.16) there was evidence for α-Al_2O_3 on the surface (see Figure 5.21 (below)) of the tool indicating that high temperatures >900°C (see chapter 6 section 6.5.3) had been reached during cutting, even after 3 minutes in cut.

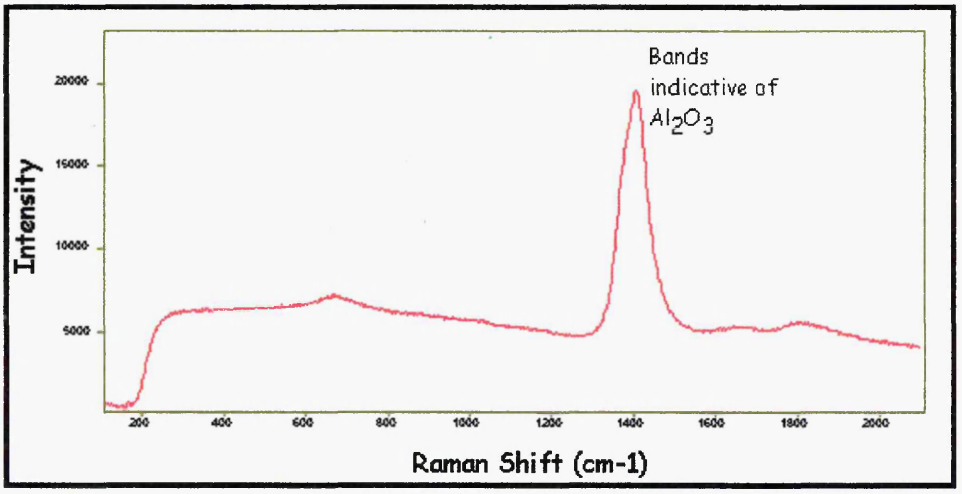

Figure 5.20 Observation of Al_2O_3 on the cutting edge

The observation of α-Al_2O_3 at position 9 and not at 12, 15 and 18 implied that the 0.2 mm position along the cutting edge was not subject to the same wear environment. It could be that at position 12, 15 and 18 an abrasive wear mechanism/sticky zone removes the oxide build up but at position 9 the tool was still subject to the high temperatures of cutting but not an abrasive mechanism. The oxide layer then prevails. The α-Al_2O_3 oxide was not fully crystalline as two sharp bands are observed for crystalline α-Al_2O_3[23].

5.7.2.2 6 Minutes Wear

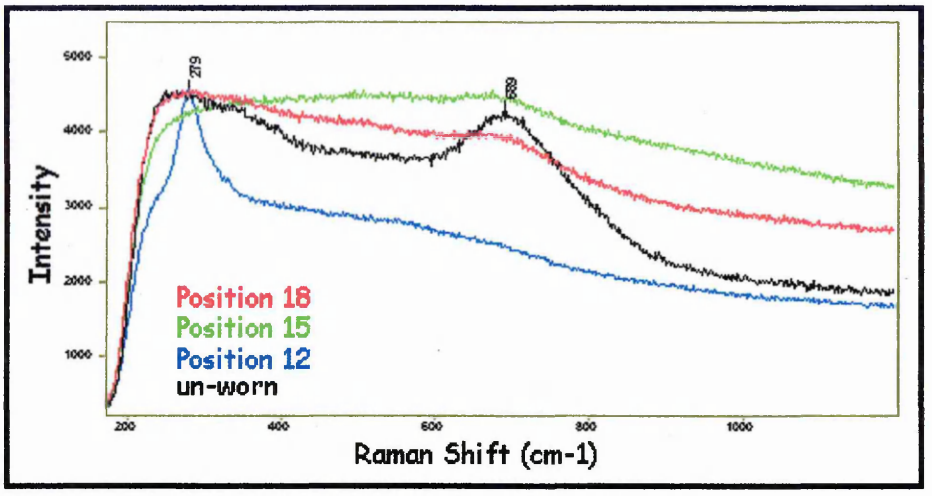

Figure 5.21 Spectra from the cutting surface of a tool worn for 6 minutes

At 6 minutes, a broad low intensity feature, similar in position to the unworn i.e. oxynitride spectrum, was observed (see section 5.5.1 (coating specifications) for a description of the oxynitride top layer and its purpose) . The low frequency acoustic modes are again diminished. A spectrum that resembled TiAlCrN had not been identified for the 3 and 6 minute wear time points which implied that the TiAlCrN main body of the coating was not reached and that the uppermost layers of oxynitride and TiAlN/CrN were still present. A high intensity low frequency mode was observed at ~280cm^{-1} for position 12 on the map, which could not be identified. The 3 and 6-minute spectra do not appear to be identical to oxynitride or the TiAlN/CrN superlattice layer and it was speculated whether a combination/mixing of Raman modes or a temperature effect could be responsible (i.e. annealing out all the defects thus resulting in essentially no Raman intensity N.B. Raman scattering is via a defect induced first-order spectrum). To investigate whether a temperature effect was responsible a heat treatment was performed on a Supercote-02 tool in an inert atmosphere (Ar gas), i.e. so that changes were due to only temperature and not oxidation. The tool was subject to a temperature of 900°C for two hours in an argon

atmosphere. A temperature of 900°C was chosen as the treatment temperature as this was thought to be a realistic cutting temperature (see chapter 6, section 6.5.3 for high temperature oxidation studies of Supercote-02). The resultant tool was measured on the cutting edge to ascertain whether any spectral changes had taken place. The optical micrograph below (Figure 5.23) shows the cutting surface and cutting edge of the heat-treated tool.

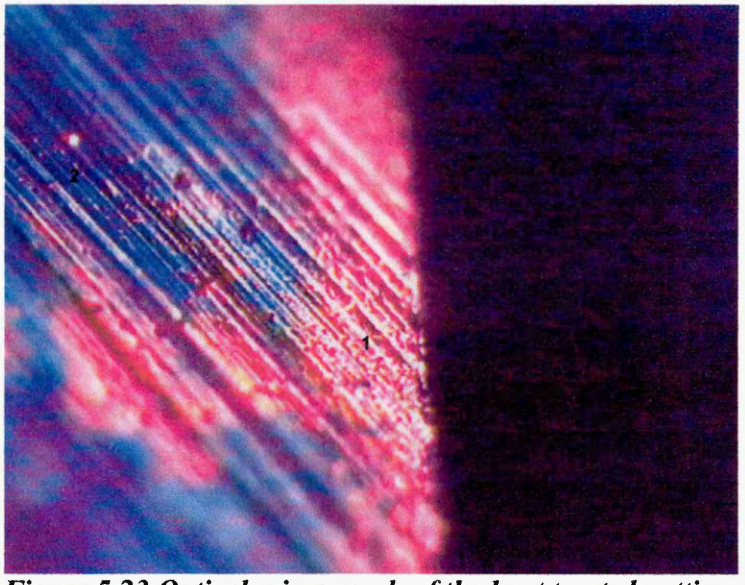

Figure 5.23 Optical micrograph of the heat treated cutting surface (N.B the marks observed on the tool surface are from the grinding process from tool manufacture, these increase the roughness quite considerably)

It may be seen that the cutting edge region had a different colour to the rest of the rake surface, that is, a pink/orange colouration similar in nature to TiN surfaces. A measurement was acquired directly on the cutting edge (directly onto this changed surface); see Figure 5.24 (below).

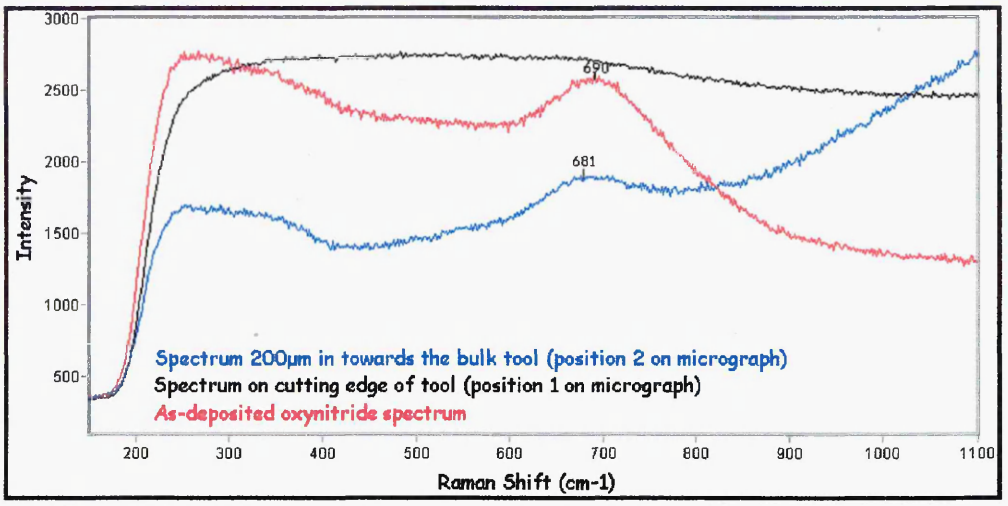

Figure 5.24 Measurement taken onto the heat- treated tool cutting surface

The resultant Raman spectrum of this area showed very little spectral intensity. A very low intensity broad feature was observed at the approximate frequency of the oxynitride optic mode. This was almost identical to the spectra of the cutting edge region at 3 and 6 minutes-in-cut. The spectrum taken ~200µm in towards the bulk of the tool showed similar features to the oxynitride layer, although more fluorescence was observed (seen as an upward sloping baseline) and the main optic mode was shifted to lower frequency and was slightly sharper. The shift could be explained by a stress annealing mechanism where by defects/dislocations are removed as a result of the high temperatures resulting in a diminished residual stress after treatment (as a consequence of this the coating also has reduced hardness). The slight sharpening can be explained as due to a coarsening of the grain structure, i.e. the grains become larger, therefore offering fewer phonon relaxation routes.

The observation of essentially no Raman spectral intensity when measurements were taken on the cutting edge region cannot be fully explained, but a diffusion mechanism may have occurred, whereby Al, which is a small and mobile metal atom within the crystal lattice may have diffused to the surface. This has been known to occur when

TiAlN coatings oxidise; a bi-layer of oxide products is generated with Al_2O_3 on the upper surface and TiO_2 below. In addition TiAlN is thermodynamically unstable, and will separate out into AlN and TiN at sufficiently high temperatures.

5.7.2.3 12 Minutes Wear

The Raman spectra resulting from the surface of the tool after 12 minutes (Figure 5.25) appear to show that the wear has progressed through the upper layers of coating structure i.e. oxynitride and superlattice, and reached the main bulk of the coating TiAlCrN.

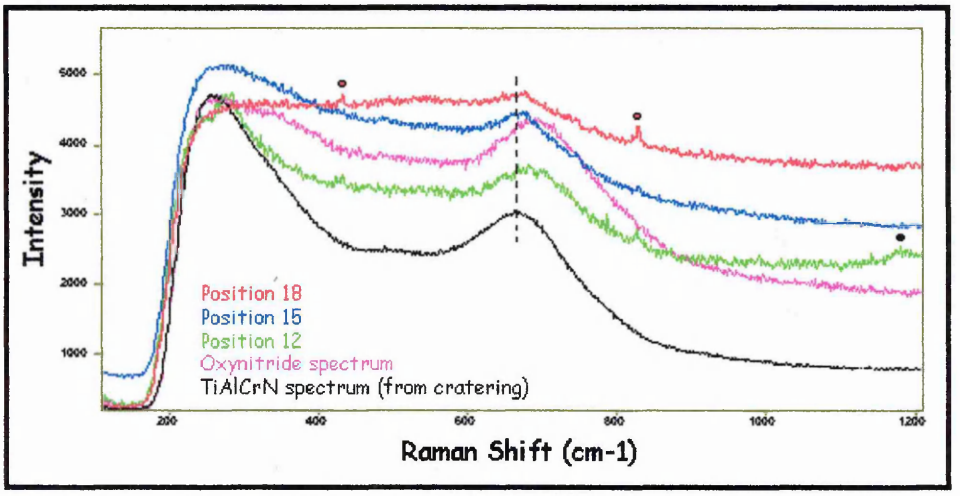

Figure 5.25 tool surface after 12 minutes of wear

The spectrum from position 12 does, however, appear to be similar in nature to the superlattice layer (see coating layer spectra, Figure 5.8) and has a small band at ~1200cm^{-1} which has been observed for TiAlN/CrN superlattice coatings previously. Small bands are observed at approximately 420 and 825cm^{-1} (marked onto Figure 5.25); these are especially prevalent for position 18 (not observed previously). The dashed line on Figure 5.25 demonstrates that the main optic mode resulting from

position 15 and 18 had shifted to lower frequency, resembling a spectrum most like TiAlCrN.

5.7.2.4 64 Minutes Wear

The spectra arising from the worn areas now most certainly resemble TiAlCrN. It was unclear what the small bands between 1200 – 1600cm^{-1} were due to, but from their frequencies it was thought that organic species were more likely (not α-Al_2O_3).

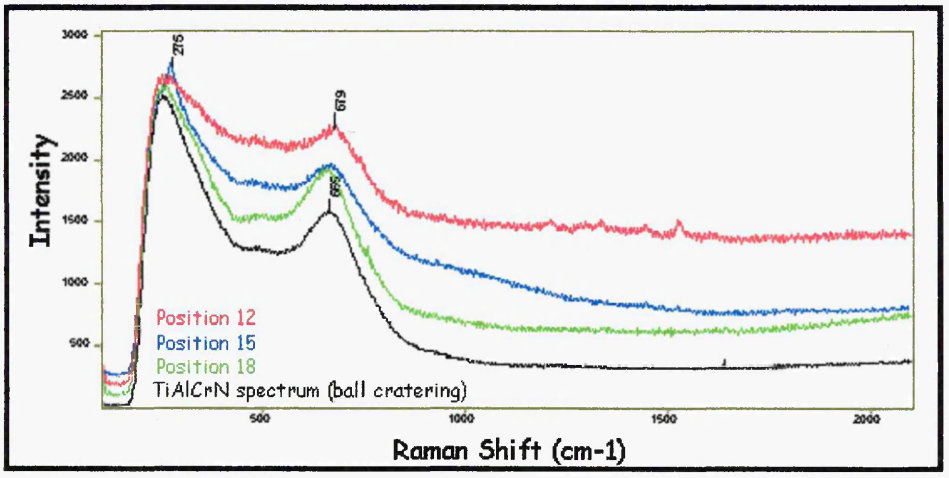

Figure 5.26 spectra after 64 minute of wear

Al_2O_3 was again observed at position 9 of the mapped region (see figure 5.15) but appeared to be more crystalline than previously observed. Figure 5.27 (below) compares the Al_2O_3 (3 minutes) with the spectrum after 64 minutes wear.

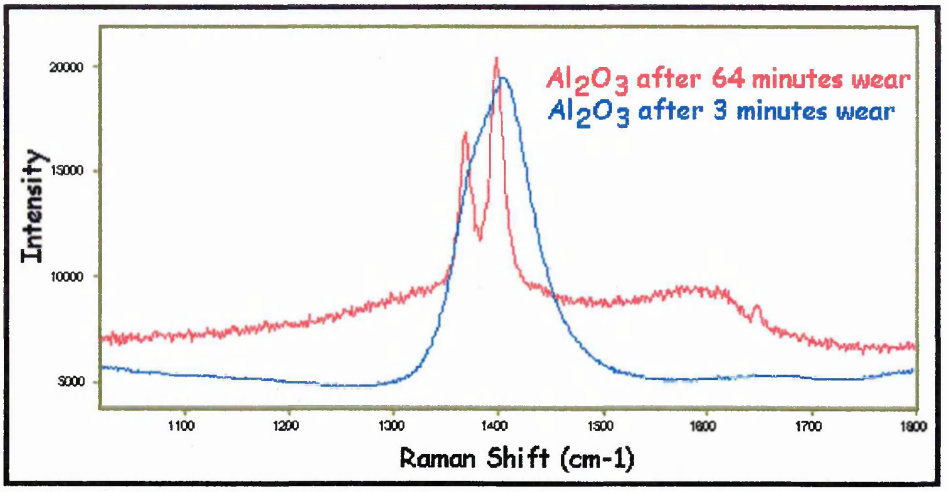

Figure 5.27 Comparison of Al_2O_3 detected after 3 minutes and 64 minutes

It may be seen that the α -Al_2O_3 on the surface of the worn tool after 64 minute wear was much more crystalline indicated by the two α -Al_2O_3 bands at 1369 and 1398 cm^{-1} becoming resolved. This suggests that higher cutting temperatures occurred for the 64minute-in-cut.

5.7.2.5 120 Minutes Wear

The spectrum that arose from the worn areas of the tool showed a different spectrum. Figure 5.28 shows a typical spectrum. This was a sharper band centred at ~670cm^{-1} (similar to 3 minutes (position 18)) and did not match any of the spectra from coating components or oxide bands previously observed (e.g. α -Al_2O_3).

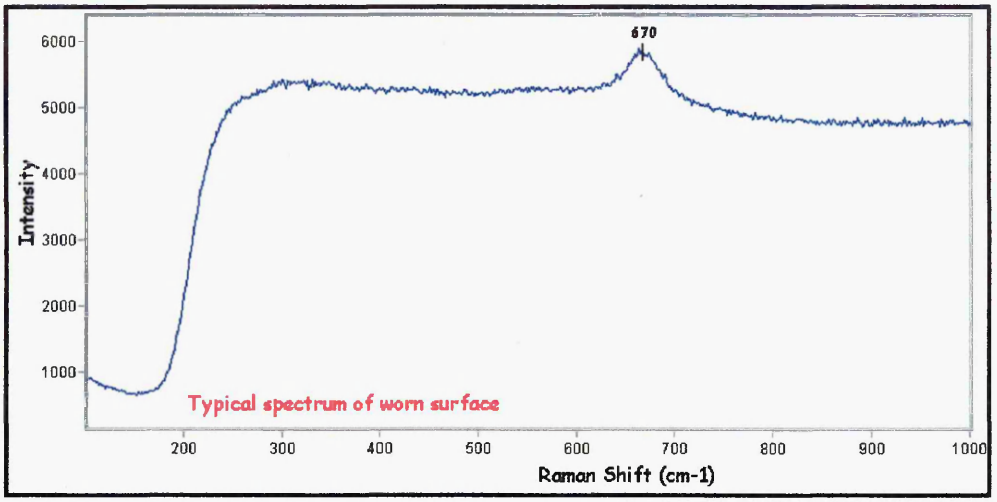

Figure 5.28 Typical spectrum of the worn surface after 120 minute wear

5.7.2.6 130 Minutes Wear

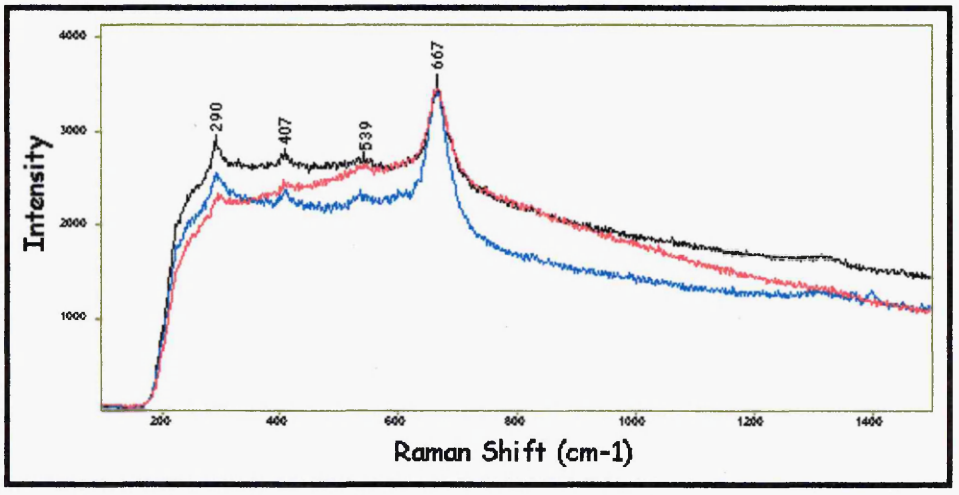

Figure 5.29 Spectra of the tool surface after 130 minutes wear

In addition to the sharp band observed at ~667cm^{-1} (which appeared to become even sharper for 130 minutes wear) further small bands at 190, 407, 539 and 1300 cm^{-1} were observed. The band observed at ~670cm^{-1} was identified from a paper by De Faria et al[24] as wustite or magnetite, FeO and Fe_3O_4 respectively, but identification was unclear as both have very similar spectra i.e. a reasonably strong band centred at ~670cm^{-1} the only difference being that small bands at ~320 and 470 cm^{-1} are

observed for magnetite (there was a possibility of these bands not being observed due to their low intensity). The small bands that are observed for the 130 minute worn tool i.e. 190, 407, 539 and 1300 cm^{-1} gave evidence of a phase transition from FeO/Fe_3O_4 to Fe_2O_3[24] taking place, indicating that a higher temperature occurred. This FeO/Fe_3O_4 spectrum resulted from spectra acquired on all the worn areas around the Raman map region i.e. all cutting-edge positions in map (figure 5.16). It was concluded from this observation that it must have been a transfer layer from the steel workpiece material or build-up-edge that had stuck to the surface of the tool and become oxidised due to the temperature from further cutting/impacts with the workpiece. The optical micrographs Figure 5.30 (below) show the flank wear comparison of a tool being used for 3 minutes and 130 minutes.

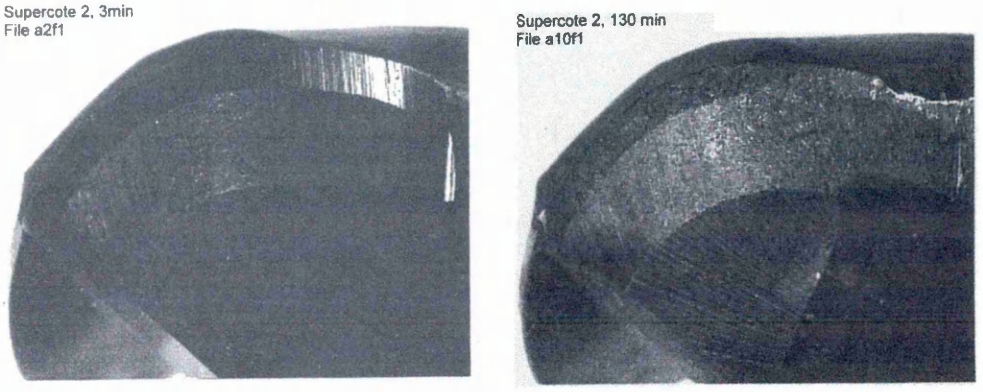

Figure 5.30 Comparison of wear (a) 3 minute-in-cut and (b) 130 minutes-in-cut

It may be seen that the tool wear after 3 minutes was slight and the majority of wear was confined to a small crater region observed at a position right round the ball nose

(i.e. top right of image), the 130 minutes-in-cut image indicated that this initial crater had grown in size and progressed round the ball nose indicating oxidation/diffusion wear (i.e. material transfer). It can be seen that much of the WC-Co base material was worn away near to the crater, i.e. ~500 μm region of the tool, after 130 minute-in-cut, thus indicating that the coating must have been removed well before this time-point in and around this specific crater event. Crater wear is indicative of diffusional/oxidative wear and is usually observed at the point on the surface where the cutting temperatures are at a maximum (see figure 5.13). This implies that as the tool becomes increasingly worn this T_{max} moves along cutting surface due to the wear region becoming larger. A mapping experiment was performed on the cutting surface of the 130 minute worn tool to ascertain, by the way of the oxide species present on the surface of the tool, if the cutting temperature increased to a maximum value in and around this crater region. A manual map was performed using the mapping stage (i.e. using the stage to move manually from measurement to measurement). Automated maps were not possible due to the complex geometry of the tool. Raman measurements were performed around the ball nose from the axis point to the depth of cut in ~200 micron steps (shown in Figures 5.31 (a) and (b) (below)).

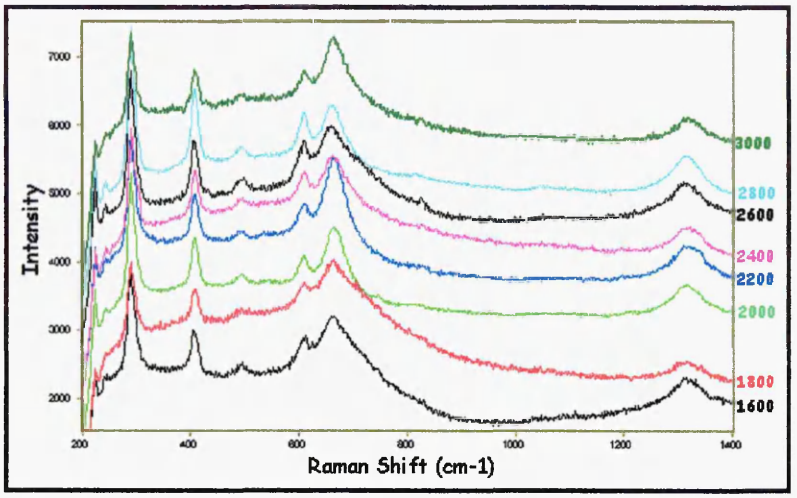

(a)

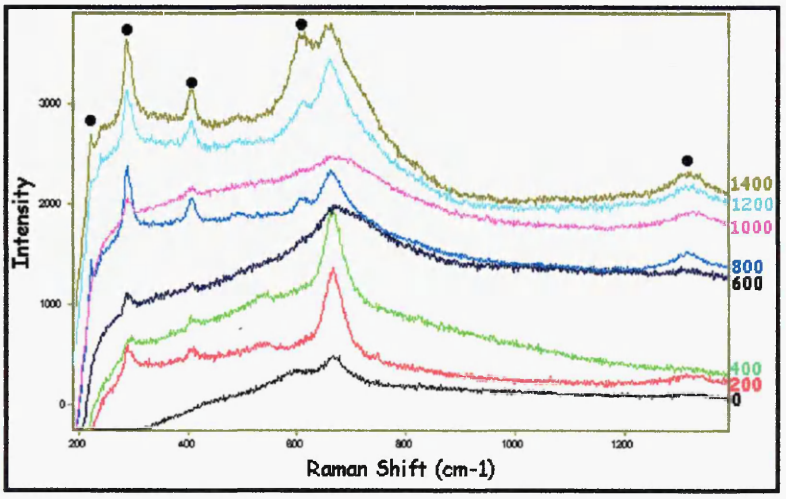

(b)

Figure 5.31 Observation of an increase in cutting temperature round the ball nose
(a) 0 –1600μm indicated on the right-hand- side y-axis (bands that are growing in are indicated) and (b) 1800-3000 μm

The phase transition of the Fe_3O_4/FeO to Fe_2O_3 (marked on Figure 5.31) indicated that the maximum cutting temperature increased as one goes round the ball nose and that (T_{max}) was indeed in and around the crater region. The consequence of this finding is that T_{max} must move round toward the axis point of the tool as steady state wear occurs and begins to resemble the case of the uncoated tool wear which showed wear virtually all the way round the ball nose (see figure 5.19(a)). This probably

occurs due to a large proportion of the coating being worn/removed in the cutting region.

5.8 Further Raman Analysis of Worn Tools From Cutting Tests

Monitoring of wear of a Supercote-02 coating was performed cutting into P20 case hardened steel (approximate elemental analysis $C_{(0.32)}$ $Mn_{(0.82)}$ $Cr_{(1.60)}$ $Mo_{(0.40)}$ (Rc Rockwell (hardness) ~55))[25].

The cutting conditions were:

	9947 rpm	**19894 rpm**
Surface speed M/min:	250	500
Depth of cut (mm):	2.5	2.5
Radial cut (mm):	0.1	0.1
Feed per Tooth:	0.06	0.11
Feed rate:	1193	4376

The graphs of wear land width (mm) VS time-in-cut (min.) (see Figure 5.32 (below) were compiled by measurement of the wear land size at intervals of 5 minutes by use of an optical imaging system. The graphs show three distinct regions.

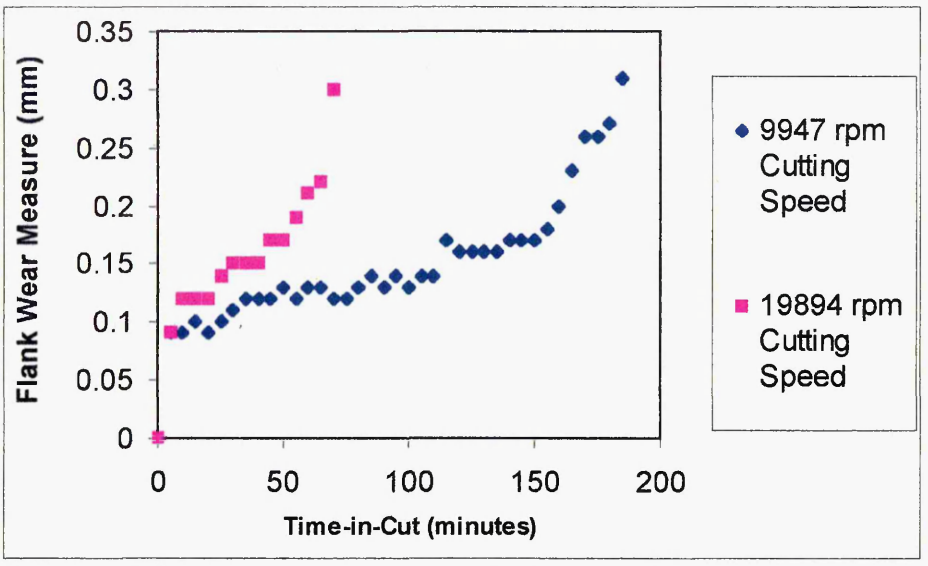

Figure 5.32 Graph of flank wear land width (mm) VS time in cut (min.) for Supercote-02 at two cutting speeds

1) Initial rapid wearing in of the tool (removal of asperities to define the cutting surface) to approximately 0.09mm.
2) Steady state wear (gradual wearing of the tool until a defined wear land size)
3) Rapid wearing of the tool until a wear land width of 0.3mm when the tool has been deemed to be at the end of its life (Hydra tools criteria). The wear land reaches a certain size that triggers rapid deterioration.

It can be seen that the tool used at the higher speed (19894rpm) as expected reaches the 0.3mm failure criteria first. This maybe explained by the higher cutting stresses and temperatures imposed onto the cutting surface. The tool used at 9947 rpm could cut for 185 minutes, over twice the lifetime achieved at the higher speed. Raman analysis of the higher cutting speed tool was performed to represent the worse case wear scenario. Raman spectra of the rake face at specific times-in-cut representative of the specific wear regime/stage (detailed above) were performed. This was

performed to ascertain whether species indicative of the extent of wear at each stage of the wear regime could be correlated.

Raman Parameters: x20 (ULWD) lens, 200seconds acquisition time and 100%Laser Power. Optical micrograph of the rake face showing wear after 5minutes in cut (19,894 RPM)

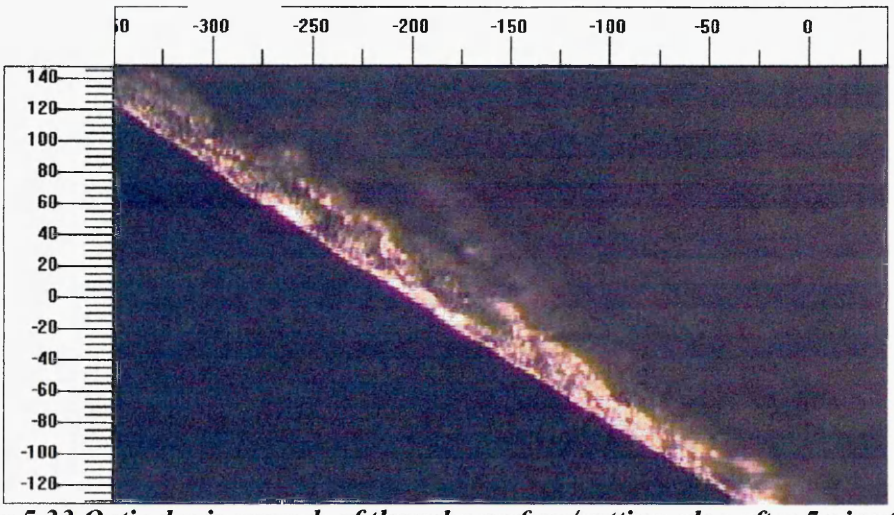

Figure 5.33 Optical micrograph of the rake surface/cutting edge after 5minutes-in-cut cutting at high speed

The Raman spectra from the worn surface observed as the shinny area in the above optical micrograph were taken and are shown in Figure 5.34 (below).

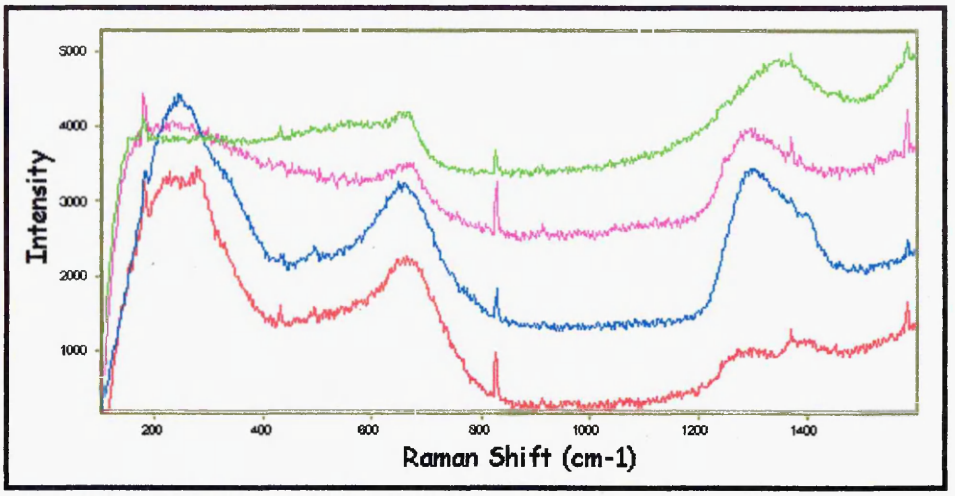

Figure 5.34 Rake wear spectra after 5 minutes-in-cut (19894 rpm) (measurements taken on the shiny area, i.e. wear zone, on the optical micrograph above)

The broad bands at ~ 1300cm^{-1} are indicative of α -Al_2O_3. The observation of this oxide, albeit semi-crystalline, indicated that high cutting temperatures had been reached. The initial wear measurements performed on Supercote-02 (discussed earlier in the chapter), (15000 rpm), also 'picked up' the presence of this oxide but only in localised positions on the surface. Although the analysis positions were different for the two sets of measurements, it was still reasonable to predict that higher temperatures occurred on the tool cutting at 19,894 rpm, as one might expect. In addition, the spectra resembled that of the superlattice layer, i.e. TiAlN/CrN (see Figure 5.8). It was not until ~12 minutes wearing, from the initial measurements, that the superlattice layer was detected. This indicated that an accelerated wear mechanism, i.e. the wear had progressed further into the coating structure, induced by the higher cutting temperatures. In addition the sharp low intensity bands observed at ~180, 290, 425, 820 cm^{-1} (assigned to the carbides within the WC- Co tool material, see Figure 5.42)) could be from the diffusion of carbides owing to high temperatures. The diffusion may have taken place through the columnar grains or cracks within the

coating possibly due to impacts or thermal cycling. The same approximate area of the rake surface was sampled after 35 minutes in cut (Figure 5.35 (Below)).

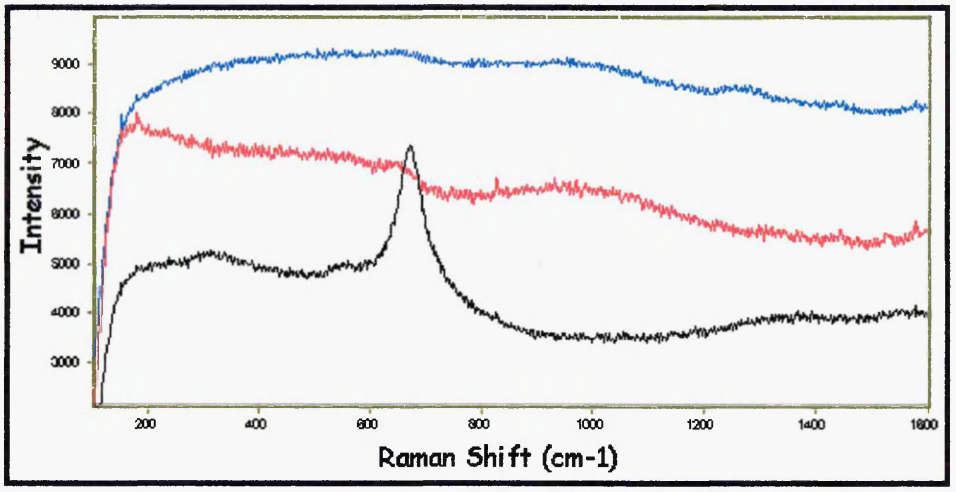

Figure 5.35 Rake wear spectra after 35minutes-in-cut (various positiosn on the cutting edge)(19894rpm)

No coating bands were observed after 35minutes and spectral features that closely resembled that of cemented carbide were observed (although without the sharp low intensity bands sometimes observed which have been attributed to the carbides within WC-Co (see figure 5.42). Magnetite spectral bands at ~320, 540 and 670 cm^{-1}, were also observed at a position on the worn surface (black spectrum above). The assignment of magnetite was possible due to the small band observed at ~320 and ~540 cm^{-1} which are not observed for FeO (wustite). This iron oxide transfer layer may therefore only occur when the coating has been removed, as it was not observed after 5 minutes of wear, where it has been ascertained that the TiAlN/CrN layer was reached. When the coating has been removed the friction coefficient increases (previously observed from pin-on-disk sliding wear experiments) and the temperature in this worn region must be greater, due to this increase in friction. The worn surface after 70 minutes of wear is shown below in the optical micrograph (figure 5.36). A deep crater region was observed where the wear had removed quite large amounts of

the WC - Co base material. It also featured a shinny surface area with what appeared to be a coating layer still present. Raman measurements were then performed within and around this wear land to determine what species were present (Figure 5.37).

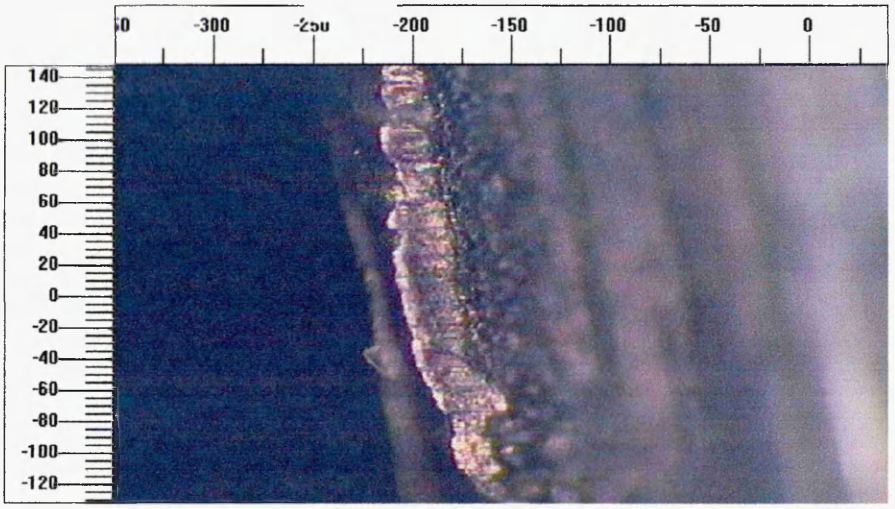

Figure 5.36 Optic micrograph of the wear land after 70minutes of wear (19894rpm)

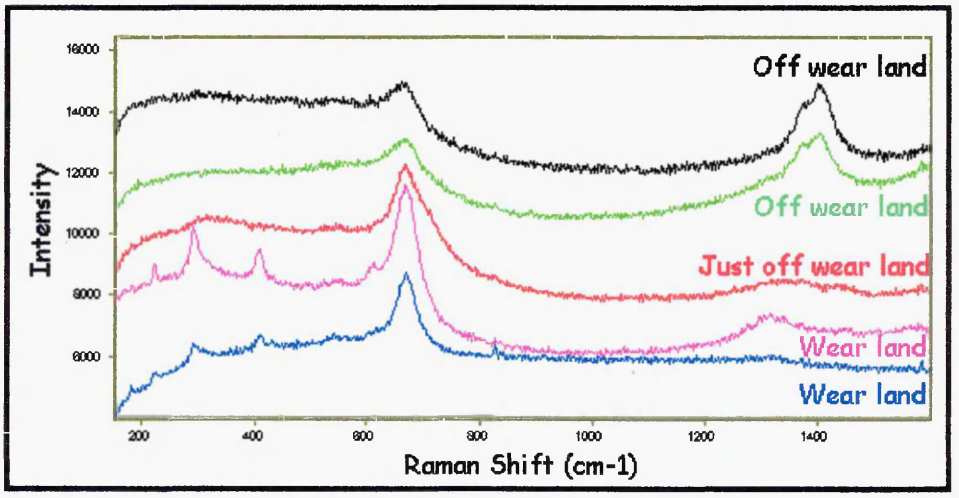

Figure 5.37 Rake wear spectra after 70 minutes-in-cut (19894rpm) (spectra taken within and along side the wear land seen in the above optical micrograph)

The spectra taken within the wear land featured iron oxide bands, namely magnetite (670, 320 and 532 cm^{-1}) and hematite (225, 293, 410, and the two magnon scattering at ~1300cm^{-1}). The observation of hematite bands within this worn surface signals

that higher temperatures were occurring at the wear site. This has caused a magnetite to hematite phase transformation to be initiated. The spectra taken around the edge of this wear land showed spectral features indicative of wustite (FeO) and magnetite (Fe_3O_4) but also bands from Al_2O_3 that indicated low crystallinity. Table 5.2 (below) gives the band positions for species detected on the surface of worn tools and from swarf analysis compared to literature values (where possible). Swarf analysis is discussed in the following section.

Species/Oxide	**Band Positions (cm^{-1}) (Frequency range 100-1600cm^{-1} w, m, s indicate the intensity bands i.e. weak, medium and strong)**			
Wustite	----------	----------	~670(m)	----------
Literature[24]	----------	----------	670(m)	----------
Magnetite	~305(w)	~530(w)	~670(m)	----------
Literature[24]	302(w),	533(w)	663(s)	----------
Hematite	~290	~407	~540	~1300
Literature[24]	227(s), 246(w), 293(s)	410(m) 497(w)	612(m)	1320(m)
Al_2O_3	----------	----------	----------	1200 – 1400(w)
Literature[23]	----------	----------	622(w), 856(m),	1000(w), 1153(w) 1356(s), 1400(s)
D-band (carbon)	----------	----------	----------	~1340(m)
Literature[5,27,28]	----------	----------	----------	1300 – 1400(m)
Anatase (TiO_2)(swarf)	144(s)	395(w)	520(w), 640(w)	----------
Literature[26]	147 (s), 198(w)	398(w/m)	515(w/m), 640(m)	----------
Unknown species	279(m)	----------	----------	----------

5.9 Swarf Analysis

The swarf or chips of removed workpiece material are known to take some of the temperature of cutting process away with them. This swarf gathered on top of the workpiece and can be easily collected. These are usually discarded but may contain information about the cutting temperature and even the wear mechanism. The swarf particles were found to have a well-defined shape (see the schematic representation Figure 5.38 below).

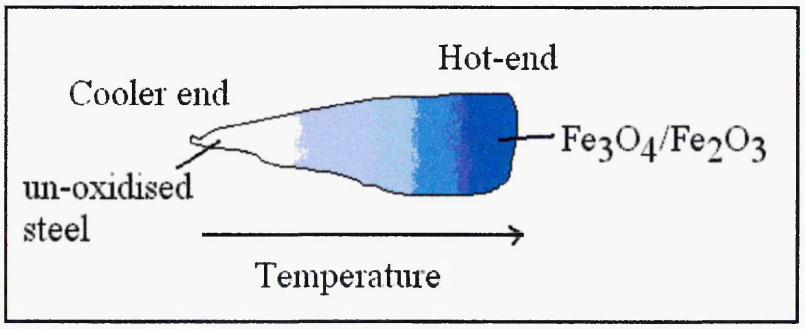

Figure 5.38 Schematic representation of the swarf from cutting processes (blue colouration to demonstrate the amount of oxide present on the surface as seen on real swarf/chip particles)

Observation of the swarf under an optical microscope showed that a hot end existed (blue colouration) where the tool mechanically engaged the workpiece material and a cooler end where it was sheared to form the chip. Raman analysis of swarf will enable the characterisation of surface oxide layers and hence give information of the cutting temperature. Figure 5.39 shows Raman spectra acquired from the hot end of a chip of swarf after 5, 35 and 70 minutes-in-cut (19894rpm).

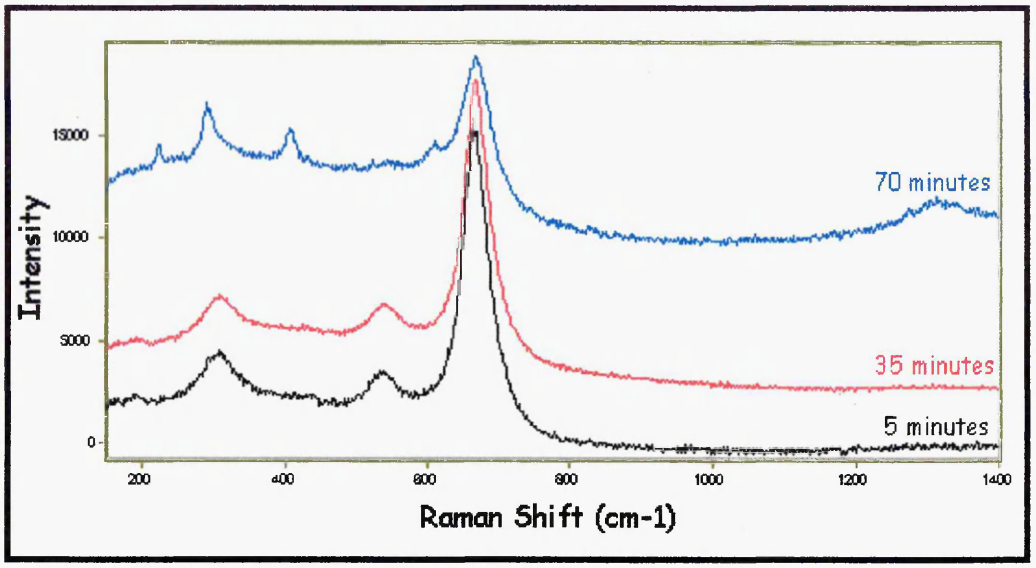

Figure 5.38 Swarf analysis: collected from a Supercote-02 coated tool cutting at 19847 rpm

The swarf analysis demonstrated that the cutting temperature increased as the tool became more worn as a magnetite to hematite phase transformation occurs for the 70 minute swarf (as previously observed on the surface of worn tools, Figure 5.30 (a and b). The 70-minute mark signalled the end of the useful life for the Supercote-02, i.e. 0.3mm of flank wear. *This observation of a phase transformation of the oxide layer present on the swarf/chip surface may negate the need to actually sample the tool to gain a handle of the extent of wear.* The observation of hematite bands on the surface of the swarf could be a signal for the end of the useful life of a cutting mill. Further evidence of tool degradation at 70 minutes-of-wear was the observation of coating element oxides on the surface of the swarf i.e TiO_2 (anatase).

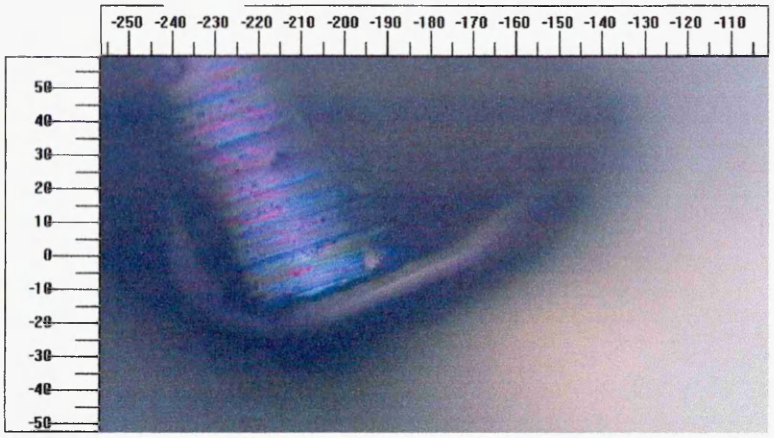

Figure 5.40 Shows a swarf/chip particles with a small white area (seen in the middle of the image) after 70 minutes.0

The Raman analysis of this particle is shown below (Figure 5.41) with comparison to other swarf spectra.

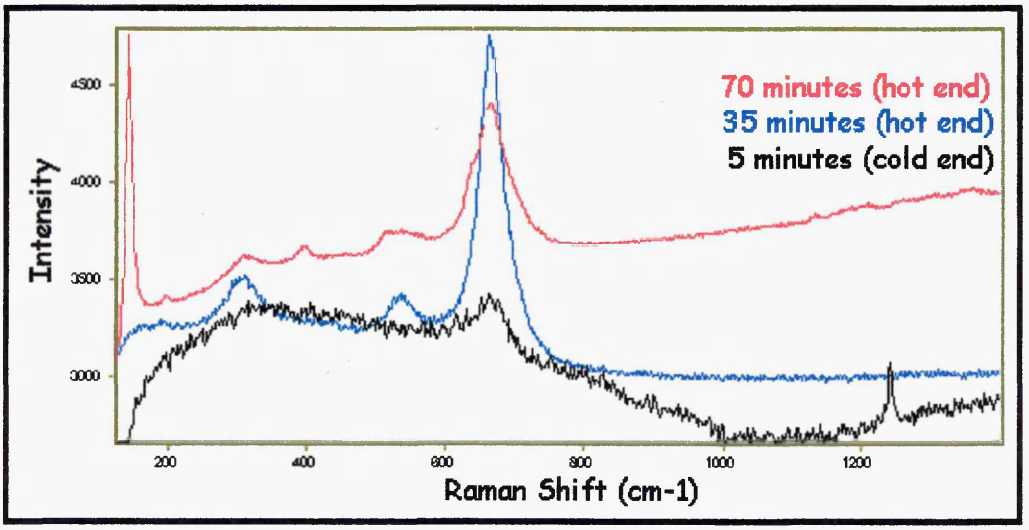

Figure 5.41 Further swarf analysis indicating coating oxidation

The analysis of the swarf particle at the cooler end (that is the shear point) demonstrates this temperature gradient occurs across the chip particles. An iron oxide peak centred at 670cm^{-1} (see Table 5.2) was observed but was low intensity signalling that only a very thin oxide layer had built up and the oxide identification was wustite, the lowest temperature iron oxide phase. The 35 minute swarf spectrum (at the hot

end) shows bands typical of magnetite and the Raman spectrum of the particle observed on the surface of the swarf showed bands typical of anatase TiO_2 which are well known[26]. Anatase is the low temperature form of TiO_2, which is metastable and is known to transform to rutile at temperatures between 600 and 1000°C. The high cutting temperatures can explain the detection of the oxidised coating particle on the swarf. At the instant the coated tool comes into contact with the work-piece material the coating is oxidising due to high contact pressures and friction, similar in nature to pin-on-disk sliding but much more extreme. The oxides that form on the surface of the coating then stick to the chips. This correlates well with the theory, detailed in section 5.6 (see Figure 5.12), of a "sticky zone" existing on the surface of the tool during cutting. This was probably the main reason why titanium oxides were not detected on the surface of worn tools.

5. 10 Chemometrics – Qualitative Analysis (Ref [27])

The use of chemometrics in this project was not to perform an in-depth study, but rather as a tool for coating and oxide discrimination. The model developed in this section could be integrated into the software associated with the remote wear monitoring instrument (the longer-term aim). The qualitative model would be able to give a "pass/fail" notification from the input of spectra from the worn tools and essentially indicate when a tool requires changing.

Qualitative chemometric analysis uses spectral information to:

(a) Confirm sample identity

(b) Distinguish between "good" and "bad" samples i.e. detecting coating layers and Al_2O_3, are good samples. Conversely, the detection of cemented carbide, (possibly FeO, Fe_3O_4) and Fe_2O_3 (in addition to detecting very little i.e. when the cemented carbide base material has been reached) are essentially "bad" samples and signal the end for the tool.

(c) Detect spectral differences (band positions, intensities, widths etc.)

(d) Detect sameness of spectra

5.10.1 Qualitative or Quantitative Analysis?

Qualitative methods are much easier logistically to set up and generally have much greater chance of success than quantitative. Whenever given a choice of solving a problem with a qualitative or quantitative analysis, the former is almost always the best approach.

5.10.1.1 Types of Qualitative Analyses

Identification – confirmation of the chemical identity of a raw material or, in some cases, a finished product. Example of models of this nature are, the detection of the density of PET poly(ethylene terephthalate)[31] and reaction monitoring of the hydrolysis of ethyl acetate[32]. Determination of change – an analysis that shows the change in a material over time, Examples include:

i) Reaction end-point determination

ii) Analysis of material degradation

iii) Mixing or blending information

iv) Physical changes over time, (for example, wear)

v) Moisture absorption or desorption

Distinction of nearly-like samples – an analysis that distinguishes materials that have very similar spectra. In general, this means that the user wants to distinguish similar but slightly different formulations/compositions.

5.10.1.2 Qualitative Analysis Methods

Non-Principle Component techniques:

1 Spectral matching (similarity match)

2 Distance matching

"Principal Component Analysis (PCA) Techniques
(Determines which parameters vary)".

The rise in popularity of chemometrics is closely associated with the improvements in microprocessor performance that has taken place over the last decade. One of the best-known chemometrics techniques is PCA. This was first proposed as early as 1901, and developed independently some years later, but for practical reasons was not widely used until the arrival of modern computing technology. PCA is a

mathematical procedure for resolving sets of data into orthogonal components whose linear combinations approximate the original data to any desired degree of accuracy. As successive components are calculated, each component accounts for the maximum possible amount of residual variance in the set of data. Types are:

1 Mahalanobis distance (disciminant analysis)

2 SIMCA (discriminant analysis with unique distribution)

PCA allows scrutiny of the data through a reduction technique that emphasises layers of variation. PCA works by allowing the first factor (or PC) to define the greatest amount of variation in the spectra. Each factor thereafter represents further residual variation until all (or a given proportion of) the variation is described. PCA is a good method to use for data exploration. It rearranges information in such a way that patterns may be revealed which, although present, were obscured in the original data.

5.10.1.3 Mahalanobis Distance (Discriminant Analysis)

The Mahalanobis distance technique uses the results of the PCA to calculate a distribution in PC space for the spectra in the library. The test spectra are then analysed to determine if they fall within this defined distribution. Its good for the distinction of unlike materials with moderate size training sets. A reasonable population is needed to generate representative PCs. Proper pre-treatments are generally important in using this technique. The removal of cosmic rays and spurious bands should be performed before generation of the model. But it is also good for the distinction of materials with moderately significant to very significant differences.

Many people like this means of modelling for routine use for identification purposes. This method is adopted for the wear model described below.

5.10.2 Windas (Windows Discriminant Analysis Software, Ref. [28])

Data Compression:

Data compression is required when the number of variates, d, is very large, and exceeds the number of observations, n. In such data sets the variates will usually be inter-correlated to some extent. In other words, the correlation between any pair of variates is likely to be non-zero. If the observations in the data set are all quite similar, as is often the case for certain types of spectroscopic data, then these correlations can be quite high. The main goal of data compression is to transform a data set comprising a large number of inter-correlated variables into a new set of variates of much more manageable size. The transformed variates are known as scores and ordered such that the first few contain most information (i.e. variance) that was spread across all of the original variates.

5.10.3 Development of a Discriminant Analysis Chemometrics Model for Wear Determination

Spectra of the Supercote-02 coating components were acquired by ball cratering and then acquiring a Raman spectrum (as for model coating systems discussed earlier). Seven Raman spectra from each of the component layers were acquired.

Five of the seven spectra were then used to create a discriminant analysis model (squared Mahalanobis distance). The remaining two spectra from each of the component layers were used to 'test' the model. The differentiation of coating layers was important as it can result in information, albeit limited, on the progression of wear i.e. how much coating material was removed. In addition to the coating layers, oxides have been built into the model (see Figure 5.42 (below)).

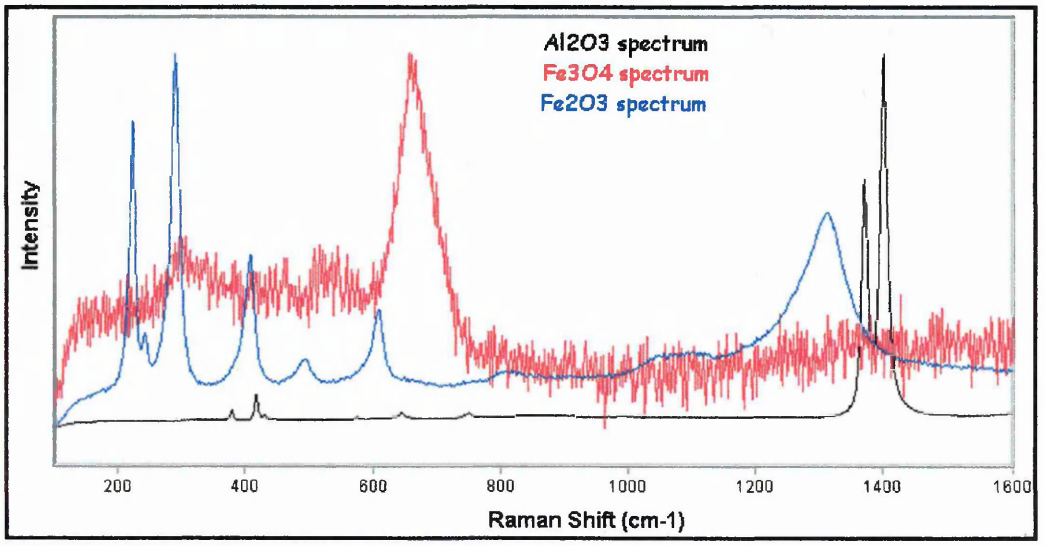

Figure 5.42 Typical oxide spectra from standard powders used in model

For example, Al_2O_3 on the surface provides information that the coating is still present; as the wear induced oxidation of the coating has occurred, but it does not give information on the extent of wear as Al is present in all coating layers. Transfer layers from the workpiece material, detected on the surface of worn tools give information indirectly on the extent of wear. The observation of FeO/Fe_3O_4 and more importantly Fe_2O_3 give an indication of the temperature during cutting. The phase transformation from FeO/Fe_3O_4 to Fe_2O_3 has been linked to coating removal indicated by an increase in cutting temperature due to the increased friction it causes. The Fe_3O_4 spectra were all low intensity with a poor signal-to-noise ratio because the

setting) the powder was seen to change to a red colour and Fe_2O_3 peaks observed in the spectrum, indicating the phase transformation had taken place. To combat this the laser was defocused using the beam expander and software to a size of ~200 μm (as described in chapter 2). This reduction in power density at the sample was sufficient to stop this transformation occurring. A laser power of 50% was therefore possible but even after an acquisition time of 500 seconds the spectra were of poor quality. An oxidised steel surface, having only the Fe_3O_4 phase present, would be a better method of obtaining standard spectra for the model.

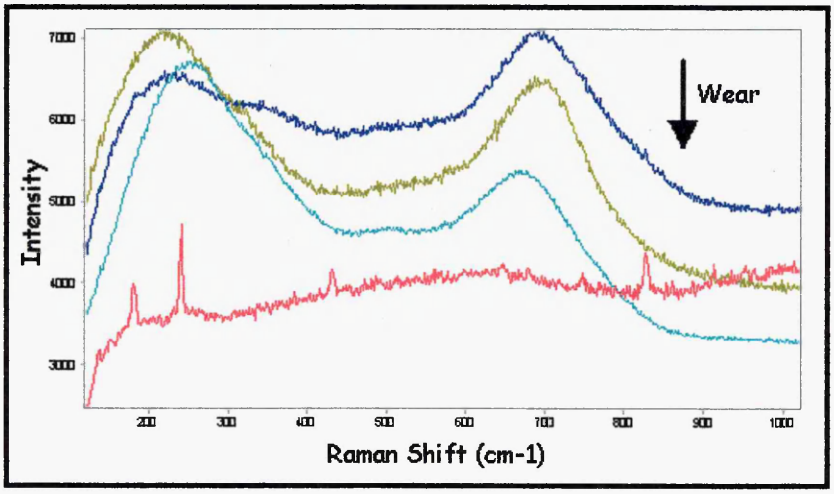

Figure 5.43 Coating component layers (highlighting similarities)

The coating spectra have only subtle differences, (see Figure 5.43 (above)). The uppermost spectrum in Figure 5.43 is of the oxynitride top layer, then the superlattice portion, the main bulk of the coating TiAlCrN and the base layer which feature sharp peaks which have been determined as plasma-lines from the HeNe laser. The similarities in the Raman spectra necessitate a technique to distinguish between these layers quickly, easily and reliably.

5.10.3.1 The PCA (Squared Mahalonobis Distance) Chemometrics Model

Firstly, the spectra were exported into the Windas software from Grams 32, as J-CAMP files i.e. *.dx. These were then separated into the seven groups. The groups are shown below (Table 5.3 (below)). The groups were: 1 (cemented carbide), 2 (TiAlCrN), 3 (TiAlN/CrN superlattice), 4 (oxynitride top coat), 5 (Al_2O_3), 6 (Fe_2O_3) and 7 (Fe_3O_4).

Group 1	Group 2	Group 3	Group 4	Group 5	Group 6	Group 7
bottom1.dx	Tialcr~1.dx	super-1.dx	top-1.dx	al2o3-1.dx	fe2o3-1.dx	fe3o4-1.dx
bottom2.dx	Tialcr~2.dx	super-2.dx	top-2.dx	al2o3-2.dx	fe2o3-2.dx	fe3o4-2.dx
bottom-3.dx	Tialcr~3.dx	super-3.dx	top-3.dx	al2o3-3.dx	fe2o3-3.dx	fe3o4-3.dx
bottom-4.dx	Tialcr~4.d	super-4.dx	top-4.dx	al2o3-4.dx	fe2o3-4.dx	fe3o4-4.dx
bottom-5.dx	Tialcr~5.dx	super-5.dx	top-5.dx	al2o3-5.dx	fe2o3-5.dx	fe3o4-5.dx

The data were compressed using the PCA (covariance method). The results of this, in PC space, for the seven groups are shown in Figure 5.44 (below).

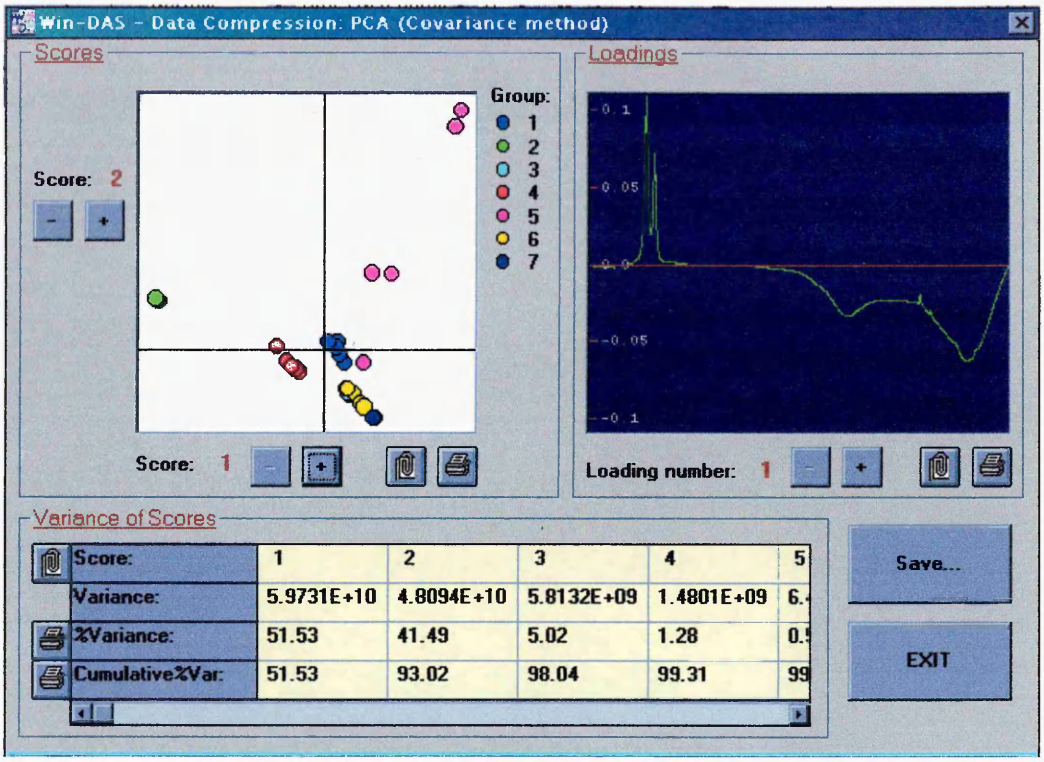

Figure 5.44 Data compression (PCA Covariance method) showing scores and loadings)

It may be seen that the majority of variance, 51.53%, was described within the first PC and 99.87% in five PCs. Therefore when the discriminant analysis model was created using Squared Mahalanobis Distance, 5 PC scores, were used i.e. to prevent "over fitting" of the data. The results of the linear discriminant analysis, with 5 PC scores, using the covariance method (squared Mahalanobis Distance) are given below (Table 5.4). It may be seen that 34 out of 35 were predicted correctly. The incorrect assignment was a Fe_2O_3 spectrum being mistaken for Fe_3O_4. Group 5 (Al_2O_3) was seen to have the most variance i.e. scatter. Groups 3 and 6 were very close together in PC space and overlapping slightly. Loading 1 was shown (on the right of Figure 5.44 (above)). This shows the areas where there was the most variance in the spectra for Principal Component 1.

Table 5.4 (below) shows the results i.e. distances of each observation/spectrum from each group and the predicted groups.

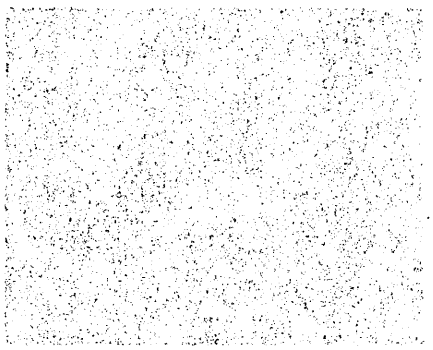

	Observa[n]:	Distance from group 1	Distance from group 2	Distance from group 3	Distance from group 4	Distance from group 5	Distance from group 6	Distance from group 7	Predicted group	
1	Bottom1.dx	6.2333E+00	6.2654E+03	1.5224E+02	9.2676E+02	4.0704E+01	1.3331E+02	1.2998E+02	1	Correct
2	Bottom2.dx	9.9914E-01	6.3755E+03	1.8569E+02	9.7772E+02	5.5947E+01	1.6324E+02	1.6640E+02	1	Correct
3	Bottom3.dx	1.2968E+01	7.0197E+03	3.2874E+02	1.2532E+03	1.3446E+02	2.8145E+02	2.9147E+02	1	Correct
4	Bottom4.dx	6.4616E-01	6.5864E+03	2.3610E+02	1.0677E+03	8.1510E+01	2.0872E+02	2.1416E+02	1	Correct
5	Bottom5.dx	4.9344E+00	6.1608E+03	1.8371E+02	9.0761E+02	5.8304E+01	1.8132E+02	1.8855E+02	1	Correct
6	Tialcr~1.dx	6.3817E+03	3.6668E-01	4.6333E+03	2.3564E+03	5.4830E+03	5.3075E+03	5.2984E+03	2	Correct
7	Tialcr~2.dx	6.5724E+03	3.6601E-01	4.7988E+03	2.4742E+03	5.6615E+03	5.4839E+03	5.4757E+03	2	Correct
8	Tialcr~3.dx	6.4777E+03	7.7857E-04	4.7162E+03	2.4156E+03	5.5727E+03	5.3955E+03	5.3872E+03	2	Correct
9	Tialcr~4.dx	6.4164E+03	1.4077E-01	4.6643E+03	2.3782E+03	5.5159E+03	5.3406E+03	5.3320E+03	2	Correct
10	Tialcr~5.dx	6.5349E+03	1.3916E-01	4.7662E+03	2.4514E+03	5.6264E+03	5.4482E+03	5.4407E+03	2	Correct
11	Super-1.dx	2.1267E+02	4.7100E+03	2.0685E-03	3.9848E+02	6.4539E+01	5.8622E+01	3.1740E+01	3	Correct
12	Super-2.dx	2.0805E+02	4.7482E+03	6.6189E-02	4.1027E+02	6.2218E+01	5.5053E+01	2.8578E+01	3	Correct
13	Super-3.dx	2.1107E+02	4.7161E+03	3.0957E-03	4.0002E+02	6.3741E+01	5.8453E+01	3.1544E+01	3	Correct
14	Super-4.dx	2.0895E+02	4.7291E+03	1.3844E-02	4.0363E+02	6.2638E+01	5.7862E+01	3.0704E+01	3	Correct
15	Super-5.dx	2.2015E+02	4.6745E+03	9.4301E-02	3.8854E+02	6.8296E+01	6.1153E+01	3.3792E+01	3	Correct
16	Top-1.dx	9.2615E+02	2.5940E+03	3.2582E+02	4.8008E+00	5.8607E+02	5.8042E+02	5.3231E+02	4	Correct
17	Top-2.dx	1.0264E+03	2.3850E+03	4.4343E+02	8.1333E+00	6.9777E+02	7.4023E+02	6.9664E+02	4	Correct
18	Top-3.dx	1.1064E+03	2.2862E+03	4.5501E+02	1.7926E+00	7.4205E+02	7.4638E+02	6.9857E+02	4	Correct
19	Top-4.dx	9.8885E+02	2.4826E+03	3.6830E+02	1.2973E+00	6.3902E+02	6.3537E+02	5.8709E+02	4	Correct
20	Top-5.dx	1.0765E+03	2.3441E+03	4.2531E+02	1.0825E+00	7.1159E+02	7.0722E+02	6.5809E+02	4	Correct
21	al2o3-1.dx	1.0023E+02	5.5786E+03	8.4826E+01	6.9111E+02	6.9508E+00	1.0670E+02	8.6300E+01	5	Correct
22	al2o3-2.dx	9.7391E+01	5.6396E+03	9.6481E+01	7.1540E+02	8.8527E+00	1.1633E+02	9.6724E+01	5	Correct
23	al2o3-3.dx	6.7012E+01	5.3433E+03	6.0719E+01	5.9300E+02	8.7041E+00	1.0969E+02	9.1814E+01	5	Correct
24	al2o3-4.dx	5.3013E+01	5.6908E+03	6.8535E+01	7.0896E+02	1.8899E+00	8.3551E+01	6.4573E+01	5	Correct
25	al2o3-5.dx	6.5833E+01	5.6444E+03	4.9024E+01	6.8925E+02	1.1934E+01	5.8495E+01	3.7369E+01	5	Correct
26	fe2o3-1.dx	1.5409E+02	5.4646E+03	5.1603E+01	6.8452E+02	6.6151E+01	1.9352E+00	2.5177E+01	6	Correct
27	fe2o3-2.dx	1.9674E+02	5.3465E+03	4.5410E+01	6.5105E+02	8.2839E+01	2.1674E+00	1.7158E+01	6	Correct
28	fe2o3-3.dx	1.7280E+02	5.4010E+03	3.3987E+01	6.4553E+02	6.2563E+01	1.0752E+01	5.2689E+00	7	Incorrect
29	fe2o3-4.dx	2.2362E+02	5.3950E+03	9.5088E+01	7.2037E+02	1.2723E+02	7.5578E+00	6.7563E+01	6	Correct
30	fe2o3-5.dx	2.2459E+02	5.3973E+03	9.4451E+01	7.2062E+02	1.2722E+02	7.1636E+00	6.6157E+01	6	Correct
31	fe3o4-1.dx	1.9207E+02	5.3972E+03	3.1939E+01	6.3472E+02	6.7585E+01	3.0313E+01	5.2841E-03	7	Correct
32	fe3o4-2.dx	1.9313E+02	5.3898E+03	3.1554E+01	6.3239E+02	6.7926E+01	3.0328E+01	8.4616E-04	7	Correct
33	fe3o4-3.dx	1.9237E+02	5.3798E+03	3.0525E+01	6.2841E+02	6.7079E+01	3.0319E+01	4.3725E-03	7	Correct
34	fe3o4-4.dx	1.9380E+02	5.3846E+03	3.1255E+01	6.3065E+02	6.8101E+01	3.0448E+01	9.3231E-04	7	Correct
35	fe3o4-5.dx	1.9342E+02	5.3815E+03	3.0916E+01	6.2944E+02	6.7772E+01	3.0352E+01	1.1935E-03	7	Correct

Table 5.4 Training group predictions for the training set using 5 pc scores with the PCA covariance method (Squared Mahalanobis Distance).

The model was then applied to the two remaining "test" spectra from each coating layer and oxide (14 spectra in all), shown below Figure 5.45 (below).

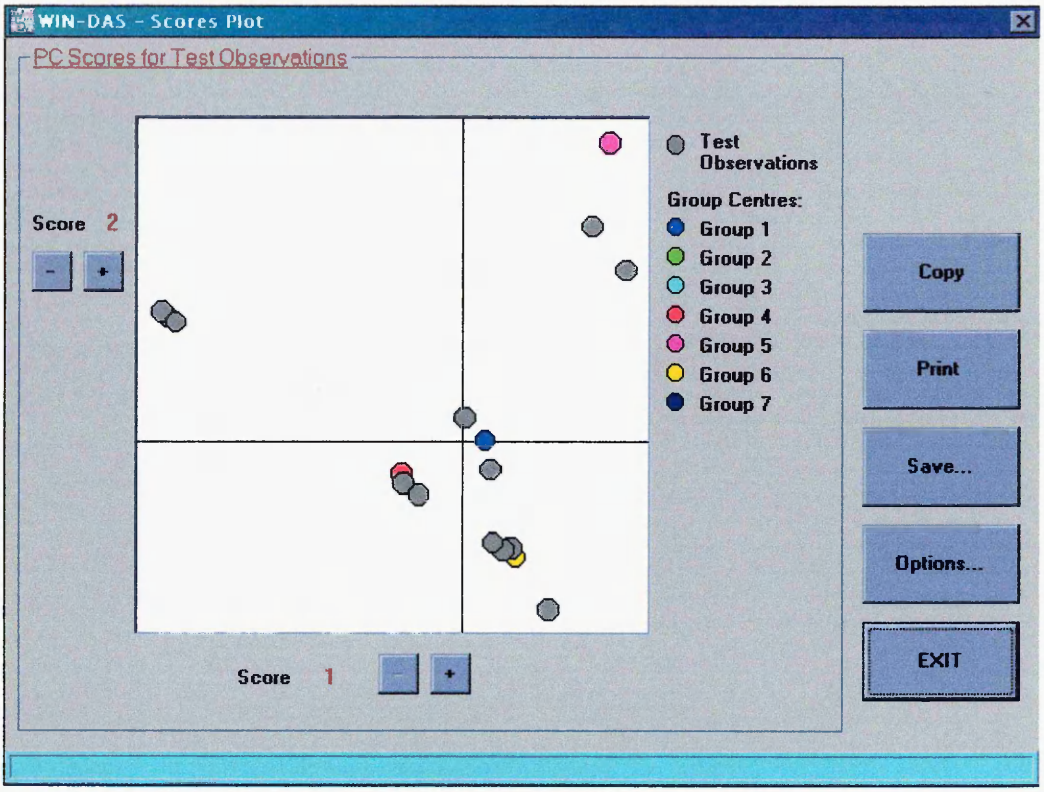

Figure 5.45 PC Scores for the test spectra

Table 5.5 (below) gives the Test group predictions from the training set using 5 pc scores with the PCA covariance method (Squared Mahalanobis Distance). It may be seen that all the spectra were correctly assigned.

Test Set Observation Number	Observation:	Distance from group 1	Distance from group 2	Distance from group 3	Distance from group 4	Distance from group 5	Distance from group 6	Distance from group 7	Predicted Group
1	al2o3-6.dx	1.1546E+02	5.6813E+03	5.3304E+01	7.1795E+02	1.9887E+01	4.5903E+01	2.1851E+01	5
2	al2o3-7.dx	5.6184E+01	5.7115E+03	6.9605E+01	7.1749E+02	1.6302E+00	8.1281E+01	6.2397E+01	5
3	bottom-6.dx	7.4152E+00	6.1243E+03	1.8749E+02	8.9493E+02	6.1388E+01	1.9502E+02	1.9852E+02	1
4	bottom-7.dx	1.1964E+01	6.0318E+03	1.2343E+02	8.3917E+02	2.9440E+01	1.1854E+02	1.1485E+02	1
5	fe2o3-6.dx	1.9973E+02	5.3677E+03	6.7980E+01	6.8287E+02	9.9357E+01	1.0711E+00	4.2450E+01	6
6	fe2o3-7.dx	1.8253E+02	5.4188E+03	6.3978E+01	6.9041E+02	8.8146E+01	4.2772E-01	3.6978E+01	6
7	fe3o4-6.dx	1.9277E+02	5.3753E+03	3.0231E+01	6.2686E+02	6.7127E+01	3.0401E+01	8.2933E-03	7
8	fe3o4-7.dx	1.9374E+02	5.3755E+03	3.0475E+01	6.2731E+02	6.7712E+01	3.0406E+01	5.8147E-03	7
9	super-6.dx	2.2092E+02	4.6618E+03	1.5997E-01	3.8435E+02	6.8748E+01	6.2832E+01	3.5262E+01	3
10	super-7.dx	2.7181E+02	4.3904E+03	5.8097E+00	3.1082E+02	9.7587E+01	8.6373E+01	5.9729E+01	3
11	Tialcr~6.dx	6.6408E+03	1.1380E+00	4.8597E+03	2.5166E+03	5.7262E+03	5.5507E+03	5.5418E+03	2
12	Tialcr~7.dx	6.2244E+03	2.5330E+00	4.4995E+03	2.2616E+03	5.3373E+03	5.1644E+03	5.1557E+03	2
13	top-6.dx	1.0932E+03	2.3199E+03	4.3486E+02	1.6456E+00	7.2479E+02	7.1815E+02	6.6931E+02	4
14	top-7.dx	9.2268E+02	2.5990E+03	3.2437E+02	4.8440E+00	5.8361E+02	5.7897E+02	5.3077E+02	4

It appears that a basic qualitative model capable of discriminating between the component layers of Supercote-02, and for oxides anticipated on the surface of worn tools, was possible. However, there are many discrepancies between the spectra used in the chemometrics model and real sample spectra (i.e. from worn tools). Six spectra acquired from real worn tools were put into the model (see Table 5.6 below). These spectra (unknowns) were chosen to further test the model, i.e. had more than one constituent featured in the spectrum (two cases) and interfering peaks (one case).

Table 5.6 Details of the real wear sample spectra (unknowns) from cutting tests that will be used to test the PCA chemometrics model

OBSERVATIONS	SAMPLE DETAILS	SPECTRAL DESCRIPTION	PREDICTED GROUP FROM VISUAL INSPECTION
tialcr1.dx	5 minutes-in-cut, 19K rpm on wear land	Superlattice or TiAlCrN layer appearance with contribution from semi-crystalline Al_2O_3	TiAlCrYN or Superlattice (Group 2 or 3)
fe3o4-8.dx	Swarf spectrum from engagement region after 5 minutes-in-cut	Three clear Fe_3O_4 peaks no other interfering bands.	Fe_3O_4 (Group 7)
fe3o4-9.dx	35 minute-in-cut, 19K rpm on wear land	Clear Fe_3O_4 peaks, with a broad low intensity hump between 250-400cm^{-1}	Fe_3O_4 (Group 7)
top-8.dx	35 minute-in-cut, 19K rpm spectrum taken away from the worn region	Spectrum indicative of the oxynitride uppermost layer, no other interfering peaks	Top (oxynitride) (Group 4)
al2o3-8.dx	Swarf spectrum, 19K rpm (engagement region)	Both Fe_3O_4 and fully crystalline Al_2O_3 peaks are observed. However the Al_2O_3 component had the greater contribution	Al_2O_3 (Group 5 or 7)
bottom-8.dx	185minutes, 9K rpm on wear land	Spectral features similar to WC- CO base material were observed	Bottom (WC – Co) (Group 1)

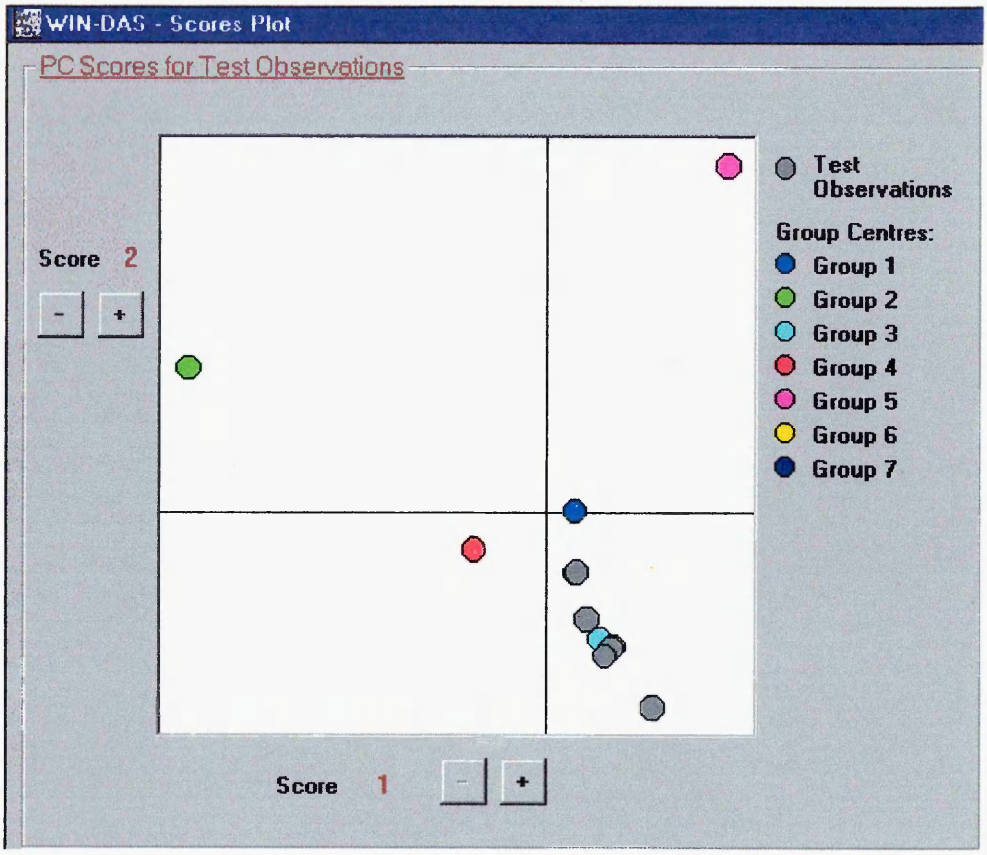

Figure 5.46 PC Scores for the wear spectra (unknowns)

Table 5.7 Test group predictions for the real wear data obtained from cutting tests using 5 pc scores with the PCA covariance method (Squared Mahalanobis Distance).

Test Set Observ^{n} Number	Observation:	Distance from group 1	Distance from group 2	Distance from group 3	Distance from group 4	Distance from group 5	Distance from group 6	Distance from group 7	Predicted Group
1	al2o3-8.dx	9.4730E+02	9.9854E+03	3.5727E+02	2.0412E+02	1.5104E+02	2.2134E+02	1.5471E+02	5
2	bottom-8.dx	2.5841E+02	9.8011E+03	9.6260E+01	6.9168E+02	9.8102E+01	8.9770E+01	9.1885E+01	6
3	fe3o4-8.dx	5.7217E+02	1.0589E+04	1.9645E+02	6.4130E+02	8.0418E+01	3.6126E+01	1.2395E-01	7
4	fe3o4-9.dx	6.2628E+02	1.0177E+04	2.1203E+02	4.0185E+02	5.7659E+01	8.6870E+01	4.6943E+01	7
5	tialcr~1.dx	3.4345E+02	9.1046E+03	3.3579E+01	6.0584E+02	1.7933E+02	6.1264E+01	6.7816E+01	3
6	top-8.dx	6.7597E+02	1.0079E+04	2.0758E+02	3.8896E+02	8.3047E+01	7.9822E+01	3.6331E+01	7

Table 5.8 Performance/rigidity of the Chemometrics PCA model for wear analysis

OBSERVATION	VISUAL PREDICTION (TABLE 5.6)	ACTUAL PREDICTION FROM THE PCA MODEL
al2o3-8.dx	Al_2O_3 **(Group 5 or 7)**	Group 5 (correct)
bottom-8.dx	Bottom (WC – Co) **(Group 1)**	Group 6 (incorrect)
fe3o4-8.dx	Fe_3O_4 **(Group 7)**	Group 7 (correct)
fe3o4-9.dx	Fe_3O_4 **(Group 7)**	Group 7 (correct)
tialcr~1.dx	TiAlCrYN or Superlattice **(Group 2 or 3)**	Group 3 (correct)
top-8.dx	Top (oxynitride) **(Group 4)**	Group 7 (incorrect)

The model appeared to perform well and was able to predict four out of the six unknown/test spectra. In the case of the spectra which featured two of the groups/constituent spectra, i.e. a coating layer and an oxide or two oxides (Fe_3O_4 and Al_2O_3), the model gave a prediction based on the component/group that had the greater contribution to the spectrum. The main problems with this model for wear prediction were:

i) The oxide spectra were acquired from standard powders. Therefore, the spectra, which were incorporated into the model, were fully crystalline forms. Oxides, which have been detected on the surface of the tools, were not fully crystalline (see Table 5.2).

ii) Spectra featuring two observations, for example, oxides and a coating layer or two different oxides will cause the model difficulties in predicting the spectra.

iii) In addition, further groups could possibly be added to the model to increase the rigidity. For example, a mixed oxide phase of Fe_3O_4 / Fe_2O_3 (see Figure 5.30). This could be achieved by acquiring spectra from Fe_3O_4 standard powder using a laser power sufficient enough to cause a phase transformation, similar to that observed by De Faria et al[24] for magnetite irradiated with 7mW laser power.

These are potential problems that will affect the ruggedness of the model in "real situations" for the monitoring of wear on cutting tools. However the preliminary PCA model has shown promising results.

References

1 B. Malliet, J.P. Celis, J.R. Roos, L.M Stals and M.Van Stappen, Wear, 142 (1991) 151-170.

2 S. Wilson and A.T. Alpas, Surf. Coat. Technol. 108-109 (1998) 369-376.

3 E. Vancoille, B. Blainpain, Ye. Xingpu, J.-P. Celis and J.R. Roos, Journal of Materials Research 9(4), (1994) 992.

4 S. Wilson and A.T. Alpas, Surf. Coat. Technol., 86-87 (1996) 75-81.

5 C.P. Constable, J. Yarwood, P. Hovsepian, L.A. Donohue, D.B. Lewis and W.-D Münz, J. Vac. Sci. Technol. A 18(4) (2000) 1681-1688.

6 B. Blainpain, M. Franck, H. Mohrbacher, E. Vancoille, J.-P. Celis and J.R. Roos, in Thin Films in Tribology: Micro-Raman spectroscopy for the characterisation of wear induced surface modifications on hard coatings, D. Dowson et al, (ed.) Elsevier, Amsterdam, 1993, p 623.

7 E. de Wit, L. Froyen and J.P. Celis, Wear 221 (1998) 125-133.

8 K. Schouterden, B. Blainpain, J.P. Celis and O. Vingsbo, Wear 181-183, (1995) 86.

9 A. Erdemir, C. Bindal, J. Pagan and P. Wilbur, Surf. Coat. Technol. 76-77 (1995) 559-563.

10 Y. Liu, A. Erdemir and E.I. Meletis, Surf. Coat. Technol.82 (1996) 48-56.

11 M. Franck, B. Blanpain, J.P. Celis and J.R. Roos, J. Vac. Sci. Technol. B 12(2) (1994) 981-985.

12 O. Wanstrand, R. Fella and N. Axen, Surf. Coat. Technol. 94-95 (1997) 469-475.

13 C-Jen Lu, D.B. Bogy, S.S. Rosenblum and G.J. Tessmer, Thin Solid Films 268(1995) 83-90.

14 E. Pfluger, A. Schroer, P. Voumard, L.A. Donohue and W.-D. Münz, Surf. Coat. Technol. 115 (1999) 17-23.

15 L.A. Donohue, I.J. Smith, W.-D. Münz, I. Petrov and J.E. Greene, Surf. Coat. Technol. 94-95 (1997) 226-231.

16 D.B. Lewis, L.A. Donohue, W.-D Münz, R. Kuzel, V. Valvoda, and C.J. Blomfield, Surf. Coat. Technol. 114 (1999) 187-199.

17 J.P. Celis, Surf. Coat. Technol. 74-75 (1995) 15-22.

18 http://www.renishaw.co.uk/spectroscopy/info/news/9712055.html

19 ASM Handbook, Vol. 18 "Friction, Lubrication, and Wear Technology" L. Alden Kendall "Friction and Wear of Cutting Tools and Cutting Tool Materials", ASM International, New York, 1992 p 609-620.

20 B.M. Kramer and N.P. Suh, Tool Wear by Solution: A quantitative understanding, J. Eng. Ind. (Trans. ASME), Vol 102, 1980, p303.

21 S.C. Lim and M.F. Ashby, Overview No. 55, Wear-Mechanism Maps, Acta Metall., Vol 35(No. 1), 1987, p 1-24.

22 Carrs special steel, Sheffield, England. P.553 data sheet on EN 24 steel

23 A. Aminzadeth, Applied Spectrosc., 51(6) (1997) 817-819.

24 D.L.A. de Faria, S. Venancio and M.T. de Oliveira, J. Raman Spectros. 28 (1997) 873-878.

25 Carrs special steel, Sheffield, England. P. 20 pre-hardened mould steel data sheet

26 U. Balachandran and N.G. Eror, Solid State chem. 42 (1982) 276.

27 A.Cuesta, P. Dhamalincourt, J. Laureyns, A. Martinez-Alonso, and J.M.D. Tascon, Carbon 32 (1994) 1523.

28 A.Cuesta, P. Dhamalincourt, J. Laureyns, A. Martinez-Alonso, and J.M.D. Tascon, J. Mater. Chem 8 (1998) 2875.

29 Presentation Notes "Getting the Most From Your Spectra – A Practicle Guide to Chemometrics", Simon Nunn, Nicolet Instrument Corporation, June 2000.

30 K. Kelmsley, WINDAS™, Wiley Scientific, London/New York, 1998.

31 H.Swierenga, A.P. de Weijer, R.J. van Wijk and L.M.C. Buydens, Chemom. Intel. Lab. Sys., 49 (1999) 1-17.

32 O. Svensson, M. Josefson, F.W. Langkilde, Chemom. Intel. Lab. Sys., 49 (1999) 49-66.

Chapter 6

High Temperature Characteristics of PVD Coatings

Chapter 6 High Temperature Characteristics of PVD Coatings

This chapter is predominantly concerned with studies of the oxidation resistance of PVD hard coatings using Raman microscopy as a tool for identifying the oxide scales that form on their surfaces. In addition, the study of wear debris formed as a consequence of sliding wear tests has been included in this chapter, owing to the fact that contact temperatures during sliding have been found to be sufficiently high to promote tribo-oxidation reactions (and thus oxide products) within the debris formed. The use of Raman microscopy can then be used to identify these products within the debris. Furthermore, a comparison of the oxide types within the debris to those formed on the surface of the same coating statically oxidised, facilitates a contact temperature, during sliding, to be estimated.

6.1 Thermal Stability of PVD Coatings

PVD hard coatings are predominantly used in conditions where high temperatures are encountered e.g. cutting operations. High temperatures are especially apparent in dry high speed machining processes when the temperature in the cutting zone is dependent on the workpiece material, linear speed, cutting speed and depth of cut. These type of cutting processes are known to induce oxidation of the coating which modifies their wear resistance and friction properties[1,2,3]. Some coatings that are deposited using PVD are only metastable and can transform at high temperatures. For example, TiAlN, which is a thermodynamically metastable system, transforms to TiN and AlN. Although TiAlN is metastable, films can be annealed to 900°C before phase conversion occurs. In fact McIntyre[4] found that precipitation of the AlN phase in

$Ti_{0.5}Al_{0.5}N$ films, determined by XRD, required 1.5 h of annealing at 900°C. Exposure to high temperatures induced microstructural modifications which resulted in non-reversible changes in mechanical properties and a well known reduction in hardness[2]. Heau et al[2] found that when CrN was treated at high temperature the coherently diffracting domains(CDD), i.e. the grain size became larger, according to the Scherrer formula. At room temperature the CrN coatings show crystalline phases that corresponded to both CrN and Cr_2N. They also found that the same effect occurred for TiN above 750K. The CDD also increased above 1200K indicating a high level of metastability. The influence of temperature on mechanical properties was also studied. The coating samples were heated under a vacuum for 2h. A scratch test was then performed which showed cohesive failure, indicating good adhesion. For CrN and Cr_2N the critical load was even found to increase with annealing temperature up to 1100K. For TiN the critical load was constant up to 900K then decreased markedly. The Vicker's microhardness test showed that the hardness of Cr_2N was constant up to 700K then it increased up to 900K and decreased back to the original value after 900K. The CrN and TiN showed decreases in microhardness above 1200K.

6.1.1 Compressive Stress Relaxation

Compressive residual stresses in nitride films can be controlled in deposition through the energetic particle bombardment (controlled by bias voltage) during film growth (see chapter 1). For magnetron sputtering, the energetic particles generated from the sputtering gas are back-scattered inert gas neutrals or ions of Ar or the reactive gas (i.e., Ar^+ and N_2^+) accelerated by negative substrate bias potentials towards the

growing film. It is assumed that the defects responsible for the residual stresses also act as obstacles for dislocation movement and thereby increase the hardness[5]. Oettle et al[6] observed a decrease in compressive residual stresses in arc-evaporated TiN and TiAlN films after annealing. Herr et al[7] has reported a decrease of the apparent hardness of TiN from 36 to 27Gpa when the compressive stress decreased from –6.7 to –2.1 Gpa upon annealing for 1h at 650°C. Stress relaxation was accompanied by a decrease in XRD peak width due to reduced inhomogeneous strain. Oettel also found that nitrogen interstitials annealed out in magnetron-sputtered TiN and TiAlN films at temperatures below 600°C[6]. Compressive stresses and stress relaxation measurements will also be discussed in chapter 7.

6.1.2 Oxidation

The oxidation of TiN has long been established as being a mechanism to the formation of rutile TiO_2 with spallation of the oxide layer due to the difference in molar volume[5,8]. $Ti_{1-x}Al_xN$, however, is a more complicated system and has been found to give a passive double layer. This occurs by outward diffusion of Al to form Al-rich oxide at the uppermost surface and inward diffusion of O_2 to form Ti-rich oxide at the interface to TiAlN[4,5]. Münz et al[9], studied the effects of adding alloying elements such as Y and Cr to TiAlN for the purpose of enhancing the oxidation resistance and interdiffusion of substrate elements such as Fe in steel, which was found to be "pipe" diffusion by Kim et al[8]. The onset of rapid oxidation, as determined from thermo-gravimetric measurements, ranged from ~600°C for TiN to 870°C for $Ti_{0.46}Al_{0.54}N$ to 920°C for $Ti_{0.44}Al_{0.53}Cr_{0.03}N$ to 950°C for $Ti_{0.43}Al_{0.52}Cr_{0.03}Y_{0.02}N$[10]. The presence of excess Y and YO_x at the grain

boundaries via a thermodynamically driven diffusion process played a decisive role in reducing bulk diffusion rates for both cation and O_2 diffusion. Hovsepian et al[11] showed that CrN/NbN superlattice coatings deposited by UBM method oxidised in air for 168h at 700°C formed an ~0.8μm thick oxide(s) layer. Combined thermogravimetric, XRD, TEM, EDX, and GDOES (Glow Discharge Optical Emission Spectroscopy) showed the formation of a double layer consisting of a porous $CrNbO_4$ top layer and a dense Cr_2O_3 underlayer. The superlattice structure was retained at these temperatures. Monolithic NbN undergoes rapid oxidation at relatively low-temperature ranging between 500-550°C[11].

6.2 Introduction and Methods Adopted for Determination of Oxidation Resistance of PVD Hard Coatings.

Many analytical techniques are utilised for the determination of oxidation resistance, a key property that describes how a particular coating will react to the harsh conditions of metal cutting, especially dry high-speed cutting. Some of the typical methods are described below:

TGA (Thermo Gravimetric Analysis): The weight-gain is plotted against a function of treatment temperature. A high accuracy weighing device is utilised to measure the weight gain, caused by the formation of oxides on the coating surface, over a specific temperature regime. The heating regime may be isothermal whereby the coating is subjected to a particular temperature for a prolonged length of time, or a ramped regime whereby the temperature is gradually raised with a specific ramp rate

(i.e. °C/min). This technique is especially good at showing the onset of rapid oxidation (see Figure 1.6). However, this method does suffer some shortcomings, the main one being that the weight gain from the oxidation of the substrate is superimposed on the weight gain from the coating. To reduce this effect, stainless steel substrates with high oxidation resistance are used. Graham and Hussey[12] describe the common methods utilised in high temperature studies of metals. These may also be utilised for metallic-like-materials such as PVD coatings. These techniques include cross sectional TEM and SEM to determine the microstructure. Various types of information may be gleaned from the aforementioned techniques. These include, elemental distribution maps (i.e. chemical maps), high resolution imaging of the oxide on the surface (SEM) and high resolution imaging using TEM (combined with X-ray analysis). The latter may be used to ascertain whether layered oxide systems occur; for example to determine that TiAlN gives a passive double layer[4,5]. Other analytical techniques utilised in high temperature corrosion studies are AES (Auger Electron Spectroscopy) allowing elemental analysis, depth profiles and imaging with a surface depth of 1-2 nm and a spatial resolution of >25 nm, SIMS (Secondary Ion Mass Spectrometry) facilitating elemental trace analysis and depth profiling with a surface depth of <1 nm (destructive to samples) and XPS (X-ray Photoelectron Spectroscopy) giving chemical bonding information with a surface depth of 1-2 nm but a poor spatial resolution of >50 μm. Many of the aforementioned techniques are combined to gain complementary information to enable full elucidation of oxide growth mechanisms on an atomic scale, interfacial segregation phenomena, and the role of reactive elements in modifying transport processes in oxides[12].

Raman microscopy is also utilised[13-20] as a technique for high temperature corrosion studies and will be discussed predominantly in this chapter. The ability of Raman microscopy to identify metal oxides and give crystal structure information, probe down to 1μm spot size and be non-destructive, with no sample preparation or vacuum restraints make it an ideal technique for studying oxidation behaviour of metals and PVD coating systems.

6.2.1 Raman Microscopy's Role in Oxidation/High Temperature Studies of Materials

Raman microscopy is a very useful tool for identification of oxide products due to the chemical bonding and structural information that it offers[13]. Raman has in the past been used for the study of iron and carbon/weathering steel corrosion [14,15,16]. These studies were performed in order to elucidate rusting mechanisms via the identification of the products on the surface of the steels[17]. Hematite, magnetite, wüstite, maghemite, goethite and lepidocrocite have all been identified on the surface of these type steels in various aqueous environments. In addition Raman microscopy has been used for the study of high temperature air corrosion products on the surface of iron chromium alloys with varying amounts of Cr[18,19]. These studies were performed to aid in the understanding of the corrosion behaviour of stainless steels especially their binary iron-chromium model counterparts. Both studies were concerned with the identification and spatial distribution of oxides as a function of temperature and alloy composition. Automated Raman mapping of the corrosion products on iron-chromium alloys has been performed[20]. This allowed the

distribution of the oxides to be monitored via a microscopic chemical mapping process.

Although Raman microscopy has played an active role in the study of high temperature and environmental corrosion of various steels, it has had a limited role to date in the analysis of PVD coatings and similar materials. There are, however, a small number of studies to be found in the literature. These include the microstructural examination of solar beam irradiated TiN hard coatings[21], in order to investigate the possibility of the formation of a lubricious oxygen-deficient rutile that could operate at higher temperatures than the conventional solid lubricants MoS_2 and crystalline graphite. The expected improvement in wear properties of sub-stoichiometric rutile on top of TiN films was due to their behaviour as a low shear strength lubricant, reducing friction in unlubricated sliding. The ~2 μm oxide layer on top of the TiN was grey in appearance, and was identified by Raman microscopy as rutile TiO_2 which had non-uniform porosity over the oxide film thickness. A further study of the same TiN system heat treated in air at 400, 600 and 800°C found that at 400°C anatase TiO_2 formed on the surface; at 600°C a mixture of anatase-rutile formed and at 800°C a full conversion to rutile had occurred. The as-formed oxide was found to be nearly stoichiometric, by analysis of the oxygen sensitive shift of the rutile E_g band[22]. Begun and Bamberger[23] studied laser-induced oxidation of transition metal borides, carbides and nitrides which were in powder and whisker form. The formation of surface oxides, which were induced by laser heating, was dependent on the particle size and the power density applied. This study was performed to investigate the possibility of laser-induced transformation of oxides that may lead to misleading or inaccurate results. Witke et al[24,25] believe that the sensitivity of some materials to laser-induced transformation can actually lead to

better deduction of structural information and can even lead to the identification of amorphous phases by transformation of spectra that can be evaluated more easily.

6.2.2 Previous Raman Microscopic Analysis of Wear and Wear Debris

To date the use of Raman microscopic analysis in the field of ceramic hard coatings has been confined to the study of the particles of tribo-chemically produced wear debris that gather at the edges of the wear zone as a result of mechanical engagement of two or more bodies[26-28,29-32]. This has included the study of wear[26,27]; for example, the study of solar beam oxidised TiN against Al_2O_3 (corundum) in fretting tests. It has been reported that slightly oxygen deficient rutile (TiO_{2-x}) is formed which can behave like a low shear strength, lubricious oxide[28]. Micro-Raman spectroscopy[28] was used to analyse wear-induced modifications of the oxidised TiN surface. They observed that the coefficient of friction for the oxidised TiN coating against a corundum ball during a test of 50,000 fretting cycles rapidly increased until a maximum value was reached at 5000 cycles. At this point an abrupt drop occurred. The sheer stresses caused by the high frictional forces acting on the contacting bodies were so high that the interface strength was exceeded in the central zone, resulting in a failure of the titanium oxide/TiN interface. A thick third layer was formed which originated from the local detachment of the oxide layer from the TiN coating and entrapment of the debris in between the contacting bodies. This third zone causes fluctuations of the friction force after 30,000 cycles. The spectrum of the original surface oxide layer on the TiN coating showed typical features of rutile and the characteristic phonon bands at 448, and 611 cm^{-1} closely match other values reported for single crystal rutile[29]. Raman spectra were taken from the peripheral contact

zone, from the wear debris scattered in and outside the contact area and the layer covering the central zone. They found no distinctive change in the Raman spectrum from the peripheral contact zone compared with that in the original state. They found the Raman spectra of the powder-like debris also exhibited rutile features. But peak broadening together with peak shifts to 444 and 600cm^{-1} occurred. Further peak shifting to 440 and 592cm^{-1} were found on the Raman spectrum of the layer covering the central contact zone. The peak shift of the 447 cm^{-1} band could be linked to the oxygen deficiency of the rutile compound. Significantly broader bands were reported in the case of an amorphous TiO_2 phase that generally exhibited a spectrum similar to that of rutile. The structure-related sensitivity of the line shapes and positions of the rutile spectrum may provide a better understanding of the role of titanium oxides.

Much work has been done trying to understand the wear mechanisms of TiN under various operating conditions, especially sliding against corundum at different speeds[26,30]. In studying wear processes, tribologists have realised that the wear debris bears the signature of the wear process. Other surface analytical techniques[31] have revealed that some material transfer always takes place between two sliding bodies, even when sliding at extremely low loads or speeds. This material can be a mixture of debris from either of the two bodies or a reaction product from the bodies with the environment[31]. Singer et al[32] studied the debris resulting from the sliding of TiN against a sapphire ball and found that tribo-oxidation of the TiN occurs and that the reaction product is exclusively rutile TiO_2.

Vancoille et al[30] studied the composition and structure of the wear debris from sliding against corundum at low, medium and high sliding speeds using Raman microscopy. White debris agglomerates of sub-micron sized particles were found to

gather along the sides of the wear track. Raman microscopic analysis of the as-formed debris from low to medium sliding speeds found three broad and weak peaks whereas the debris formed at the high sliding speed gave rise to only two broad peaks. When the characteristic peak features of rutile and anatase, (the two most prominent polymorphs of TiO_2) were compared to the as-formed spectra it was not evident that both or either of the polymorphs were present. When a high powered laser (150mW) was incident on the debris formed, clear anatase and rutile peaks developed for the debris created at low and medium sliding speeds, only rutile peaks were observed for the debris formed at high sliding speed[30]. TiO_2 can exist in three crystalline modifications, namely rutile, anatase (both tetragonal), and brookite (orthorhombic)[33,34]. Anatase has a metastable structure, which transforms to rutile at temperatures between 600 and 1000°C. Under annealing conditions the regions of crystalline ordering expand (grain growth process), rather than a true crystallisation of an amorphous structure[24].

6.2.3 Raman Microscopy of Oxide Standards and Oxide Systems

Possibly one of the most studied of all metal oxides is titanium dioxide. Ever since the first spectrum was collected by Narayanan[35], there has been much interest in titanium dioxide and its three common forms (anatase, rutile and brookite) whether it be in powder[33,36,37], films/coatings[34,38] and layers[39,40] because of the many technological applications in a variety of catalytic, electronic and magnetic devices. Other oxides such as Al_2O_3 have also received attention due to their wide-ranging applications, and the many phases have been identified and the Raman spectra acquired[41]; niobium oxides have also been reported to exist in different

polymorphic forms and that the phase transformations are strongly dependent on the heat treatment[42,43], and zirconium oxides having tetragonal and monoclinic structures have also been studied[44].

These studies have created a wealth of standard spectra available from the literature that can be applied to unrelated topics such as the high temperature oxidation of titanium, aluminium, niobium and zirconium containing PVD coatings (discussed in sections 6.4 and 6.5 of this chapter).

6.3 Why is it Important to Know the Oxidation Behaviour of PVD Hard Coatings?

PVD hard coatings are predominantly used as protective coatings for cutting tools. There is an increasing demand in the industry to move to dry cutting (i.e. without lubrication). This reduces costs, as the maintenance of these fluids is expensive (see chapter 5 section 5.6). In many cases these fluids also cause a health hazard. Dry cutting as expected, reaches high temperatures due to friction and cutting forces, which are not removed by the fluids. This puts increasing pressure on the coatings themselves to withstand these higher temperatures. The cutting speeds are also increasing and it is now commonplace to hear of cutting speeds ranging from 20,000 – 45,000 rpm being adopted. These lead to higher and higher temperatures being generated during cutting operations with which the coatings have to withstand. It is therefore essential to screen candidate coatings before they are used in these harsh environments.

High temperature performance and oxidation resistance are very important because oxidational mechanisms account for the major deterioration/wear mechanisms for these type of coatings (see chapter 5). The oxide types that occur on the surface are also important. Various oxides can be beneficial:

i) Al_2O_3 is a well-known thermal barrier and is also very hard. This helps to protect the underlying coating, and is thought to be the major reason for TiAlN's better tribological properties than TiN.

ii) Some oxides can be lubricious, i.e. act as intrinsic solid lubricants, and can enhance the dry running long-term performance of coatings. These substances must be stable in air up to high temperatures and guarantee a high wear resistance. Some examples are titanium dioxides, molybdenum trioxides, vanadium oxides and tungsten trioxides all of which have crystallographic slip ability similar to that of graphite.

iii) Oxides with a high volume expansion coefficient (e.g. rutileTiO_2) can be enormously detrimental/catastrophic to coatings. These can break apart coatings as they form and lead to accelerate deterioration. If there are diffusion pathways to the substrate (i.e. down voids or cracks), this can lead to substrate oxides forming beneath the coating and can also have the same effect. These include tungsten oxide(tungsten being the main component of cemented carbide) and iron oxides (on high speed steel).

6.4 Results from Oxidation and Wear Debris Analysis

To address the important interest in wear debris and associated wear mechanisms a series of PVD deposited hard coatings were investigated using Pin-on-Disk sliding against corundum. The debris generated were characterised using Raman microscopy to identify compounds especially oxides, generated during the wear process to gain a better understanding of tribochemical reactions. All generations of coatings were investigated i.e. Binary, multicomponent, multilayered and superlattice. Contact temperatures during sliding were estimated by comparison of the tribochemical products generated during sliding with the formation temperatures of oxides on the surface of heat treated coatings i.e. static oxidation.

6.4.1 Ti(C, N) Coating

Debris Analysis

This coating was a multilayered coating consisting of six layers, (Figure 6.1 coating architecture (below)), which include a 1.5μm base layer of TiN with alternating layers of TiCN (0.4 μm) and TiN (0.6 μm). The outermost layer was TiCN, and the total coating thickness was ~3.9 μm.

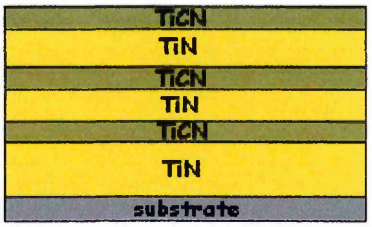

Figure 6.1 Ti(C, N) coating architecture

The as-formed debris spectrum showed bands associated with crystalline rutile TiO_2. Figure.6.2 shows the Raman spectra arising from the as-formed debris and Table 6.1 the Results of band fitting (50% Gaussian - 50% Lorentzian peak shapes).

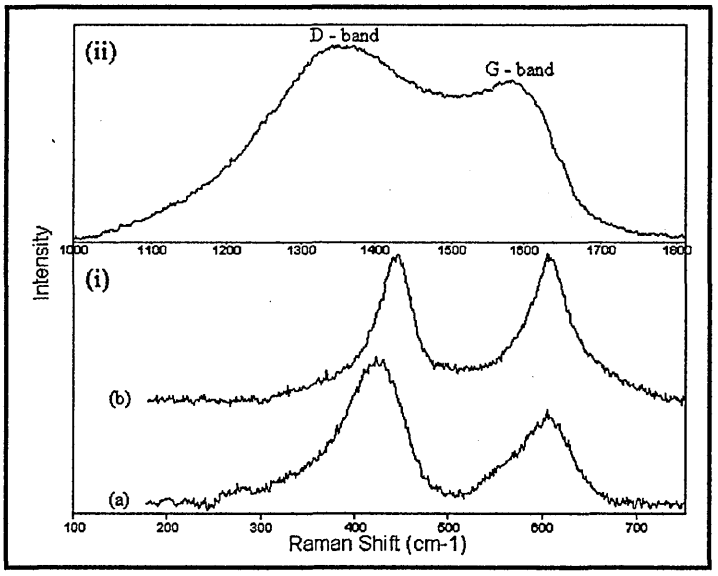

Figure 6.2 Spectra of debris (a) from the top TiCN layer (b) through additional lower layers of the Ti(C, N) coating (l.p: 0.25 mW).(ii) spectrum of amorphous carbon detected in the debris from top TiCN layer (l.p: 0.25 mW).

Table 6.1 *(Band positions determined from curve fitting using Galactic Industries Corporation Grams/32 package).*

	Peak 1			Peak 2		
As-formed debris	Position (cm^{-1})	FWHM (cm^{-1})	Area (%)	Position (cm^{-1})	FWHM (cm^{-1})	Area (%)
TiCN layer	426	60	57	602	59	43
Ti(C, N) layers	443	43	42	600	60	58

The rutile 426 cm^{-1} band resulting from the TiCN debris was broad (Figure 6.2(a) + Table 1) and shifted by 18 cm^{-1} to lower frequency from the value 444 cm^{-1} shown in Figure 6.3(f)). Parker and Siegel[29] have reported that the Raman E_g modes of both anatase and rutile are sensitive to oxygen deficiency. Therefore this shift may be an indicator for a slight deviation from stoichiometry of the rutile TiO_2 structure. A small shoulder near 512 cm^{-1} was also observed on the 602 cm^{-1} band. This could be

from anatase in the debris and may indicate that a slightly lower contact temperature (and therefore lower friction coefficient) occurred during sliding. The Raman spectrum also showed bands due to amorphous carbon D (defect) band at 1351 cm^{-1} and the G (graphite) band at 1599 cm^{-1} (Figure 6.2 (c)), which may act as a solid lubricant. The Raman spectrum of carbon is well known [46, 47] and the value of $I_{(D)}/I_{(total)}$ can give a measure of the amount of disorder[47]. The $I_{(D)}/I_{(total)}$ value obtained for the carbon detected within the debris was 71%, indicating a highly disordered structure similar to that of micro-crystalline carbon[47]. The Raman spectrum from the debris deeper into the coating structure incorporating TiN layers (Figure 6.2 (b)) was in good agreement with the rutile standard spectrum (Figure 6.3 (f)).

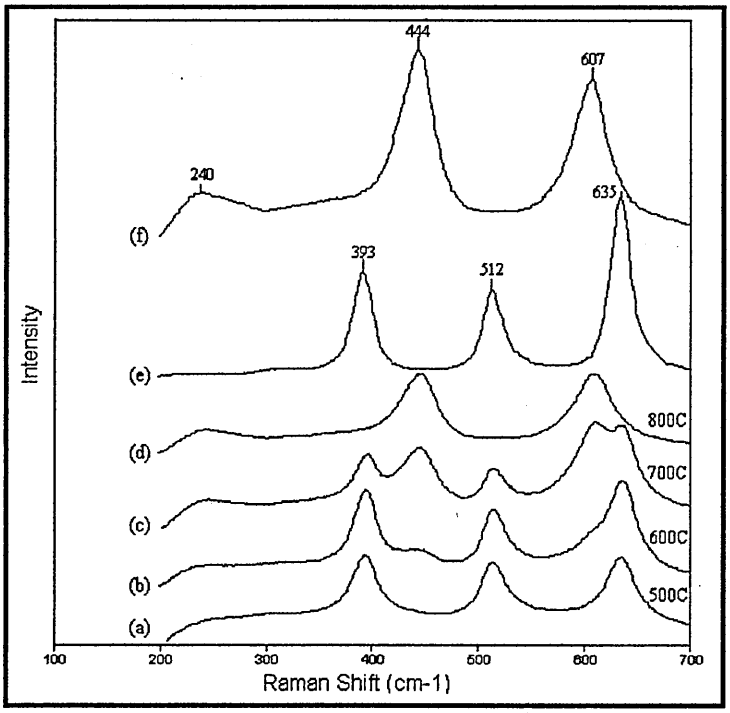

Figure 6.3 Spectra of the Ti(C, N) coating heat treated in a furnace (in air) (a) 500°C 1 hour (b) 600°C 1 hour (c) 700°C 1 hour (d) 800°C 1 hour (lp: 25 mW) and spectra of standard TiO_2 powders (e) anatase (f) rutile (lp: 0.25 mW).

Static Oxidation

Successive oxidation was performed at 500, 600, 700 and 800°C for 1 hour. The furnace heat treatment of the Ti(C, N) multilayered coating showed TiO_2 oxides to be present on the surface (Figure 6.3). The phonon modes of anatase and rutile phases are well known[33]. At 500°C, the oxide identified on the surface was anatase, which has a metastable structure, transforming to rutile between 600 and 1000°C. Upon subsequent increase in temperature an expected anatase - rutile phase transformation occurred. At 700°C there was approximately 50% anatase and 50% rutile present on the surface. The 800°C spectrum indicated that full conversion to rutile had occurred. Unlike the case of the debris analysis, almost no amorphous carbon was detected on the surface of the heat treated Ti(C, N) coating.

Although tribochemical reactions are non-equilibrium reactions it was interesting to correlate wear debris measurements with the static oxidation of the Ti(C, N) coating to enable an approximate value for the contact temperature during sliding to be postulated. Debris from both the top TiCN layer and from debris generated from deeper into the Ti(C, N) coating consisted of predominantly rutile TiO_2. The static oxidation of the Ti(C, N) coating determined that, at temperatures in excess of 700°C, rutile TiO_2 became the principal phase. Therefore contact temperatures >700°C may occur at the tribo-contact for the Al_2O_3 - TiCN / Ti(C, N) systems, under the test conditions used.

6.4.2 CrN Coating

Debris Analysis

Although the as-formed debris spectrum was weak (Figure 6.4(a)), Cr_2O_3 bands were clearly observed at 305, 546, and 606 cm^{-1} (see Figure 6.5(d)).

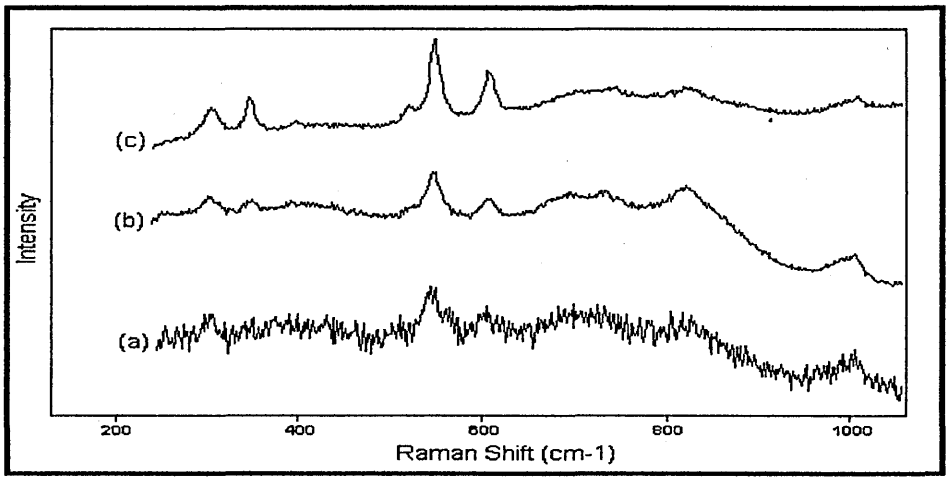

Figure 6.4 Spectra of debris produced on a CrN coating (a) as-formed debris: 0.25 mW (b) 5 mW (c) 12.5 mW.

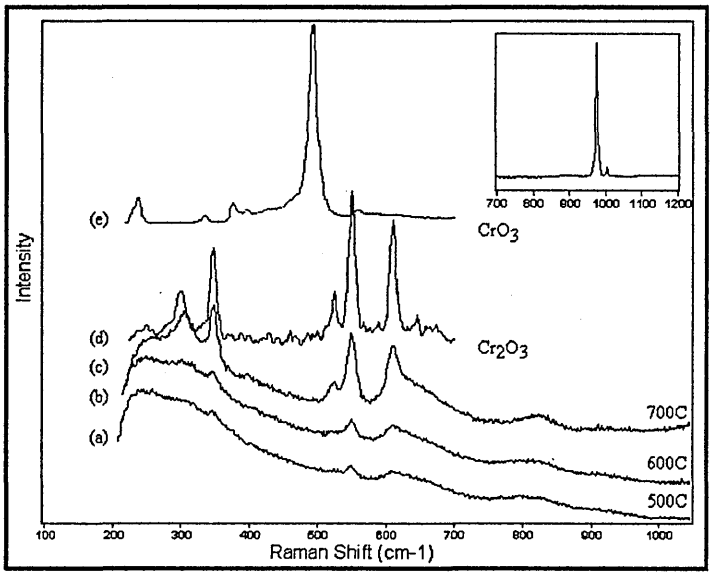

Figure 6.5 Spectra of CrN coating heat treated in a furnace (in air) (a) 500°C 1 hour (b) 600°C 1 hour (c) 700°C 1 hour (lp: 25 mW) and spectra of reference chromium oxide powders (d) Cr_2O_3 (e) CrO_3. Inset: 900-1000 cm^{-1} region associated with CrO_3 vibrations (lp: 0.25 mW).

Other broad bands were observed between 675-900 cm^{-1} which are of unknown origin. Two further bands are observed at ~1000 cm^{-1}. The strong band associated with CrO_3 at lower frequency (Figure 6.5(e)) was not observed at ~490 cm^{-1}, and it is unlikely that CrO_3 was present. With an increase in laser power, a crystallisation process occurred in which sharper and better-defined bands associated with Cr_2O_3 were observed. The broad features observed between 675-900 cm^{-1} were retained.

Static Oxidation

The furnace heat treatment of the CrN coating showed a small amount of Cr_2O_3 oxide formation on the surface at 500°C indicated by small bands at 343, 546 and 607 cm^{-1} (Figure 6.5(a)). These bands grew in intensity as the temperature was increased until at 700°C sharp high intensity well resolved bands were observed. At 700°C (Figure 6.5(c)) there appeared to be underlying un-oxidised coating remaining, signified by low frequency broad acoustic modes and higher frequency optic modes of the fcc lattice. This indicated high resistance to oxidation of the CrN coating, in which Cr_2O_3 oxide scale may be acting as a protective layer.

It was found that the as-formed wear debris from CrN coating consisted of predominantly Cr_2O_3. Static oxidation of the CrN coating showed Raman bands from Cr_2O_3 formed on the surface at 500°C that grew in intensity as the temperature was increased. It can therefore be estimated that temperatures of 500°C (or above) may occur at the tribo-contact for the Al_2O_3 - CrN system, under the test conditions used.

6.4.3 NbN Coating

Debris Analysis

The Raman spectrum of the as-formed debris (Figure 6.6(a)) featured two strong and broad features in the range 500-1000 cm^{-1} and a very low intensity band centred at ~300 cm^{-1}.

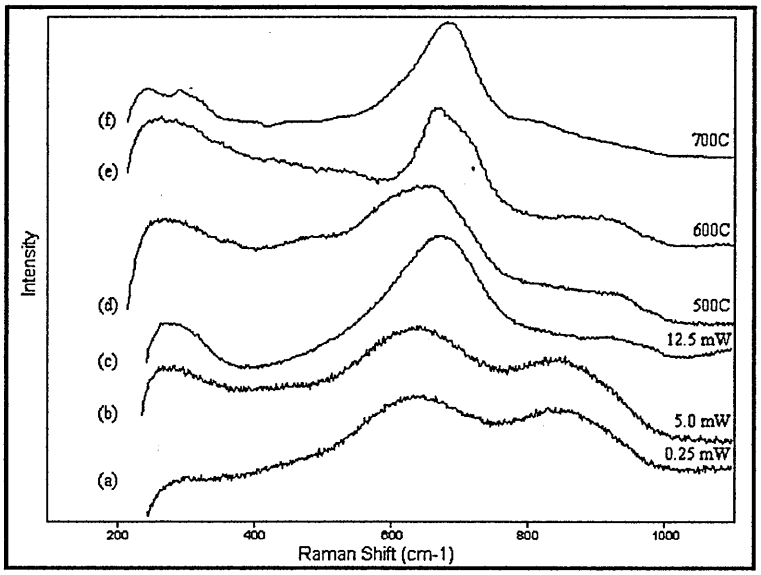

Figure 6.6 Spectra of debris (a) as-formed debris (0.25 mW) (b) 5 mW (c) 12.5 mW and spectra of the NbN coating heat treated in a furnace (in air) (d) 500°C 1 hour (e) 600°C 1 hour (f) 700°C 1 hour (Laser power: 25 mW).

These became sharper as crystallisation/phase transformation occurred during irradiation with higher laser intensities. Very little change was observed in the 5 mW spectrum (Figure 6.6(b)) but at 12.5 mW the band observed at ~300 cm^{-1} grew in intensity and the broad band centred at ~850 cm^{-1} was diminished. The band centred at ~650 cm^{-1}, which had previously been assigned to the symmetric stretching modes of the niobia polyhedra for amorphous $Nb_2O_5.nH_2O$[42] became sharper and shifted ~20 cm^{-1} to higher frequency to 670 cm^{-1} (Figure 6.6(c)). The as-formed debris spectrum showed similar broad features to that of $Nb_2O_5.nH_20$, as reported by Wachs

et al[42]. Upon irradiating the debris with 12.5 mW laser power (Figure 6.6(c)) the spectrum transformed to resemble TT-Nb_2O_5 and T-Nb_2O_5 orthohombic phases[42].

Static Oxidation

Furnace oxidation of the NbN coating (Figure 6.6 (d-f)) showed amorphous Nb_2O_5 oxide to be present on the surface at 500°C (Figure 6.6 (d)), similar to the spectrum of $Nb_2O_5.nH_2O$[42]. Upon increasing the temperature the amorphous niobium oxide increased in crystallinity, signified by the sharpening of bands and resolution of further bands, especially in the 200-550 cm^{-1} region. The oxide spectrum formed on the 700°C treated coating (Figure 6.6 (f)) was almost identical to the spectra identified as either TT-Nb_2O_5 / T-Nb_2O_5 prepared by calcination of bulk niobium oxide at 500 and 800°C respectively [42]. The TT-Nb_2O_5 and T-Nb_2O_5 both have crystalline orthohombic Nb_2O_5 phase structure determined by XRD[42] and HRTEM[43]. The as-formed debris spectrum had similar features to the 500°C treated NbN coating, although there was not an exact correlation. A clear contact temperature was therefore difficult to estimate. The evidence for the symmetric stretching mode at ~650 cm^{-1} of the niobia polyhedra from an amorphous $Nb_2O_5.nH_2O$ oxide and the resemblance with the 500°C treated coating spectra did allow an estimate of around 500°C to be postulated as a contact temperature for the Al_2O_3 - NbN system, under the test conditions used.

6.4.4 CrN/NbN Superlattice Coating

Debris Analysis

The main feature of the as-formed debris spectrum (Figure 6.7 (a)) was a high intensity band centred at ~780 cm^{-1}. Low intensity bands were also observed at 289, 447, 544, 600, 987, and 1018 cm^{-1}. The 544 and 600 cm^{-1} bands, and possibly the 289cm^{-1} band, can be attributed to Cr_2O_3 (Figure 6.5 (d)).

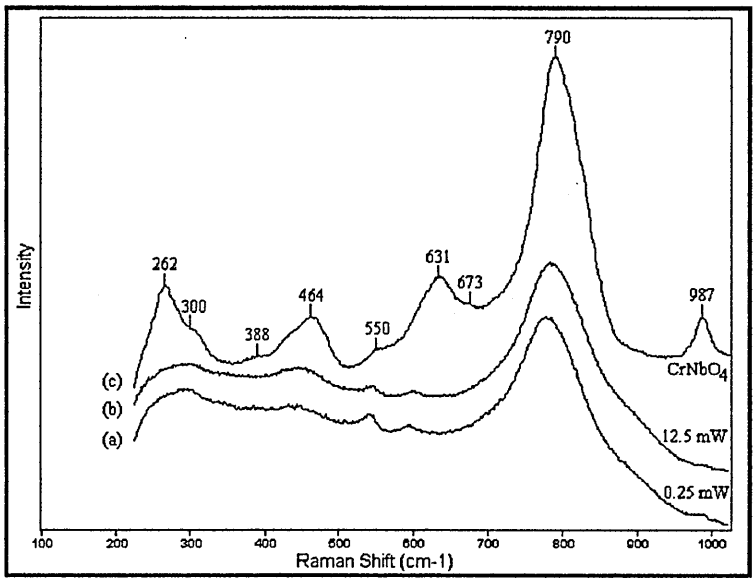

Figure 6.7 Spectra of debris (a) as-formed debris (0.25 mW) (b) 12.5 mW and (c) spectrum of as-synthesised $CrNbO_4$ standard (Laser power: 0.25 mW).

Very little change occurred in the spectrum upon higher laser irradiation and only a very slight shift to higher frequency of the 780 cm^{-1} band was observed which demonstrated the debris was structurally stable (Figure 6.7 (b)). Very good spectral agreement of the synthesised $CrNbO_4$ oxide (Figure 6.7 (c)) and the as-formed debris spectra was seen (additional bands seen in the standard spectrum were probably due to residual Cr_2O_3 and Nb_2O_5 (see Figure 6.8). The main band position (~790cm^{-1}) of the $CrNbO_4$ standard and the as-formed debris differed by only 10 cm^{-1}, indicating the

debris almost certainly contained $CrNbO_4$ oxide. This slight frequency shift may be explained by a small difference in the Cr:Nb stoichiometry, indicating the as-formed debris contained slightly more Nb within the crystalline lattice than the standard. The standard was prepared by heating Cr_2O_3 and Nb_2O_5 in a 1:1 ratio in a furnace (in air) at 1000°C for 24 hours. The resultant powder had a greyish yellow - green colour. The powder was studied using XRD to confirm the correct preparation (Figure 6.8 below). However residual Cr_2O_3 and Nb_2O_5 oxides were also detected.

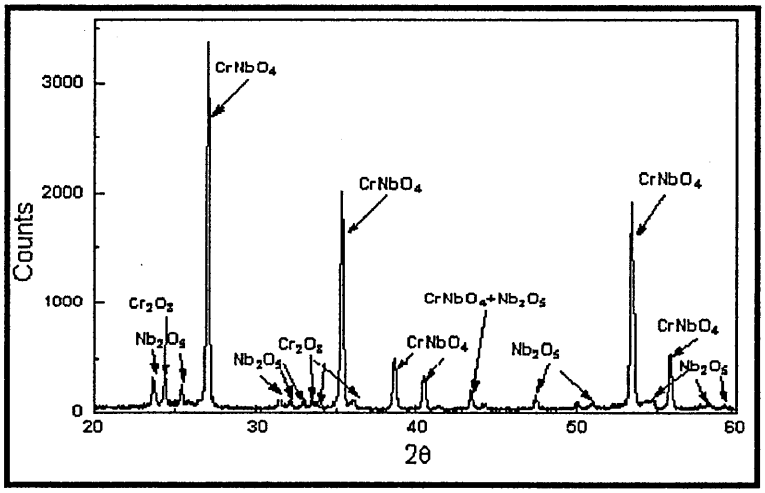

Figure 6.8 XRD pattern of as-synthesised $CrNbO_4$ (JCPDS - ICDD method: Natl. Bur. Stand. (U.S.) Monogr. 25, 19 38 (1982)).

Static Oxidation

The oxidation of the CrN/NbN superlattice coating has shown that much of the underlying coating was still retained even after heat treatments of up to 900°C (Figure 6.9 (c) below). This was shown by the phonon modes, indicating that PVD polycrystalline coating was still present throughout the static oxidation regime[48]. This demonstrated the high oxidation resistance of the CrN/NbN superlattice coating.

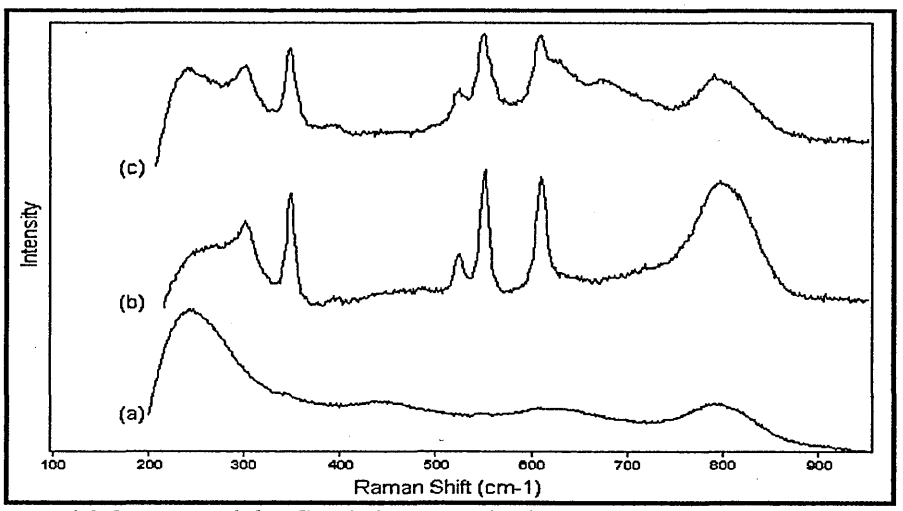

Figure 6.9 Spectra of the CrN/NbN superlattice coating heat treated in a furnace (in air) (a) 700°C 1 hour (b) 800°C 1 hour and (c) 900°C 1 hour (lp: 25 mW).

The Raman spectrum of the 700°C treated coating (Figure 6.9 (a)) showed two very small bands at 343 and 546 cm^{-1} which have been attributed to Cr_2O_3 and the 790 cm^{-1} band characteristic of $CrNbO_4$ oxide. The latter grew in intensity greatly upon an increase of 100°C in the treatment temperature to 800°C. High intensity bands at 343, 546 and 606cm^{-1}due to Cr_2O_3 were also seen. The intensity of the $CrNbO_4$ oxide band then appeared to decrease in intensity for the 900°C treated coating. An additional broad feature also appeared at ~680 cm^{-1}. This may be due to Nb_2O_5 oxide formation as observed for the NbN coating. A further band was seen as a shoulder on the 606 cm^{-1} Cr_2O_3 band. A similar investigation of the same coating system by Hovsepian et al[11] found by utilising XRD, TEM, EDX and glow discharge optical emission spectroscopy (GDOES) that a double layer of a $CrNbO_4$ porous oxide (uppermost surface) with a denser layer of Cr_2O_3 formed beneath. The CrN/NbN coating was subjected to a treatment temperature of 700°C (in air) for 168 hours. An oxide double layer of 0.8μm thickness was found. This means that the oxide layer detected by this study after 1h at 700°C must have been very thin indicating the

sensitivity of Raman microscopy. This work nicely complemented the findings from Hovsepian et al[11].

The oxides $CrNbO_4$ and Cr_2O_3 were identified in the as-formed wear debris by a very good correlation with $CrNbO_4$ and Cr_2O_3 standard spectra. The static oxidation of CrN/NbN performed at 700°C also showed this mixed metal oxide to exist on the surface, as did the 800 and 900°C treated coatings. Thus, an estimated temperature of ~700°C may occur at the tribo-contact for the Al_2O_3 - CrN/NbN superlattice system, under the test conditions used.

6.4.5 TiAlN/VN Superlattice Coating

Debris Analysis

The as-formed debris spectrum (Figure 6.10 (a)) showed firm evidence for the presence of V_2O_5, by a good comparison with the standard V_2O_5 spectrum (Figure 6.11 (d)). This was indicated by weak bands at frequencies of 281, 405 and 692cm^{-1} and by a slightly larger band at ~990 cm^{-1}, although the bands of crystalline V_2O_5 at ~480 and 530cm^{-1} were not observed. The observation of four bands corresponding in frequency to V_2O_5 was sufficient to indicate its presence within the debris perhaps in a less crystalline form.

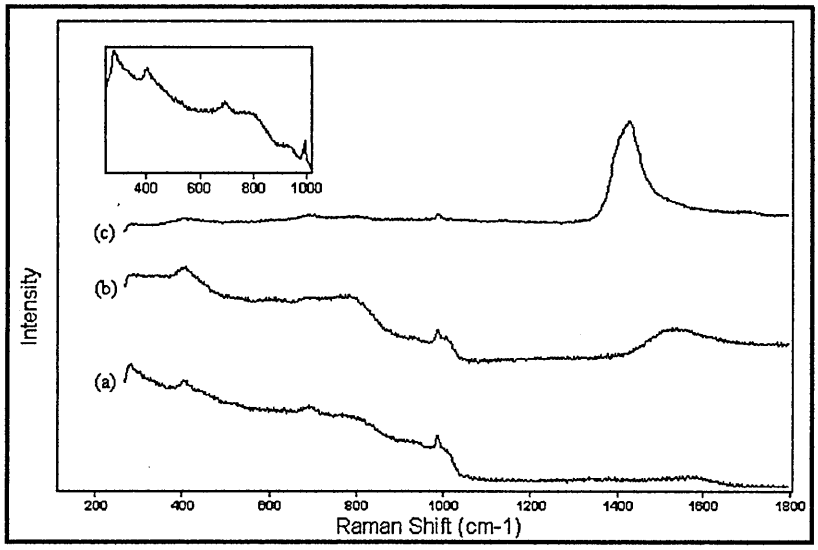

Figure 6.10 Spectra of debris (a) as-formed debris (0.25 mW) (b) 5 mW (c) 25 mW (INSET: 250 - 1025 cm^{-1} region of the as-formed debris spectrum).

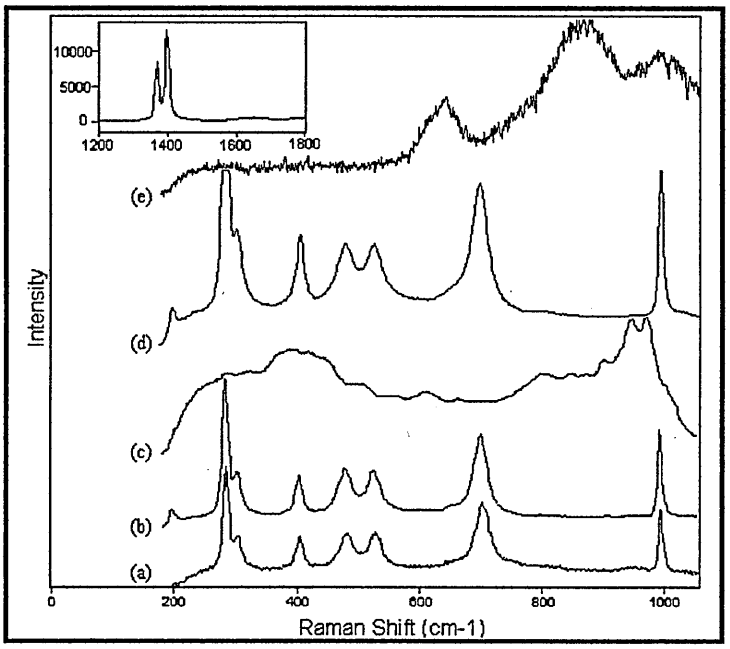

Figure 6.11 Spectra of the heat treated TiAlN/VN superlattice coating in a furnace (in air) (a) 600°C 1 h (b) 650°C 1 h (c) 700°C 1 h (lp: 25 mW) and spectra of reference oxide powders (d) V_2O_5 (e) α-Al_2O_3 (lp: 0.25 mW; INSET: high frequency region of α-Al_2O_3 spectrum, showing two very intense characteristic bands).

Strong α - Al_2O_3 bands became visible in the frequency range 1350-1450 cm^{-1}, (Figure 6.10 (c)), characteristic of the Al-O stretching mode, when the debris was

irradiated with 25 mW laser power. These bands were not fully resolved indicating the oxide was not fully crystalline when compared with the standard spectrum (Figure 6.11(inset)). A possible phase transition from γ- Al_2O_3 or a crystallisation of disordered α - Al_2O_3 oxide may have occurred. It is well known that Al_2O_3 has several phases and the nature of these phases depends strongly on the method and the temperature of production[41]. For example, with boehmite as the starting material, γ - Al_2O_3 is formed at 500-850°C, θ - Al_2O_3 is formed from 850 °C to about 1100°C, while above 1100°C from any starting material, only α - Al_2O_3 is obtained[41]. The broad diffuse band seen in Figure 6.10 (b) which covered the range 1400-1650 cm^{-1} was very similar in nature to the spectrum of γ- Al_2O_3 collected using 632.8 nm excitation reported by Aminzadeh[41]. The Al_2O_3 detected in the debris cannot be from worn particles of the ball material because bands associated with α - Al_2O_3 (Figure 6.11 (e) + (inset)) would have been visible in the as-formed debris spectrum, as the laser was positioned on the same spot throughout the debris analysis. Furthermore, Al_2O_3 bands have not been detected previously when studying debris from the other coatings, indicating that little wear of the corundum ball takes place. This was evident when upon an ESEM investigation of the ball surface (Figure 6.12 below) the image shows a transfer film, probably V_2O_5, on the surface of the ball i.e. the contact point. Very little wear of the ball can also be seen which was probably due to the occurrence of the transfer film.

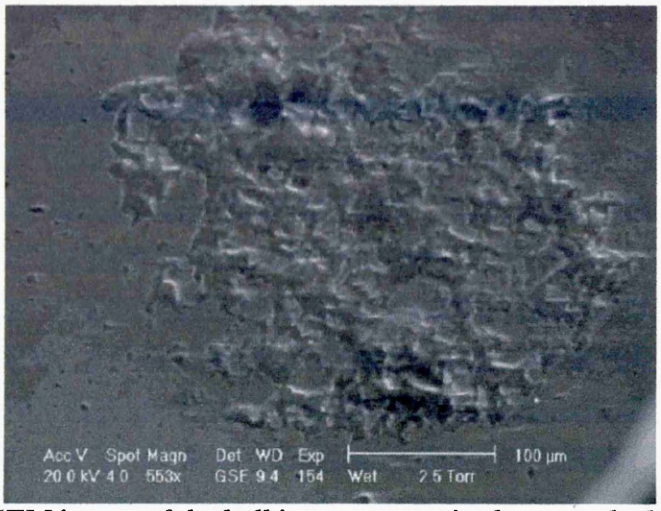

Figure 6.12 ESEM image of the ball i.e. contact point between the ball and coating during sliding

Small bands due to V_2O_5 in the debris were still present after irradiation with 25 mW laser light.

Static Oxidation

Heat treatment of the TiAlN/VN superlattice coating at 600°C (Figure 6.11 (a)) showed clear V_2O_5 oxide bands present on the surface. These bands were retained upon heat treatment to 650°C (Figure 6.11 (b)). At 700°C the TiAlN/VN coating was destroyed and a complicated spectrum resulted in which many bands were observed which were mainly broad (Figure 6.11 (c)). The spectrum will feature bands due to reaction products of Fe, V, Ti, Al and oxygen. There was definitely no evidence of V_2O_5 at 700°C.

The evidence for V_2O_5 in the as-formed debris and the appearance of this oxide on the surface of the TiAlN/VN coating after heat treatment at 600°C allowed an estimate of

~600°C for the contact temperature for the Al_2O_3 - TiAlN/VN system, under the conditions used.

6.4.6 Conclusions

A comparison with oxide 'standards' and from oxide spectra from previous publications (by other authors) has enabled the distinction between many different forms of metal oxides that were present within the debris and enabled laser-induced phase transformations to be monitored.

Carbon was detected in the debris resulting from sliding against the TiCN top layer of the Ti(C, N) multilayered coating, which was micro-crystalline in nature. A lower friction coefficient of 0.18 arose during sliding and a possible decrease in the contact temperature may have taken place due to the formation of an oxygen deficient rutile phase and possible evidence for anatase within the as-formed TiCN debris. This indicated a strong possibility that the amorphous carbon was acting as a lubricant during sliding wear. The incorporation of thin layers of VN to the TiAlN system and the subsequent evidence for V_2O_5 in the debris and the lower friction coefficient of 0.54 when compared to 0.8-0.9 that is known to occur for TiAlN, realises the lubricating action of V_2O_5 during sliding wear.

A mixed metal solid solution oxide, $CrNbO_4$, was detected within the as-formed debris from the CrN/NbN superlattice coating, indicating a reaction product from the metallic components of the superlattice coating with oxygen had taken place. This has shown that high contact temperatures do exist, which are sufficient in magnitude,

to result in complicated tribo-oxidation reactions. The determination of these approximate contact temperatures by a comparison of the tribo-chemical products detected in the wear debris with the formation temperatures of thermally attained reaction products appears to have worked well. Contact temperatures for the coating systems studied were estimated as greater than 500°C but below 800°C (see Table 6.2). The observed frictional heating effects resulted in oxidational wear mechanisms for the coating systems studied.

Table 6.2 Summary of Results (sliding at 10cm/s against corundum)

Tribo-Couple	Friction	Sliding Dist.(km)	Appearence	Structure and Composition of Debris	Oxides Detected (Static Oxidation)	Estimated Contact Temp. (°C)
TiCN - Al_2O_3 (top layer)	0.18	3	white powder (small amount)	TiO_2 (rutile) + small amount of anatase + disordered carbon	TiO_2 (anatase and rutile)	>700
Ti(C, N) - Al_2O_3 (additional layers incorporating TiN)	~0.72	3	white powder	TiO_2 (rutile)	As above	>700
CrN - Al_2O_3	0.45	1	pale green powder	Cr_2O_3	Cr_2O_3	>500
NbN - Al_2O_3	0.66	1	white powder	amorphous $Nb_2O_5.nH_2O$	$Nb_2O_5.nH_2O$ and TT- Nb_2O_5/T-Nb_2O_5	~500
CrN/NbN - Al_2O_3	0.69	1	grey-green powder	Cr_2O_3, $CrNbO_4$	Cr_2O_3, $CrNbO_4$ Nb_2O_5?	~700
TiAlN/VN - Al_2O_3	0.54	9	light brown powder (v. small amount)	V_2O_5, γ/α–Al_2O_3	V_2O_5, complicated oxide involving Fe, V, Ti, Al and Oxygen	~600

6.5 Further Static Oxidation Studies of Various Coating Systems

6.5.1 ZrN Coating

The static oxidation was performed as detailed previously i.e. successively. Figure 6.13 below shows a ZrN coating heat treated in a furnace in air up to 600°C.

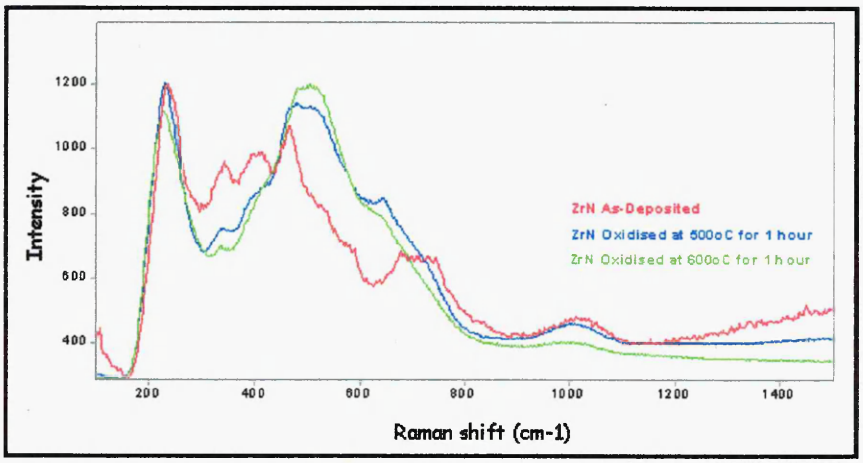

Figure 6.13 Static oxidation of ZrN (as-deposited, 500 and 600°C)

The phonon modes of the lattice appear to be still present on oxidation at 600°C although the optic modes around 500-575cm^{-1} appear to have shifted. The shift in position of the modes was probably due to compressive stress relaxation detailed in section 6.1.1 of this chapter.

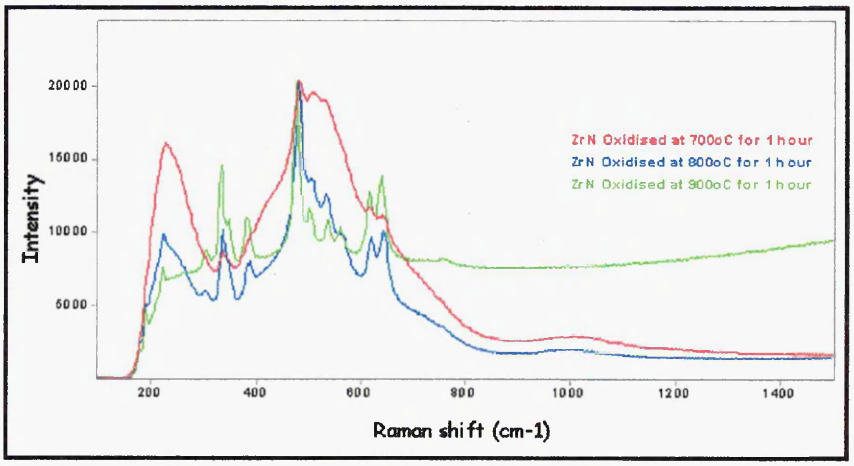

Figure 6.14 Static oxidation of ZrN (700, 800 and 900°C)

At 700°C (Figure 6.14 above) the phonon modes are still present but small oxide bands which were attributed to monoclinic ZrO[44] were observed, typified by the presence of a sharp 475cm^{-1} band. These bands become more intense and sharpen at 800, and 900°C.

6.5.2 TiAlN/CrVN Coating

This coating is an example of how the addition of certain elements can increase the system oxidation resistance, as studied by Münz et al[9]. Addition of Cr to TiAlN was found to increase the oxidation resistance from 870 to 920°C and the addition of small amounts of Cr and Y was seen to increase this further to 950°C. To utilise these favourable results for TiAlN, Cr (~20at%) was added to TiAlN/VN (debris and static oxidation shown in section 6.4.5 of this chapter) to form TiAlN/CrVN. The oxidation resistance of TiAlN/VN was quite poor and the coating was completely destroyed >675°C owing to the V_2O_5 melting at this temperature (thus providing no protection against substrate oxidation). The Cr containing coating was statically oxidised to assess its oxidation resistance (Figure 6.15 below).

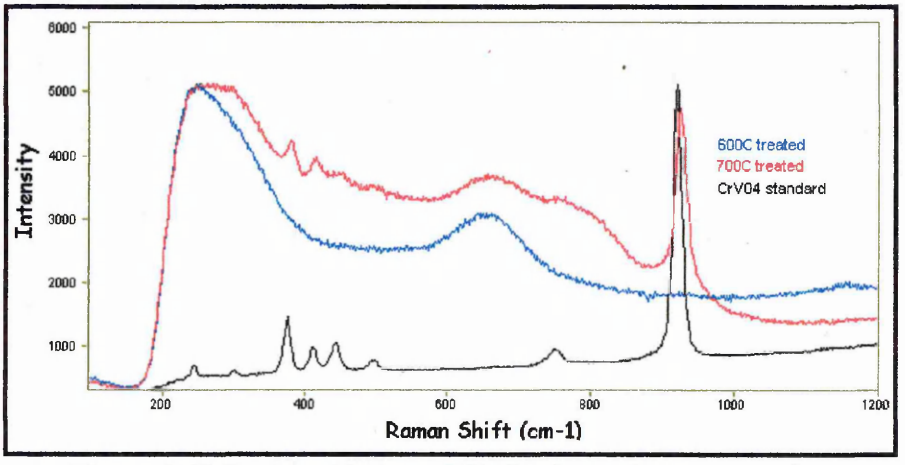

Figure 6.15 Static oxidation of TiAlN/CrVN (600 and 700°C)

At 600°C the broad phonon modes indicative of the acoustic and optic phonon modes of the polycrystalline coating were observed but the non-Cr coating oxidised at 600°C gave a spectrum featuring intense V_2O_5 bands (section 6.4.5), indicating that appreciable oxidation had already taken place. This was an indicator that the oxidation resistance had been increased for the new, Cr containing, coating. At 700°C, the temperature at which the TiAlN/VN coating was completely destroyed, the Cr-containing coating still showed evidence of phonon modes of the coating lattice, but other low intensity, low frequency, bands and a higher intensity band at ~930cm^{-1} were observed. These were not identified as V_2O_5 but were thought, nevertheless, to be due to a surface oxide/(s). These bands did not correlate to any Cr, V, Al or Ti oxide; therefore a mixed metal solid solution oxide similar in nature to $CrNbO_4$ (as detected for CrN/NbN oxidation) was sought. A $CrVO_4$ species was thought to be the most probable; neither Al nor Ti oxides were detected for TiAlN/VN. A standard $CrVO_4$ was then prepared for comparison following the JCPDS method (heating Cr_2O_3 and V_2O_5 in a 1:1 mixture in a furnace at 800°C for 120 hours) and a spectrum was acquired (black spectrum featured in Figure 6.15). An XRD pattern of the resultant powder was also acquired and thus indicated that the correct composition oxide was formed. The Raman spectrum of this oxide powder showed unequivocally that the oxide found on this coating at 700 was $CrVO_4$. The $CrVO_4$ oxide bands became more intense at 800°C (Figure 6.16 (below)). Bands attributed to the underlying coating were still observed at 800°C indicating a massive increase in oxidation resistance of this Cr-containing system. At 850°C there was no evidence for any remaining underlying coating. A different spectrum (probably a more complicated mixed system) resulted that could not be identified but was thought to be $Ti_xV_yCr_z$ oxide. Al_2O_3 was not thought to be present or take part in this mixed oxide

due to it being a slow forming oxide which does not start to form appreciably until >850°C. In addition the main band of this new oxide at ~840cm^{-1} was shifted ~100cm^{-1} from the band attributed to $CrVO_4$. This indicated that a further heavy element (probably Ti) was incorporated within the oxide lattice. There may also have been Fe present as a consequence of diffusion from the substrate material as the coating deteriorated.

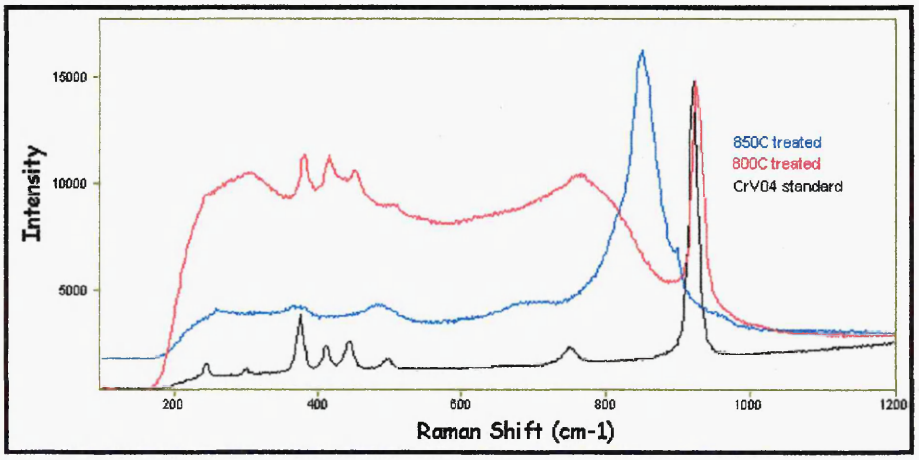

Figure 6.16 Static oxidation of TiAlN/CrVN 800 and 850°C)

Although the oxidation resistance of this Cr-containing system was increased by ~125°C to ~800°C the favourable tribological properties (observed in sliding tests) of low friction and wear rate were lost resulting in a poorer wear resistant coating. This was attributed to the lack of lubricious V_2O_5 being generated from the TiAlN/CrVN system, and the mixed $CrVO_4$ species preferentially forming in its place.

6.5.3 Heat Treatment of Supercote-02

Supercote 02 is the commercial coating on which comprehensive wear analysis has been performed (chapter 5). An understanding of how this coating reacts at high temperatures, comparable to those encountered during dry high-speed cutting

operations was essential. The Supercote-02 coating was deposited onto a cemented carbide substrate and was heat-treated, successively, in a furnace (in air) at 800, 900, 950 and 1000°C each for 1 hour. A Raman spectral analysis of the treated coating at each temperature was acquired to determine the surface oxide species. For the un-treated (i.e. as-deposited) and 800, 900°C treated coatings detailed spectral analysis was performed (Figure 6.18). The coating structure remained intact at these treatment temperatures (Figure 6.17 below) and the spectral analysis was undertaken in order to gain a better understanding of what occurs to the polycrystalline lattice by monitoring the main optic mode at ~ 680cm^{-1}. The notch filter, as described in chapter 2 section 2.4.2.2, complicates this very low frequency region of the spectrum i.e. 100-200cm^{-1} as an abnormally high initial background is generated. Although there will be spectral intensity in this region from Brillouin/acoustic modes of the polycrystalline lattices these are superimposed onto this initial rise in the spectrum. However, at frequencies greater than ca. 150-200cm^{-1} the Raman intensity in the spectrum is from real Raman scattering processes and is not affected by the notch filter. This does, however, present a significant problem when curve fitting the spectra. To generate accurate and reproducible data for the optic modes, i.e. in the region 550-700cm^{-1}, the whole of the spectrum should be fitted i.e. including the artificial notch filter rise at low frequency.

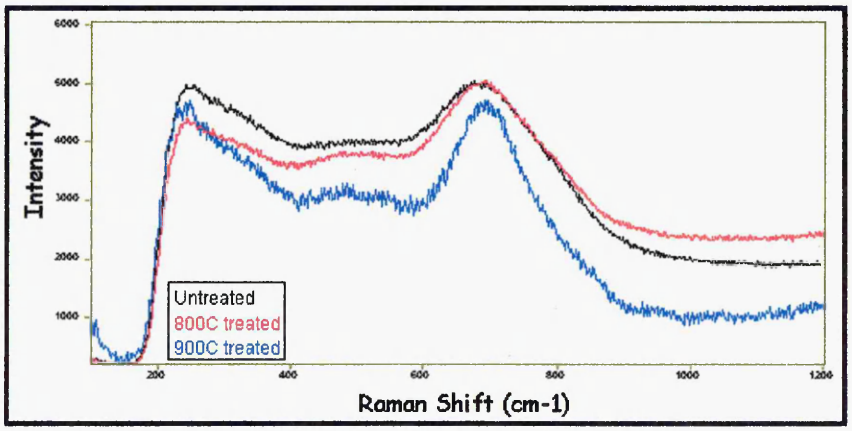

Figure 6.17 Comparison of the heat-treated Supercote-02 spectra (un-treated, 800 and 900°C)

The band fitting (Figure 6.18) is shown below:

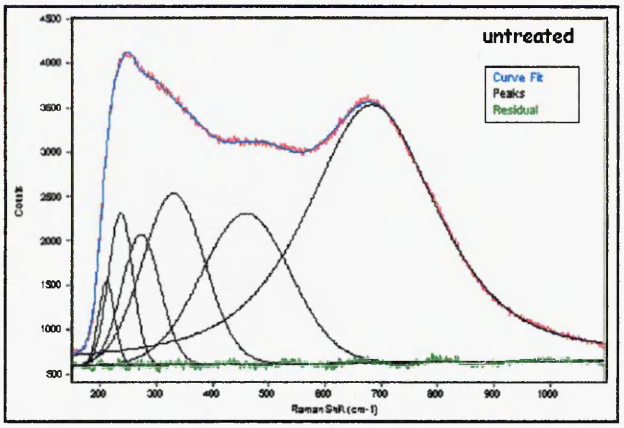

(a)

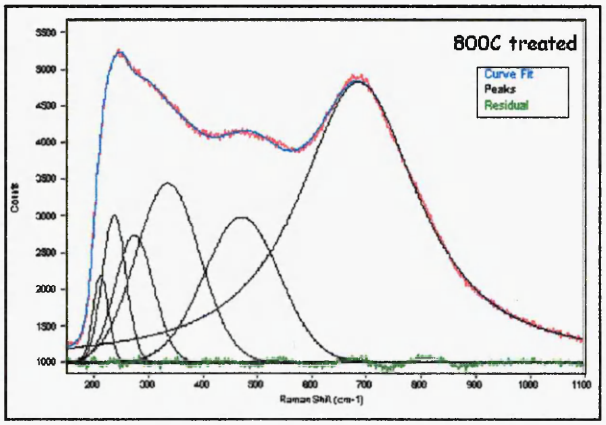

(b)

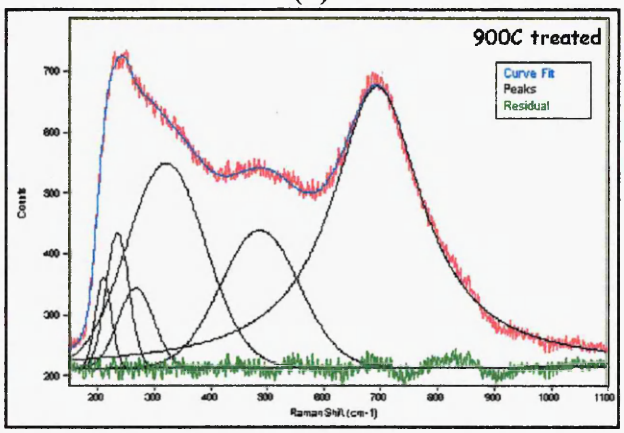

(c)

Figure 6.18 Band fitting of the (a) Untreated (b) 800°C treated and (c) 900°C treated Supercote-02 coating

The incorporation of six bands under the overall band structure was performed merely to allow a good reproducible fitting of the main optic mode at ~680cm^{-1}. The fitting would be inaccurate if only this band region were taken for the fitting owing to the nature of the spectrum i.e. high spectral density in the gap region between the acoustic and optic modes. Values obtained from fitting mixed Gaussian-Lorentzian peak shapes are shown in Table 6.3 (below):

Treatment (°C)	Position (cm^{-1})	Width (cm^{-1})	Height	Area	Chi^2	RMS Noise	R^2
Untreated	683.9	275.6	2905.2	972044	1.9	19.1	0.9994
800	686.1	263.8	3820.2	1284291	3.2	20.4	0.9992
900	693.9	193.4	462	122061	1.8	7.5	0.9958

When the Supercote-02 coating was heat treated there was a shift to higher frequency of the main optic mode, whereby after subsequent treatment at 800 and 900°C for 1h there was a total shift of ~10 cm^{-1}. This would seem to indicate that there was an increase in compressive stresses but this would contradict the literature, detailed in section 6.1.1 whereby annealing should result in stress relaxation. The Raman laser beam penetration is such that the uppermost layer of Supercote-02, i.e. the $TiAlCrO_xN_y$ (oxynitride), would be the predominant coating layer sampled but there may have also been a contribution from the TiAlN/CrN superlattice beneath (for Supercote-02 coating architecture see chapter 5 (section 5.5.1)). The oxynitride layer is already partially oxidised in its constitution as a way of reducing initial wear during dry cutting operations. The further incorporation of more of the slightly heavier oxygen atoms, i.e. inward diffusion of oxygen[49] to form a more oxygen rich oxynitride layer, or the outward diffusion of other coating elements from within the

bulk of the coating, for example Ti, Al and Cr as detected previously[49], may conceivably distort the lattice and change the composition resulting in a frequency shift of the optic mode. In addition there was a decrease in the intensity which could be due to a very thin amorphous oxide layer being present on the surface[49] thus reducing the sampling depth and resulting in diminished coating bands. A decrease in the band width was also observed after annealing which signifies that an ordering process also took place. This may be explained by a coarsening of the grain structure during annealing thus increasing the size of the columnar grains and reducing the number of phonon relaxation pathways. The effect of annealing on the band width and band position is shown in Figure 6.19.

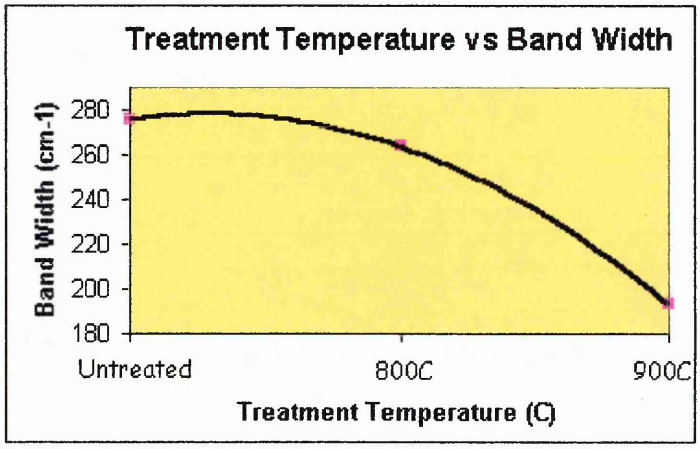

(a)

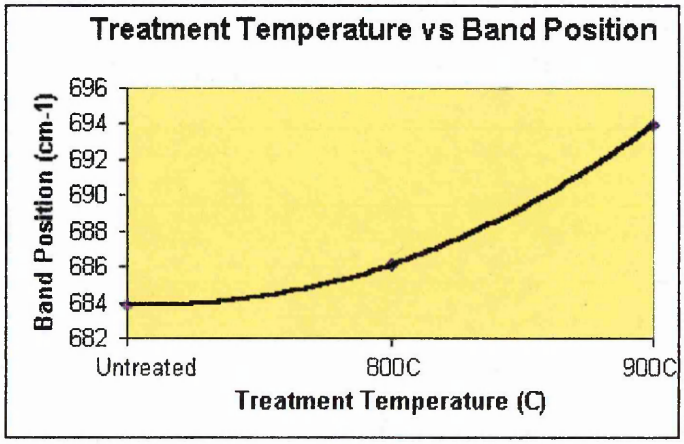

(b)

Figure 6.19 Graphic representation of the effect of annealing on the (a) band width and (b) band position

The 950 and 1000°C treated coating spectra are shown below in figure 6.20.

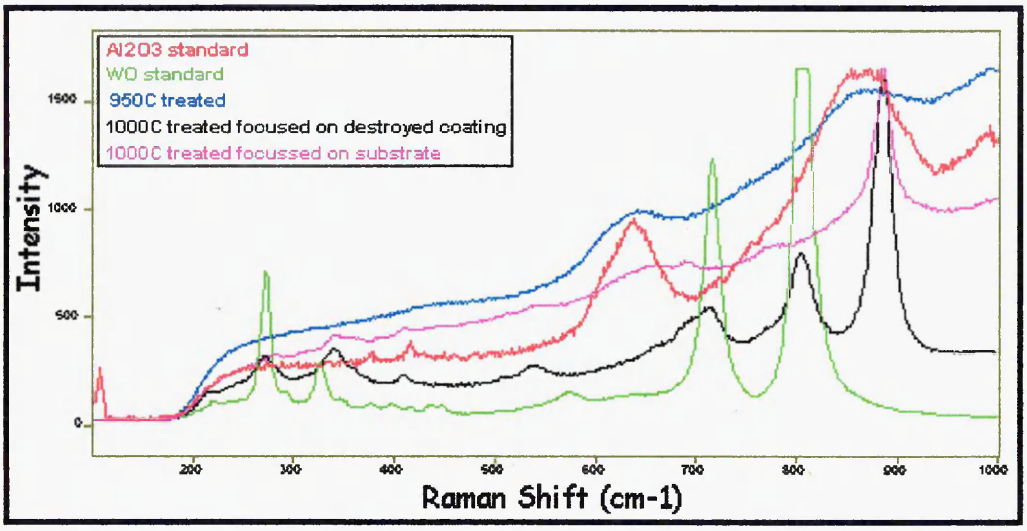

(a)

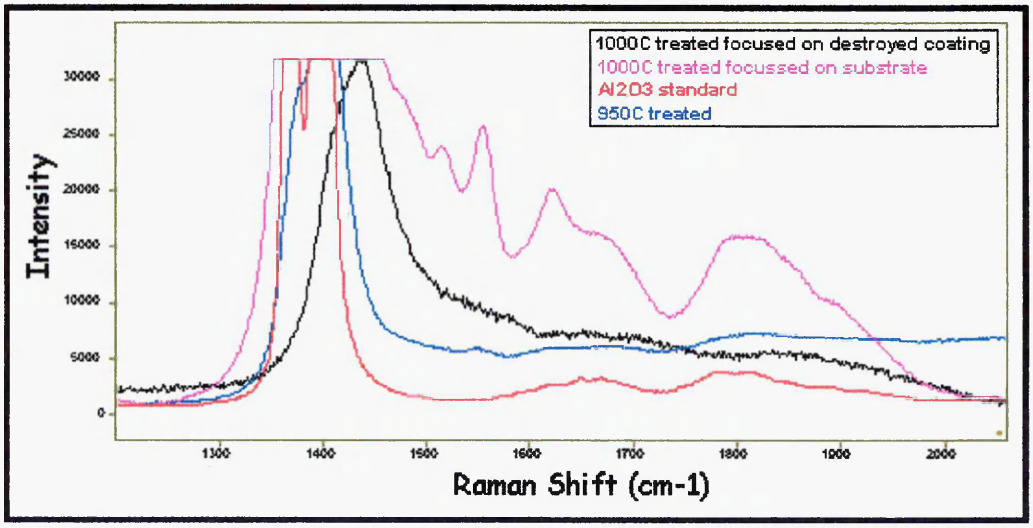

(b)

Figure 6.20 Raman spectra of the 950 and 1000°C treated Supercote-02 coating (a) low frequency region and (b) higher frequency region N.B. for (b) the tungsten tri-oxide spectrum was omitted, as there were no bands in this region.

The 950°C spectrum indicated that the coating was almost fully oxidised, the process being accompanied by the appearance of low frequency α -Al_2O_3 bands. Note,

however, that the laser may not have been able to penetrate through the oxide layer and there could possibly be underlying coating remaining. At 1000°C the coating was completely destroyed and the substrate was revealed over the majority of the surface. Bands due to α-Al_2O_3[41] and orthorhombic WO_3[50] were identified and also a band at 900cm^{-1} that could not be assigned. A possibility was that this band could be due to cobalt oxide (oxidised cobalt binding agent which was 9% of the WO-Co substrate material) or a mixed Cobalt tungsten oxide.

The observation of α-Al_2O_3 on the surface of the Supercote-02 coating heat treated at 950 – 1000°C and the previous observation of this oxide on the surface of worn tools indicates that temperatures ranging between 950 - 1000°C must indeed occur during cutting operations and lead to an oxidational wear mechanism that largely contributes to the deterioration of the coating.

References

1 J.A. Sue, T.P. Chang, Surf. Coat. Technol. 76 (1995) 61.

2 C. Heau, R.Y. Fillit, F. Vaux and F. Pascaretti, Surf. Coat. Technol. 120-121 (1999) 200-205.

3 F.H. Shott and D.R.G. Mitchell, Mater. High. Temp. 9(4) (1991) 185-192.

4 D. McIntyre, J.E. Greene, G. Hakansson, J-E. Sundgren and W-D. Münz, J. Appl. Phys. 11 (1990) 1542.

5 L. Hultman, Vacuum 57 (2000) 1-30.

6 K. Oettel, R. Wiedemann and S. Preissler, Surf. Coat. Technol. 74 (1995) 273.

7 W. Herr, E. Broszeit, Surf. Coat. Technol. 97 (1997) 335.

8 Kim B-J, KimY-C, Nah J-W, Lee J-J, J. Vac. Sci. Technol. A 17 (1999) 133.

9 I.J. Smith, W-D. Münz, L.A. Donohue, I. Petrov and J.E. Greene, Surf.Eng.. 14 (1998) 37.

10 L.A. Donohue, I.J. Smith, W-D. Münz, I. Petrov and J.E. Greene Surf. Coat. Technol. 94-5 (1997) 226.

11 P. Hovsepian, D.B. Lewis, Q. Luo, W-D. Münz and M. Meyer, Proceedings of European Congress Adv Materials Proc, Munich, 27-30 September (1999) (in press)

12 M.J.Graham and R.J. Hussey, Oxidation of metals, 44(1/2) (1995) 339-374.

13 D.J. Gardiner and C.J. Littleton, Comm. Eur. Communities [Rep] EUR 1987, EUR 11365, High Temp Alloys 155-164.

14 J.T. Keisler, C.W. Brown and R.H. Heidersbach, American Laboratory, April (1982) 17-25.

15 H.E. Townsend, T.C. Simpson and G.L. Johnson, Corrosion Science July (1994) 546-554.

16 P. Fabis, C. Brown, T. Rockett and R. Heidersbach, Oxid. Metals 16 (5/6) (1981) 399-407.

17 D.L.A. de Faria, S. Venacio Silva and M.T, de Oliveira, J. Raman Spectros. 28 (1997) 873-878.

18 D.J. Gardiner, C.J. Littleton, K.M. Thomas and K.N. Strafford, Oxid. Metals, 27(1/2) (1987) 57-72.

19 S.C. Tjong, Mater. Res. Bull., 18 (1983) 157-165.

20 D.J. Gardiner, C.J. Littleton and M. Bowden, Appl. Spectros. 42 (1) (1988) 15-19.

21 B.C. Oberlander, M. Franck, J.-P. Celis and J.R. Roos, Surf. Coat. Technol. 63 (1994) 25-34.

22 M. Franck, J.-P. Celis and J.R. Roos, J. Mater. Res. 10(1) (1995) 119-125.

23 G.M. Begun and C.E. Bamberger, Appl. Spectrosc. 43(1) (1989) 134-138.

24 K. Witke, D. Klaffke, A. Skopp and J.P. Schreckenbach, J. Raman Spectrosc. 29 (1998) 411-415.

25 K. Witke, D. Klaffke, T. Schneider and J.P. Schreckenbach, Appl. Surf. Sci. 151 (1999) 33-39.

26 B. Blainpain, M. Franck, H. Mohrbacher, E. Vancoille, J.-P. Celis and J.R. Roos, in Thin Films in Tribology: Micro-Raman spectroscopy for the characterisation of wear induced surface modifications on hard coatings, D. Dowson et al, (ed.) Elsevier, Amsterdam, 1993, p 623.

27 K. Schouterden, B. Blainpain, J.P. Celis and O. Vingsbo, Wear 181-183, (1995) 86.

28 M.N. Gardos, MRS Symp. Proc., 140, (1989) 325.

29 J.C. Parker, R.W Siegel, Journal of Materials Research 5, (1990) 1246.

30 E. Vancoille, B. Blainpain, Ye. Xingpu, J.-P. Celis and J.R. Roos, Journal of Materials Research 9(4), (1994) 992.

31 S.Wilson and A.T. Alpas, Surf. Coat. Technol., 108-109 (1-3) (1998) 369-376.

32 I.L. Singer, S. Fayeulle and P.D. Ehni, Wear 149, (1991) 375.

33 U. Balachandran and N.G. Eror, J. Solid State Chem.42 (1982) 276-282.

34 M.P. Moret, R. Zallen, D.P. Vijay and S.B. Desu, Thin Solid Films 366 (2000) 8-10.

35 P.S. Narayanan, Proc. Indian Acad. Sci. Sect. A 32 (1950) 279.

36 V.Zh. Ushanov, I.S. Kolodina, D.Kh. Sembaev and O.V. Agashkin, translated from Zhurnal Analiticheskoi Khimii, Vol. 47, No. 4, (1992) 749-751.

37 L.E. Depero, L. Sangaletti, E. Bontempi, R. Salari, C. Casale, M. Musci and M. Notaro, Mat. Res. Soc. Symp. Proc. 454 (1997) 241-246.

38 L.S. Hsu, R. Solanki, G.J. Collins and C.Y. She, Appl. Phys. Lett. 45(10) (1984) 1065-1067.

39 A. Felske and W.J. Plieth, Electrochimica Acta 34(1) (1989) 75-77.

40 S. Mandi, G. Thorwarth, M. Schreck, B. Stritzker and B. Rauschenbach, Surf. Coat. Technol. 125 (1-3) (2000) 84-88.

41 A. Aminzadeh, Applied Spectroscopy 51(6) (1997) 817-819.

42 J-M. Jehng and I.E. Wachs, Chem. Mater., 3(1) (1991) 100-107.

43 J.G. Weissman, E.I. Ko, P. Wynblatt and J.M. Howe, Chem. Mater 1(2) (1989) 187-193.

44 P. Barberis, T. Merle-Mejean and P. Quintard, J. Nuc. Mater., 246 (1997) 232.

45 M. Woydt, A. Skopp, I. Dorfel and K. Witke, Wear 218 (1998) 84-95.

46 A. Cuesta, P. Dhamalincourt, J. Laureyns, A. Martinez-Alonso and J.M. D. Tascon, Carbon 32 (1994) 1523.

47 A. Cuesta, P. Dhamalincourt, J. Laureyns, A. Martinez-Alonso and J.M. D. Tascon, J. Mater. Chem. 8 (1998) 2875.

48 C.P. Constable, J. Yarwood and W.-D. Münz, Surf. Coat. Technol. 116-119 (1999) 155.

49 M. Lemke, D.B. Lewis, J.M. Tichmarsh and W.-D. Münz, Surface Engineering (submitted 2000).

50 E. Cazzanelli, C. Vinegoni, G. Mariotto, A. Kuzmin and J. Purans, Solid State Ionics, 123 (1999) 67-74.

Chapter 7

Residual and Mechanically Induced

Strain/Stress Analysis

Chapter 7 Residual and Mechanically Induced Strain/Stress Analysis

This chapter is concerned with the study of Raman microscopy for the determination of intrinsic residual stress within PVD hard coatings. Spectral shifts due to the application of applied stress on the phonon modes will also be studied to ascertain the possibility of creating a Raman based method for determination of the residual stresses to complement the established XRD method.

7.1 Origin of Residual Compressive Stresses Within PVD Coatings

Compressive stress in hard Physical-Vapour-Deposited coatings up to the values of several giga-pascals (GPa) is found to be strongly dependent on the process parameters, especially on the energy of ion bombardment (see chapter 1, page 8). An increase in this energy usually leads to a corresponding increase in residual stress. Internal stress levels are crucially important as they have a profound influence on many other coating properties, e.g. adhesion, hardness and wear resistance. It is therefore very important to understand the origin of compressive stresses within PVD coatings.

The creation of stresses is attributable to either differences in the coefficient of thermal expansion of substrate and coating materials[1], or to so-called growth-induced stresses produced via the coating deposition process.

The total internal stresses, σ, are the sum of the thermal stresses σ_t and the growth stress σ_g, such that:

$$\sigma = \sigma_t + \sigma_g \qquad \textbf{Equation 7.1}$$

For thin films, expansion-dependent stresses, σ_t, may be regarded as approximately constant throughout the thickness[1]. Growth-induced stress generally manifest itself as a compressive stress whose value is strongly dependent on the type of PVD process (see chapter 1, section 1.2.1) and on the selected process parameters[1]. Increasing compressive stresses lead to an expansion of the lattice parameter in polycrystalline films normal to the substrate surface[2]. At the same time, an increasing dispersion of the lattice parameters perpendicular to the substrate surface is observable[2]. This is associated with increasing incorporation of argon atoms in sputtered coatings[3]. Process conditions leading to compressive stresses promote the formation of growth textures in which the most densely occupied planes run parallel to the substrate[4]. High compressive stresses reduce the adhesive strength of coatings on the substrate up to a point where spalling occurs during, or subsequent to, deposition. Conversely, they also cause a significant increase in hardness[4].

7.1.1 Dependence of Growth-Induced Residual Stresses on Process Parameters

7.1.1.1. Substrate Temperature

Virtually all process parameters affect the form and intensity of the particle flow to the substrate, as does the geometry of the process. Depending on the particle flow,

direct supply and loss of heat, a certain coating temperature is attained at the substrate surface. A fall in growth-induced internal stresses with increasing substrate temperatures has been observed under identical test parameters[1]. The decrease in stresses at higher substrate temperatures may be attributed to an increase in the mobility of the lattice atoms due to diffusion and plastic flow[1].

7.1.1.2 Bias Voltage

Positive ions are accelerated on to the substrate surface by applying a negative potential to the substrate. High negative substrate potentials cause a larger quantity of ions to be accelerated onto the substrate at higher speeds. As a result, growth-induced compressive stresses attaining extreme values at higher negative potentials are observed[6].

7.1.1.3 Total Pressure

As the total pressure of the vacuum atmosphere rises, the mean free path length in PVD processes is reduced. The paths by which neutrals, non-decelerated particles, can travel or along which ionised particles can be accelerated by electric fields are shortened[1]. The kinetic energy of the particles on the substrates decreases. A decrease in growth-induced compressive stresses with rising total pressure is observed[1].

7.1.1.4 Reactive Gas Partial Pressure

If the reactive component of the vacuum atmosphere is increased at constant pressure, the number of dissociated and ionised gas particles that can be accelerated on to the substrate, be incorporated in the coating, and contribute to the formation of the lattice, rises. At higher reactive gas pressures, higher stresses occur[1].

7.1.1.5 Coating Thickness

As the coating thickness increases, a decrease in the growth-induced compressive stresses is generally observed[6]. Spalling, however, may occur during or after the process, where high stresses are combined with increasing coating thickness. Coating failure of this kind indicates, however, that as the coating thickness increases, the stresses in the interface have exceeded the limiting failure value[1]. If one takes into account the curve for stress vs. coating depth by Hirsch and Mayr[7] reproduced in Figure 7.1, it will be apparent that a compressive stress maximum occurs in the vicinity of the interface zone. The stress then appears to remain virtually constant over the coating depth (below).

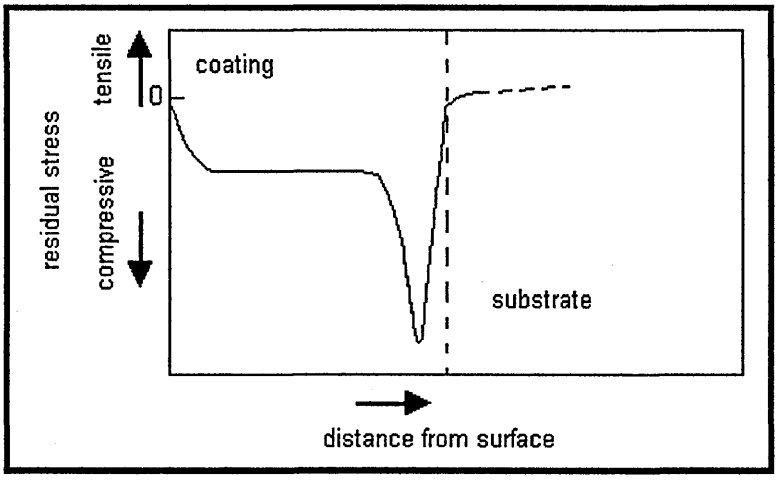

Figure 7.1 Qualitative stress curve in the film-substrate composite of PVD films according to Hirsch and Mayr[7].

The contribution of higher interface stress to a measured mean value will therefore decrease continuously as the coating thickness rises. In addition, X-ray measuring techniques have a limited depth penetration, so that the interface zone is virtually excluded from measurements of thick coatings (10 - 20 μ m).

A Depth vs Stress experiment giving results which are very similar in nature to the above Hirsch and Mayr findings is shown in section 7.6 of this chapter.

7.1.2 The Lattice Distorted by Compressive Stresses

The compressive stresses acting normal to the substrate surfaces, within the films, approximate closely to a plane[1]. The principle stresses, σ_{I} and σ_{II}, are equal and negative, while stress, σ_{III}, at right angles to the surface can expand freely. In crystalline materials, this structure can readily be demonstrated by means of X-ray

measurements of the lattice parameter using the $\sin^2 \psi$ method (see section 7.2 and Ref[8]). The example of a cubic interstitial lattice may be used to illustrate the changes produced by compressive stresses (Figure 7.2).

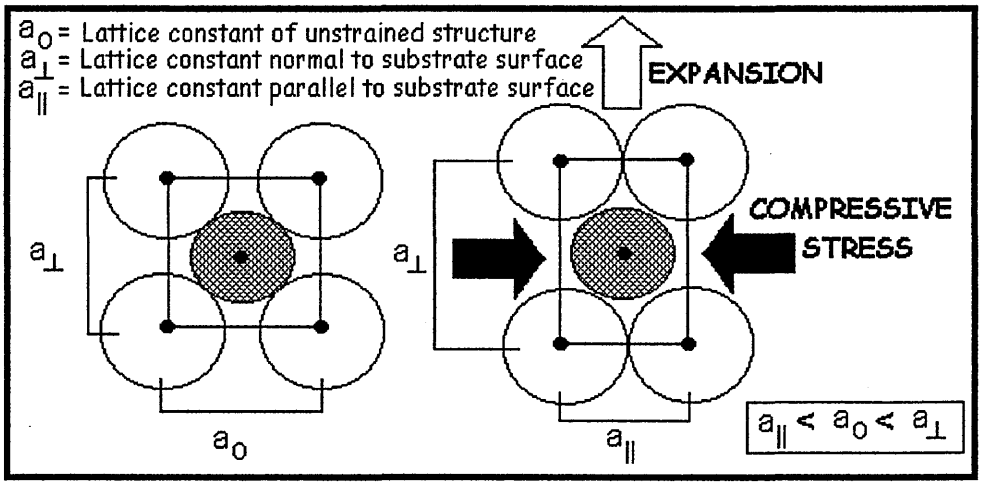

Figure 7.2 Diagram of a lattice distorted by high compressive stresses

The creation of compressive stresses can be divided into three phases[1]:

Phase 1 *Agglomeration of coating constituents on the substrate surface*

Gaps into which no coating atoms actually fit remain at the boundaries of the clusters coalescing at the surface. Additionally, in hard materials with interstitial compounds, not all interstitial atom lattice sites are occupied, so that cells with smaller lattice parameters are formed.

Phase 2 *Incorporation of atoms and ions in confined positions in the bonding lattice.*

Ions or atoms of the vapourised or sputtered material occupy sites that would normally be too small for them owing to their high kinetic energy or as a result of impacting with high-velocity particles. Reactive gas ions or atoms are forced into previously unoccupied interstitial sites for the same reason. Inert gas ions and atoms are implanted in the lattice owing to their high kinetic energy and remain in a constrained position. These processes result in the creation of an extremely dense structure.

Phase 3 *Anisotropic expansion of the lattice*

Owing to the forces of repulsion, the atoms incorporated in confined positions in the lattice encourage a universal expansion of the lattice. At right angles to the surface this is unimpeded. Parallel to the substrate surface, however, adjacent atoms impede this expansion. In addition, due to the impeded expansion parallel to the substrate surface, the agglomerated atoms attempt to make optimum use of the available space. As a result of rearrangement processes, the most densely packed planes lie parallel to the substrate surface[1] (see Figure 7.2).

7.2 Analytical Methods Used for Stress Analysis of PVD Coatings

7.2.1 X-Ray Diffraction (XRD)

X-ray diffraction by crystals can be used to investigate the fine structure of matter by indirectly revealing detail on internal structure down to the order of 1Å. A detector measures the intensity of the diffracted x-rays. During diffraction, a collimated beam with wavelength, λ, strikes a sample which has a regularly repeating lattice (distance D) from which the x-rays are diffracted in all directions. The scattered beams are completely in phase and will be recombined only under an angle θ defined by Braggs law, where λ is the wavelength and n is the order of diffraction.

$$n\lambda = 2D\sin\theta \qquad \textbf{Equation 7.2}$$

From the resulting pattern (or diffractogram) the structure, texture, lattice parameter and the internal stress of the diffracting crystal system can be determined. There are different arrangements of sweeping the detector and sample during the analysis. The most common are $\theta/2\theta$ and the 'glancing angle' methods. Glancing angle ($\sin^2\psi$ - method) was used in these studies to determine the residual stress in PVD deposited TiAlN/VN superlattice coatings (section 7.5). With the $\sin^2\psi$ method the specimen was kept under a constant incident angle whilst the detector moved on a unit circle. Figure 7.3 shows a schematic of the glancing angle technique.

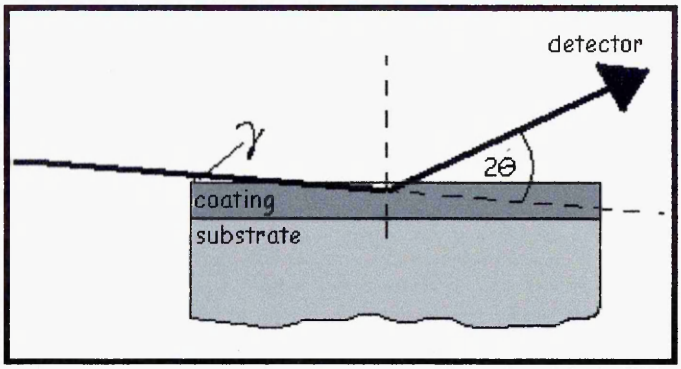

Figure 7.3 Schematic of the glancing angle set-up

The advantage of this method over $\theta/2\theta$ method is that the penetration depth of the x-rays can be controlled, i.e. the smaller the angle, γ, the less penetrating are the x-rays. This has many advantages; such as reducing the substrate contribution and the ability to measure thin surface layers (e.g. oxides). The maximum depth of penetration, X_p, is defined as the depth from which the diffracted intensity is reduced by a factor of e of the incident beam intensity and for a linear adsorption coefficient, μ, and a given diffracting plane.

$$X_p = \frac{\sin\gamma \sin(2\theta - \gamma)}{\mu(\sin\gamma + \sin(2\theta - \gamma)} \qquad \textbf{Equation 7.3}$$

The dependence of the depth of penetration on the angle 2θ is weak, with a deviation below 10%. The arrangement of the glancing angle method is such that when the Bragg condition is satisfied all the allowed planes diffract. From those series of diffraction peaks corresponding to individual lattice spacing from the planes nearly parallel to the surface to those nearly normal to the surface, as the Bragg angle is increased. The 2θ angles for every peak are determined and the lattice parameter can be calculated for every plane. For a thin film in a state of equi-biaxial stress the

relation describing the reflecting lattice planes (a_{hkl}) is given in equation 7.4, where a_0 is the unstressed lattice parameter derived from a Bragg/Brentano ($\theta/2\theta$) scan, ν is Poisons ratio and E is Young's modulus[8].

$$a_{(\theta-\gamma)} = \sigma\, a_0\left[\frac{1+\nu}{E}\sin^2(\theta-\gamma) - \frac{2\nu}{E}\right] + a_0 \qquad \textbf{Equation 7.4}$$

The stress can be determined from the gradient of the least-squares fit of the lattice parameter vs. $\sin^2\psi$ plot (see Figure 7.11).

$$\sigma = \frac{slopeE}{a_0(1+\nu)} \qquad \textbf{Equation 7.5}$$

The linear absorption coefficient of the coating system can be derived by calculating the composition in weight percent, c, and mass absorption coefficients (μ_m) for the contained elements at a given wavelength [Equation 7.6 and 7.7].

$$\mu_m = \sum c_i \mu_{mi} \qquad \textbf{Equation 7.6}$$

The transformation from the mass absorption coefficient into the linear absorption coefficient (μ) is as follows:

$$\mu = \mu_m\, \rho \qquad \textbf{Equation 7.7}$$

The density of the coating (ρ) can be calculated using equation 7.8 (below) where the number of atoms per unit cell (Z), average molecular mass (M_{av}) and Avogadro's constant (N_a) all form the mass of the system and the lattice parameter (a^3) is the volume of a unit cell in a cubic system[8].

$$\rho = \frac{ZM_{av}}{a^3 N_a}$$ **Equation 7.8**

Table 7.1 (below) gives some of the properties for common PVD coating elements [16].

	Ti	Al	C	N	Cr	Y
ρ(g/cm^3)[8]	4.51	2.7	2.27	$1.16.10^{-3}$	7.19	4.48
μ_m(cm^3/g) (CuKα) (1.542Å)[8]	202.4	50.23	4.22	7.14	252.3	127.1
Relative Atomic Mass	47.9	26.98	12.01	14.01	52.0	88.91

7.2.2 Significance and Use

The advantage of the X-ray diffraction method is its capability for measuring residual stress directly and non-destructively. However, it is difficult to measure residual stresses in extremely thin coatings and, for some cases, even in highly textured coatings. Furthermore, X-ray diffraction is inapplicable to amorphous coatings, and a larger scatter in stress measurement is often encountered in coatings with large grain size.

X-ray stress analysis has been applied to many coating systems to evaluate residual stress, because it has a significant influence on the mechanical properties. For example, TiN on milled surfaces[10] whereby a milling procedure was performed to the substrates prior to deposition of a thin TiN layer. A strong plastic deformation in the surface was observed which changed the preferred orientation of crystallites. This

in turn led to an inhomogeneous distribution of residual stress in the TiN coatings. This would presumably happen to a cemented carbide substrate after undergoing the grinding process to form the correct geometry of cutting tool prior to deposition (related to coated tools). Evaluation of the stress in TiN coatings deposited onto biocompatible substrates, such as Ti-6Al-4V, has also been performed because of their significance as materials for surgical implants and total-joint-replacements[11]. On the whole, residual stresses in titanium nitride PIRAC (Powder Immersion Reaction Assisted Coating) onto Ti-6Al-4V alloy were significantly lower than those reported for PVD TiN layers on similar substrates[11]. More complicated superlattice coating systems have been evaluated for example TiAlN/CrN as a function of layer thickness[12]. TiAlN/CrN coatings were grown using PVD technology and adjusting the power to the Cr target between 1 and 12kW varied the CrN layer thickness. The residual stress state in all the coatings was found to be compressive. Residual stresses were found to increase systematically with an increase in P_{Cr} (i.e. power to the Cr target) to a maximum value of 7.37Gpa at 10kW. In addition, an approximate linear dependence of Cr power on period thickness was observed as the superlattice period increased from 2.2nm at 1kW to 4.8nm at 12kW. A maximum hardness value was obtained of $3500HK_{0.025}$ at P_{Cr} = 8kW, when the thickness of the individual layers was measured to be equal[12].

7.2.3 Other Methods of Stress Determination

7.2.3.1 Deflection Method[13]

The deflection method is the most widely used technique for determining the residual stress in a coating system. The basic principle involves the measurement of the amount of bending in a metal strip after deposition of a coating. Consider a coating deposited on one side of a strip substrate. Both coating and substrate are assumed to be homogeneous. A mismatched force at the coating/substrate interface results in residual stress in the coating, which bends the strip either upward (concave) or downward (convex), depending on whether the stress is tensile or compressive.

7.2.3.2 Hole-Drilling Method[13]

This involves drilling a shallow hole in the test specimen to a depth approximately equal to the hole diameter. Typical hole diameters range from 0.8 to 5.0mm. The creation of the hole redistributes the stresses in the material surrounding the hole. A specially designed three-element strain gauge 'rosette' measures the associated partial strain relief. The in-plane residual stresses that originally existed at the hole location can then be calculated from the measured strain relief.

7.3 Measurement of Stress Using Raman Microscopy

There are few techniques that can provide direct experimental information on stresses. Presently, Raman spectroscopy is the only one that can provide such high spatial

resolution. The determination of stresses by spectroscopic means is based on the piezo-spectroscopic effect. That is, on the spectral shift induced by stress. Any applied or residual stress changes the electronic and vibrational levels of the material under examination[14]. Although, the Raman signal is directly sensitive to strain and not stress, the conversion to stress is straightforward, with knowledge of the appropriate elastic constants. When these are not known, performing a piezo-spectroscopic calibration can circumvent the problem. The piezo-spectroscopic coefficients are determined by means of appropriate calibrations. A known stress is applied to the material, and the corresponding frequency change with respect to the unstressed state is recorded[14].

Silicon, for example, has three Raman active optical phonon modes[15]. In the absence of stress, these modes all have the same frequency of $\omega_0 = 520$ cm^{-1}. In the presence of stress the frequency of each of the modes changes/shifts. The relation between the Raman frequency of each mode ω_i (i = 1 to 3) and the components, ε_{ij}, of the strain tensor is given by:

$$\Delta\omega_i = \omega_i - \omega_0 = \lambda_i / 2\omega_0 \qquad i = 1,2,3 \qquad \textbf{Equation 7.9}$$

Where λ_i are the eigenvalues of the secular equation, p, r *and* q are the phonon deformation potentials of silicon.

$$\begin{vmatrix} p\varepsilon 11 + q(\varepsilon 22 + \varepsilon 33) - \lambda & 2r\varepsilon 12 & 2r\varepsilon 13 \\ 2r\varepsilon 12 & p\varepsilon 22 + q(\varepsilon 33 + \varepsilon 11) - \lambda & 2r\varepsilon 23 \\ 2r\varepsilon 13 & 2r\varepsilon 23 & p\varepsilon 33 + q(\varepsilon 11 + \varepsilon 22) - \lambda \end{vmatrix} = 0$$

Equation 7.10

Solving this secular equation (Equation 7.10) results in complicated relations between the $\Delta\omega_i$ and the 6 elements of the strain tensor. As a result, for each position on the sample, one has a relation between one experimental value, that is the frequency shift of the Raman peak ($\Delta\omega$), and 6 unknown variables, i.e. the ε_{ij}. In order to get a first estimation of the magnitude of the stress one can assume uniaxial stress[15]. In this case, the relation between $\Delta\omega_i$ and stress is linear.

7.3.1 Previous Raman Studies of Stress

Raman microscopy has been applied for the study of stresses in polycrystalline AlN[14] where sintered samples were prepared and then a piezo-spectroscopic calibration applied to a polycrystalline Si sample. The calibration was conducted by applying uniaxial stress, so that a piezo-spectroscopic coefficient averaged over all crystallographic directions was derived. The determined coefficient was then used to map the residual stresses around a Vickers indentation in a sample prepared without a sintering aid. The residual stresses were different along different directions of the indentation. This was attributed to the presence of cracks. These cracks were responsible for the larger experimental scatter that was observed at low load along the diagonal. This highly inhomogenous stress field translated to a large scatter, absent in data collected perpendicular to the indentation edge, where cracks were not present. The region just at the edge of a crack was subjected to a stress completely different from one a few micrometers away (given the very high spatial resolution, and the fact that minor cracks were not always visible under the microscope). It was evident that the long-range crystalline order was increasingly disrupted, moving toward the indentation centre, which was the point with the highest stress concentration due to

the loading of the indenter. The crystalline disruption was thought to be due to a high dislocation density introduced just beneath the surface by the indenter, but partial amorphization was also not ruled out[14].

Fibre deformation and residual strain in silicon carbide reinforced glass composites have also been studied[16]. It was found that well-defined Raman spectra could be obtained from such fibres and that the peak positions of the Raman bands of these type fibres were sensitive to the level of any externally applied stress/strain. The $1600cm^{-1}$ band of the Nicalon fibres was sensitive to the level of applied stress/strain, which was attributed to graphite within the fibres. Raman spectra were obtained from the freestanding fibres in air during deformation in a small straining rig that was fitted directly onto the microscope. After applying tensile deformation of the fibres with 1.4% strain, a shift to lower frequency was observed, which was approximately linear. This shift was attributed to macroscopic deformation resulting directly in the increase of the C-C interatomic distance, i.e., the bond stretching which caused a red shift in the position. In addition, during tension, due to the inhomogeneous microstructure of the fibres, the local strain on the interatomic bonds varied with local environments such that the application of tension generally caused some band broadening. It was then found that fibres near the surface of the composites examined were subject to a residual compressive strain of the order 0.6%[16]. The same group then went on to study the residual thermal stresses in Nicalon SiC fibres and also for alumina-zirconia fibres[17]. They found that the values obtained experimentally agreed well with those calculated analytically. Heat treatment of a model SiC/Pyrex composite at high temperature was found to cause crystallisation of the matrix that consequently led to a considerable increase in the measured residual fibre strain. In the absence of

crystallisation they found that the fabrication temperature of the fibres did not influence the magnitude of the residual fibre strain[17].

Graphite/epoxy composites loaded in compression can fail by kink-band formation/microbuckling and this has limited the use of graphite/epoxy composites in structural applications[18]. The observation of kink-band formation was monitored by means of Raman microscopy by Narayanan et al[18] in the hope that this would pave the way to understanding compression micromechanics and in turn help improve the design and development of high performance composites. A four-point bending set-up was used to test single-tow composites. A micro-strain gauge measured the strain on the top surface of the composite and as the fibres began to fail a colour 'mavigraph' was used to capture the surface profile. They determined the sequence of events in the breaking of a fibre and found that it was essential to obtain the strain profile by 5μm intervals in order to obtain the strain along the fibre[18].

The relationship between processing, structure and properties for high-modulus PBO fibres (p-phenylene benzobisoxazole) was investigated by Kitagawa et al[19]. This high strength super fibre, which has a Young's modulus higher than that of any other commercial fibre, has been studied to determine how the different processing conditions that led to different morphology affected the mechanical properties. The 1618cm^{-1} of the fibre was seen to shift to a lower wavenumber and broaden with tensile deformation but shift in the opposite direction (and narrow) in compression[19]. The values of stress-induced Raman shift for the PBO fibres were around –4.0 cm^{-1} / GPa[19].

Collagen fibres have also been studied using Raman microscopy. These were subjected to in-vitro axial tension as a way to monitor the vibrational changes and specific assignments of the Raman spectrum of collagen[20]. Two distinct responses were observed, depending on whether the vibrations were axial to, or normal to, the collagen backbone[20]. The former response produced a shift to lower wavenumber, indicating tension, whereas the latter produced a shift to higher frequency, indicating compression. The rate of wavenumber shift with applied strain was non-linear, with a marked increase at higher levels of applied stress/strain. There was also evidence for ordering after stretching of the helices and straightening of the molecular kinks via a decrease in band width of the $822cm^{-1}$ mode[20].

Ceramics have also been the subject of much attention. Pezzotti[21] describes how the use of Raman mapping can be employed to study a variety of internal microscopic stress fields which exist in polycrystalline ceramics, as a consequence of thermal expansion mismatches or from fracture and deformation. Internal residual stresses could exist both in monolithic and composite polycrystalline ceramics as a result of thermal expansion anisotropy. The magnitude of the stresses was dependent on the inherent physical properties of the constituent phases, as well as on the processing and machining conditions[21]. For ceramics, the microscopic residual stress fields play a decisive role in the overall mechanical performance of the material. Residual stresses arising from thermal expansion anisotropy of the grains in single phase polycrystals can result in spontaneous cracking, primarily along grain boundaries, with a dramatic drop in material strength[21]. Piezo-spectroscopy was adopted for the study of residual stresses in an Al_2O_3-matrix (average grain size $\sim 10cm^{-1}$) containing a volume fraction of 20% α -SiC (platelet-shaped) dispersoids (average diameter and thickness

~20μm and ~3 μm respectively). The map of residual stress in this Al_2O_3 composite, demonstrated areas of GPa-order tensile stresses. These were found to exist locally in correspondence with the matrix-platelet interfaces or in sites where, although not visible, a platelet was placed in the sub-surface region[21]. Stress mapping of Al_2O_3 has also been performed by other authors who have also used the well established method of measuring the peak shift in the characteristic optical fluorescence line produced by Cr^{3+} impurities in the Al_2O_3 lattice[22]. The in-situ stress variation in chromia (α-Cr_2O_3) oxide scales as they formed on the surface of chromium metal at 800°C was performed by Gardiner et al[23]. They also determined the stress state in protective chromia scales that developed on the surface of 20Cr-25Ni-Nb stainless steels after a treatment temperature of 1000°C. A stress map of a grain of Cr_2O_3 showed that stress valleys and plateau regions (corresponding to the grain centre) existed[23]. They concluded that both ex-situ and in-situ oxidation experiments gave semi-quantitative stress values by comparison with static high pressure measurements in a diamond anvil cell[23]. Initial Raman stress mapping experiments performed by Gardiner[24] were applied to silicon devices whereby the highly regular structure of integrated circuitry was used to asses the spatial resolution of the instrumentation. These maps were generated using the strong optical phonon of silicon at 520cm^{-1}. A further example of this imaging capability was demonstrated with stress-stabilised zirconia (ZrO_2)[24]. The white light images gave neither indication of structural features, nor the distribution of the components of interest. The tetragonal to monoclinic phase transformations were followed on an MgO stabilised sintered ZrO_2 ceramic that was polished and Vickers indented with a 30kg load. A significant phase transformation to the monoclinic form in the region adjacent to the indent was observed[24]. A further investigation was performed across a grain boundary to study

the extent of stress-induced phase transformation[25]. The Raman mapping across a grain boundary gave clear evidence that the sample was predominantly the tetragonal phase but with higher monoclinic phase at the boundaries[25]. In addition, the broadening of the monoclinic phase distribution after applied stress (indentation) was thought to provide a possible route for stress relief[25].

Raman microscopy has also been adopted for the determination of stress in polycrystalline diamond cutting tools[26]. A three-layered polycrystalline diamond cutter was cross-sectioned and measured along the centre line. The Raman shift in each of the three layers was determined and was found to be approximately biaxial within the dense outer layer, and hydrostatic throughout the two inner layers. The stress measured along the thickness of the outer diamond layer was found to be compressive with an average value of 1300Mpa. The two inner layers were found to be lower, ranging from 870-950Mpa[26].

7.4 Results From Raman Analysis of Residual Stresses in TiAl(Y)N/VN Coatings

A series of TiAl(Y)N/VN coatings were deposited onto stainless steel and cemented carbide substrates with varying bias voltage (-75 to –125V) such that 4 different coatings were prepared.

TiAlN/VN and $TiAlY_{(2at\%)}N$/VN (–75V bias)

TiAlN/VN (-95V bias)

TiAlN/VN (-125V bias)

The effect of bias voltage and Y incorporation on the residual stresses in the aforementioned coatings were investigated. Figure 7.4 shows the shift in the main optic mode at ~650cm^{-1} with increasing bias voltage and yttrium incorporation.

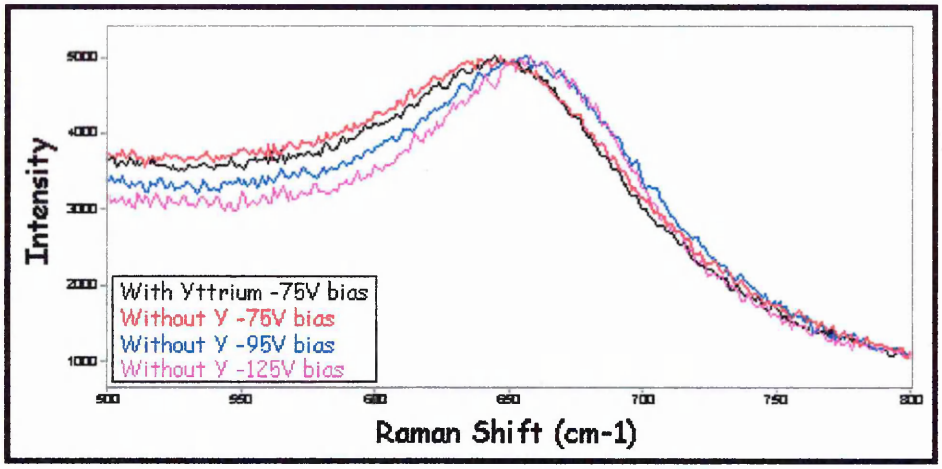

Figure 7.4 Shift in the main optic mode with bias voltage / yttrium incorporation

It may be seen that there was a shift to high frequency of the Raman band with a corresponding increase in bias voltage. In addition, there was also a slight shift in the coating band with yttrium incorporated within the structure when compared to the non-yttrium containing coating deposited with the same bias voltage i.e. –75V. This indicated that there was an increase in compressive residual stresses with an increase in bias voltage. This agrees well with the theory described in section 7.1.1 of this chapter. The further small increase in compressive stress with Y incorporation can be explained due to the fact that Yttrium has a large atomic radius and thus distorts/expands the crystal lattice further. The optic mode at ~650cm^{-1} was band fitted with 50/50 mixed Gaussian / Lorentzian band profiles. The results are tabulated below (Table 7.2).

Table 7.2 Band Fitting Results

Sample	Position (cm^{-1})	Width (cm^{-1})	Area (Arb. Units)
-75 V (with Y)	650.1	95.3	2823925
-75V non-Y	649.4	101.6	278183
-95V non-Y	658.9	102. 8	298810
-125V non-Y	660.1	88.5	172708

There was a maximum shift in the band position of ~$10cm^{-1}$, the band width appeared to become narrower with an increase in bias voltage. In addition the Yttrium-containing coating had a narrower band width when compared to the non-yttrium coating (-75V). This may be explained by the different microstructures in which a interrupted columnar growth occurred for the yttrium containing coating as compared with the typical columnar growth structure found for non-Y coatings[27]. Figure 7.5 (below) shows ESEM images of the coating surfaces/microstructure.

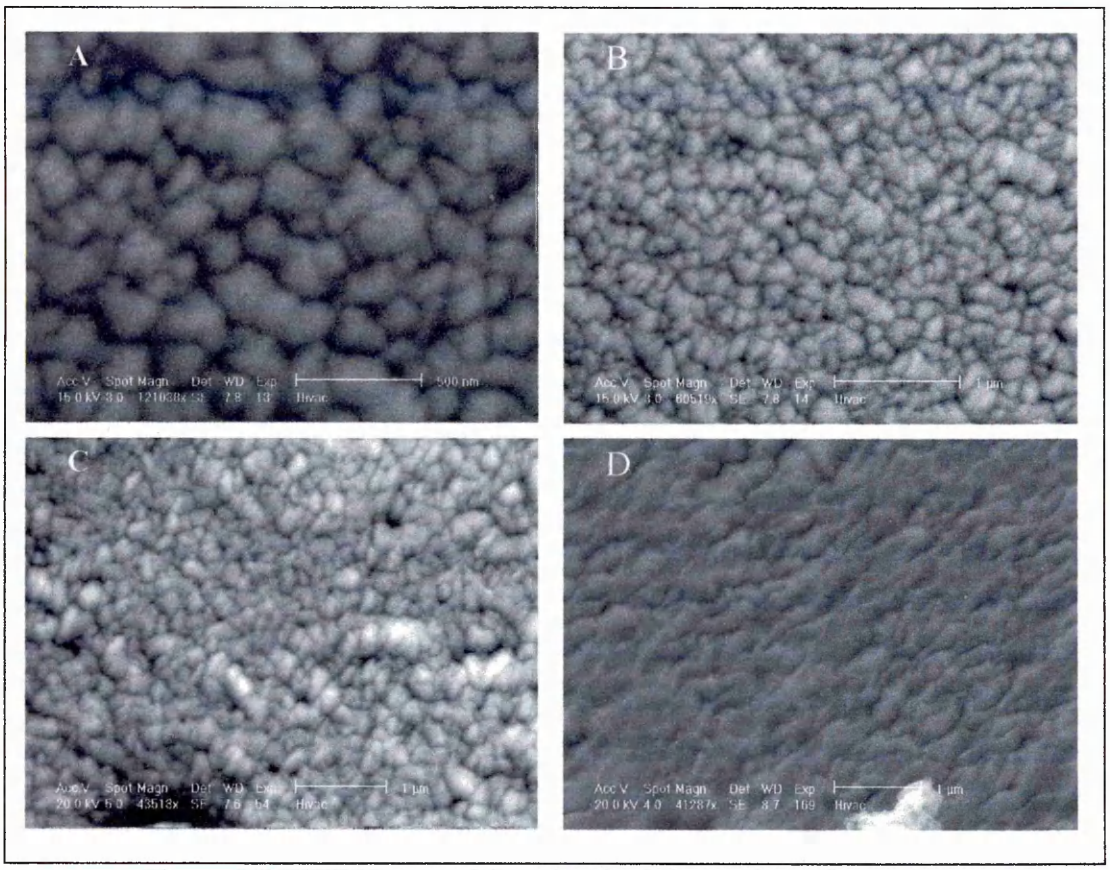

Figure 7.5 ESEM images (plan views) of the coating microstructures Image A and B: TiAl(Y)N/VN –75 V bias; C: TiAlN/VN –75 V bias; D: TiAlN/VN – 125 V bias

The images allowed the surface topography of the coatings to be investigated, especially the columnar growth. It was uncertain as to the effect of Yttrium incorporation. What was evident from the images was that A to C were definitely columnar growth with well-defined grain boundaries (i.e. –75 V bias TiAl(Y)N and the non-yttrium containing coatings) whereas D, at a –125 V bias, appeared to have a different microstructure with a larger grain size with smaller spaces in between the columns, i.e., reminiscent of near-equiaxed microstructure (see the structure zone model predicted by Movchan and Demchishin (page 9 chapter 1). The effect of

different laser wavelengths (514.5, 633 and 782nm) on the Raman spectra arising from Supercote-33 (TiAlN/VN) (i.e. the main optic mode at ~650cm^{-1}) was studied and values obtained from band fitting are displayed graphically in figures 7.6 (band position), 7.7 (band width) and 7.8 (band area).

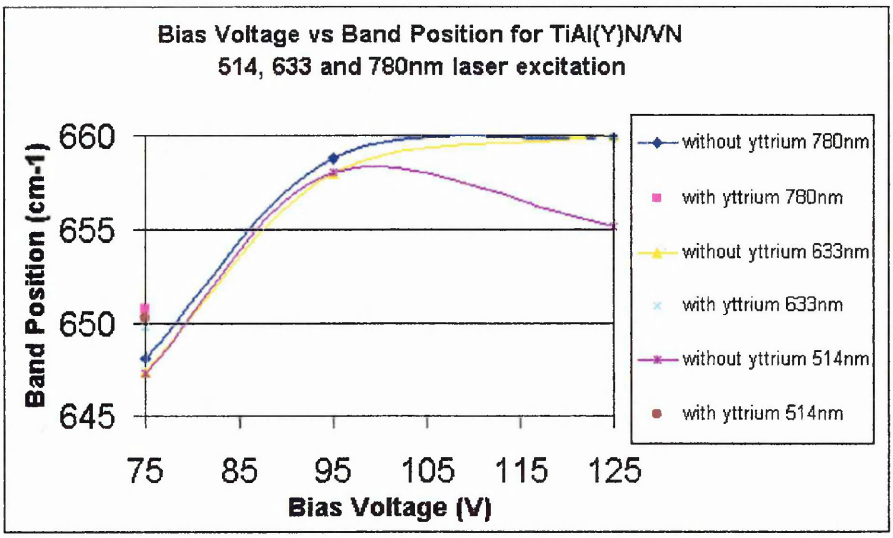

Figure 7.6 Plot of bias voltage vs. band position for TiAl(Y)N/VN (N.B. The band positions were calculated from a mean of 5 different measurements at various positions on each coating)

It was evident from the graph that for all excitation wavelengths there was an increase in the band position with bias voltage, indicating an increase in compressive stress. What was also interesting was the difference in band positions with excitation wavelength. The data points from 514.5 and 633nm excitation were essentially overlaid, until the -125 v bias spectrum taken with 514.5nm excitation where there was a strange effect with the stress level seemingly reducing. The band position changed going from –95 to –125 v but for the 633 and 780nm data points it appeared to plateaux. This phenomenon could possible be due to the lower penetration depth when using 514.5nm excitation. Fewer grains would have been sampled, especially in the Z-direction, which may have lead to this difference. PVD coatings are known to have a stress gradient[7], with the highest stresses occurring at the interface region

between the coating and substrate, due to lattice mismatch and thermal effects. The stress then decreases outwards from this interface region. The stress gradient in these coatings is investigated in Section 7.6 of this chapter. A further interesting outcome was the band position acquired at 633nm. This was for the Yttrium containing –75 v bias coating that appeared to signal the lowest stress of the three spectra, although the three spectra had band positions that were very similar. There were also band width discrepancies when using different energies of excitation (Figure 7.7 below).

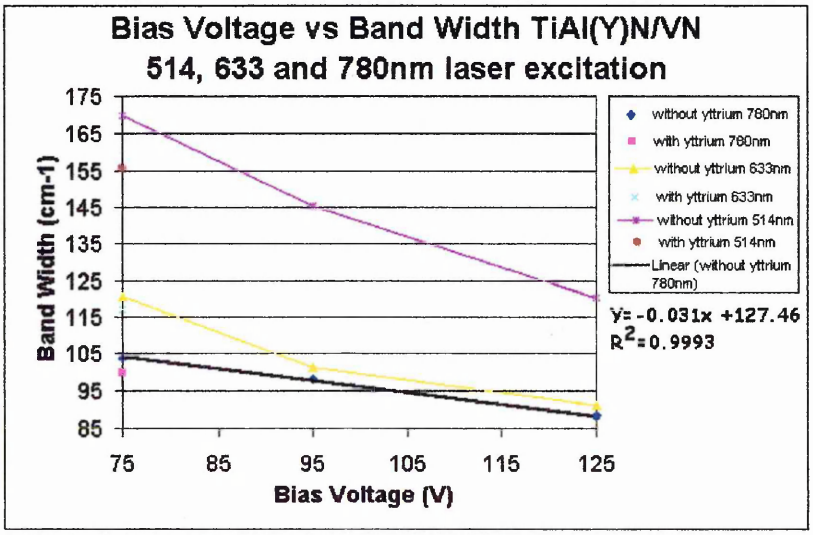

Figure 7.7 Plot of bias voltage vs. band width for TiAl(Y)N/VN

Quite dramatic differences were observed with a pattern that appeared to suggest the higher the energy/lower the penetration of the incident beam resulted in the broadest detected band. This may be due to the laser sampling the column tops, which will be more disordered than the bulk coating as not every column will be terminated with a full unit cell, and, in addition, will not have gone through the same thermal cycle (i.e. deposited last). With all excitations, the coatings appeared to become more ordered. This was evidenced by a decrease in the band width with an increase in bias voltage. A linear trend line was fitted to the data-points acquired with 780nm excitation. A

correlation coefficient of 0.9993 was found indicating that the linear relationship was a well-established one. The other data-points also showed a near linear dependence. This may be explained by the fact that at higher voltages the ions have more energy in which to find favourable sites, thus giving a more ordered structure. The Yttrium containing coating (-75 V bias) gave a band width which was narrower than that of –75 non-Y containing coating. This indicated that the coating structure was more ordered with yttrium incorporation (even at such low levels (0.02at%)). This must be due to a small difference in microstructure with yttrium incorporation. Incorporation of Y within TiAlN coatings does result in substantially different microstructures[28]. For non-uniform incorporation a columnar growth mechanism was apparent but for uniform Y distributions a surprisingly equiaxed microstructure resulted, determined from cross sectional X-TEM[28]. A difference in band area was apparent with excitation energy (see Figure 7.8 (below)).

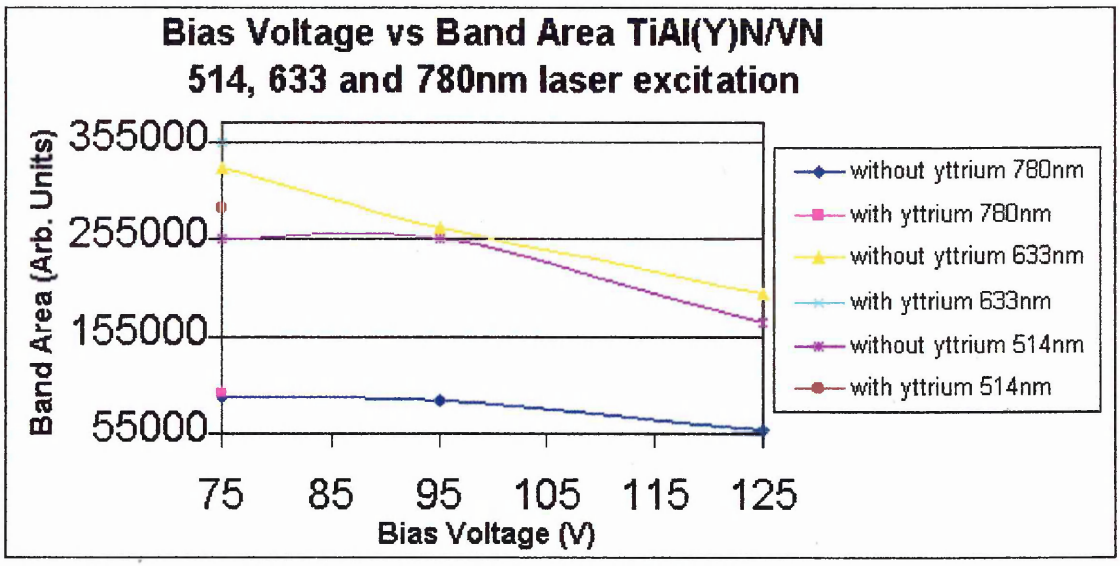

Figure 7.8 Plot of bias voltage vs. band area for TiAl(Y)N/VN

This can mostly be attributed to the $1/\lambda^4$ dependence on Raman scattering with excitation wavelength. The 780nm spectra had the lowest intensity bands for the

same exposure time; the 514.5nm spectra were then next, followed by 632.8nm. This apparent reversal of the 514.5 and 633nm band intensities can probably be attributed to a better alignment of the Raman system (increased energy throughput) of the 633nm system when compared to the 514.5nm system. A defect induced first-order Raman scattering mechanism occurs for fcc polycrystalline PVD coatings (discussed in chapter 3). The increase in bias voltage (as previously mentioned) gives the arriving atoms more energy in which to find energetically favourable sites and thus results in a structure with fewer defects, and thus, a reduction in Raman scattering.

A comparison of the residual stresses arising from coatings deposited onto different substrates, i.e. HSS and SS, was performed. The coating deposited onto stainless steel should, from the theory, have higher intrinsic stresses. This is predicted due to a higher thermal component of the residual stress occurring (see Equation 7.1). Stainless Steel has a higher thermal expansion coefficient than HSS and will result in a greater difference in the SS-coating system than for the HSS-coating system. The non-yttrium containing coatings were investigated on both HSS and SS substrates. Figure 7.9 (below) shows the band position vs. bias voltage for these coatings.

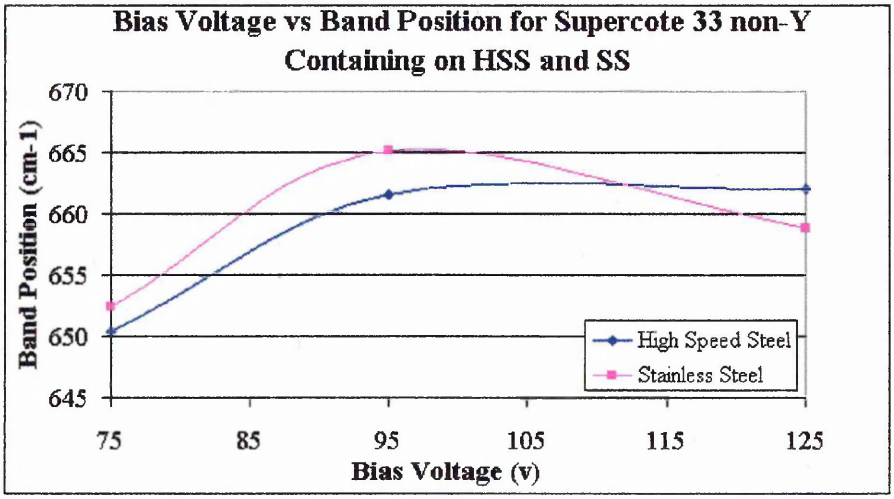

Figure 7.9 Plot of bias voltage vs. band position for TiAlN/VN for SS and HSS substrates (633nm excitation)

The band position arising from the coatings deposited onto stainless steel was at higher frequency than that of HSS samples. This indicated that higher intrinsic residual stress occurred for the coatings deposited at –75 and –95 bias on SS. This appeared to be reversed for the –125v bias coating in which the coating deposited onto HSS appeared to have the higher residual stress.

This work has shown that Raman microscopy is sensitive, via band position shifts, to residual stresses within TiAl(Y)N/VN coatings. A correlation of Raman microscopy (band position/shifts) with glancing angle XRD measurements was then performed to assess the complementarity of the two techniques.

7.5 XRD Stress Analysis ($\sin^2 \psi$ - method)

XRD measurements of the coatings were performed at 2 and 10° incidence on both HSS and SS substrates (N.B. the Yttrium containing coating was only on HSS (not SS)). The graph below (figure 7.10 XRD stress analysis of coating deposited onto HSS and SS.

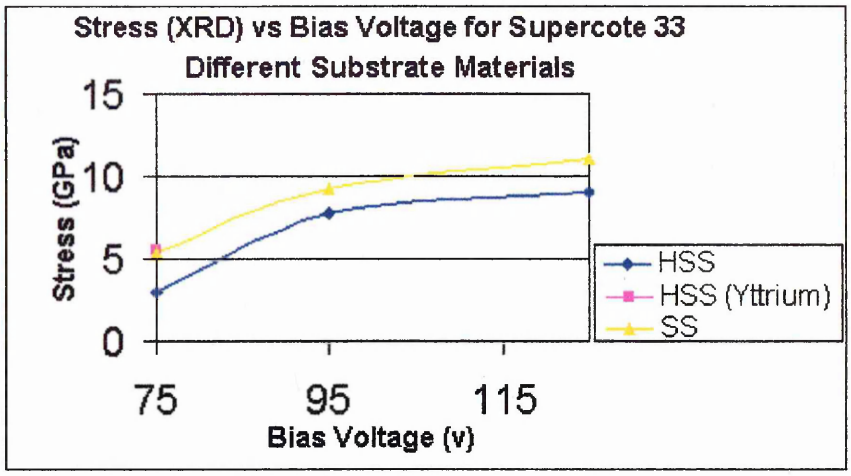

Figure 7.10 Stress vs. bias voltage for all the coatings on both SS and HSS (10^{o} incidence).

This demonstrated essentially, the same result as the Raman analysis, i.e., that coatings deposited onto stainless steel substrates have higher residual stresses than for coatings on HSS. The consequence of this is that higher residual stresses will be recorded for routine XRD stress analysis, as SS is the preferred substrate material for analysis due to a smaller substrate contribution in the patterns. Coatings deposited onto HSS substrates can only be studied with XRD at 2^{o} incidence due to the larger number of interfering peaks associated with the HSS (carbide within the structure). Raman microscopy does not suffer from substrate issues (owing to the small penetration depth) but does, however, measure a lower than average stress level due to the stress gradient which is at a maximum in the coating-substrate interface for the same reason. The cross over in the band position for the –125V bias that was observed for the Raman analysis (Figure 7.9) was not observed in the XRD stress analysis. This indicated that a parameter, which was sensitive in Raman microscopy, might have been the cause for the shift, i.e., a small compositional change perhaps.

The sin ^{2} ψ plots obtained from the XRD stress analysis are displayed below:

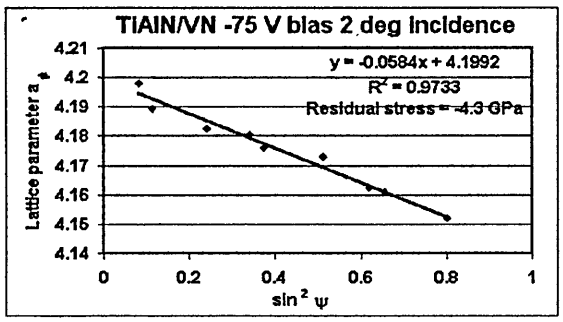

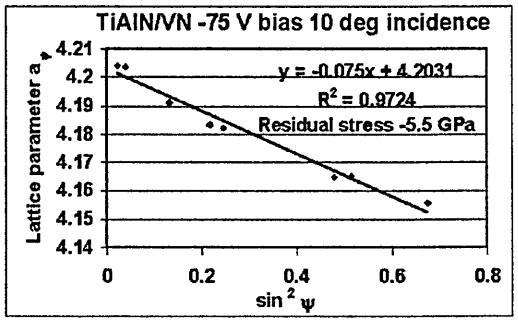

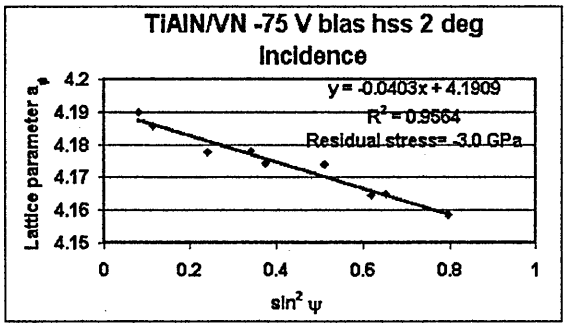

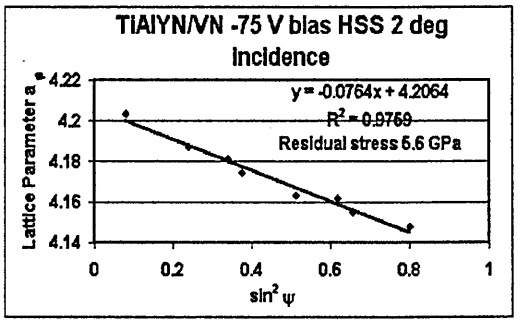

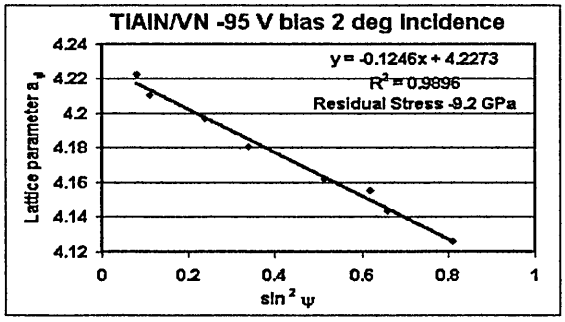

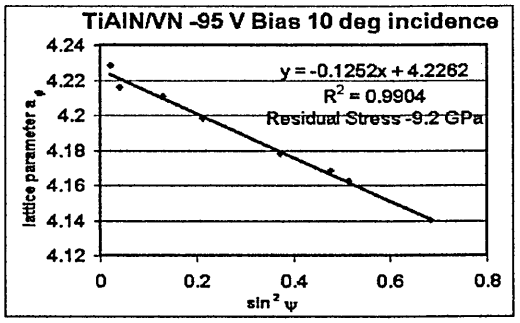

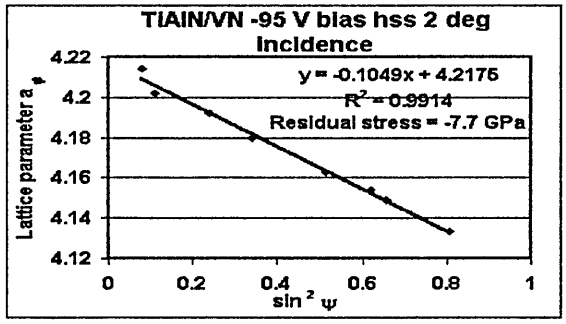

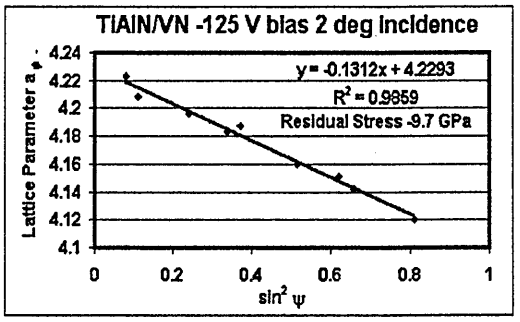

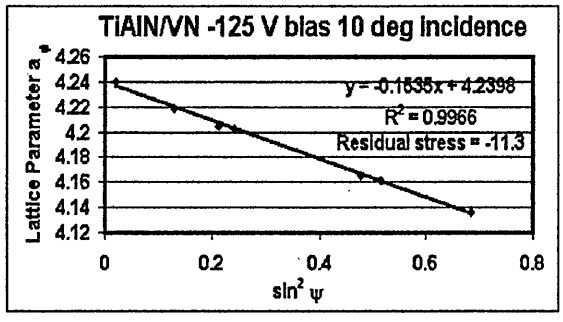

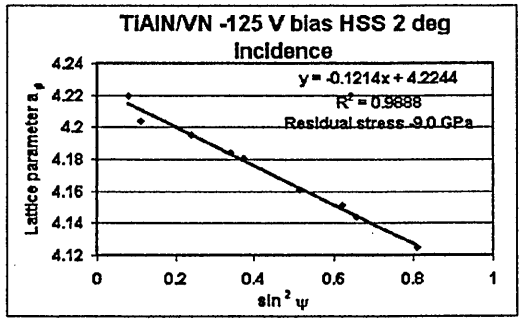

Figure 7.11 show the sin^2 ψ plots obtained from the XRD stress analysis

Table 7.3 (below) shows all the stress values obtained from XRD analysis (all bias voltages, incidence angles, substrates and yttrium/non yttrium contents are displayed):

Bias Voltage	Stainless Steel		HSS
	2°	10°	2°
-75	-4.3	-5.5	-3
-75 (yttrium)	----------	----------	-5.6
-95	-9.2	-9.2	-7.7
-125	-9.7	-11.3	-9.0

A comparison between stress values obtained from XRD analysis with the observed band positions from Raman analysis (514.5, 633 and 782nm excitation) was performed to ascertain if there was any correlation. Figure 7.11 shows a graphical representation. The 2° incidence angle (HSS substrates) data was used. This was thought to be more comparable in terms of penetration depth of the laser beam than that of 10°.

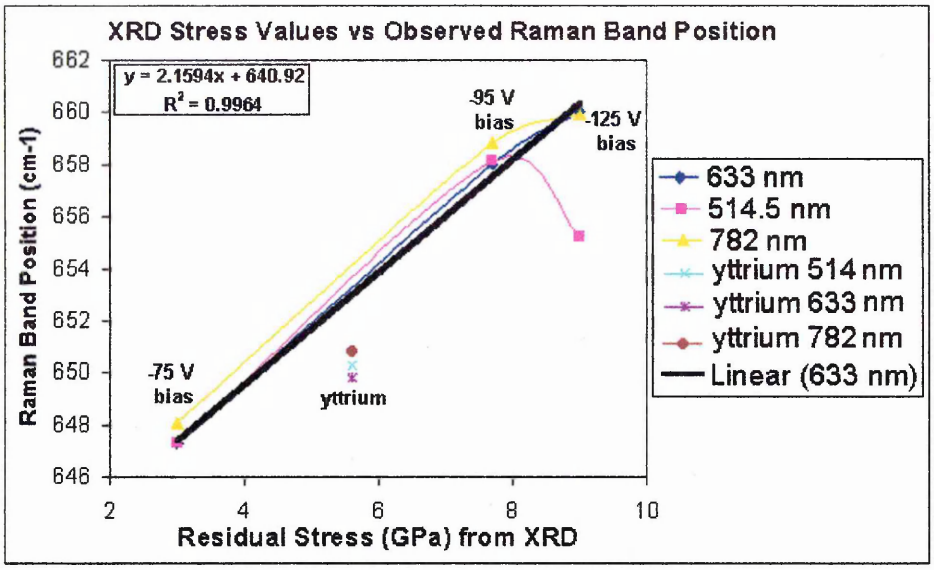

Figure 7.12 Raman band position vs. XRD stress values (N.B. the Raman band positions were calculated from the mean of 5 measurements-per-sample at each laser wavelength and bias voltage value).

What could be seen from the above graph is that there was a definite correlation between stress values obtained from X-ray diffraction and band positions from the Raman analysis. The spectra acquired using 633nm had the best correlation with an R^2 value of 0.996. The yttrium containing coating did not correlate well (but there was only one sample). This may be because of the addition of yttrium with a high RAM = 88.91, in addition, to increasing the stress value by distortion of the lattice, it may also have shifted the band position to lower frequency, i.e., a further heavy atom within the crystal lattice. The 514.5nm data at 125v bias showed a large deviation from the line that appeared to demonstrate a drop in residual stress level. This is also evident, albeit to a lesser extent, in the 780nm data. The explanation for this is difficult to predict however it is thought to be due to a penetration depth effect, but is not fully understood.

The residual stress values within coatings is also known to have an effect on the coating hardness[4]. It was therefore interesting to investigate if there was a

correlation of the residual stress levels measured using XRD with the Vickers hardness values(0.0025N). Figure 7.14 shows the hardness vs. stress value (measured using 2° incidence). This was because the indentation depths are usually in the order of 50-200nm, therefore the hardness information coming from the coating without interference from the substrate material[31].

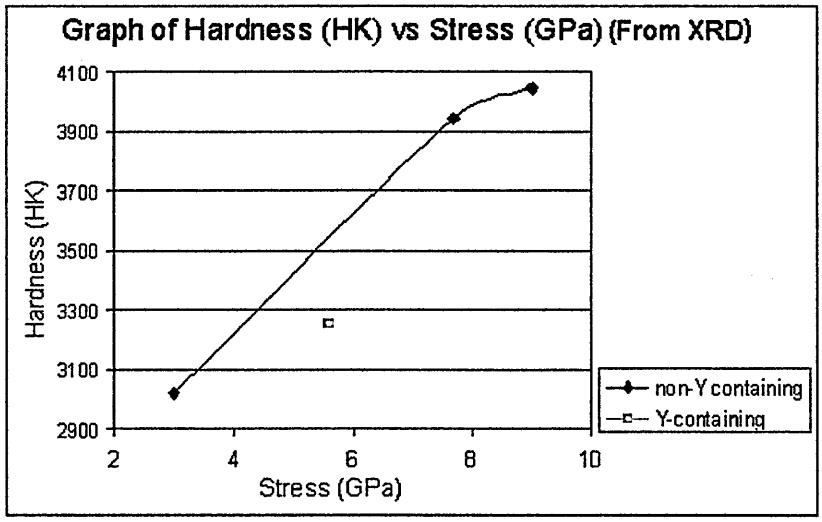

Figure 7.13 Correlation of hardness with stress values obtained from XRD measurements

The yttrium containing coating deviated the most from the trend but also there was a discrepancy on going from –95 — 125 V bias. There was therefore a poorer correlation of the hardness vs. stress. A comparison of the correlation between Raman band position with hardness was then investigated. Figure 7.15 (below) shows the results from this comparison.

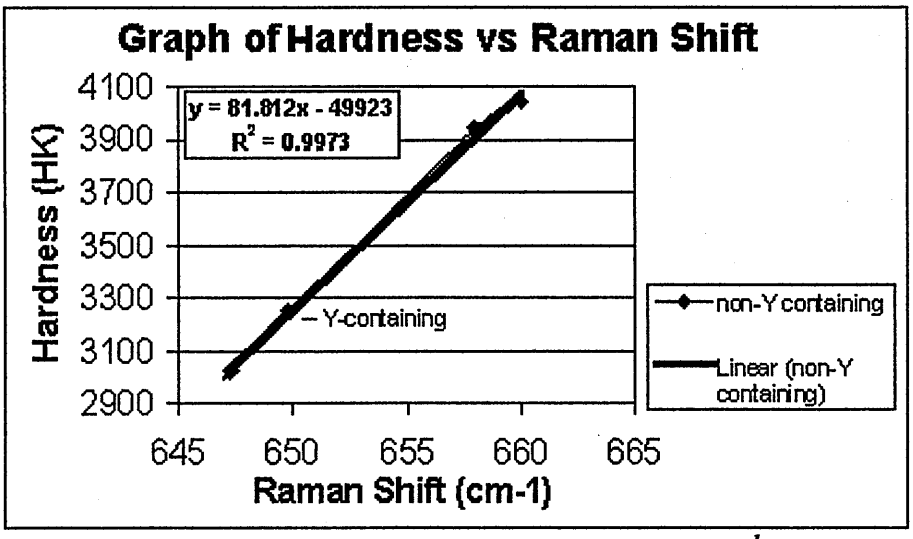

Figure 7.14 Hardness (HK) vs. Raman Shift (cm^{-1})

A linear trend line was used as an indicator of the overall fit/correlation. It appears that there is a very good correlation (R^2 value = 0.997) between hardness and Raman shift for the TiAlN/VN coating systems (even for the yttrium containing coating which has deviated the most from prior comparisons). To fully investigate the applicability of using the Raman shift of the optic modes of PVD coatings as a predictor of hardness needs further investigation.

7.6 Depth Profiling of Residual Stresses Using Raman - GDOES

It is well known that a stress gradient exists within PVD deposited hard coatings (see section 7.1.1 (Stress Dependence on Coating Thickness)). Due to the very low penetration depth of the laser beam into the coating structure, although sampling a spatial number of unit cells, Raman measurements will not give an average stress value but a value close to the coating surface (~30 - 100nm). It was then interesting to observe if Raman microscopy could indeed measure this stress gradient. Initial thoughts for doing this was to use ball cratering to remove layers of material to

gradually profile through the coating, i.e., take measurements at intervals through the coating. Ball cratering was thought to be a poor method as additional stress/disorder may have been introduced into the coating via the abrasive mechanism of coating removal. Glow Discharge Optical Emission Spectroscopy was suggested[29] as a technique of sputtering away coating layers to depth profile the coating structure. GDOES uses accelerated Ar^+-ions (in a partial vacuum) to remove coating material and is usually used to gain information on the depth distribution of elements. The amount of damage caused to the underlying coating by this method is minimal (i.e. a damage to a depth of ~20 Angstroms)[29]. The GDOES method was therefore chosen for this analysis. The –95 and –125 V bias coatings (on HSS) were used for the analysis. The graph below (figure 7.13) shows the depth vs. sputtering time for the GDOES coating removal. The depth of the GDOES craters were measured using a Rank-Taylor-Hobson Talysurf profiling equipment which uses a diamond stylus to profile surface topography with a depth resolution of ~10nm[30].

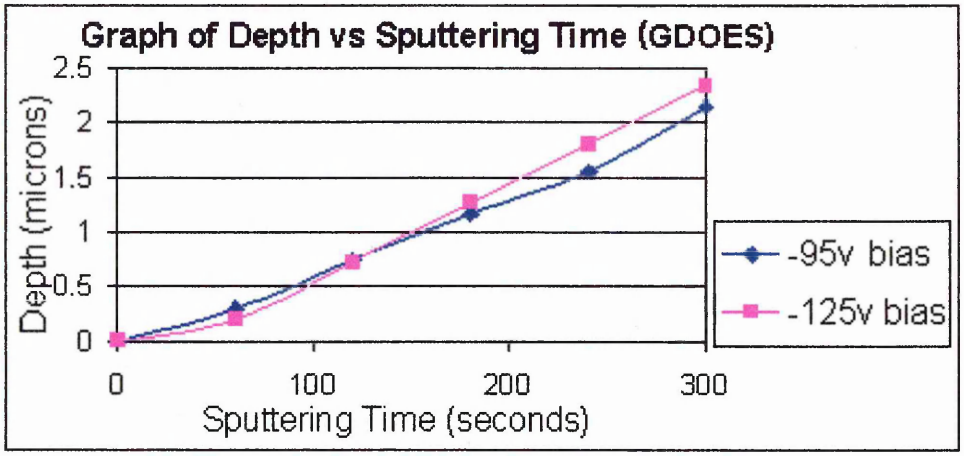

Figure 7.15 Depth vs. sputtering time for GDOES coating removal technique

A Raman measurement was acquired from the centre of each crater and was plotted against depth (figure 7.15 (below)).

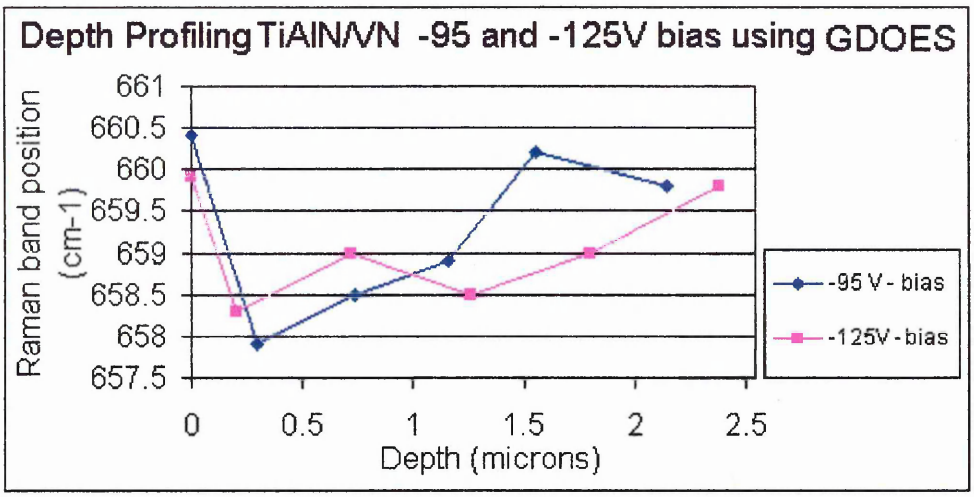

Figure 7.16 Raman analysis of the GDOES craters i.e. depth profiling of the coating structure.

The Raman band position did change with depth into the coating structure toward the coating – substrate interface (assuming there was no modification due to sputtering). At 200nm, just beneath the surface, the band position appeared to indicate that there was a rapid reduction in stress. The deeper into the film, toward the coating – substrate interface, the stress appeared to rise to almost the value measured on the surface. The shape of the graph was similar to the one published by Hirsh and Mayr[7] which was for thicker coating systems (figure 7.1). The coupling of GDOES with Raman to depth profile through PVD coatings seemed successful and could be implemented for other such investigations.

7.7 Investigation of Externally Applied Stress on the Raman Spectral Bands of TiAlN

This investigation was conducted to investigate the possibility of creating a Raman based and calibrated method for residual stress analysis.

7.7.1 Design and Construction of a Four-Point Stress Rig

A four-point stress rig was suggested similar to the one implemented by Oettle et al[32], in which critical tensile stresses for cohesive failure and critical compressive stresses for delamination were studied using in-situ (four-point bending) XRD measurements. A dial gauge was utilised in the aforementioned measurements as a way of determining bending displacement/deflection. The initial idea for the Raman four-point stress rig is shown schematically below (Figure 7.17).

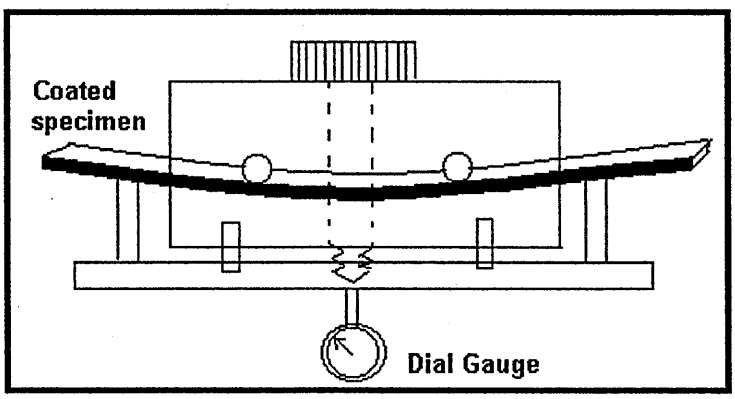

Figure 7.17 Initial idea for the four-point bending device for Raman analysis

The above device would be ideal for studying compressive stresses but a further device would be required if tensile stresses were to be investigated. A device that could measure both was desired. A small modification of the above device would allow both compressive and tensile stresses to be studied. This was to incorporate a V-shaped grove in the outer bending points (see Figure 7.18 (below)).

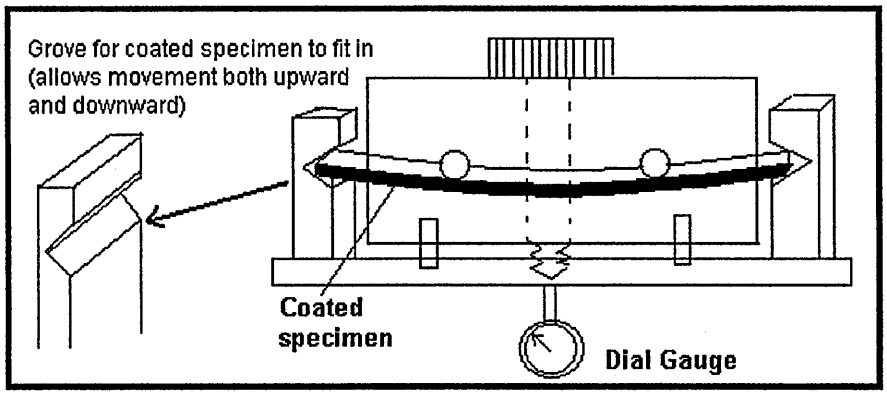

Figure 7.18 Improved four-point bending rig design

The bending experiments were performed on TiAlCrN coated specimens (1 x 5 cm x 3mm) of stainless steel. The coatings were 1 μm thick and were deposited onto both sides of the substrates. A bending displacement of 1.6mm in the compressive direction was performed with measurements being taken after every 0.2 mm. This compared to the work of Oettel et al who used deflections of 4 mm[32]. Although the deflection used in this experiment was relatively small, the coated specimen was plastically deformed. Therefore another coated specimen was required to perform tensile stressing (1.6mm).

A further complication was that there was a slight inhomogeneity of band position on the surface of the unstressed coated specimens. This was probably due to the grains of the austenitic stainless steel beneath the coating (see Figure 7.19). These grains become evident after the ion-etching phase of the deposition process[33]. A preferential etching occurs revealing the SS structure. Each individual grain of the austenitic SS will result in a particular orientation of the coating growing on top and due to the lattice mismatch between the coating and the different grain a slightly different stress state will result. This can be observed under an optical micrograph (see Figure. 7.19).

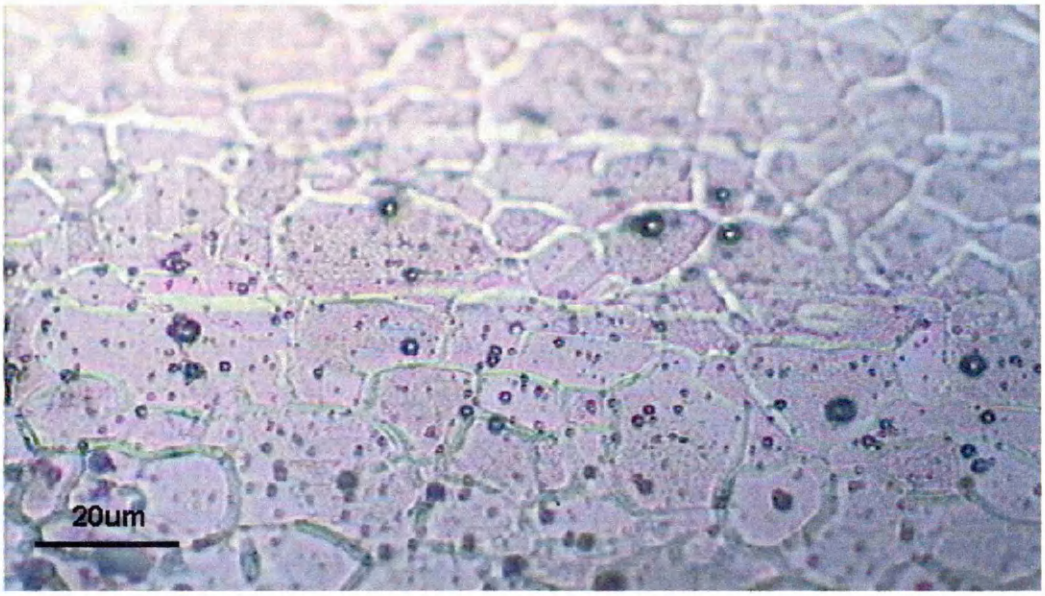

Figure 7.19 Optical micrograph showing the surface characteristics of coated specimens

To minimise the effect of these grains the same position on the surface of the sample was investigated each time (for the same bending test). This was possible by marking the surface with a scratch (for ease of location of sampling area when under the optical microscope) and choosing a grain in which to take the measurements from in the vicinity of the scratch but further enough away so as not to have an influence on the measurements (see chapter 4). This appeared to reduce the overall scatter. The results of the bending test is displayed in figure 7.20 (below)

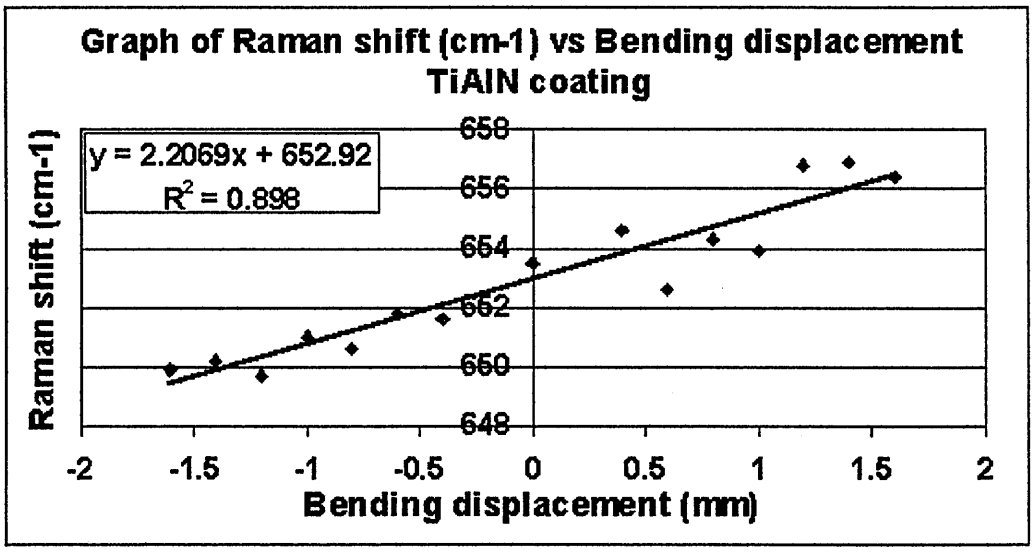

Figure 7.20 Raman shift vs. bending displacement for tensile and compressive loading.

A band position shift was observed with applied mechanical stress. The tensile side appeared to have less scatter in the data than the compressive side. This could be due to cracking occurring as the compressive stresses imparted by the stress rig are superimposed on the residual compressive stresses, whereas the tensile stressing will be relieving the compressive stress therefore reducing the overall residual stress value up to a certain point. $R^2 = 0.9$ was observed for Raman shift vs. bending displacement.

References

1 O. Knotek, R. Elsing, G. Kramer and F. Jungblut, paper presented at the 17th International Conference on Metallurgical Coatings, San Diego, CA, April 2-6, 1990.

2 D.W. Hoffmann, Thin Solid Films, 107 (1983) 353-358.

3 A. Pan and J.E. Greene, Thin Solid Films, 78 (1981) 25-34.

4 P.J. Burnett and D.S. Rickerby, Thin Solid Films, 154 (1987) 403-416.

5 J.A. Sue and H.H. Trone, Surf. Coat. Technol. 36 (1988) 695-705.

6 J.S. Bull, D.S. Rickerby, A. Matthews, A. Leyland, A.R. Pace and J. Valli, Surf. Coat. Technol., 36 (1988) 743-754.

7 T. Hirsch and P. Mayr, Surf. Coat. Technol., 36 (1988) 729-741.

8 B.D. Cullity, Elements of X-ray Diffraction. Addison-Wesley Co.1978, p512-515.

9 Ch. Genzel and W. Reimers, Surf. Coat. Technol. 116-119 (1999) 404-409.

10 Z. Novotna, R. Kralova, R. Novak and J. Marek, Surf. Coat. Technol. 116-119 (1999) 424-427.

11 A. Shenar, I. Gotman, S. Radin, P. Duckeyne and E.Y. Gutmanas, Surf. Coat. Technol. 126 (2000) 210-218.

12 D.B. Lewis, I. Wadsworth, W.-D. Münz, R Kuzel Jr and V. Valvoda, Surf. Coat. Technol. 116-119 (1999) 284-291.

13 Analytical and experimental methods for residual stress effects in fatigue ; Robert L. Champoux, John H. Underwood, and Joseph A. Kapp, editors Philadelphia, PA: ASTM, 1988.

14 N. Muraki, V. Sergo, G. Pezzotti, G. Katagiri, S. Meriani and T. Nishida, Applied Spectroscopy, 51(11) (1997) 1761-1765.

15 I. De Wolf, G. Pozzat, K. Pinardi, D.J. Howard, M. Ignat , S.C. Jain and H.E. Maes, Microelectron. Reliab., 36(11/12) (1996) 1751-1754.

16 X. Yang and R.J. Young, British Ceramic Transactions 93 (1) (1994) 1-10.

17 X. Yang and R.J. Young, Composites 25(7) (1994) 488-493.

18 S. Narayanan and L.S. Schadler, Comp. Sci. Technol. 59 (1999) 1589-1596.

19 T. Kitagawa, K. Yabuki and R.J. Young, Polymer 42 (2001) 2101-2112.

20 Y.-N. Wang, C. Galiotis and D.L. Bader, J. of Biomechanics, 33 (2000) 483-486.

21 G. Pezzotti, Comp. Sci. Technol., 59 (1999) 821-831.

22 Q. Ma and D.R. Clarke, J. Am. Ceram. Soc., 76 (1993) 1433.

23 J. Birnie,C. Craggs, D.J. Gardiner and P.R. Graves, Corrosion Science, 33(1) (1992) 1-12.

24 M. Bowden, G.D. Dickson, D.J. Gardiner and D.J. Wood, Applied Spectroscopy 44(10) (1990) 1679- 1684.

25 M. Bowden, G.D. Dickson, D.J. Gardiner and D.J. Wood, J. Mater. Sci. 28 (1993) 1031-1036.

26 S.A. Catledge, Y.K. Vohra, R. Ladi and G. Rai, Diamond and Related Materials, 5 (1996) 1159-1165.

27 M.I. Lemke, D.B. Lewis, W.-D. Münz and J.M. Titchmarsh, Surf. Eng. (submitted 2000).

28 D.B. Lewis, L.A. Donohue, M. Lembke, W.-D. Münz, R. Kuzel Jr., V. Valvoda and C.J. Blomfield, Surf. Coat. Technol. 114 (1999) 187-199.

29 Personal communication with Dr M. Symmonds (Reponsible person for GDOES equipment within the Material Research Institute).

30 Personal communication with Mr M. Jackson (Technician in the School of Engineering and responsible person for Talysurf profiling equipment).

31 CSEM instruments Advanced Mechanical Surface Testing "Application Bulletin; Advances in Surface Mechanical Properties Characterisation" autumn 1996.

32 H. Oettle, T. Bertram, V. Weihnacht, R. Wiedemann and S.V. Zitzewitz, Surf. Coat. Technol. 97 (1997) 785-789.

33 Cornelia Schonjahn, PhD Thesis, Sheffield Hallam University (submitted 2001).

Chapter 8

General Discussion

Chapter 8 General Discussion and Further Work

8.1 General Discussion

Physical Vapour Deposited coatings have been studied using Raman microscopy. It has been shown that good quality spectra can be obtained from binary, multicomponent, multilayered and superlattice coatings. Two pronounced groups of bands occur related to acoustical (150 – 300cm^{-1}) and optical (400-700cm^{-1}) parts of the phonon spectrum. Further second order intensity (combinations and overtones) was observed in the range 700-1200cm^{-1} but was inherently weaker. Assignments of the acoustical and optical phonon modes agreed well with previous work on TiN and ZrN, further assignments were compiled for the next generation coating structures. Differences in the spectral features resulted from the diverse classes of coating architectures. Multicomponent coatings were generally more intense due to the additional element(s) within the lattice acting as further defects. These and other findings allowed a greater understanding of the phenomenon of Raman scattering from polycrystalline coatings. The use of different excitation wavelengths was seen to result in subtle to more dramatic changes in the coating spectra. For example, when using 514.5nm green laser light, for TiAlN coatings a further band was observed on the shoulder of the 640cm^{-1} optic modes which was attributed to an enhancement of an optic phonon mode otherwise lost beneath the broad band observed at ~640cm^{-1}. This aside, it was found that 632.8nm excitation gave the most intense and ultimately the best quality spectra therefore the majority of subsequent work was performed with 632.8nm light. The penetration depths of the lasers were unknown because the absorption coefficients were not available in the literature, but the high density, dark colouration, metallic-like reflectivity of these materials was

thought to result in a low depth in the range of 50 - 200 nm. Despite the dark colouration of some of these coatings 100% laser power, approximately 5mW at the sample, did not cause any sample degradation and the sample heating effects were thought to be minimal due to these materials being deposited onto HSS and SS substrates, which dissipated any heat generated. An exposure time of 200 seconds was sufficient to obtain spectra of good quality, although a reduction of this time was possible if static acquisition was performed i.e. if only a narrow range of frequencies was desired (static scanning allowed a range of ~700 - 800cm^{-1}). This static scanning range was dependent on what part of the spectrum was required, a reduced static range results when one goes to higher wavenumbers owing to the reduction in the dispersion capabilities of the single grating. Evidence was gathered to support the theory that the optic modes were mainly due to the vibrations of the lighter elements e.g. N and C, and the acoustical modes were due to vibrations of the heavier elements within the polycrystalline lattice. This was deemed to be the case owing to the fact that binary coatings (TiN, ZrN, NbN etc.) had optic and acoustic modes that were approximately the same intensity. Multicomponent coatings, with additional metallic elements within the lattice, had acoustical modes that were far greater in intensity than their optical modes. The spectra that resulted from each class of coating, whether it be binary, multicomponent, or superlattice, were unique i.e. a fingerprint. The Raman spectra are dependent on the atoms that make up the lattice, the crystallinity/order, residual stress and defect density.

The study of mechanically induced deformation on the Raman spectral bands of PVD coatings found that scratching increased the optical mode band widths and shifted the frequency. These changes in the spectral features due to scratching were attributed to

the deformation caused to the PVD coating structure. The width of the main optical phonon mode of TiAlN at ~640cm^{-1} was broadened by up to 80cm^{-1} by scratching, which was a significant amount. The load applied by the indenter in a scratch test correlated quite nicely to the observed band width, indicating a broader band resulted as the deformation proceeded. In addition the stress-state of the coating was also changed owing to the observed shifts in band position, especially at the edges of scratches. Cracking of the coatings during deformation, especially during a scratch test was responsible for the higher than expected experimental scatter. This highly inhomogenous stress field observed was important because the region just at the edge of a crack was subjected to a stress completely different from one a few micrometers away: given the very high spatial resolution and the fact that minor cracks are not always visible under the microscope. This cracking could, however, be a signal for when the, L_c i.e. the critical load, was breached. In addition this would be a much more consistent way of determining this value, as opposed to visible inspection. The band position obtained for mapping across a scratch on a TiZrN coating resulted in a very interesting result. It appeared that on one edge of the scratch had increased in compressive stress but the other a tensile stress was observed, however tensile shifts from these coatings might indicate that a reduction in compressive stress had occurred owing to the fact that compressive residual stresses of up to 10GPa occur for these coatings. The observed band broadening for scratching TiAlN was much greater than for the equivalent tests on TiZrN, indicating a resistance to deformation of the TiZrN coating. It was postulated that the large Zr atoms within the TiN structure might have created, due to lattice distortion effects, a tougher coating system. This was probably due to increased dislocation density and their reduced mobility. In addition the incorporation of Zr within TiN resulted in higher residual compressive stresses, which

in turn increased the hardness. This hardness increase may also be responsible for the observed resistance to deformation. The removal of droplets during the scratch test resulted in areas of increased deformation around such events (larger than expected band widths were observed). The effect of droplet incorporation into coatings and subsequent Raman scattering phenomenon was also studied. It was found that the coating that grew on top of droplets was highly defective/disordered owing to a broadening of the phonon mode. It also appeared that the neighbouring areas around the droplet were affected also. The stress state on and around droplets was also found to increase. A maximum compressive shift of around $10cm^{-1}$ was observed when measurements were taken on the droplet.

The mapping of wear tracks resulting from pin-on-disk sliding tests found that the wearing action increased the compressive stresses within the underlying coating. The maximum shift was observed in the central region of the wear track, where the contact pressures were the highest.

The knowledge obtained from the study of Raman scattering from PVD coatings, the spectral database of coatings (binary, multicomponent and superlattice) and the deformation studies were all taken into consideration in the development of a Raman based method for the quantification of wear. Initially layered model coating systems were studied which had significant difference in the spectra between the layers. These were then subjected to a simulated wearing exercise using the abrasive mechanism of ball cratering. The removal of one layer and subsequent detection of the underlying layer / or monitoring the disappearance of the upper layer spectrum and having a "safety zone" of 1 μm of very low scattering cross section material

beneath, were found to work well. Additional ideas of using marker layers, i.e. high scattering cross section materials, to indicate wear were not feasible as the substrate-coating adhesion would have been compromised and additional steps in the process would increase costs of production and make it uneconomical. This investigation then moved on to the real wear of a commercial available coating Supercote-02, a highly popular general-purpose coating, which also had a layered structure. Mapping experiments of this coating after wearing (time-in-cut), found that removal of material did occur because of the highly abrasive environment and high cutting temperatures, estimated at being 900 – 1000°C, found in high speed cutting. Additional bands due to oxides were detected at localised positions on the worn tool surfaces. For earlier time-points this was found to be Al_2O_3 that became more crystalline with increasing wear, indicating that the cutting temperatures had increased over time. After 64 minutes-in-cut the coating bands were no longer observed and an additional sharper band at 670cm^{-1} was observed. This was due to an iron transfer layer/built-up-edge from the workpiece material, which had oxidised after further wearing to form FeO/Fe_3O_4 on the surface. Additional time-in-cut saw a further rise in the cutting temperatures as indicated by a phase transformation i.e. FeO/Fe_3O_4 to Fe_2O_3; as small bands at 290, 407, 539 and ~1300cm^{-1} (two magnon scattering) were observed indicative of Fe_2O_3. This was also observed when measurements were taken around the cutting edge, indicating that the temperature of cutting increased further round the ball nose to a maximum T_{max}, where a diffusional/oxidational wear mechanism occurred i.e. crater wear. This transfer layer appeared to be present on all the worn surfaces. The use of Raman microscopy as a "thermometer" has allowed the detection of wear indirectly. The phase transformation of the oxides present in the transfer layers was followed, giving a useful correlation of increased cutting

temperatures with time for cutting tools. This increase in cutting temperature was attributed to the removal of the protective coating and subsequent roughening of the friction/wear zones. In addition, analysis of the swarf particles found that a hot and cold region existed. The hot region corresponded to the where the tool had engaged the work piece (i.e. the thicker end of each particle). This was evident as Fe_3O_4 and Fe_2O_3 bands were observed. Also in localised positions coating oxides were found i.e. TiO_2 (anatase). The observation of a phase transformation, i.e. magnetite – hematite, for the final time-points (i.e. reaching the 0.3mm flank wear criteria) may negate the need to actual sample the tool itself to gain a handle on the extent of wear.

A chemometrics model incorporating;

The three component layers, i.e. $TiAlCrO_xN_y$, TiAlN/CrN and TiAlCrN;

The tool material WC – Co;

Oxides that were detected, i.e. Al_2O_3 and the indicators of wear FeO/Fe_3O_4;

(essentially identical spectra) and Fe_3O_4 enabled a quick determination of the extent of wear.

The wear gradients that occur on cutting tools do, however, make it imperative that an area indicative of the overall wear is sampled. The high spatial resolution of the Raman system was actually a disadvantage in this case and a systematic defocusing of the laser may hold the key to enable larger areas of the surface to be sampled without loss of collection efficiency. Line focussing could be a possibility.

The study of high temperature characteristics of PVD coatings generated some interesting results. It became apparent that Raman microscopy was an ideal technique for studying wear debris resulting from pin-on-disk sliding wear. The high spatial

resolution, sensitivity to structure (even polymorphs) enabled compounds especially oxides to detected and structure/composition to be determined. Tribochemical reactions were found to occur during sliding, especially tribo-oxidation owing to the high contact temperatures due to the high pressures and friction. Complicated reactions such as the formation of the mixed metal oxides, for example $CrNbO_4$ in the debris resulting from CrN/NbN superlattice, were unexpected. Synthesis of mixed metal oxides was possible with guidance from JCPDS files, which enabled positive identification. The correlation of the species detected on the surface of coatings from static oxidation, with oxides detected in the wear debris facilitated an estimate of the contact temperatures during sliding. Values in the range of 500 - >700°C were found to occur for the binary, multicomponent and superlattice coating - corundum tribocouples. The static oxidation of coating systems also presented information on the possibility of generating lubricious oxides, for example V_2O_5 in the case of TiAlN/VN, to enable explanations for favourable friction properties for some coating systems. Further strategies designed to improve oxidation resistance of coating systems can be followed and the subsequent friction and wear/debris analysis (Raman) can determine functional properties i.e. information on how they will perform in real wear situations. The ability of Raman microscopy to determine oxide species on the surface of PVD coatings quickly without sample preparation or vacuum constraints make it a very powerful analytical tool for surface engineer, which has to date been vastly under used. It could replace XRD as the preferred choice for oxide analysis.

The study of residual stresses using Raman microscopy resulted in some interesting results. The TiAl(Y)N/VN samples with engineered residual stresses (via bias

voltage) gave band shifts which were indicative of increased compressive stress. An increase in residual stress was observed with an increase in bias voltage, which correlated well with the theory. The addition of small amounts of yttrium within the coating structure was also seen to increase the intrinsic stresses. XRD stress analysis ($\sin^2 \psi$ - method) and subsequent comparison with Raman band shifts agreed very well with an experimental correlation of 0.99 being observed when 632.8nm excitation was used. This indicated the complementarity of the two analytical techniques, and highlighted the possible use of Raman microscopy, routinely, as a very rapid method of determining residual stresses within PVD coatings. A further interesting possibility was the use of Raman microscopy as a hardness test. It was found that the observed band position when compared to hardness values had an experimental correlation of 0.997. To fully evaluate this would require further investigation but the possibility of gaining an estimate of coating hardness non-destructively and quickly seems amazing. It would even be possible to perform hardness analysis on strongly curved surfaces, for example on difficult geometry components and cutting tools enabling cutting edge analysis. In addition to this the ability of Raman to depth profile the residual stress gradient present in the PVD coating structure by use of GDOES as a way of sputtering away material revealing lower layers worked well. It has given the possibility of determining the quality/stress of individual layers within complex coating architectures. The design and construction of a four-point bending rig also provided the means of evaluating stresses. Although a limited amount of experiments were performed owing to the fact that it was developed in the latter stages of the project. The bending experiments and subsequent Raman analysis enabled spectral shifts due to tensile and compressive stresses imparted by the rig to be monitored. This highlighted that piezo-

spectroscopic calibrations were possible that could essentially result in a Raman based method for residual stress analysis.

The analysis of PVD coatings has resulted in the generation of many interesting results. Some of the methodologies developed from this project could potentially be developed further into routine coating analysis methods. These include:

i) As a method of assessing coating quality on the production line via bandwidths, band positions and band intensities of various coating compositions.

ii) As a tool for use with the scratch adhesion tester in which the critical load could be determined via band widths and by increased scatter due to cracks.

iii) The use of ball cratering / GDOES – Raman microscopy as methods of depth profiling coating structures or simulating wear.

iv) Residual stress analysis of coatings via band shifts of the main optical modes of PVD coatings owing to the piezo-spectroscopic effect.

v) Coating hardness via the above phenomenon.

vi) Wear quantification (the initial remit of this project), monitoring the removal of layers or from the oxides that occur on wear surfaces.

It was possible to develop a Raman microscopy based method for determination of the extent of wear on Supercote-02 hard coatings. Raman microscopy has also been shown to be an analytical technique that has great scope and potential in the study of

many areas of PVD hard coating quality. Areas where increased understanding are highlighted below.

8.2 Further Work

1 The penetration/sampling depth of the laser beam into PVD hard coatings is an important unknown. This important parameter could help give further understanding on certain aspects of the observed phenomenon detailed in this project. A set of experiments, possibly elipsometry, that could ultimately provide the absorption coefficients of coatings and hence the penetration depth in PVD coating systems should be sought (possibly a whole PhD project in itself).

2 The coupling of a fibre-optic Raman system to cutting equipment/tool docking bay in a machine shop environment should be performed. To date only laboratory testing in sterile surroundings with instrumentation of high sensitivity has been possible. The study of real wearing of coated tools i.e. with Supercote-02 and other similar coatings using a fibre optic system should be performed to further assess the possibility of such devices being used for routine wear determination in an industrial environment. The use of a fibre optic Raman system to obtain spectra from rotating tools would finally "lay to rest" whether *in-situ* acquisition of spectra was possible.

3 Generation of better oxide standards (i.e. that follow more closely those which are found on real worn tools i.e. semi-crystalline) for the chemometrics model

would be beneficial. The input of real spectra into the model should also be performed and the essential pre-treatments decided (baseline correction, zapping (for spurious peaks), offsetting etc.

4 Possibilities of using macro sampler systems to investigate wear, needs evaluating. The high spatial resolution of Raman microscopy was found a disadvantage for wear test studies, as the wear indication was highly dependent on the location of the spot on the tool. A system that defocuses the laser beam to a larger spot size (either a spot or line focus) to gain information from a larger area on the worn tools would be an advantage and should be studied.

5 The further study of other coating systems with engineered stresses (i.e. from process parameters) should be investigated to fully evaluate the use of Raman microscopy as a method of residual stress analysis. These coatings should ideally have a range of hardness values so that the Raman shift vs. hardness correlation can be fully evaluated also.

6 Bending experiments of coatings on different substrates, i.e. mild steel and tungsten carbide, would be beneficial. The utilisation of a strain gauge to gain values of strain/stress as bending was performed would also be beneficial and allow a Raman shift vs. strain plot to be drawn from the experiments. A greater understanding a how the deflection/displacement relates to strain/stress in the coatings should be sought.

Conferences Attended

1) The 4th Martin and Willis Prize Meeting, University of Leeds, 31st March 1998, and 156th Meeting of the IRDG, 1st April 1998, University of Leeds. Poster presented: "Raman Microscopic Studies of Monolithically Grown PVD Hard Coatings".

2) Sixth International Conference on Plasma Surface Engineering Garmisch-Partenkirchen, September 14-18, 1998. Oral Presentation: Raman Microscopic Studies of Monolithically Grown PVD Hard Coatings.

3) 4th ABS days, Sheffield Hallam University, 22-23 July 1998. Oral presentation: "The Use of Raman Microscopy For the Determination of the Structure of Wear Debris".

4) Material Research Institute Research Day (1999) Sheffield Hallam University, Poster presentation: "Identification of Oxides on Heat Treated PVD Coatings" Poster Prize awarded (Oral presentation of the above named poster as part of the prize).

5) 46th International Symposium of the American Vacuum Society, Washington State Convention Center, Seattle, Washington, USA. October 25-29, 1999. Oral presentation: "Structural Determination of Wear Debris Using Raman Microscopy".

Reprinted from

SURFACE & COATINGS TECHNOLOGY

Surface and Coatings Technology 116–119 (1999) 155–159

Raman microscopic studies of PVD hard coatings

C.P. Constable *, J. Yarwood, W.-D. Münz

The Materials Research Institute, Sheffield Hallam University, Pond Street, Sheffield S1 1WB, UK

ELSEVIER

SURFACE AND COATINGS TECHNOLOGY

Scope
The increasing requirement for high technology materials with specific performance characteristics in various types of environments has dictated that these materials possess near-surface properties different from their bulk properties. This journal is a principal forum for the interchange of information on the science, technology and applications of thin and thick coatings and modified surfaces which alter the properties of materials. The scope includes all types of coatings and surface modification techniques (including physical vapour deposition, chemical vapour deposition, electroplating and surface modification by directed energy techniques). Of particular emphasis are the emerging advanced processes such as thermal spraying, sputter deposition, activated reactive evaporation, ion plating, molecular beam epitaxy, ion implantation and pulsed laser surface deposition. Contributions range from original scientific articles concerned with applied research or direct applications of coatings to reviews of current technology in specific areas. Papers are solicited on topics which include one or more of the following areas: (1) characterization of coatings and modified surfaces, which includes the determination of composition, structure, adhesion, and internal stresses; (2) the application of coatings and modified surfaces to alter the mechanical, chemical or optical properties of materials. Mechanical properties include friction, wear, erosion, hardness and load bearing capacity. Chemical properties include corrosion and oxidation. Optical and electro-optical properties include reflectivity, selective absorption and electroluminescence. Particular emphasis is also placed on the emerging surface engineering technologies and coatings with a diversity of applications such as diamond, diamond-like carbon, and cubic boron nitride. Other interdisciplinary areas include thermal barrier coatings and coatings for biomedical applications and materials conservation.

Abstracting/Indexing Services
This journal is cited by the following services:
Engineering Index, FIZ Karlsruhe, Metal Finishing Abstracts, Current Contents — Engineering, Technology and Applied Sciences, Physikalische Berichte, Cambridge Scientific Abstracts, Chemical Abstracts, Fluid Abstracts, Metals Abstracts, Physics Abstracts, PASCAL/Centre National de Recherche Scientifique, Solid State Abstracts.

Pre-publication abstracts of articles in *Surface and Coatings Technology* and other related journals are now available weekly in electronic form via CoDAS, a new direct alerting service in condensed matter and materials science run jointly by Elsevier Science and Institute of Physics Publishing. For details on a free one-month subscription contact Paul Bancroft on fax +44 1179 294318 or e-mail bancroft@ioppublishing.co.uk.

Publication Information: *Surface and Coatings Technology* (ISSN 0257-8972). For 2000 volumes 122–134 are scheduled for publication. Subscription prices are available upon request from the Publisher or from the Regional Sales Office nearest you or from this journal's website (http://www.elsevier.nl/locate/surfcoat). Further information is available on this journal and other Elsevier Science products through Elsevier's website: (http://www.elsevier.nl). Subscriptions are accepted on a prepaid basis only and are entered on a calendar year basis. Issues are sent by surface standard mail (surface within Europe, air delivery outside Europe). Priority rates are available upon request. Claims for missing issues should be made within six months of the date of dispatch.

Orders, claims and product enquiries: please contact the Customer Support Department at the Regional Sales Office nearest you:

New York: Elsevier Science, PO Box 945, New York, NY 10159-0945, USA;
phone: (+1) (212) 633 3730 [toll free number for North American customers: 1-888-4ES-INFO (437-4636)];
fax: (+1) (212) 633 3680;
e-mail: usinfo-f@elsevier.com

Amsterdam: Elsevier Science, PO Box 211, 1000 AE Amsterdam, The Netherlands;
phone: (+31) 20 4853757; fax: (+31) 20 4853432;
e-mail: nlinfo-f@elsevier.nl

Tokyo: Elsevier Science, 9-15 Higashi-Azabu 1-chome, Minato-ku, Tokyo 106-0044, Japan;
phone: (+81) (3) 5561 5033; fax: (+81) (3) 5561 5047;
e-mail: info@elsevier.co.jp

Singapore: Elsevier Science, No. 1 Temasek Avenue, #17-01 Millenia Tower, Singapore 039192;
phone: (+65) 434 3727; fax: (+65) 337 2230;
e-mail: asiainfo@elsevier.com.sg

Rio de Janeiro: Elsevier Science, Rua Sete de Setembro 111/16 Andar, 20050-002 Centro, Rio de Janeiro - RJ, Brazil;
phone: (+55) (21) 509 5340; fax: (+55) (21) 507 1991;
e-mail: elsevier@campus.com.br [Note (Latin America): for orders, claims and help desk information, please contact the Regional Sales Office in New York as listed above]

US mailing notice: *Surface and Coatings Technology* (ISSN 0257-8972) is published semimonthly by Elsevier Science S.A. (PO Box 211, 1000 AE Amsterdam, The Netherlands). Annual subscription price in the USA US$ 4969.00 (valid in North, Central and South America), including air speed delivery. Periodical postage rate paid at Jamaica, NY 11431.
USA POSTMASTER: Send address changes to *Surface and Coatings Technology*, Publications Expediting, Inc., 200 Meacham Avenue, Elmont, NY 11003.
AIRFREIGHT AND MAILING in the USA by Publications Expediting Inc., 200 Meacham Avenue, Elmont, NY 11003.

ELSEVIER

Surface and Coatings Technology 116–119 (1999) 155–159

SURFACE & COATINGS TECHNOLOGY

www.elsevier.nl/locate/surfcoat

Raman microscopic studies of PVD hard coatings

C.P. Constable *, J. Yarwood, W.-D. Münz

The Materials Research Institute, Sheffield Hallam University, Pond Street, Sheffield S1 1WB, UK

Abstract

A series of PVD ceramic hard coatings (TiN, ZrN, TiAlN, TiZrN and TiCN) were deposited on steel substrates using the cathodic arc/unbalanced magnetron deposition technique. These coatings were characterised using Raman microscopy to elucidate the behaviour of the optic and acoustic phonon modes of the (cubic) crystalline lattices. Defect-induced first- (and second-) order spectra have been observed in the 200–300 and 500–800 cm^{-1} regions and these have been assigned and correlated with coating composition. Changes in the position, intensity and shape of the principal TO band (640–560 cm^{-1}) have been interpreted.

Raman microscopy has been shown to be a very useful non-destructive complementary technique to XRD for the characterisation of PVD hard coatings.

Keywords: TiN; TiAlN; F.c.c.; Hard coatings; Raman microscopy; Phonon modes

1. Introduction

Over the last 10 years Raman spectroscopy has experienced a revival of fortunes, brought about by the advent of new technology. New instrumentation has been developed utilising high stability laser excitation, efficient holographic notch filters and sensitive charge coupled device detectors (CCDs). The coupling of a Raman spectrometer with an optical microscope has also been implemented and enabled the user to obtain high quality spectra from micrometre-sized particles. These advances have resulted in many more research groups realising the potential of Raman microscopy.

Raman microscopy is a non-invasive technique that gives vibrational information about organic and inorganic molecules. In the field of surface engineering Raman microscopy has in the past been used to study wear [1] and wear debris [2], stress [3], oxidation [4,5] and also the effect of deposition parameters [6] on PVD hard coatings. Up to now the majority of the work has been performed on first generation PVD hard coatings especially on TiN. There has been very little work (if any) performed on advanced multicomponent, multilayered or superlattice PVD hard coatings. Possible reasons for this lack of research are as follows: Raman scattering from materials with metallic properties is restricted by prohibitive selection rules, low penetration depth of the incident light (due to high reflectivity), etc. The resulting penetration depth is small ($d=\lambda/4\pi k$, k denoting the absorption coefficient) for these coatings but the spectra obtained still arise from a spatial range corresponding to many unit cells.

The phonon bands of TiN have been studied extensively by a number of authors [7–10] who have attributed the scattering in the acoustic range to be primarily determined by the vibrations of the heavy Ti ions (typically 150–300 cm^{-1}) and in the optic range by vibrations of the lighter N ions (typically 400–650 cm^{-1}).

The Raman effect stems from vibration-induced changes in the electronic polarisability of a molecular system. In a perfect crystal with f.c.c. structure every ion is at a site of inversion symmetry and consequently first-order Raman spectra are forbidden [7–11]. However, PVD coatings are known to contain many microscopic defects, i.e. both heavy metal ion and also lighter nitrogen ion site vacancies are present. These defects reduce the effective symmetry and certain atomic displacements of neighbouring atoms have non-zero first-order polarizability derivatives. The first-order Raman spectrum of a perturbed crystal reflects the density of states for those atomic displacements rendered Raman active by the presence of the impurity/defect [11].

* Corresponding author. Tel.: +44-114-2252034; fax: +44-114-2253501.

E-mail address: c.p.constable@shu.ac.uk (C.P. Constable)

0257-8972/99/$ – see front matter
PII: S0257-8972(99)00072-9

Table 1
Summary of assignments for the optic and acoustic phonon modes (cm^{-1}) for the thin film coatings studied

Mode	TA / LA	TO / LO	2A	A+O	2O
TiN (Fig. 1)	215, 327	566–609	464	825	1128
Literature [7–10]	200, 340	520–590	400–500	~800	~1100
ZrN (Fig. 2)	173, 241	473–580	355, 424	750	1041
Literature [8]	160, 260	460–560	325–525	~710	~1025
TiAlN (Fig. 3)	~250	621	484	(732[a])	1189
TiZrN (Fig. 4)	193, 261	527	~400	788	1060
TiCN (Fig. 5)	232, 332	568–661	–	810	1100

[a] Appears to be too low in frequency.

In this paper we describe the Raman spectra which arise from a range of coating compositions, focusing on the changes in the spectral density on going from first generation coatings to multicomponent, monolithically grown, second generation coatings.

2. Experimental

All coatings were grown using combined cathodic arc/unbalanced magnetron deposition. The PVD equipment used is described in detail in Ref. [12]. The Ti, Zr and TiAl targets were produced by vacuum casting, whereas the TiZr target consisted of small Ti and Zr segments which were bound on a backing plate. Typical deposition recipes are given in Ref. [13]. The coatings were deposited on HSS and Stainless steel substrates and had a thickness of 2–3 μm, deposited at 1–2 μm h^{-1}. All our samples were polycrystalline and for the binary coatings TiN and ZrN it is well established that they exhibit f.c.c. crystal structures. The multicomponent second generation coatings TiAlN, TiZrN and TiCN have been shown by XRD [14–16] to have cubic (f.c.c.) crystal structures.

A Renishaw Ramascope System 2000 spectrometer was used for these experiments. This system comprised an integral Raman microscope, a stigmatic single spectrograph, and a Peltier-cooled CCD detector (400 × 600 pixels). The microscope attachment was an Olympus BH2 system. The excitation wavelength used was 514 nm Ar^+ ion (25 mW laser). Power of 2–3 mW was incident on the samples in a 2 μm diameter spot through a standard ×50 microscope objective. The spectra were collected with a 200 s data point acquisition time, a spectral range of 100–1500 cm^{-1} and a spectral resolution of 3–4 cm^{-1}. Spectra are presented as intensity (counts) versus Raman shift (cm^{-1} in air).

3. Results and discussion

The nitride coatings examined in this paper crystallise in f.c.c. form, with O_h site symmetry. However, it is

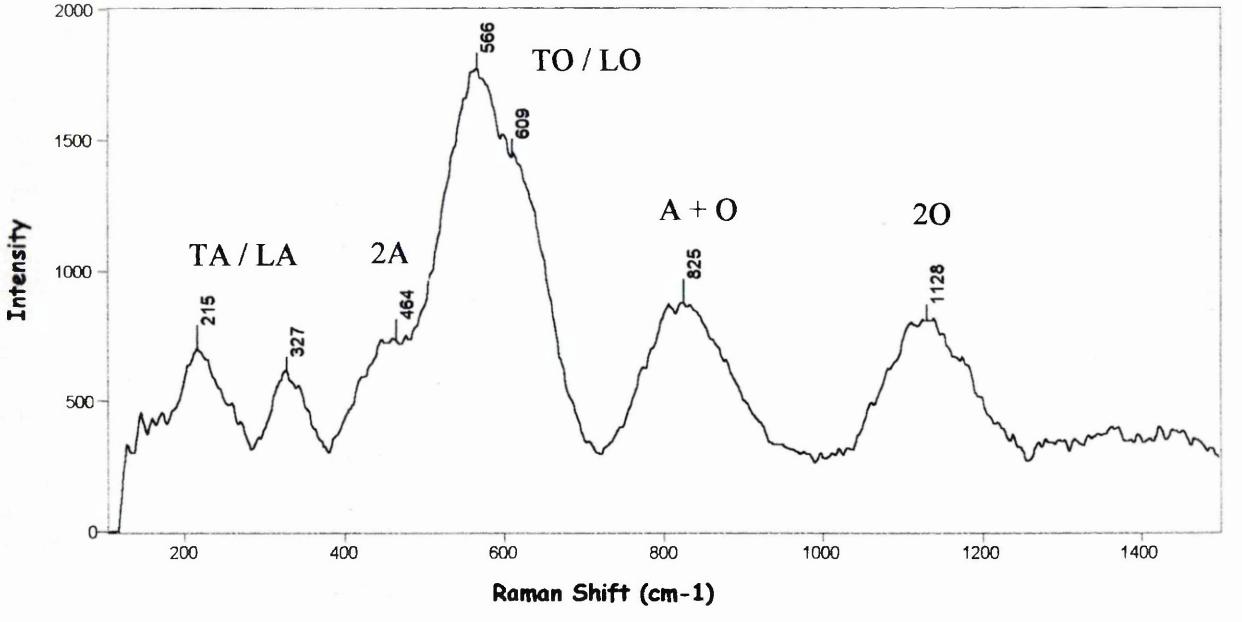

Fig. 1. Spectrum of TiN coating.

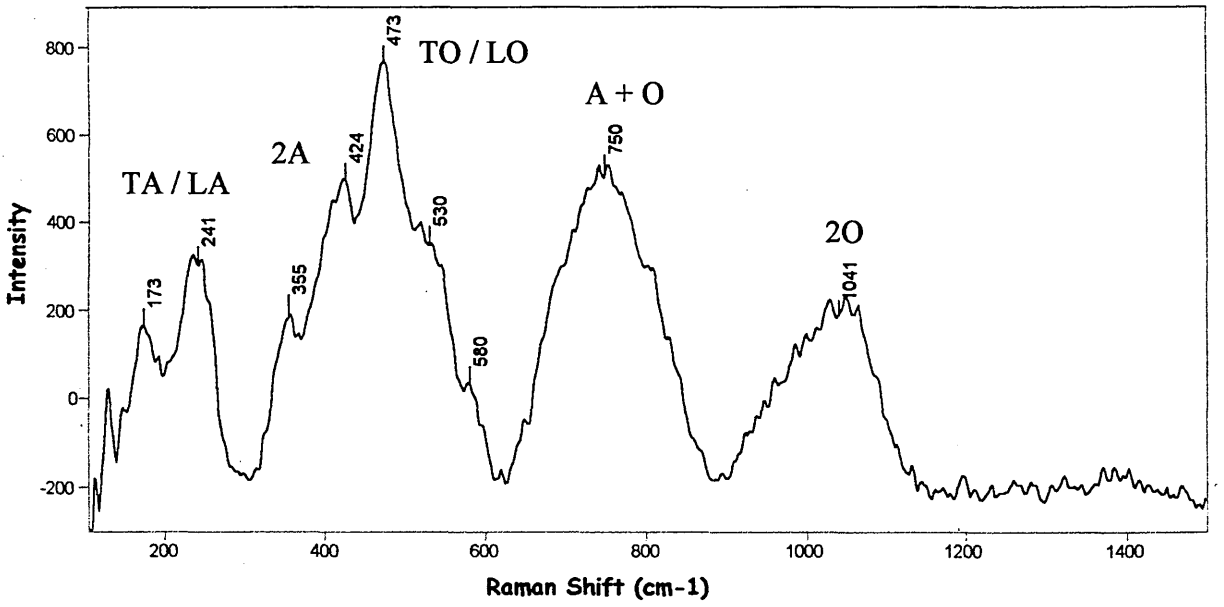

Fig. 2. Spectrum of ZrN coating.

expected that the lattices will carry stoichiometric and crystalline defects. The detailed theory of how 'defect'-induced first-order phonon spectra arise is well established [11,17] and it has previously been found that both optic and acoustic branches give rise to observed Raman bands according to $\Gamma = A_{1g} + E_g + T_{2g}$ in the O_h impurity-site symmetry.

Indeed the Raman phonon spectra of TiN and ZrN have been reported previously [8], and have been shown to reflect a superposition of first- and second-order phonon densities of states, fitting generally into the spectral pattern expected for a 'defect'-containing f.c.c. crystalline phase. From these Raman data [8] and others on pure [18,19] and doped alkali halide crystals [11,16] it has been concluded that the dispersion curves lead to a group of 'lines' (bands) due to acoustic transitions in the 150–300 cm^{-1} region (LA and TA) and another set of lines due to optic modes in the 400–650 cm^{-1} region (LO and TO). Higher frequency spectral density then arises via second-order transitions (A+O, 2O etc.). Clearly, there is a high probability of strong overlap between the optic modes of the crystalline lattice and overtones (second-order spectra) of the acoustic modes. However, using previous data it is possible to draw up a list of assignments for the thin film structures studied here (Table 1, values in cm^{-1}).

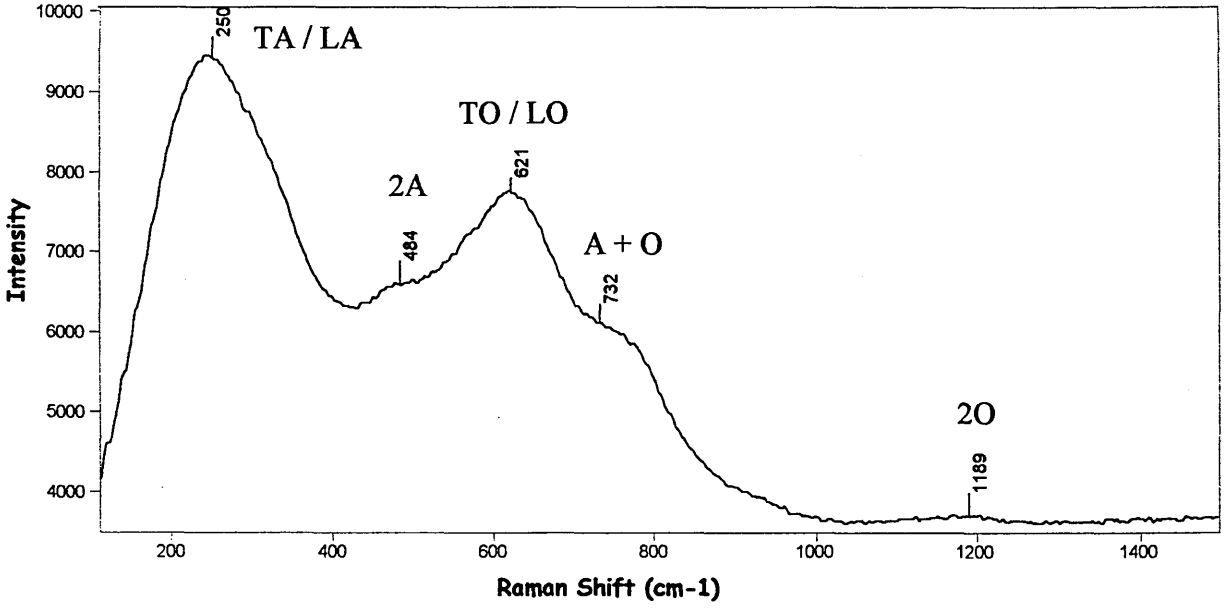

Fig. 3. Spectrum of TiAlN coating.

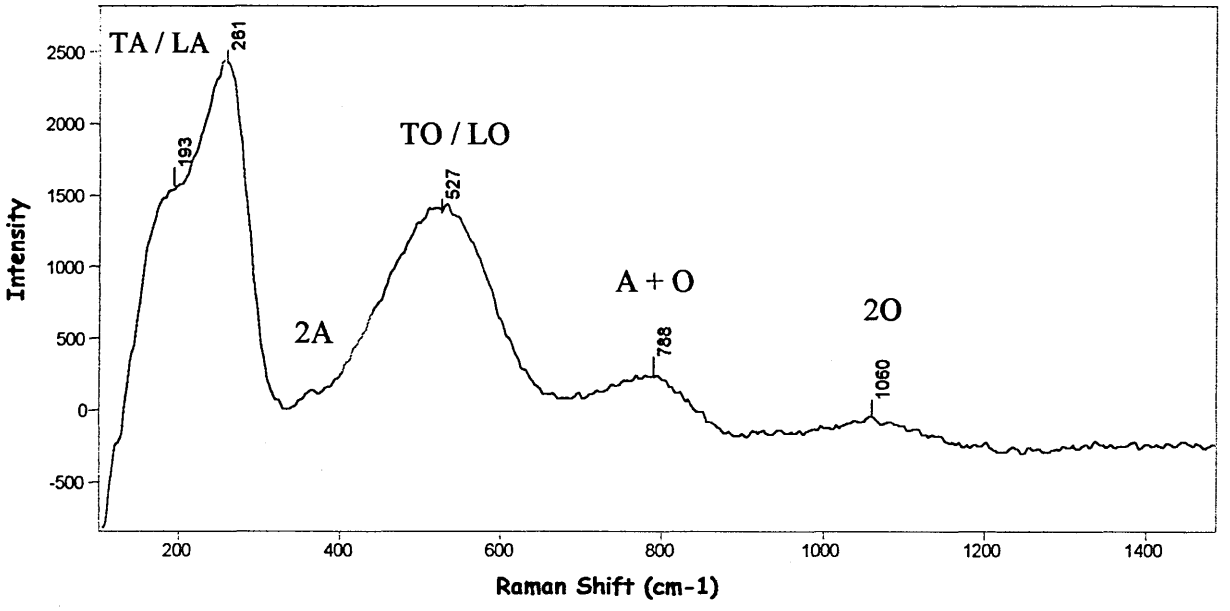

Fig. 4. Spectrum of TiZrN coating.

In most cases the pattern fits well on going from a binary lattice to a ternary lattice. As the lattice gets more complex, e.g. on going from TiN to TiAlN, it appears that the total spectral density in the 'gap' region (380–500 cm^{-1}) between the acoustic and optic modes increases (see TiAlN, Fig. 3). This could be due to a wider distribution of stoichiometric defects and a greater population of both first- and second-order density of states. It would appear that the difference between the TiN and TiAlN spectra (Figs. 1 and 3, respectively) (both with f.c.c. crystal structures, but in the latter case with a definite Ti site Al 'defect'), is connected with changes in the first-order optical branch density of states at $\sim 620\ cm^{-1}$ with a shift to higher frequencies, as quoted by Spengler [10]. However, there is also the possibility that second-order acoustic modes could also contribute in this region (see Table 1).

4. Summary

It has been shown that first-order, defect-induced Raman spectra of good quality can be obtained from multicomponent coatings. The list of assignments compiled fits well with previous work on TiN and ZrN. On going from binary TiN to the multicomponent coating

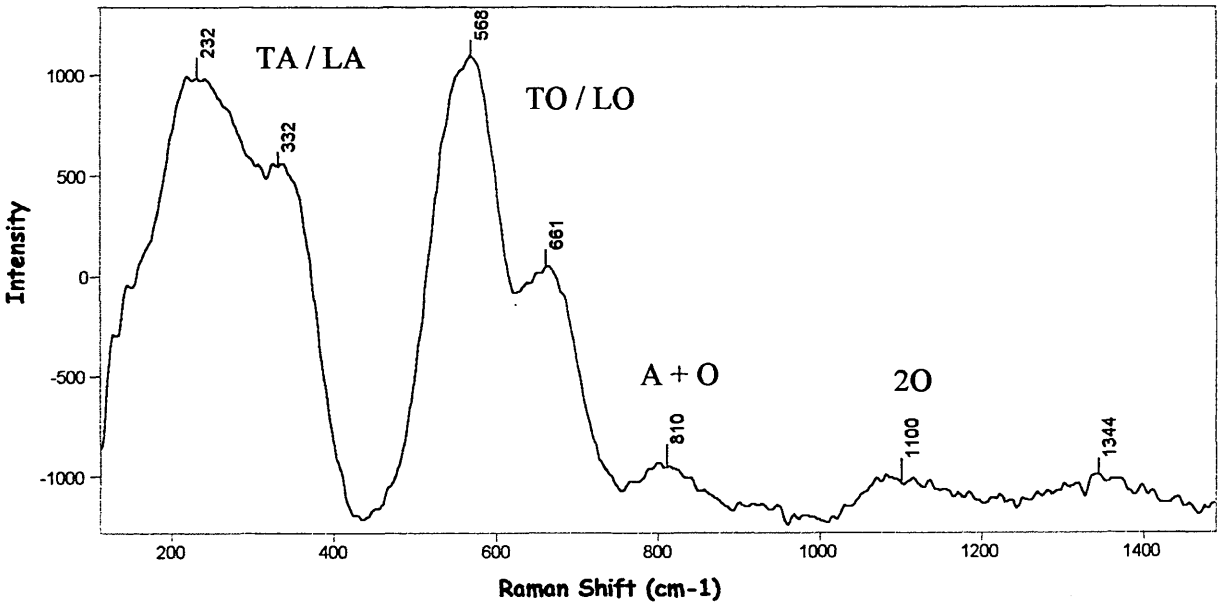

Fig. 5. Spectrum of TiCN coating.

TiAlN the total spectral density in the 'gap' region (380–500 cm^{-1}) between the acoustic and optic modes appears to increase.

The bands due to acoustic modes in the multicomponent coatings also appear to be more intense than those of the binary coatings. This supports the theory that the acoustic range of phonons can be attributed to the heavier ions (rather than nitrogen) since the multicomponent coatings studied generally have a second heavy ion substituted within the lattice (i.e. TiN to TiAlN and ZrN to TiZrN). In both the above examples the acoustic modes are much more intense than the optic modes, which suggests that the second heavy ion must be contributing in the acoustic range. In the case of TiCN the acoustic modes are not as intense. This is probably because the carbon atom is relatively light and small and is known to occupy the nitrogen sites, therefore contributing to the optic modes rather than the acoustic modes.

Raman microscopy clearly provides an important complementary non-destructive technique for the characterisation of ceramics with much scope for enhanced understanding of the structural and optical properties of future generations of PVD coatings.

Acknowledgements

The author would like to thank Prof. G.D. Pitt (Renishaw plc; Transducer Systems Department) and Dr. D.B. Lewis (Sheffield Hallam University) for their valuable discussion. The author would like to gratefully acknowledge Renishaw plc for their financial support.

References

[1] B. Blainpain, M. Franck, H. Mohrbacher, E. Vancoille, J.-P. Celis, J.R. Roos, in: D. Dowson et al. (Eds.), Thin Films in Tribology: Micro-Raman Spectroscopy for the Characterisation of Wear Induced Surface Modifications on Hard Coatings, Elsevier, Amsterdam, 1993, p. 623.
[2] E. Vancoille, B. Blainpain, Ye. Xingpu, J.-P. Celis, J.R. Roos, J. Mater. Res. 9 (4) (1994) 992.
[3] N. Muraki, V. Sergo, G. Pezzotti, G. Katagiri, S. Meriani, T. Nishida, Appl. Spectrosc. 51 (11) (1997) 1761.
[4] G.M. Begun, C.E. Bamberger, Appl. Spectrosc. 43 (1) (1989) 134.
[5] M. Franck, J.-P. Celis, J.R. Roos, J. Mater. Res. 10 (1) (1995) 119.
[6] R. Chowdhury, R.D. Vispute, K. Jagannadham, J. Narayan, J. Mater. Res. 11 (6) (1996) 1458.
[7] C.C. Chen, N.T. Liang, W.S. Tse, I.Y. Chen, J.G. Duh, Chin. J. Phys. 32 (2) (1994) 205.
[8] W. Spengler, R. Kaiser, Solid State Commun. 18 (1976) 881.
[9] W. Spengler, R. Kaiser, A.N. Christensen, G. Muller-Vogt, Phys. Rev. B 17 (3) (1978) 1095.
[10] W. Spengler, R. Kaiser, H. Bilz, Solid State Commun. 17 (1975) 19.
[11] G.P. Montgomery Jr., M.V. Klein, B.N. Ganguly, R.F. Wood, Phys. Rev. B 6 (10) (1972) 4047.
[12] W.-D. Münz, D. Schulze, F.J.M. Hauzer, Surf. Coat. Technol. 50 (1992) 169.
[13] I. Petrov, P. Losbichler, D. Bergstrom, J.E. Greene, W.-D. Münz, T. Hurkmans, T. Trinh, Thin Solid Films 302 (1997) 179.
[14] L.A. Donohue, I.J. Smith, W.-D. Münz, I. Petrov, J.E. Greene, Surf. Coat. Technol. 94–95 (1997) 226.
[15] L.A. Donohue, J. Cawley, J.S. Brooks, Surf. Coat. Technol. 72 (1–2) (1995) 128.
[16] J.M. Schneider, A. Voevodin, C. Rebholz, A. Mattews, J.H.C. Hoggs, D.B. Lewis, Surf. Coat. Technol. 74–75 (1–3) (1995) 312.
[17] G. Benedek, G.F. Nardelli, Phys. Rev. 154 (3) (1967) 154.
[18] R.T. Harley, J.B. Page Jr., C.T. Walker, Phys. Rev. B 3 (4) (1971) 1365.
[19] C. Raptis, Phys. Rev. B 33 (2) (1986) 1350.

Instructions for Authors

Submission of Papers

Manuscripts (original and two clear copies) should be submitted to one of the Editors:

for authors in the Americas
Dr. B. D. Sartwell, Surface Chemistry Branch, Naval Research Laboratory, Code 6170, Washington, DC 20375, USA;

and for authors elsewhere
Professor A. Matthews, Director, The Research Centre in Surface Engineering, The University of Hull, Cottingham Road, North Humberside, HU6 7RX, UK.

Contributions are accepted on the understanding that the authors have obtained the necessary authority for publication. Submission of a manuscript implies that it is not under consideration for publication elsewhere.

Types of contributions

— original papers
— invited or contributed reviews on specific topics
— brief communications on topics of immediate interest
— notices of meetings, symposia and short courses
— technical notes for "Current Industrial Practices" section

Languages

Papers will be published in English. Both English and US spelling are permitted, provided that spelling is consistent within an article.

Authors in Japan please note that information about how to have the English of your paper checked, corrected and improved (*before submission*) is available from: Elsevier Science K.K., Editorial Service, 1-9-15 Higashi Azabu, Minato-ku, Tokyo 106-0044, Japan; Tel.: +81 3 5561 5032; Fax: +81 3 5561 5045.

Manuscript preparation

Three copies of the manuscript should be submitted, in double-spaced typing on pages of uniform size with a wide margin on the left. The title page should be a separate sheet, bearing title, author(s)' name(s) and their full addresses, and a footnote with the corresponding author's Telephone, Fax numbers and E-mail Address.

Some flexibility of presentation will be allowed but authors are urged to arrange the subject matter clearly under such headings as Introduction, Experimental details, Results, Discussion etc. Each paper should have an abstract of 100–200 words.

References should be numbered consecutively (numerals in square brackets) throughout the text and collected together in a reference list at the end of the paper. Journal titles should be abbreviated according to the Chemical Abstracts Service Source Index, 1970 edition, and supplements. The abbreviated title should be followed by volume number, year (in parentheses) and page number.

Submission of electronic text

The final text should be submitted on a 3.5 in or 5.25 in diskette (in addition to a hard copy with original figures). Double density (DD) or high density (HD) diskettes formatted for MS-DOS or Apple Macintosh compatibility are acceptable, but must be formatted to their capacity before the files are copied on to them. The files should be saved in the native format of the wordprocessing program used. Most popular wordprocessor file formats are acceptable. It is essential that the name and version of the wordprocessing program, type of computer on which the text was prepared, and format of the text files are clearly indicated.

Illustrations

Line drawings and cyclic or aromatic formulae should be in a form suitable for reproduction. They may be drawn in black ink on drawing paper (letter height, 3–5 mm), but the use of good quality computer-generated figures is encouraged. They should preferably all require the same degree of reduction, and should be submitted on paper of the same size as, or smaller than, the main text to prevent damage in transit. Photographs should be submitted as clear black-and-white prints on glossy paper. Each illustration must be clearly numbered.

Illustrations can be printed in colour when they are judged by the Editor to be essential to the presentation. The publisher and the author will each bear part of the extra costs involved. Further information concerning colour illustrations and the costs to the author can be obtained from the publisher.

Legends to the illustrations must be submitted in a separate list.

All tables and illustrations should be numbered consecutively and separately throughout the paper.

Proofs

Authors will receive proofs, which they are requested to correct and return as soon as possible. No new material may be inserted in the text at the time of proofreading. All joint communications must indicate the name and full postal address of the author to whom proofs should be sent.

Further information

All questions arising after the acceptance of manuscripts, especially those relating to proofs, should be directed to: Elsevier Science Ireland Ltd. Elsevier House, Brookvale Plaza, East Park, Shannon, Co. Clare, Ireland. Tel.: +353 61 709609; fax: +353 61 709107.

The full and complete instructions to authors can be found on the World Wide Web: please visit our website which is accessible via the Elsevier Surfaces and Interfaces HomePage at http://www.elsevier.nl/locate/surfaces

Offprints

Twenty-five offprints will be supplied free of charge to the author(s). Additional offprints can be ordered at prices shown on the offprint order form which accompanies the proofs.

Structural determination of wear debris generated from sliding wear tests on ceramic coatings using Raman microscopy

C. P. Constable,[a] J. Yarwood, P. Hovsepian, L. A. Donohue, D. B. Lewis, and W.-D. Münz
The Materials Research Institute, Sheffield Hallam University, Pond Street, Sheffield S1 1WB, United Kingdom

(Received 30 September 1999; accepted 17 April 2000)

In order to address the important interest in wear debris and associated wear mechanisms, we have studied a series of physical-vapor deposition ceramic hard coatings (CrN/NbN, CrN, NbN, TiAlN/VN, and TiCN) using a ball-on-disk sliding configuration against corundum. The debris generated were characterized using Raman microscopy to identify compounds, especially oxides, generated during the wear process to gain a better understanding of tribochemical reactions. The high spatial resolution (2 μm), sensitivity to structural changes, and nondestructive nature make this technique ideal for the study of such small amounts of wear debris. This article examines binary, multicomponent, multilayered, and superlattice coatings. Under dry sliding conditions of 5 N normal load and 10 cm/s speed, titanium-based alloy coatings were found to provide TiO_2 (rutile) debris. However, the addition of thin layers of VN to the TiAlN system provided a lower friction coefficient, and much less debris through the possible formation of a lubricious surface oxide. CrN- and NbN-based coatings were also found to produce debris with Raman bands corresponding to oxides. Contact temperatures were also estimated by comparison of the tribochemical products generated during sliding wear with the formation temperatures of oxides detected from static oxidation. [S0734-2101(00)16604-7]

I. INTRODUCTION

When components in relative motion are mechanically engaged, for example, during sliding wear, the region of contact experiences a temperature rise.[1] This arises as a result of the mechanical energy required to overcome frictional resistance as sliding at the contact interface occurs.[1] At the micron level, this increase in temperature can be substantial and can result in a localized change in material properties inducing increased chemical reactivity. The chemical reactions at the interfaces of the tribocouples are strongly influenced by the high local pressures and the flash temperatures, which can be over 1000 °C, at spots where asperities collide.[2] Continuous sliding leads to the continuous formation and destruction of individual asperity contacts.[3] Attempts to quantify these flash temperatures have led to the formation of models.[1,4] These, however, are restricted by uncertainties, namely, (i) real area of contact (area of asperity contacts); (ii) time of heat source exposure; and (iii) consistency of material properties. Cowan and Winer[1] proposed that for a stationary ball in elastic contact with a rotating disk, the flash temperature is dependent on the sliding speed. Vancoille *et al.*[5] have demonstrated this with sliding wear tests on TiN performed at low, medium, and high speeds against corundum. In all these cases oxidation was observed and anatase and rutile phases were identified using Raman microscopy. The ratio of anatase-to-rutile TiO_2 was dependent on the sliding speed. They concluded that at sufficiently high sliding speeds, and thus correspondingly high temperatures, only rutile was formed in the tribocontact.[5] New Raman instrumentation has been developed utilizing high-stability laser excitation, efficient holographic notch filters, and sensitive charge-coupled-device (CCD) detectors. The coupling of an optical microscope to a Raman spectrometer to create a Raman microscope enables users to obtain high-quality spectra from small particles (typically, down to one or two micrometers in diameter). Raman microscopy has several advantages over other techniques for wear test studies, namely, (i) short sampling times (typically, 1–15 min); (ii) little or no sample preparation is required and data are collected under ambient conditions; and (iii) molecular information regarding the material in question is the analysis output.

Raman scattering involves photon interactions with phonon modes of the lattice,[6–9] making it very sensitive to changes in atomic lattice arrangement and able to distinguish between polymorphic forms.[10] However, it cannot detect non-Raman-active species or low-scattering cross-section materials like amorphous species. Furthermore, localized sample heating is possible due to the high-power small laser focus/spot (2 μm) and thermal degradation and/or polymorphic transitions can occur. On the other hand, Witke *et al.*[11] consider that the sensitivity of certain materials to laser-induced transformation can be an advantage and lead to additional information on otherwise unidentifiable amorphous phases that can then be interpreted with greater reliability.

The utilization of Raman microscopy in the field of tribology include: (a) MoS_2-based thin-film systems solid lubricants;[12] (b) wear-induced surface modification studies on hard coatings; physical-vapor deposition (PVD) TiN, solar-beam oxidized TiN, chemical-vapor deposition dia-

[a]Author to whom correspondence should be addressed; electronic mail: c.p.constable@shu.ac.uk

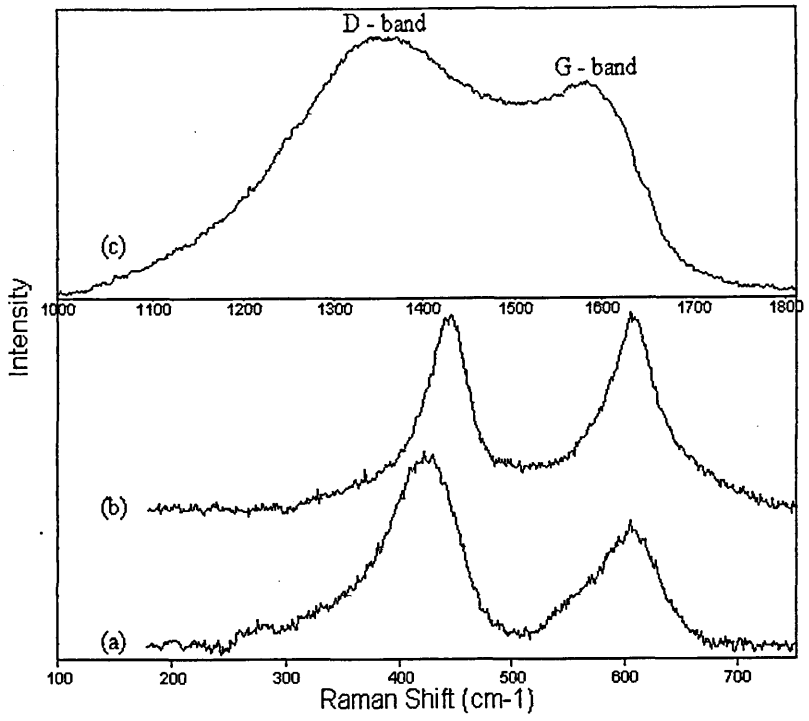

FIG. 1. Raman spectra of debris produced on a Ti(C, N) coating (a) from the top TiCN layer (b) through additional lower layers of the Ti(C, N) coating (laser power: 0.25 mW). (c) Raman spectrum of amorphous carbon detected in the debris from the top TiCN layer (laser power: 0.25 mW). Band positions determined from curve fitting the region 950–1800 cm^{-1} using 50% Gaussian–50% Lorentzian bands using Galactic Industries Corporation Grams/32 package.

mond, and diamond-like carbon coatings;[13] (c) fretting studies of TiN;[14] (d) friction studies of PVD coatings with carbon-rich outer layers;[15] and (e) dry sliding wear of TiN-based ternary PVD coating against corundum.[16] In this article, ball-on-disk tribotests on binary, multicomponent, multilayered, and superlattice coatings have been performed against corundum. Raman microscopy was utilized to determine the chemical nature of compounds within the wear debris to gain a better understanding of tribochemical reactions and also of contact temperature effects. The aim was to broaden the discussion beyond that of TiN to include other more complex, second and third generation, PVD coatings which can now be made routinely and which have enhanced tribological properties.[17]

II. EXPERIMENT

All coatings were grown using combined cathodic arc/unbalanced magnetron deposition. The PVD equipment used is described in detail in Ref. 18. Typical deposition recipes are given in Ref. 19. The coatings were deposited on flat high-speed steel and stainless-steel disk substrates polished to a shiny surface quality. The coatings had a thickness between 2.5 and 4 μm and a roughness of between 0.02 and 0.03 μm R_a.

A CSEM tribometer test rig was used under ambient laboratory conditions with no strict temperature or humidity control (25 °C and a measured relative humidity of between 30% and 35%). Corundum polycrystalline 6-mm-diam balls (Saphirwerk, Industrieprodukte AG) with a hardness of 1900 HVN and a surface quality $R_a = 0.2\ \mu$m were used as counterbodies. The coatings were placed and held rigid in the horizontal plane and the corundum counterbody was loaded on top of the disk. The normal load was constant at 5 N by applying a dead load and a medium sliding speed of 10 cm/s was used for all the coatings studied. Raman spectra of the debris sticking to the disks shortly after the wear tests were acquired using a Renishaw System 2000 spectrometer which comprised an integral Raman microscope (Olympus BH2 system), a stigmatic single spectrograph, and a Peltier-cooled CCD detector (400×600 pixels). The holographic notch filters allowed a lower spectral limit of ~200 cm^{-1}. The excitation wavelength used was a 632.8 nm (25 mW) HeNe laser. A maximum throughput of 4–5 mW was possible at the sample in a 2-μm-diam spot through a standard 50 ×microscope objective. A laser attenuation filter was utilized in the experiments to enable variation of the laser power hitting the debris samples. A 1% transmission filter was used to give a low-intensity beam of 0.25 mW (~0.05

TABLE I. Results of band fitting (50% Gaussian–50% Lorentzian shape) the Raman spectra of the as-formed debris.

	Peak 1			Peak 2		
As-formed debris	Position (cm^{-1})	FWHM (cm^{-1})	Area (%)	Position (cm^{-1})	FWHM (cm^{-1})	Area (%)
TiCN layer	426	60	57	602	59	43
Ti(C, N) layers	443	43	42	600	60	58

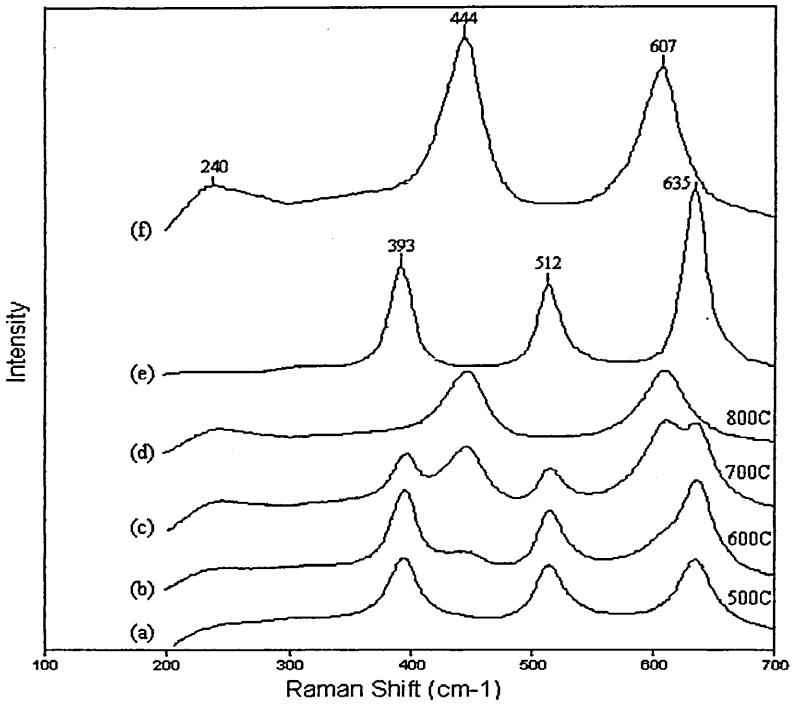

FIG. 2. Raman spectra of the Ti(C, N) coating heat treated in a furnace (in air): (a) 500 °C 1 h, (b) 600 °C 1 h, (c) 700 °C 1 h, and (d) 800 °C 1 h, (laser power: 25 mW) and spectra of standard TiO_2 powders (e) anatase and (f) rutile (laser power: 0.25 mW).

mW at the sample) to generate spectra in the as-formed state. This required relatively long exposure times of up to 15 min to obtain reasonable signal-to-noise ratios. The appearance before and after the spectra were acquired was noted and no optical change was apparent for any of the debris samples. Higher intensities of up to 25 mW were employed to study the structural integrity of the debris. Spectra were collected with a spectral resolution of 3–4 cm^{-1} and represented as intensity versus Raman shift (cm^{-1}). Static oxidation of the coatings were performed in a furnace in air.

III. RESULTS

A. Ti(C, N) coating: Debris analysis

The Ti(C, N) multilayered coating consisted of six layers, which include a 1.5 μm base layer of TiN then alternating layers of TiCN (0.4 μm) and TiN (0.6 μm), the outermost layer being TiCN, with a total thickness of ~3.9 μm. The as-formed debris spectrum showed bands associated with crystalline rutile TiO_2 (see Fig. 1 and Table I). The rutile 426 cm^{-1} band resulting from the TiCN debris was broad [see Fig. 1(a) and Table I] and shifted by 18 cm^{-1} to lower frequency from the standard value of 444 cm^{-1} [Fig. 2(f)]. Parker and Siegel[20] have reported that the Raman E_g modes of both anatase and rutile are sensitive to oxygen deficiency, therefore, may be an indicator for a slight deviation from stoichiometry of the rutile TiO_2 structure. A small shoulder near 512 cm^{-1} was also observed on the 602 cm^{-1} band, which could be from anatase in the debris. This may indicate that a slightly lower contact temperature, and therefore lower friction coefficient, occurred during sliding. The Raman spectrum also showed bands due to the amorphous carbon D (defect) band at 1351 cm^{-1} and the G (graphite) band at 1599 cm^{-1} [Fig. 1(c)], which may act as a lubricant. The Raman spectrum of carbon is well known[21,22] and the value of $I_{(D)}/I_{(total)}$ can give an idea of the amount of disorder.[22] The $I_{(D)}/I_{(total)}$ value obtained for the carbon detected within the debris was 71%, indicating a highly disordered structure similar to microcrystalline carbon.[22] The Raman spectrum from the debris deeper into the coating structure incorporating TiN layers [Fig. 1(b)] was in good agreement with the rutile standard spectrum [Fig. 2(f)].

1. Static oxidation

Successive oxidation was performed at 500, 600, 700, and 800 °C for 1 h. The furnace heat treatment of the Ti(C, N) multilayered coating showed TiO_2 oxides to be present on the surface (Fig. 2). Phonon modes of anatase and rutile phases are well known.[23] At 500 °C the oxide identified on the surface was anatase, which has a metastable structure that transforms to rutile between 600 and 1000 °C. Upon subsequent increase in temperature, an expected anatase–rutile phase transformation occurred. At 700 °C there was approximately 50% anatase and 50% rutile present on the surface. The 800 °C spectrum indicated that full conversion to rutile had occurred. Unlike the case of the debris analysis, almost no amorphous carbon was detected on the surface of the heat-treated Ti(C, N) coating.

Although tribochemical reactions are nonequilibrium reactions, it is interesting to correlate wear debris measurements with the static oxidation of the Ti(C, N) coating to enable an approximate value for the contact temperature during sliding to be postulated. Debris from both the top TiCN layer and from debris generated from deeper into the Ti(C, N) coating consisted of predominantly rutile TiO_2. The static oxidation of the Ti(C, N) coating determined that at temperatures in excess of 700 °C rutile TiO_2 became the main phase,

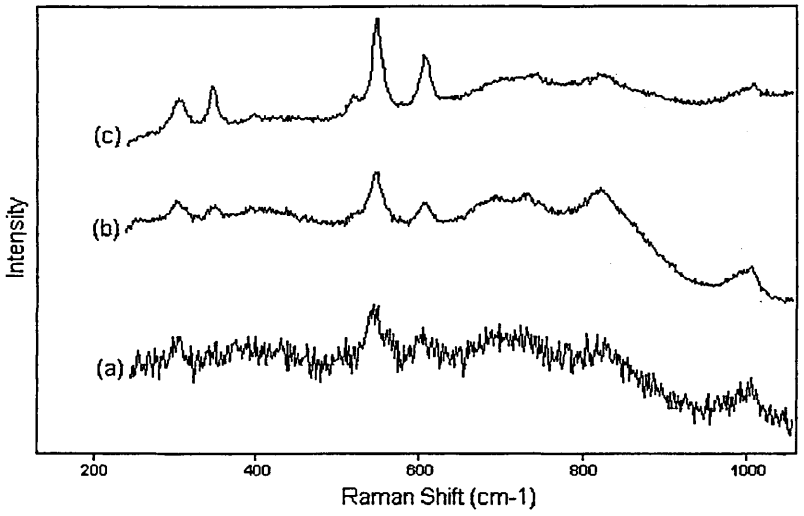

FIG. 3. Raman spectra of debris produced on a CrN coating. (a) AS-formed debris: 0.25 mW, (b) 5 mW, and (c) 12.5 mW.

therefore, contact temperatures >700 °C may occur at the tribocontact for the Al_2O_3–TiCN/Ti(C, N) systems, under the test conditions used.

B. CrN coating: Debris analysis

Although the as-formed debris spectrum was weak [Fig. 3(a)], Cr_2O_3 bands were clearly observed at 305, 546, and 606 cm^{-1} [see Fig. 4(d)]. Other broad bands were observed between 675 and 900 cm^{-1} which are unknown. Two further bands are observed at ~1000 cm^{-1}. The strong band associated with CrO_3 at lower frequency [Fig. 4(e)] was not observed at ~490 cm^{-1}, therefore, it was unlikely that CrO_3 was present. With an increase in laser power, a crystallization process occurred in which sharper and better-defined bands associated with Cr_2O_3 were observed. The broad features observed between 675 and 900 cm^{-1} were retained, ruling out any possibility of amorphous oxide phases.

1. Static oxidation

The furnace heat treatment of the CrN coating showed a small amount of Cr_2O_3 oxide formation on the surface at 500 °C indicated by small bands at 343, 546, and 607 cm^{-1} [Fig. 4(a)]. These bands grew in intensity as the temperature was increased until at 700 °C sharp high-intensity well-resolved bands are observed. At 700 °C [Fig. 4(c)] there appeared to be underlying unoxidized coating remaining, signified by low-frequency broad acoustic modes and higher-frequency optic modes of the fcc lattice, indicating high resistance to oxidation of the CrN coating, in which Cr_2O_3 oxide may be acting as a protective layer.

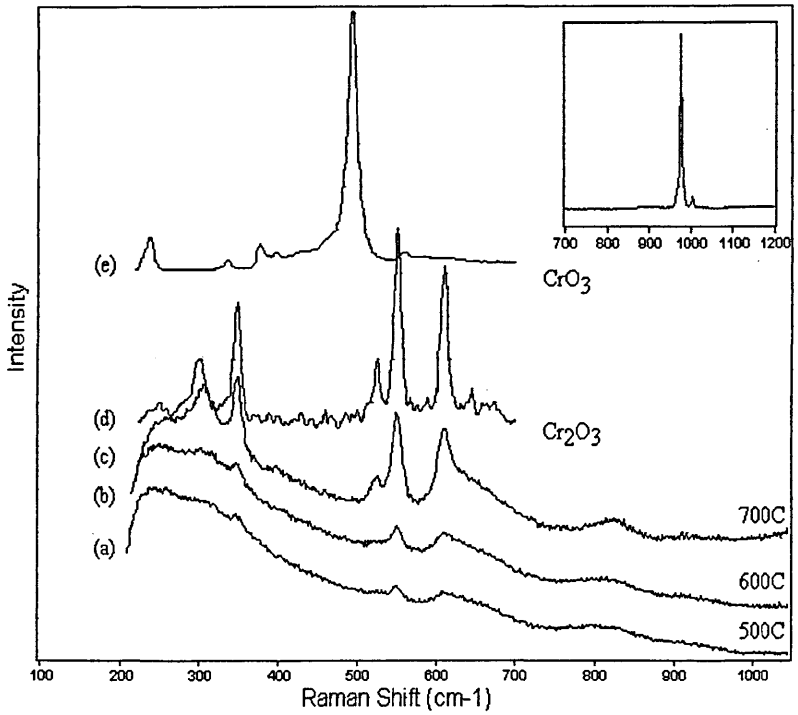

FIG. 4. Raman spectra of CrN coating heat treated in a furnace (in air): (a) 500 °C 1 h, (b) 600 °C 1 h, and (c) 700 °C 1 h, (laser power: 25 mW) and spectra of reference chromium oxide powders (d) Cr_2O_3 and (e) CrO_3. Inset shows bands between 900 and 1000 cm^{-1} associated with CrO_3 vibrations (laser power: 0.25 mW).

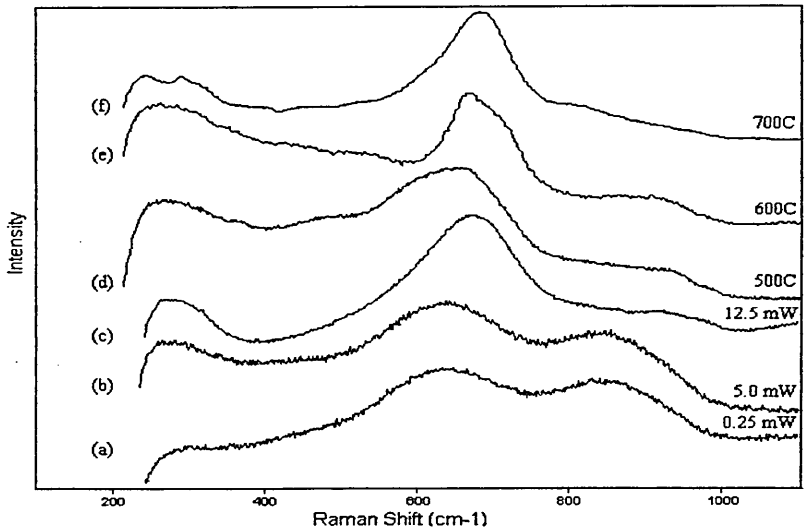

FIG. 5. Raman spectra of debris produced on a NbN coating: (a) as-formed debris (0.25 mW), (b) 5 mW, and (c) 12.5 mW, and spectra of the NbN coating heat treated in a furnace (in air) (d) 500 °C 1 h, (e) 600 °C 1 h, and (f) 700 °C 1 h (laser power: 25 mW).

It was found that the as-formed wear debris from CrN coating consisted of predominantly Cr_2O_3. Static oxidation of the CrN coating showed Raman bands from Cr_2O_3 formed on the surface at 500 °C, which grew in intensity as the temperature was increased. It can, therefore, be estimated that temperatures of 500 °C (or above) may occur at the tribocontact for the Al_2O_3–CrN system, under the test conditions used.

C. NbN coating: Debris analysis

The Raman spectrum of the as-formed debris [Fig. 5(a)] featured two strong and broad features in the range 500–1000 cm^{-1} and a very low-intensity band centered at ~300 cm^{-1}. These became sharper as crystallization/phase transformation occurred during irradiation with higher laser intensities. Very little change was observed in the 5 mW spectrum [Fig. 5(b)], but at 12.5 mW the band observed at ~300 cm^{-1} grew in intensity and the diffuse band centered at ~850 cm^{-1} was diminished. The band centered at ~650 cm^{-1}, which has previously been assigned to the symmetric stretching modes of the niobia polyhedra for amorphous $Nb_2O_5 \cdot nH_2O$,[10] became sharper and shifted ~20 cm^{-1} to higher frequency to 670 cm^{-1} [Fig. 5(c)]. Two additional small bands also became resolved, centered at 923 and 979 cm^{-1}. The as-formed debris spectrum showed similar broad features to that of $Nb_2O_5 \cdot nH_2O$, as reported by Wachs and Jehng.[10] Upon irradiating the debris with 12.5 mW laser power [Fig. 5(c)], the spectrum transformed to resemble TT–Nb_2O_5 and T–Nb_2O_5 orthohombic phases.[10]

1. Static oxidation

Furnace oxidation of the NbN coating [Figs. 5(d)–5(f)] showed amorphous Nb_2O_5 oxide to be present on the surface

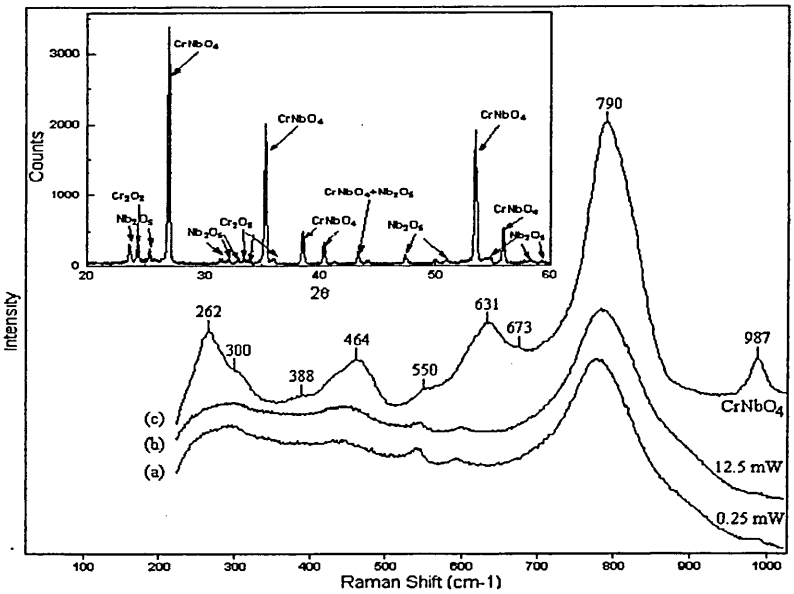

FIG. 6. Raman spectra of debris produced on a CrN/NbN superlattice coating: (a) as-formed debris (0.25 mW), (b) 12.5 mW, and (c) spectrum of as-synthesised $CrNbO_4$ standard (laser power: 0.25 mW). Inset: XRD pattern of as-synthesised $CrNbO_4$ [JCPDS-ICDD method: Natl. Bur. Stand. Monogr. 25, 19 38 (1982)]. Residual Cr_2O_3 and Nb_2O_5 phases observed.

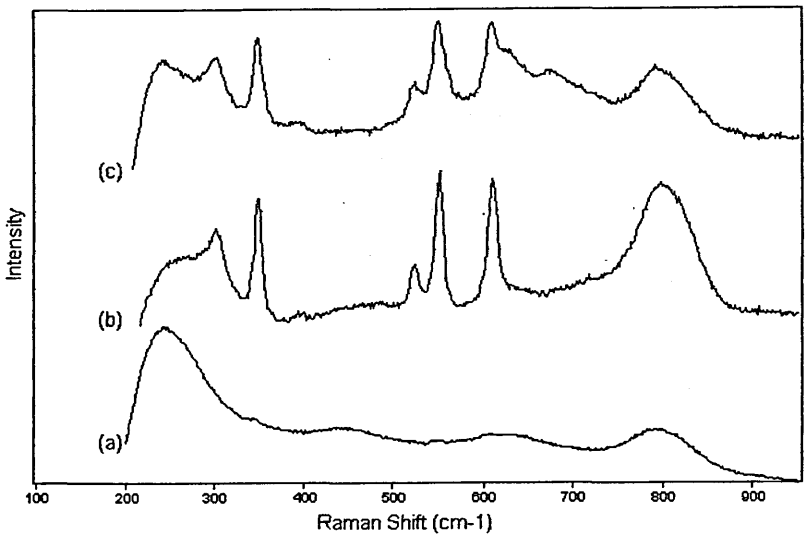

FIG. 7. Raman spectra of the CrN/NbN superlattice coating heat treated in a furnace (in air): (a) 700 °C 1 h, (b) 800 °C 1 h, and (c) 900 °C 1 h (laser power: 25 mW).

at 500 °C [Fig. 5(d)], similar to the spectrum of $Nb_2O_5 \cdot nH_2O$.[10] Upon increasing the temperature the amorphous niobium oxide increased in crystallinity, signified by the sharpening of bands and resolution of further bands, especially in the 200–550 cm^{-1} region. The oxide spectrum formed on the 700 °C treated coating [Fig. 5(f)] was almost identical to the spectra identified as either $TT-Nb_2O_5/T-Nb_2O_5$ prepared by calcination of bulk niobium oxide at 500 and 800 °C, respectively.[10] The $TT-Nb_2O_5$ and $T-Nb_2O_5$ both have a crystalline orthohombic Nb_2O_5 phase structure determined by x-ray diffraction (XRD).[10] The as-formed debris spectrum had similar features to the 500 °C treated NbN coating, although there was not an exact correlation. A clear contact temperature was, therefore, difficult to estimate. The evidence for the symmetric stretching mode at ~650 cm^{-1} of the niobia polyhedra from an amorphous $Nb_2O_5 \cdot nH_2O$ oxide and the resemblance with the 500 °C treated coating spectra did allow an estimate of around 500 °C to be postulated as a contact temperature for the Al_2O_3–NbN system, under the test conditions used.

D. CrN/NbN superlattice coating: Debris analysis

The main feature of the as-formed debris spectrum [Fig. 6(a)] was a high-intensity band centered at ~780 cm^{-1}. Low-intensity bands were also observed at 289, 447, 544, 600, 987, and 1018 cm^{-1}. The 544 and 600 cm^{-1} bands and possibly the 289 cm^{-1} band can be attributed to Cr_2O_3 [Fig. 4(d)]. Very little change occurred in the spectrum upon higher laser irradiation and only a very slight shift to higher frequency of the 780 cm^{-1} band was observed, which demonstrated the debris was structurally stable [Fig. 6(b)]. Very good spectral agreement of the synthesized $CrNbO_4$ oxide [Fig. 6(c)] and the as-formed debris spectra was seen. The main band position for the $CrNbO_4$ standard and the as-formed debris differed by only 10 cm^{-1}, indicating the debris

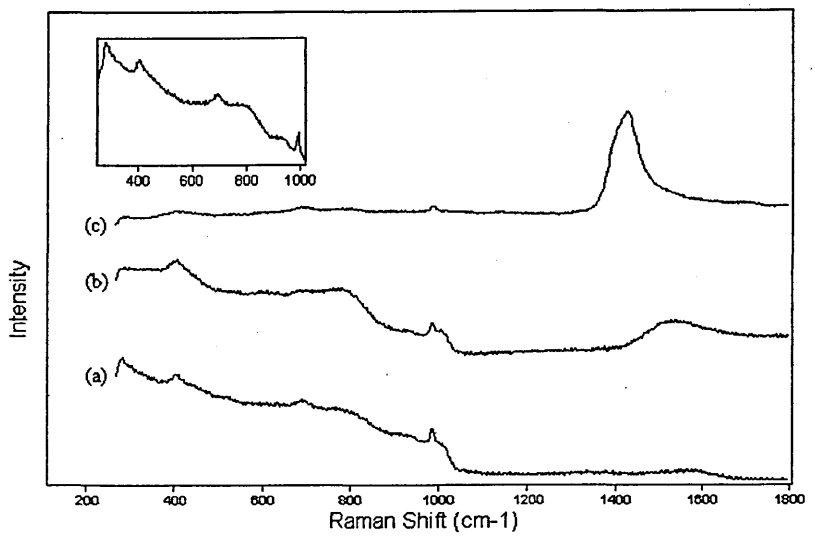

FIG. 8. Raman spectra of debris produced on a TiAlN/VN superlattice coating sliding against a corundum ball (a) as-formed debris (0.25 mW), (b) 5 mW, and (c) 25 mW (inset: 250–1025 cm^{-1} region of the as-formed debris spectrum).

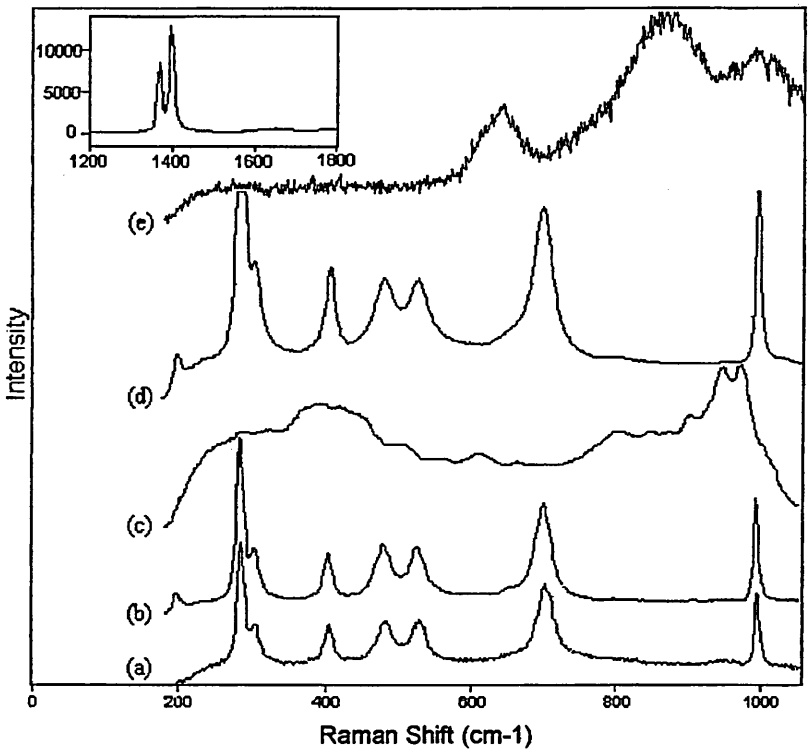

FIG. 9. Raman spectra of the TiAlN/VN coating heat treated in a furnace (in air): (a) 600 °C 1 h, (b) 650 °C 1 h, and (c) 700 °C 1 h (laser power: 25 mW) and spectra of reference oxide powders (d) V_2O_5 and (e) α-Al_2O_3 (laser power: 0.25 mW; Inset: high-frequency region of α-Al_2O_3 spectrum, showing two very intense characteristic bands).

almost certainly contained $CrNbO_4$ oxide. This slight frequency shift may be explained by a small difference in the Cr:Nb stoichiometry, indicating the as-formed debris contained slightly more Nb within the crystalline lattice than the standard. The standard was prepared by heating Cr_2O_3 and Nb_2O_5 in a 1:1 ratio in a furnace (in air) at 1000 °C for 24 h. The resultant powder had a grayish yellow-green color. The powder was studied using XRD to confirm the correct preparation (Fig. 6, inset). This showed that the powder was composed of mainly $CrNbO_4$, but residual Cr_2O_3 and Nb_2O_5 oxides were also detected.

1. Static oxidation

The oxidation of the CrN/NbN superlattice coating has shown that much of the underlying coating was still retained even after heat treatments of up to 900 °C [Fig. 7(c)]. This was shown by the phonon modes, indicative of PVD polycrystalline coatings still being present throughout the static oxidation regime.[8] This demonstrated the high oxidation resistance of the CrN/NbN superlattice coating. The Raman spectrum of the 700 °C treated coating [Fig. 7(a)] showed two very small bands at 343 and 546 cm^{-1}, which have been attributed to Cr_2O_3 and the 790 cm^{-1} band characteristic of $CrNbO_4$ oxide. The latter grew in intensity greatly upon an increase of 100 °C in the treatment temperature to 800 °C, also large intensity bands due to Cr_2O_3 are seen. The intensity of this $CrNbO_4$ oxide band then appeared to decrease in intensity for the 900 °C treated coating. An additional broad feature also appeared at ~680 cm^{-1}, which may be due to Nb_2O_5 oxide formation as observed for the NbN coating. A further band was seen as a shoulder on the 606 cm^{-1} Cr_2O_3 band. Further investigations of the 900 °C treated coating are required to fully understand the static oxidation.

The oxides $CrNbO_4$ and Cr_2O_3 were identified in the as-formed wear debris by a very good correlation with $CrNbO_4$ and Cr_2O_3 standard spectra. The static oxidation of CrN/NbN performed at 700 °C also showed this mixed metal oxide to exist on the surface, as did the 800 and 900 °C treated coatings. Thus, an estimated temperature of ~700 °C may occur at the tribocontact for the Al_2O_3–CrN/NbN system, under the test conditions used.

E. TiAlN/VN superlattice coating: Debris analysis

The as-formed debris spectrum [Fig. 8(a)] showed firm evidence for the presence of V_2O_5, by a good comparison with the standard V_2O_5 spectrum [Fig. 9(d)]. This was indicated by weak bands at frequencies of 281, 405, and 692 cm^{-1} and by a slightly larger band at ~990 cm^{-1}. Additional broad features were observed between 720 and 970 cm^{-1} that increased in intensity as the debris was irradiated with higher laser intensities. Strong α-Al_2O_3 bands became visible in the frequency range 1350–1450 cm^{-1}, [Fig. 8(c)], characteristic of the Al–O stretching mode, when the debris was irradiated with 25 mW laser power. These bands were not fully resolved, indicating the oxide was not fully crystalline when compared with the standard spectrum (Fig. 9, inset). A possible phase transition from γ-Al_2O_3 or from a crystallization of disordered α-Al_2O_3 oxide may have occurred, if the bands between 720 and 970 cm^{-1} were due to α-Al_2O_3. It is well known that Al_2O_3 has several phases and the nature of these phases depends strongly on the method and the temperature of production.[24] For example, with boe-

TABLE II. Summary of results (sliding at 10 cm/s against corundum).

Tribocouple	Coefficient of friction	Sliding length (km)	Appearence of debris	Structure and composition of debris	Oxides detected (static oxidation)	Estimated contact Temp. (°C)
TiCN–Al_2O_3 (top layer)	0.18	3	White powder (small amount)	TiO_2(rutile)+small amount of anatase +disordered carbon	TiO_2 (anatase and rutile)	<700
Ti(C, N)–Al_2O_3 (additional layers incorporating TiN)	0.50–0.72	3	White powder	TiO_2 (rutile)	As above	<700
CrN–Al_2O_3	0.45	1	Pale green powder	Cr_2O_3	Cr_2O_3	<500
NbN–Al_2O_3	0.66	1	White powder	Amorphous $Nb_2O_5 \cdot nH_2O$	$Nb_2O_5 \cdot nH_2O$ and TT–Nb2O5 /T–Nb2O5	~500
CrN/NbN–Al_2O_3	0.69	1	Gray-green powder	Cr_2O_3,$CrNbO_4$	Cr2O3,CrNbO4 Nb2O5?	~700
TiAlN/VN–Al_2O_3	0.54	9	Light brown powder (very small amount)	V_2O_5,γ/α–Al_2O_3	V_2O_5, complicated oxide involving Fe, V, Ti, Al, and oxygen	~600

hmite as the starting material, γ-Al_2O_3 is formed at 500–850 °C, θ-Al_2O_3 is formed from 850 to about 1100 °C, while above 1100 °C with any starting material only α-Al_2O_3 is obtained.[24] The broad diffuse band seen in Fig. 8(b), which covered the range 1400–1650 cm^{-1}, was very similar in nature to the spectrum of γ-Al_2O_3 collected using 632.8 nm excitation reported by Aminzadeh.[24] The Al_2O_3 detected in the debris cannot be from worn particles of the ball material because bands associated with α-Al_2O_3 [Fig. 9(e), and inset] would have been visible in the as-formed debris spectrum, as the laser was positioned on the same spot throughout the debris analysis. Furthermore Al_2O_3 bands have not been detected previously when studying debris from the other coatings, indicating little or no wear of the corundum ball takes place during sliding. Small bands due to V_2O_5 in the debris were still present after irradiation with 25 mW laser light.

1. Static oxidation

Heat treatment of the TiAlN/VN superlattice coating at 600 °C [Fig. 9(a)] showed clear V_2O_5 oxide bands present on the surface. These bands were retained upon heat treatment to 650 °C [Fig. 9(b)]. At 700 °C the TiAlN/VN coating was destroyed and a complicated spectrum resulted in which many bands were observed which were mainly broad [Fig. 9(c)]. The spectrum will feature reaction products of Fe, V, Ti, Al, and oxygen. There was definitely no evidence of V_2O_5 at 700 °C.

The evidence for V_2O_5 in the as-formed debris and the appearance of this oxide on the surface of the TiAlN/VN coating after heat treatment at 600 °C allowed an estimate of ~600 °C for the contact temperature for the Al_2O_3–TiAlN/VN system, under the condition used.

IV. CONCLUSION

Raman microscopy has been shown to be a powerful technique for the identification of compounds, especially oxides, within wear debris resulting from ball-on-disk experiments. A comparison with oxide standards and from oxide spectra from previous publications by other authors has enabled the distinction between many different forms of metal oxides that were present within the debris and enabled laser-induced phase transformations to be monitored. Carbon was detected in the debris resulting from sliding against the TiCN top layer of the Ti(C, N) multilayered coating, which was microcrystalline in nature. A lower friction coefficient of 0.18 arose during sliding and a possible decrease in the contact temperature may have taken place due to the detection of an oxygen-deficient rutile phase and possible evidence for anatase within the as-formed TiCN debris. This indicated a strong possibility that the amorphous carbon was acting as a lubricant during sliding wear. The incorporation of fine layers of VN to the TiAlN system and the subsequent evidence for V_2O_5 in the debris and the lower friction coefficient of 0.54 when compared to 0.8–0.9, which is known to occur for TiAlN, realizes the lubricating action of V_2O_5 during sliding wear.

A mixed metal solid solution oxide, $CrNbO_4$, was detected within the as-formed debris from the CrN/NbN superlattice coating, indicating a reaction product from the metallic components of the superlattice coating with oxygen had taken place. This has shown that high-contact temperatures do exist, which are sufficient in magnitude, to result in complicated tribo-oxidation reactions. The determination of these qualitative contact temperatures by a comparison of the tribochemical products detected in the wear debris with the formation temperatures of thermally attained reaction prod-

ucts correlated very well. Contact temperatures for the coating systems studied were estimated as greater than 500 °C but below 800 °C (see Table II). The observed frictional heating effects resulted in oxidational wear mechanisms occurring for the coating systems studied.

ACKNOWLEDGMENT

The authors would like to gratefully acknowledge Renishaw plc for their financial support.

[1]R. S. Cowan and W. O. Winer, in *ASM Handbook, Friction, Lubrication and Wear Technology*, edited by P. Blau (ASM, Materials Park, OH, 1992), Vol. 18, p. 39.
[2]K. Holmberg and H. Ronkainen, in *Coatings Tribology: Properties, Techniques and Applications in Surface Engineering—Contact Mechanisms and Surface Design*, edited by A. Matthews (Elsevier, Amsterdam, 1994), p. 251.
[3]I. M. Hutchings, *Tribology: Friction and Wear of Engineering Materials*, Metallurgy and Materials Science Series (Hodder, London, 1992), p. 82.
[4]D. Kuhlmann-Wilsdorf, Mater. Sci. Eng. **93**, 107 (1987).
[5]E. Vancoille, B. Blanpain, Y. Xingpu, J.-P. Celis, and J. R. Roos, J. Mater. Res. **9**, 992 (1994).
[6]W. Spengler and R. Kaiser, Solid State Commun. **81**, 881 (1976).
[7]C. C. Chen, N. T. Liang, W. S. Tse, I. Y. Chen, and J. G. Duh, Chin. J. Phys. (Taipei) **32**, 205 (1994).
[8]C. P. Constable, J. Yarwood, and W.-D. Münz, Surf. Coat. Technol. **116-119**, 155 (1999).
[9]G. Lucazeau and L. Abello, Analusis **23**, 301 (1995).
[10]J.-M. Jehng and I. E. Wachs, Chem. Mater. **3**, 100 (1991).
[11]K. Witke, D. Klaffke, A. Skopp, and J. P. Schreckenbach, J. Raman Spectrosc. **29**, 411 (1998).
[12]N. T. McDevitt, M. S. Donley, and J. S. Zabinski, Wear **166**, 65 (1993).
[13]B. Blanpain, M. Franck, H. Mohrbacher, E. Vancoille, J.-P. Celis, and J. R. Roos, in *Thin Films in Tribology. Micro-Raman Spectroscopy for the Characterisation of Wear Induced Surface Modifications on Hard Coatings*, edited by D. Dowson *et al.* (Elsevier, Amsterdam, 1993), pp. 623–630.
[14]K. Schouterden, B. Blanpain, J.-P. Celis, and O. Vingsbo, Wear **181-183**, 86 (1995).
[15]O. Wänstrand, R. Fella and N. Axén, Surf. Coat. Technol. **94-95**, 469 (1997).
[16]E. Vancoille, J.-P. Celis and J. R. Roos, Wear **165**, 41 (1993).
[17]W. D. Sproul, J. Vac. Sci. Technol. A **12**, 1595 (1994).
[18]W.-D. Münz, D. Schulze, and F. J. M. Hauzer, Surf. Coat. Technol. **50**, 169 (1992).
[19]I. Petrov, P. Losbichler, D. Bergstrom, J. E. Greene, W.-D. Münz, T. Hurkmans, and T. Trinh, Thin Solid Films **302**, 179 (1997).
[20]J. C. Parker and R. W. Siegel, J. Mater. Res. **5**, 1246 (1990).
[21]A. Cuesta, P. Dhamalincourt, J. Laureyns, A. Martínez-Alonso, and J. M. D. Tascón, Carbon **32**, 1523 (1994).
[22]A. Cuesta, P. Dhamalincourt, J. Laureyns, A. Martínez-Alonso, and J. M. D. Tascón, J. Mater. Chem. **8**, 2875 (1998).
[23]U. Balachandran and N. G. Eror, Solid State Chem. **42**, 276 (1982).
[24]A. Aminzadeh, Appl. Spectrosc. **51**, 817 (1997).

Investigation of Wear Processes on Worn Tools Using Raman Microscopy

C P Constable*, J Yarwood, G Robinson, Q Luo, D.B. Lewis and W-D Münz

Materials Research Institute, Sheffield Hallam University, Sheffield S1 1WB, UK

ABSTRACT: In order to address the industry-driven interest in wear and associated mechanisms of coated tools during dry High-Speed Machining applications, two commercially available Physical-Vapour-Deposited (PVD) coatings were studied. These were TiAlN based and had multilayered architectures deposited on to cemented carbide 8mm ball-nosed two flute end mills. Raman microscopy and SEM-EDX analysis were used to characterise the molecular and elemental species, respectively, present on the worn surfaces of tools after controlled lifetime tests milling into A2 HRC58 die steel. This was performed to gain a better understanding of tribochemical reactions that occur during the highly complex wear environment during milling. Cutting temperatures were estimated as ≤950°C, indicated by oxide phase transformations and corroborated by static oxidation studies. In addition, transfer layers of iron/steel and iron oxide species (FeO, Fe_3O_4 and Fe_2O_3), oxidation products of the coating (TiO_2 and α-Al_2O_3), and spectral changes due to deformation and stress-state were observed as a consequence of wear. The high spatial resolution (2μm), sensitivity to structural/chemical changes and the non-destructive nature of the technique make Raman microscopy ideal for the study of wear on tools with complex geometry that cannot be readily studied by other techniques without difficult sample preparation.

Keywords: Raman microscopy, PVD coatings, milling, oxides and wear

1. INTRODUCTION

Dry high-speed machining operations require durable, oxidation resistant PVD coatings to protect cemented carbide tools against wear and oxidation. TiAlN coatings are widely used because they exhibit oxidation resistance up to 750°C, compared with standard TiN coatings of 550°C[1]. Further improvements in mechanical and thermal properties result when small amounts of Cr and Y are incorporated within the TiAlN structure, resulting in state of the art coating systems that can out-perform the current UK market leaders[2-4]. However, to enable further development of tool coatings it is imperative to have an understanding of the physical and chemical processes associated with tool wear. Wear occurs because of the high normal loads imparted by the chips and work-piece which move rapidly over the tools wear surfaces[5]. In addition, the related friction at these contacting surfaces increases with temperature, which further accelerates tool wear. The chips carry some of this thermal energy away from the tool, however, even with the best tools their hardness, toughness, and chemical stability properties eventually degrade with both increasing temperature and exposure at temperature. Average temperature conditions are approximated using the following type of relationship[5].

$$T = u\left(\frac{Vt}{Kpc}\right)$$

* Corresponding author. Tel.: +44 114 2253715; email: c.p.constable@shu.ac.uk

Where T is the mean temperature of the tool-chip interface, u is the specific cutting energy (i.e. energy used per-unit-volume of material removed), V is the cutting speed, t, is the un-deformed chip thickness and K, p, and c are the conductivity, density, and specific heat, respectively of the workpiece material[5]. Wear progresses along the cutting edge and on adjacent surfaces and is localised to specific areas where stress/strain, velocity, and temperature are above critical levels. The temperature distribution in the cutting region may be in a regime where parts of the tool are exposed to dangerously high temperature levels (i.e. hot spots), which are well above the mean predicted temperature.

The majority of wear analysis to date utilising Raman microscopy has concentrated on PVD TiN coatings in sliding/fretting wear environments. Various counterbody materials (including chromium steel[6,7] corundum[8] and silicon nitride[9]) have been used and have primarily been concerned with the detection of reaction/transfer layers[7]; surface modifications[10] and characterisation of wear debris[8,11,12]. The initial investigation reported here is believed to be the first of its kind to apply Raman microscopy to the analysis of worn PVD coated tools. The aim of this work was to identify chemical species, especially oxides, prevalent on the worn surfaces after highly controlled lifetime tests to give an insight into the tribochemistry and contact temperatures during dry high-speed milling.

2. EXPERIMENTAL

TiAlCrN (SUPERCOTE-02) and TiAlCrYN (SUPERCOTE-11) coatings were deposited by arc bond sputtering (ABS) technology using an industrially sized PVD equipment (Hauzer HTC 1000 ABS) by Bodycote-SHU coatings Ltd[13]. End mills were coated using typical deposition recipes described in Ref[2]. A unique feature of these coatings is a double layered overcoat consisting of a lower fine multilayered TiAlCr(Y)/CrN with a periodicity of 1.6nm combined with an upper glassy amorphous TiAlCr oxynitride[2]. The importance of the nanostructured oxynitride overcoat is to reduce the friction coefficient during the initial stages of cutting[2,13,14].

Milling tests were performed on a MAZAK FJ 25 machine tool, shown schematically along with cutting test parameters in Fig. 1. The workpiece material was A2 die steel HRC58 (Chemical composition (wt%) C: 1.0, Mn: 0.65, Cr: 5.0, Mo: 1.0 and V: 0.3). Quantification of wear was determined by measurement of the wear-land size at intervals of 5 minutes using an optical imaging system. Analyses of the worn surfaces of the tool, chip particles and a statically oxidised tool were performed using a Renishaw Raman System 2000 spectrometer. This system comprised of an integral Raman microscope, a stigmatic single spectrograph, and a Peltier-cooled CCD detector (400 x 600 pixels)[15]. The microscope attachment was an Olympus BH2 system. The holographic notch filters allowed a lower spectral limit of ~150cm^{-1}. The excitation wavelength used was 632.8-nm (25 mW laser) from a HeNe laser. A maximum throughput of 4-5 mW was possible at the sample in a 10μm diameter spot through a 20X ultra long working distance microscope objective.

A Philips XL-40 Scanning Electron Microscope (SEM) was employed to examine the cutting edge at an accelerating potential of 20kV. Details at the worn edges were observed using both secondary electron imaging (for surface morphology) and by

back-scattered electron imaging (atomic number contrast). The XL-40 SEM was supported with an attached ultra-thin-window Oxford Link ISIS X-ray energy dispersive X-ray (EDX) analysis system which allowed elemental identification and 2-dimensional element mapping.

3. RESULTS AND DISCUSSION

The wear amount (mm) vs. time-in-cut (minutes) is illustrated in Fig. 2 for a SUPERCOTE-02 mill at cutting speeds of 10,000 and 20,000rpm. The wear progress, as indicated, can be divided into three distinct stages.

I) Initial rapid wearing of the tool to approximately 0.09mm (running-in-period i.e. removal of local asperities to define the cutting surface).
II) Steady state wear (progressive wearing of the tool to a defined wear land size)
III) Rapid wearing of the tool to a width of 0.3mm when the tool was deemed to be at the end of life (i.e. would result in machining out-of-tolerance parts in real situations).

The tool used at the higher spindle speed i.e. 20,000rpm reached the 0.3mm failure criteria after a shorter time-in-cut, as expected. This can be explained by the higher cutting stresses and temperatures imposed on to the surfaces due to the higher cutting energy. The tool used with a spindle speed of 10,000rpm had a lifetime of 185 minutes which was over twice that achieved at 20,000rpm. In contrast, SUPERCOTE-11 tools showed improved performance and could cut for 220 minutes at 10,000rpm and 85 minutes at 20,000rpm, before reaching the failure criteria.

An example of combined SEM-EDX morphological and spectroscopic analysis of a worn SUPERCOTE-11 coated cutting tool after 30 minutes-in-cut (20,000rpm) is presented in Fig. 3.

Coating failure was observed as spalling (rake side) to a width ~500μm (Fig. 3(a)), the region of spalling wear exhibited flat and smooth morphology (Fig. 3(b)) and bright back-scattered imaging electron contrast (Fig. 3(c)), indicative of partial and even complete removal of the SUPERCOTE-11 coating revealing the exposed cemented carbide (bright regions). Further information on coating removal and substrate exposure was facilitated by two-dimensional mapping of characteristic X-rays, as shown in Fig. 3(d). The Kα-Al and Kα-Ti originated only from the SUPERCOTE-11 coating itself, the intensity distributions of which suggest retained coating. Note the presence of Al and Ti in the spalling pool indicated progressive wear of the SUPERCOTE-11 instead of prompt adhesive detachment. Moreover, the co-existence of Kα-O and Kα-Fe, implied attached iron oxide on the surface. The iron oxide generated an intermediate back-scattered electron contrast between the dark SUPERCOTE-11 (i.e. lower average atomic number) and bright cemented carbide (i.e. higher average atomic number (Fig. 3(c)). The iron, which then oxidised on the tool, was clearly transferred from the workpiece during cutting and implied elevated temperatures. Raman microscopic analysis was then employed to give additional information on the specific chemistry of the oxides formed during wear, elucidating further the material transfer issue and on contact temperatures. The rake of worn tools was investigated at various time-points that represented the three stages of wear (outline above) to gain a handle of the wear amount and tribochemical species

present at each regime. Fig. 4 demonstrates the analysis of a SUPERCOTE-02 coating after various stages of wear milling at 20,000rpm.

The as-deposited coating spectrum (Fig. 4(a)) featured broad bands centred at ca. 300cm^{-1} and 685cm^{-1} which are due to the acoustical (150-350cm^{-1}) and optical (550-850cm^{-1}) vibrational modes of the polycrystalline lattice[16]. The 5 minutes-in-cut spectrum (Fig. 4(b)) compared favourably, albeit less defined, to the as-deposited coating indicating that the protective coating layer was still present. However, there were two key spectral changes: i) a shift in the position of the main optical mode from 685cm^{-1} to 660cm^{-1} and, ii) a slight broadening of this mode (ca. 10cm^{-1}). Both these phenomena can be explained by: (a) mechanical deformation processes occurring in the wear zone resulting in micro-cracks forming in the coating[17,18] and (b) stress annealing from the high cutting temperatures[19] (the latter having the greater contribution). These deformation and annealing effects cause compressive stress relief which was detected by a Raman spectral shift to lower frequency[20-22]. Moreover, the spectral line width gives information on both the amount of deformation and disorder. The broadening of bands arising from solid-state systems is due to phonon relaxation pathways created as a result of disordering processes[23]. In this case damage as a result of mechanical collisions with the workpiece during milling was the probable cause of the band broadening, due to an increased number of crystal defects, dislocations and fractured grains[17]. After 35 minutes-in-cut (Fig. 4(c)) a different spectrum featuring a sharper band at ca. 670cm^{-1} (N.B. this was not a sharpening of the coating band) and evidence of two smaller bands at ca. 310 and 530cm^{-1} resulted. These are not typical of the coating thus indicating a new species. This species was identified as Fe_3O_4 (magnetite) (see Fig. 5(a)) indicating a transfer layer. This was surprising as coating oxidation products or exposed WC–Co/WO_3 generated as a result of the high cutting temperatures were thought more probable (see Fig. 9(a)). Higher friction will result when the protective (lower friction) coating layer was removed, (spallation was confirmed from SEM studies, Fig. 3), such that during further cutting more extreme temperatures occur on the cutting edge. This was evidenced by Fig. 4(d) (end point for the tool) which featured additional peaks attributed to Fe_2O_3 (hematite). The higher temperatures in the cutting edge region with increased wear triggered this Fe_3O_4 to Fe_2O_3 transformation. The mean cutting temperatures, perhaps 950°C, will result in mobile iron at the tool-chip interface which consequently adheres to the tool surface and oxidises.

Raman mapping (100μm steps over a distance of 2900μm) was implemented to probe for chemical species around the cutting edge from the axis point round to the point of highest radial speed (Figs. 5 and 6). Iron oxide species Fe_3O_4 and Fe_2O_3 were detected.

Fig. 5(c), a spectrum taken from near to the axis of the tool, (i.e. at 500μm) featured a large Fe_3O_4 band with a very small contribution from Fe_2O_3 at 288, 406 and 1308cm^{-1}. Further measurements taken round the cutting edge, at 1300 and 2200μm (i.e. Fig. 5(d) and (e) respectively) showed that the hematite bands grew in intensity indicating a transformation due to higher temperatures with larger tool radii. Fig. 6 shows the integrated intensity of Fe_2O_3 (hematite) bands a function of distance (μm) around the cutting edge.

Hematite is the highest temperature iron oxide phase and has the highest ratio of Fe to O[24]. This phase was monitored as a means of tracking iron oxide phase transformations i.e. "hot-spots". The graph gave evidence of a gradual change from Fe_3O_4 to Fe_2O_3 with superimposed "hot-spot" regions that show higher levels of transformation. Higher temperatures are expected as one goes around the ball nose from the axis point to the point of highest radial speed. However, temperatures were further enhanced at "hot-spot" regions which almost certainly correlated to positions on the tool where deformation and exposed tool material were apparent (see Fig. 3(a)).

It has been well documented[8,11,12] that wear debris from pin-on-disk sliding tests can actually bear the "signature of the wear process" and give additional information on tribochemically produced species and on contact temperatures in the wear zone[11]. Moreover, the chips of material arising from cutting operations can, by the same token, give similar information on the wear process. Therefore chips at various time-points were collected and analysed. An important finding was that a temperature gradient across the chips existed, such that the point on the particle that the tool engaged the work material was the hottest and the point at which the chip was sheared from the workpiece was the coolest. This is represented in Fig. 7, which shows measurements on a chip particle after 70 minutes-in-cut.

From Fig. 7(a) it was apparent that very little oxide was present on the surface of the chip at the shear end since only a low intensity oxide band was observed. The structure of this oxide was identified as being FeO (wüstite) which is meta-stable below 570°C and decomposes to α-Fe and Fe_3O_4[25]. It should be noted that FeO and Fe_3O_4 have almost identical spectra. However, Fe_3O_4 has two additional bands at ca. 305 and 530cm^{-1}[25]. The spectrum taken from the engagement region (Fig. 7(b)) featured a sharp intense band at ~670cm^{-1} in addition to two smaller bands at ~305 and 530cm^{-1}. This was identified as Fe_3O_4 (magnetite), indicating that a phase transformation had occurred due to the higher temperatures at the engagement region. Moreover, as well as oxidation products arising from the work material itself, there were distinct particles of white colouration, 2-5μm in size, adhered to the surface of the engagement end of the chips. These were investigated and found to be oxidation products of the coating. Fig. 8 shows these in comparison with standard spectra of TiO_2 and α-Al_2O_3 oxides (see inset).

The particle observed on the chip arising from cutting at 10,000rpm for 185minutes (Fig. 8(a)) was identified unequivocally as α-Al_2O_3 from good agreement with the standard powder spectrum. It is well known that Al_2O_3 has several phases and the nature of these phases depend strongly on the method and temperature of production[26]. For example, with boehmite as the starting material, γ-Al_2O_3 is formed at 500-850°C, θ-Al_2O_3 is formed between 850 and 1100°C; while above 1100°C with any starting material, only α-Al_2O_3 is formed[26]. To ascertain the temperature at which α-Al_2O_3 forms on the surface of the SUPERCOTE-11 coating a static oxidation experiment was performed (shown in Fig. 9). The temperature of formation of α-Al_2O_3 on the surface of the tool (on the cutting edge) was approx. ≤950°C as signalled by the observation of two intense bands at 1369 and 1398cm^{-1} (see Fig. 8 (inset (iii)) for the standard α-Al_2O_3 spectrum). The exposed cemented carbide material on the shank of the tool was analysed after 700°C (1 hour) and both

WO_3 and a mixed $CoWO_4$ oxide were found (Fig. 9(a)). This further emphasised that the WC - Co should oxidise during cutting after the coating had been removed due to the wear process and indeed these phases were observed after static oxidation of cemented carbide at temperatures >600°C[27]. However, we predict that the transfer layer of iron/iron oxide is partially protecting the underlying tool material from oxidation.

The observation of α-Al_2O_3 on the chip as well as after 950°C on the tool (static oxidation) strongly suggests that when a worn tool nearing the end of life engages the workpiece very high temperatures, perhaps 950°C, are generated at the tool-chip interface. This corresponds favourably to the literature which states that the edge and crater wear increase the stress and strain and also change the cutting forces during milling[5]. From this we can conclude that the mean contact temperature will be greater as the tool becomes increasingly worn thus generating more heat in the cutting region. This is further corroborated by the observation of TiO_2 (anatase) adhered to a chip generated from cutting at 20,000rpm after 35 minutes (Fig. 8(b)) i.e. only within the steady state (II) as opposed to the rapid (III) wear regime. Anatase has a metastable structure which transforms to rutile above 700°C. This implies a much lower contact temperature i.e. ≤700°C and identifies the pronounced effect of the amount of wear on contact temperatures during dry high-speed milling.

4. CONCLUSIONS

Raman microscopy was shown to be a valuable tool in the quest for further understanding of wear processes during dry high-speed milling, giving chemical information on tribochemically produced species. Transfer layers of Fe_3O_4 and Fe_2O_3 were identified on the cutting edge with increased levels of Fe_2O_3 (hematite, the higher temperature phase) around the cutting edge to higher radial speeds, indicating a phase transformation triggered by higher temperatures. Iron oxide species appeared to be most prevalent at sites where spallation and damage had occurred, relating to higher friction / "hot-spot" regions. Chip particle investigations enabled additional information on contact conditions during cutting. Oxidation products of the coatings, i.e. TiO_2 and α-Al_2O_3, adhered to the particles, highlighted oxidational wear as a degradation mechanism. This, in conjunction with static oxidation studies, enabled an estimate of contact temperatures at the tool-chip interface during cutting as ≤950°C with a prominent effect with tool wear.

REFERENCES

1 W.-D. Münz, J. Vac. Sci. Technol. A, 4(6) (1986) 2701.

2 M.I. Lembke, D.B. Lewis, W.-D. Münz, and J.M. Titchmarsh, Surf. Eng. 17(2) (2001) 153-158.

3 L.A. Donohue, I.J Smith, W.-D. Münz, I. Petrov and J.E. Greene, Surf. Coat. Technol. 94-95 (1997) 226-231.

4 I.J. Smith, W.-D. Münz, L.A. Donohue, I. Petrov and J.E. Greene, Surf. Eng. 14 (1998) 37-41.

5 ASM Handbook, Vol. 18 "Friction, Lubrication, and Wear Technology" L. Alden Kendall "Friction and Wear of Cutting Tools and Cutting Tool Materials", ASM International, New York, 1992 p 609-620.

6 B. Malliet, J.P. Celis, J.R. Roos, L.M Stals and M.Van Stappen, Wear, 142 (1991) 151-170.
7 S. Wilson and A.T. Alpas, Surf. Coat. Technol. 108-109 (1998) 369-376.
8 E. Vancoille, B. Blainpain, Ye. Xingpu, J.-P. Celis and J.R. Roos, J. Mater. Res. 9(4), (1994) 992.
9 S. Wilson and A.T. Alpas, Surf. Coat. Technol., 86-87 (1996) 75-81.
10 B. Blainpain, M. Franck, H. Möhrbacher, E. Vancoille, J.-P. Celis and J.R. Roos, in Thin Films in Tribology: Micro-Raman spectroscopy for the characterisation of wear induced surface modifications on hard coatings, D. Dowson et al, (ed.) Elsevier, Amsterdam, 1993, p 623.
11 C.P. Constable, J. Yarwood, P. Hovsepian, L.A. Donohue, D.B. Lewis and W.-D Münz, J. Vac. Sci. Technol. A 18(4) (2000) 1681-1688.
12 E. de Wit, L. Froyen and J.P. Celis, Wear 221 (1998) 125-133.
K. Schouterden, B. Blainpain, J.P. Celis and O. Vingsbo, Wear 181-183, (1995) 86.
13 W.-D. Münz, D. Schulze and F.J.M. Hauzer, Surf. Coat. Technol. 50 (1992) 169.
14 I.J. Smith, D. Gillibrand, J.S. Brooks, W.-D. Münz, S. Harvey and R. Goodwin, Surf, Coat. Technol. 90 (1997) 164-171.
15 C. Dyer and B.J.E. Smith, J. Raman Spectrosc., 26 (1995) 777-785.
16 C.P. Constable, J. Yarwood and W.-D. Münz, Surf. Coat. Technol. 116-119 (1999) 155-159.
17 Q. Luo, W.M. Rainforth and W.-D. Münz, Wear 225-229 (1999) 74-82.
18 Q. Luo, W.M. Rainforth and W.-D. Münz, Scripta Materialia 45 (2001) 399-404.
19 W.-D. Münz, Q. Luo, D.B. Lewis, M. Lembkke, P.Eh. Hovsepian and G. Robinson, conference paper "Wear of TiAlCrYN Coated Ball Nosed Solid Carbide End Mills During Dry High-Speed Milling" p399, Proceedings of the Third Int. Conference on Metal Cutting and High Speed Machining, June 27 (2001) Metz, France.
20 N. Muraki, V. Sergo, G. Pezzotti, G. Katagiri, S. Meriani and T. Nishida, App. Spectrosc. 51(11) (1997) 1761-1765.
21 I. De Wolf, G. Pozzat, K. Pinardi, D.J. Howard, M. Ignat, S.C. Jain and H.E. Maes, Microelectron. Reliab., 36(11/12) (1996) 1751-1754.
22 G. Pezzotti, Comp. Sci. Technol., 59 (1999) 821-831.
23 L.A Falkovsky and J. Camassel, Physica B 284-288 (2000) 1145-1146.
24 Lawrence S. Darken and Robert W. Gurry in "Physical Chemistry of Metals" McGraw Hill, London, 1953, p. 347-359.
25 D.L.A. de Faria, S. Venancio and M.T. de Oliveira, J. Raman Spectros. 28 (1997) 873-878.
26 A. Aminzadeh, Appl. Spectrosc. 51 (1997) 817.
27 M.I. Lembke, D.B. Lewis and W.-D Münz, Surf. Coat. Technol. 125(1-3) (2000) 263-268.

Figures:

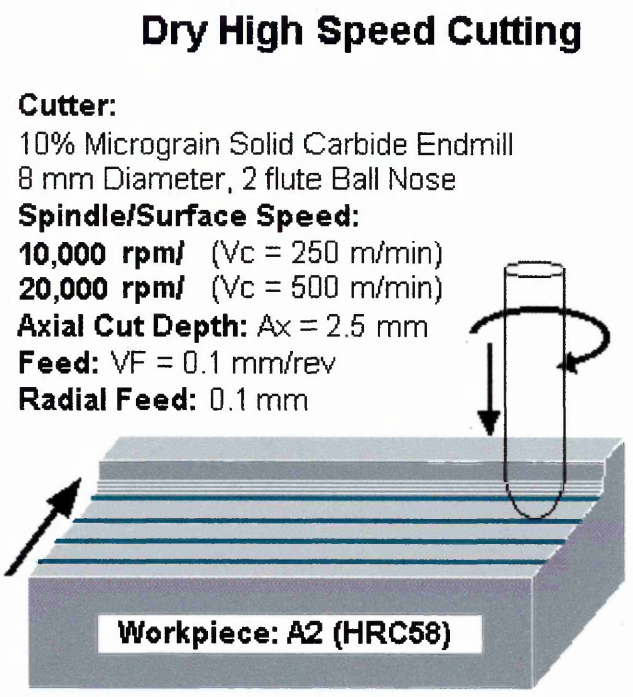

Fig. 1: Schematic diagram showing dry high-speed milling parameters (MAZAK FJ 25 machine tool)

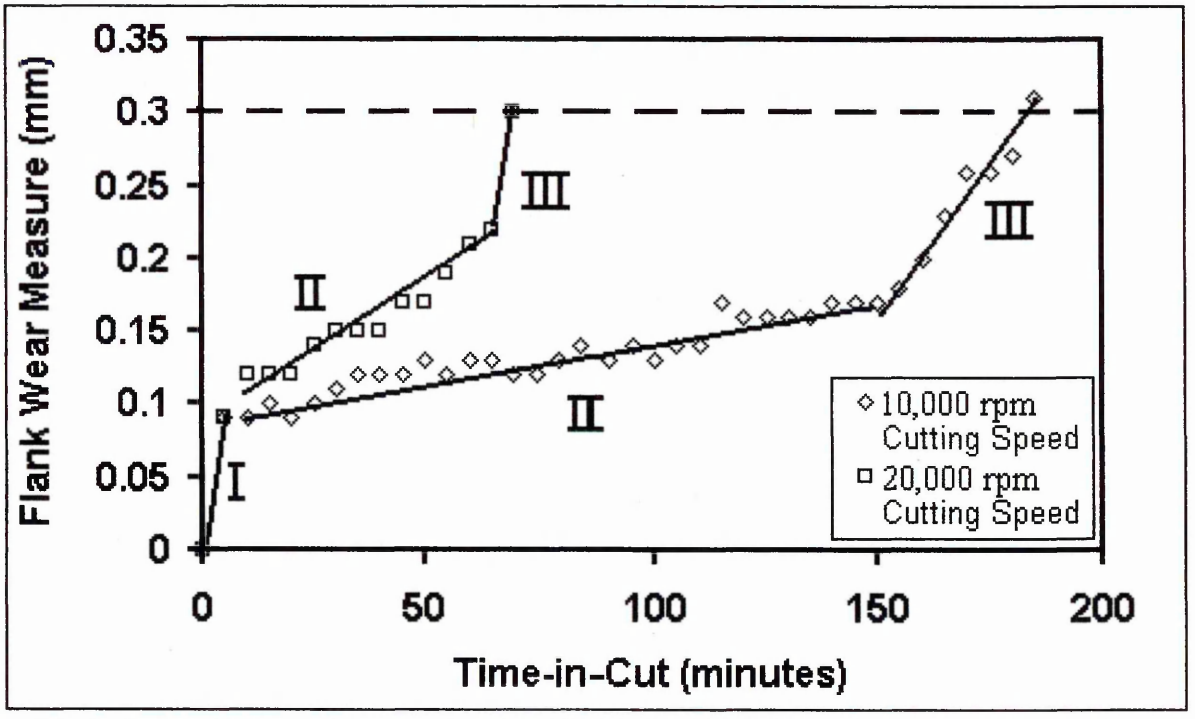

Fig. 2: Graph of flank wear (mm) vs. time-in-cut (min.) for SUPERCOTE-02 at two cutting speeds (dashed line at 0.3mm signifies the wear amount at which the tool is deemed to be at the end of life)

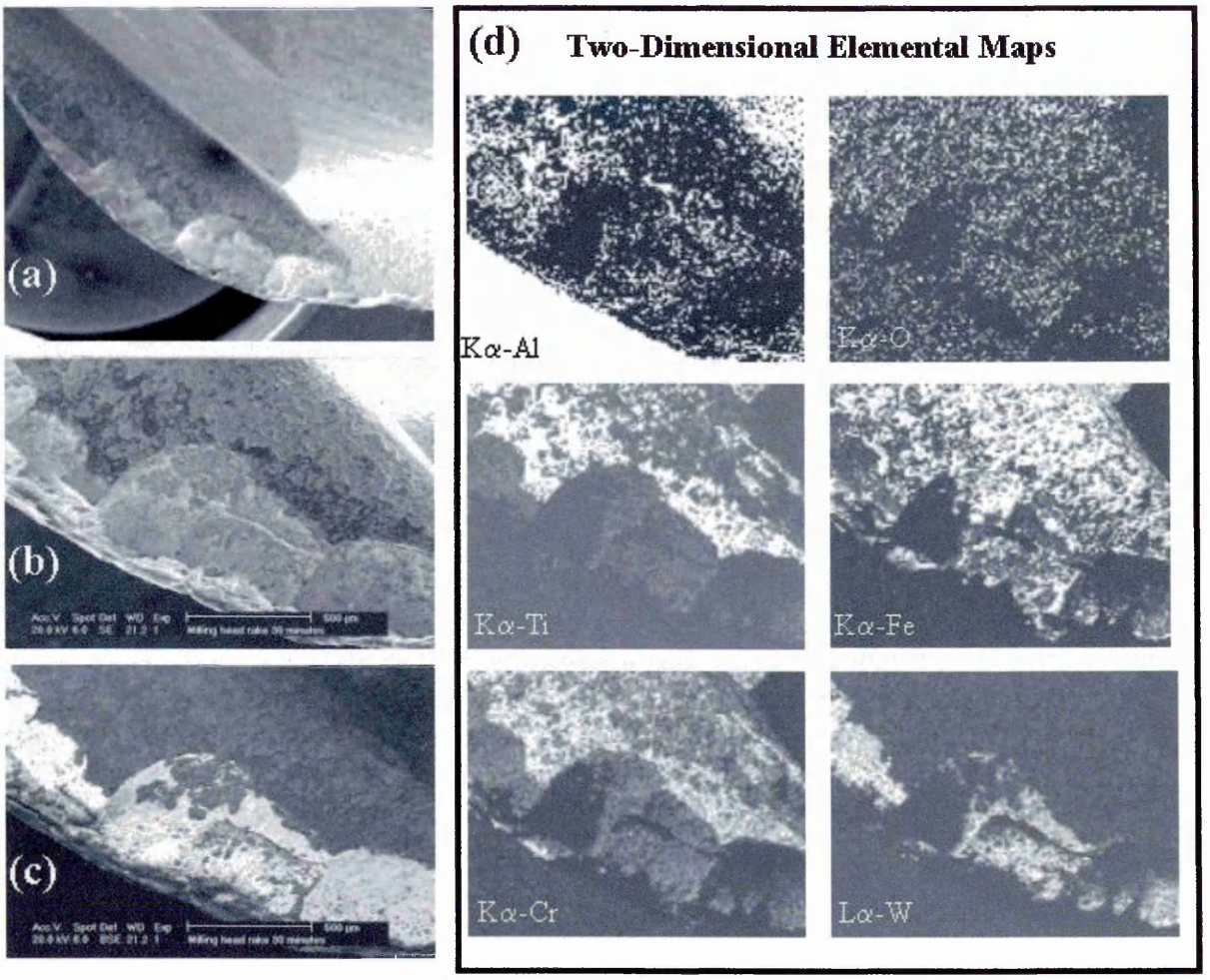

Fig. 3: Secondary electron images (a and b) and back-scattered electron image (c) of the worn cutting edge of a SUPERCOTE-11 coated cemented carbide milling tool after 30 minutes. 3(d) Two-dimensional characteristic X-ray maps of Kα-Al, Kα-Ti, Kα-Cr, Kα-O, Kα-Fe and Lα-W in the corresponding wear features.

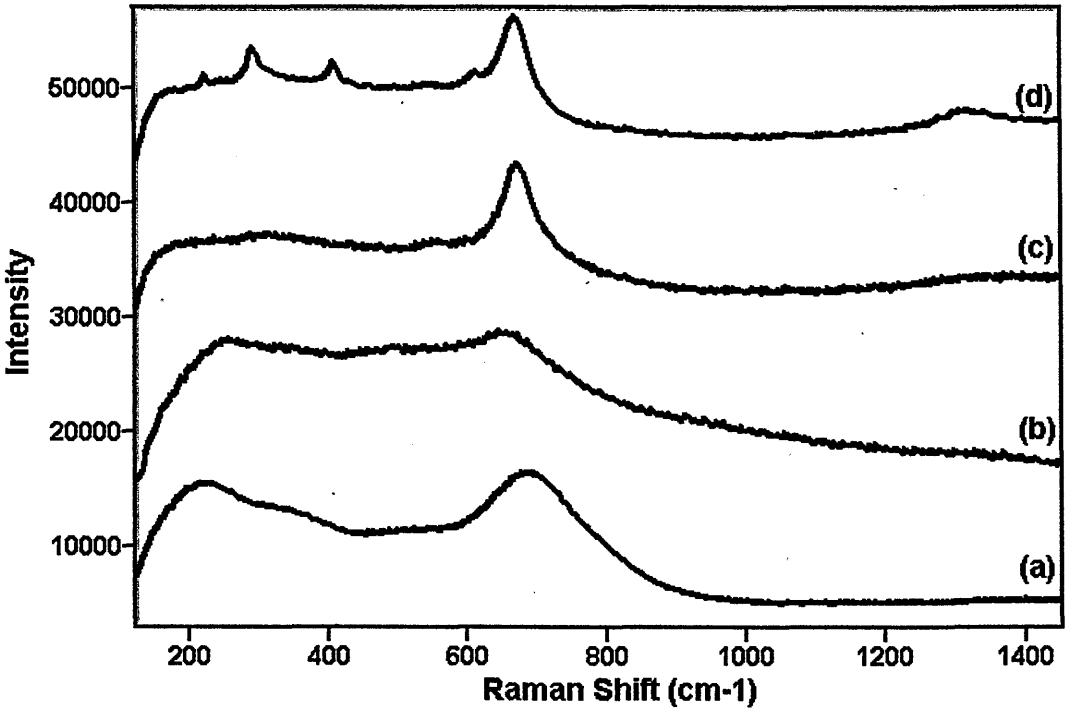

Fig. 4: Rake face of a SUPERCOTE-02 coating after (a) 0 minutes (as-deposited) (b) 5 minutes (c) 35 minutes and (d) 70 minutes (end-point) (N.B. the laser spot was positioned ~2000μm around the cutting edge for each analysis)

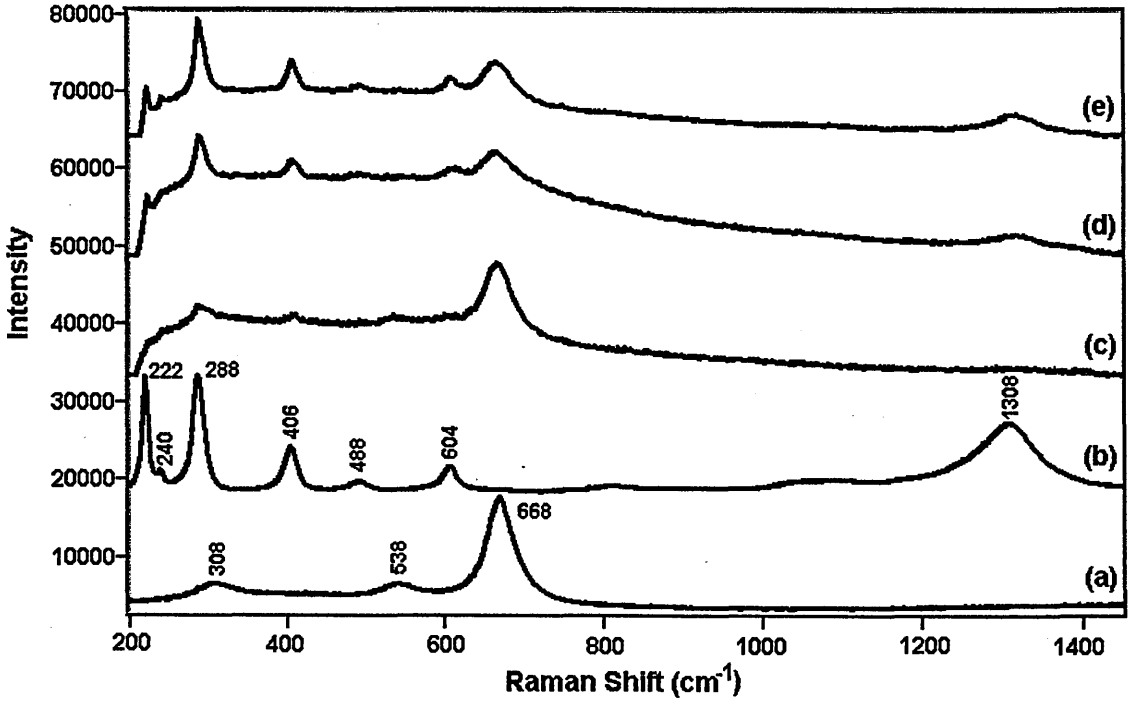

Fig. 5: Analysis positions around the cutting edge (a) and (b) Fe_3O_4 and Fe_2O_3 standard powder spectra respectively (c) 500μm (d) 1300μm and (e) 2200μm

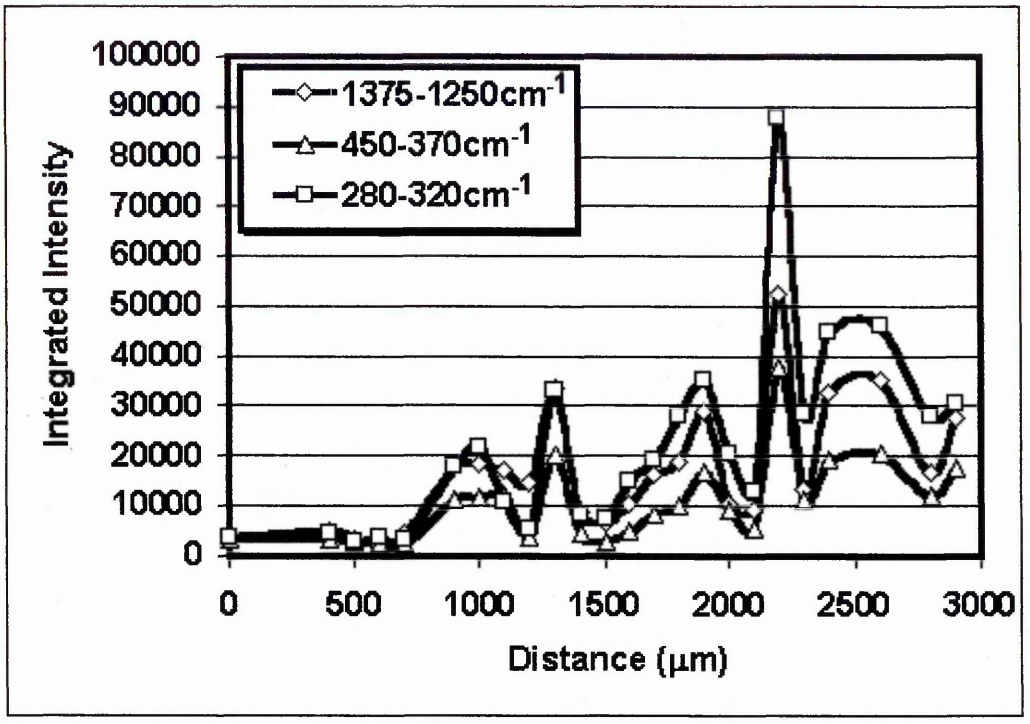

Fig. 6: Graph of integrated intensity of the Fe_2O_3 oxide bands indicating "hot spots" on the tools surface around the cutting edge.

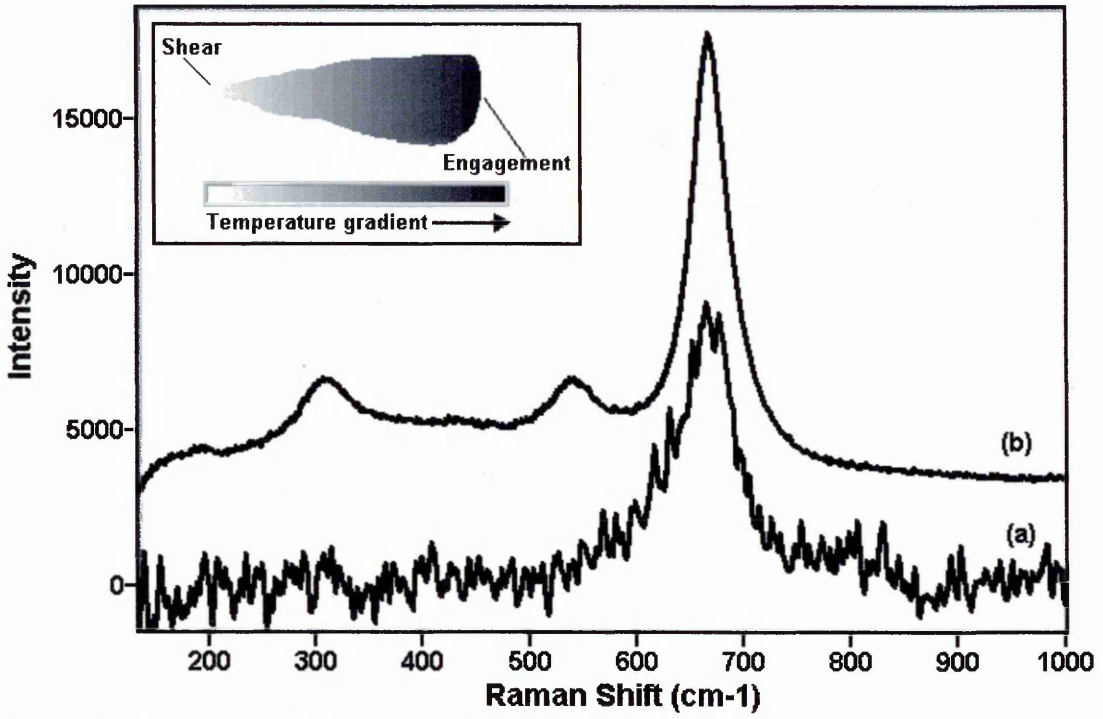

Fig. 7(a) Spectrum taken from the shear zone, and (b) Spectrum taken from the engagement zone after 70 minute-in-cut at 20,000 rpm (inset – schematic of the chip shape and temperature gradient that existed)

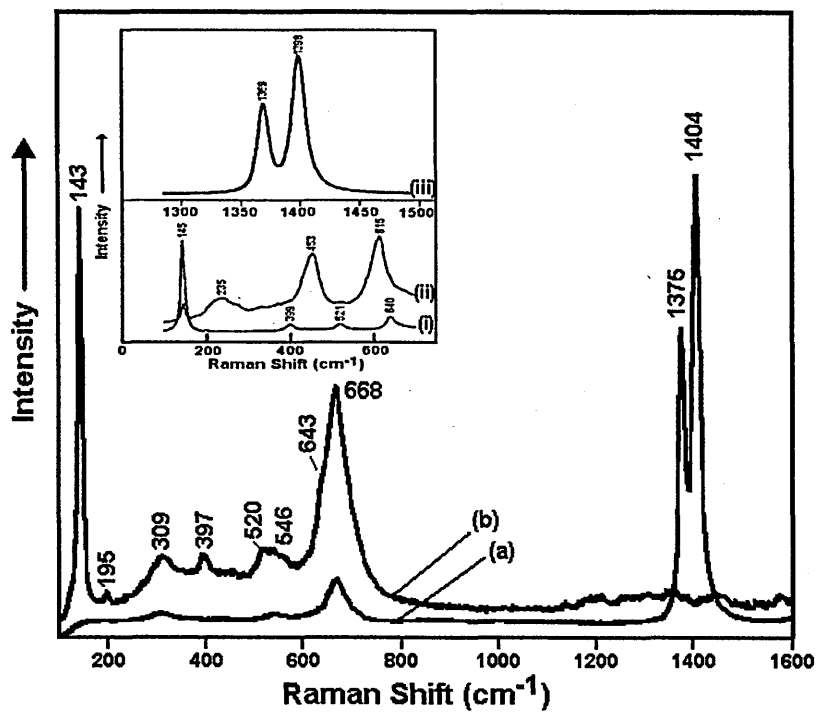

Fig. 8: Specta of coating degradation products adhered to the engagement region of chip particles (a) from cutting at 10,000 rpm for 185 minutes with a SUPERCOTE-11 coated tool and (b) after 35 minutes at 20,000 rpm with a SUPERCOTE-02 coated tool. Inset shows standard spectra of (i) anatase (ii) rutile TiO_2 and (iii) of α–Al_2O_3

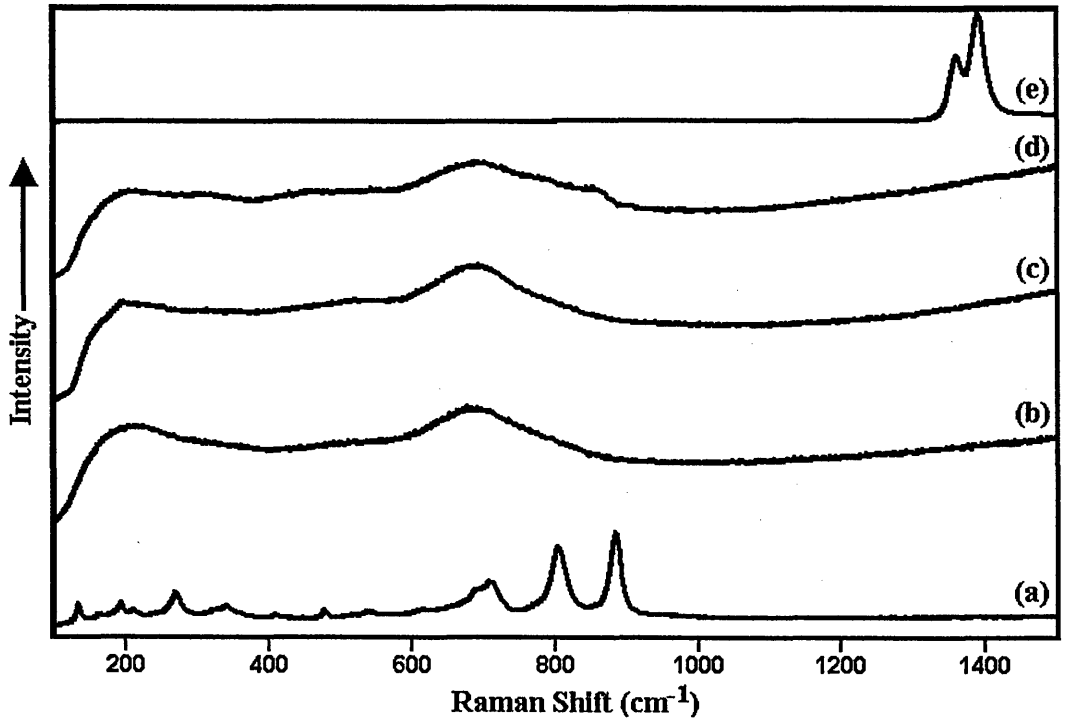

Fig. 9: Static oxidation of a SUPERCOTE-11coated tool (a) shank of the tool after 700°C and the cutting edge (b) after 700°C 1h (c) after 800°C 1h (d) after 900°C 1h and (e) after 950°C 1h